MULTISCALE MODELING OF HYDROGEN ADSORPTION AND STORAGE INTO POROUS FRAMEWORKS FOR CARBON-NEUTRAL ENERGY

Ph.D. Thesis

By

Himani Joshi

DISCIPLINE OF PHYSICS

INDIAN INSTITUTE OF TECHNOLOGY INDORE

February 2026

MULTISCALE MODELING OF HYDROGEN ADSORPTION AND STORAGE INTO POROUS FRAMEWORKS FOR CARBON-NEUTRAL ENERGY

A THESIS

Submitted in partial fulfillment of the requirements for the award of the degree
of
DOCTOR OF PHILOSOPHY

by
HIMANI JOSHI

DISCIPLINE OF PHYSICS
INDIAN INSTITUTE OF TECHNOLOGY INDORE
February 2026

INDIAN INSTITUTE OF TECHNOLOGY INDORE

I hereby certify that the work which is being presented in the thesis entitled **MULTISCALE MODELING OF HYDROGEN ADSORPTION AND STORAGE INTO POROUS FRAMEWORKS FOR CARBON-NEUTRAL ENERGY** in the partial fulfillment of the requirements for the award of the degree of **DOCTOR OF PHILOSOPHY** and submitted in the **DEPARTMENT OF PHYSICS, Indian Institute of Technology Indore**, is an authentic record of my own work carried out during the time period from December 2020 to February 2026 under the supervision of Dr. Srimanta Pakhira, Associate Professor, Department of Physics, Indian Institute of Technology Indore

The matter presented in this thesis has not been submitted by me for the award of any other degree of this or any other institute.

12/06/2026

signature of the student with date
MISS. HIMANI JOSHI

This is to certify that the above statement made by the candidate is correct to the best of my/our knowledge.

Dr. Srimanta Pakhira, Ph.D.
Associate Professor
Department of Physics and
Centre for Advanced Electronics
Indian Institute of Technology Indore, M.P., India

Signature of Thesis Supervisor with date

Dr. SRIMANTA PAKHIRA

MISS. HIMANI JOSHI has successfully given her Ph.D. Oral Examination held on **12 June 2026**.

Dr. Srimanta Pakhira, Ph.D.
Associate Professor
Department of Physics and
Centre for Advanced Electronics
Indian Institute of Technology Indore, M.P., India

Signature of Thesis Supervisor with date

Dr. SRIMANTA PAKHIRA

ACKNOWLEDGEMENTS

First and foremost, I bow in gratitude to my **Isht Dev**, whose divine blessings gave me the strength and courage to begin and successfully complete this PhD journey. Without Your grace, this path would have been impossible. I also express my deepest gratitude to **Sant Premanand Ji Maharaj**, whose teachings continuously illuminated my path, removed negativity from my life, and filled my heart with faith and peace.

I carry my family with me at every step of this journey. **Papa**, I miss you every single day. Your words still echo in my heart: *"Hinnu mera beta hai, bahut bada aadmi banega ek din."* I wish you were here to witness this milestone in my life. Though you are not physically present, your blessings have been my strongest shield, giving me the courage to fulfil my dreams. I am eternally grateful to my **mother**, whose love is deeper than the oceans and whose sacrifices shaped my life. You gave up your own comfort so that we could build a better future. Your progressive mindset, support, and belief in education empowered me to chase my ambitions and stand on my own feet. Whatever I am today is because of you. My heartfelt thanks go to my **younger sister Shivani**. During my five-year absence, you carried the burden of family responsibilities and financial challenges on your shoulders so that I could focus on my career. Your strength, patience, and silent sacrifices will always remain unforgettable. I also thank my **younger brother, Harshit,** for continuously motivating and encouraging me with your kind words and positive energy.

I sincerely thank my PhD supervisor, **Dr Srimanta Pakhira**, for trusting me, accepting me into his research group, and guiding me throughout this journey. Your mentorship, constructive feedback, and scientific insights shaped my growth as a researcher. Your vast knowledge constantly inspired me to think deeper and aim higher. Thank you for recognizing my potential, providing collaborative opportunities, and recommending me for better prospects. I hope to reach a position where you will feel proud of my achievements. I would like to acknowledge the professors (**Dr Santanu Bhattacharya, Dr Ujjawal Pal, Dr Avijit Chowdhury and Prof. Sabuj Kundu**) for their experimental collaboration with us. I extend my gratitude to my **PSPC members, Prof. Sudeshna Chattopadhyay and Prof. Apurba Das**, for their valuable suggestions, constructive feedback, and careful evaluation of my thesis. I also thank the **Department of Science and Technology (DST), Government of India**, for providing financial support through the PhD fellowship. I am thankful to **IIT Indore** for providing excellent research facilities and a supportive academic environment.

I would like to acknowledge my lab members and seniors—**Dr. Nilima, Dr Shrish, Dr Vikash, Dr Ashok, Dikeshwar, Lokesh, Kahkasha, Naveen, Anshuman, Deepesh, and MSc students Kashika and Harshit**—for their collaboration and help. A very special thanks to **Dr Ashok**, whose dedication and discipline deeply inspired me. I learned invaluable lessons from you, both professionally and personally. Thank you for standing beside me during my weakest moments.

I am thankful to all the members of the Animal Welfare Cell for creating unforgettable memories for me. Special thanks to **Moupia and Kirtika** for constantly motivating me, appreciating my efforts, and pushing me to grow as a person. Working with this cell helped me discover a better version of myself. Here, I learned compassion, empathy, and kindness. I am not only earning a PhD but also becoming a better human being. Finally, my deepest love and gratitude go to my **furry babies**. I cannot imagine my five years at IIT Indore without you. When I felt lonely and lost, you gave me a reason to smile, to heal, and to keep going. Your unconditional love, trust, and loyalty transformed my life. Every wagging tail, every excited run towards me erased my stress and pain. You gave me a family away from home, and for that, I will be forever grateful.

In loving memory of my father

SYNOPSIS

1. Motivation and Introduction

Hydrogen storage and its transportation at operational temperatures remain major issues for its commercialization in onboard vehicular applications. The U.S. Department of Energy (DOE) has set hydrogen storage targets for 2025, with ultimate goals of 6.5 wt.% gravimetric capacity and 50 g/L volumetric uptake.[1] To achieve these targets, solid-state hydrogen storage by adsorbing H_2 in porous materials has emerged as the most promising technology, since gas-phase hydrogen storage requires a high-pressure tank and liquid hydrogen can be stored at cryogenic temperatures, which require sophisticated tanks and raise safety concerns.[2] Porous materials such as metal-organic frameworks (MOFs) and covalent-organic frameworks (COFs) offer great promise for enhancing gas storage (especially H_2-storage), CO_2 capture and gas separation performance with minimal effort.[3–6] These materials have attracted significant attention in recent years from the scientific community due to their high surface area, tunable pores, and open metal sites in MOFs, which facilitate stronger binding of adsorbates.[7–9] In 2003, Yaghi *et al.* reported remarkable gravimetric uptake capacities of 4.5 wt.% at 77 K and pressures below 1 atm, and 1 wt.% at room temperature under 20 bar for MOF-5.[10] **Omar Yaghi, Susumu Kitagawa, and Richard Robson were awarded the Nobel Prize in Chemistry in 2025 for the development of MOFs, which can be used to harvest water from desert air, capture carbon dioxide, store toxic gases or catalyze chemical reactions.**

Although numerous MOFs and COFs exhibit high hydrogen uptake capacities at cryogenic conditions (77 K), but their lower performance under ambient conditions hinders their large-scale implementation. At high pressure, adsorbed H_2 molecules gain some thermal energy, so they escape from the binding sites and consequently decrease the binding energy and uptake capacities. Various studies have shown that, at cryogenic conditions, hydrogen storage capacity generally depends on surface properties, such as surface area, pore volume, and pore diameter.[11] However, at an optimal temperature, H_2 storage generally requires high binding enthalpies in the range of -7 to -15 kJ/mol, indicating a transition region between physisorption and chemisorption.[2,7,9] MOF materials with open metal sites have the capability to attract H_2 molecules and thus enhance the

binding enthalpy, and the highest value of H_2 binding enthalpy of -32 kJ/mol was obtained for a newly designed Cu^{I}Zn-MFU-4*l* MOF.[12] As COF materials are purely constituted by the light elements (C, H, N, O, B and Si) due to the absence of active sites, these pristine COF materials show very low H_2 binding. Various strategies are used in COFs to introduce active sites into their structures to enhance H_2 binding and uptake. Some of the most widely used strategies are alkali metal atom doping, transition metal doping or chelation, ligand functionalization, and intercalation of metal atoms.[13–19] Few adsorbents balance high gravimetric and volumetric capacities, although MOFs have recently been recognized as helpful for minimizing this research gap. Computational methods are highly valuable in accelerating this research. In gas storage, multiscale modelling has enabled screening of MOFs and COFs with high potential for gas storage applications. Promising MOF and COF materials could be identified by integrating the density functional theory (DFT) calculations with Grand Canonical Monte Carlo (GCMC) simulations.

2. Computational Details

DFT calculations were performed to obtain equilibrium geometries and to calculate binding enthalpies. The periodic DFT computations were carried out using the CRYSTAL 17,[20] Non-periodic calculations were performed using the Gaussian 16 software.[21] The exchange correlation hybrid functional B3LYP was used with Grimme's dispersion correction (-D3) to get the accurate values of binding energies.[22,23] It has also been reported that the B3LYP hybrid functional was the best among the commonly used functionals for the cluster models. LANL2DZ and cc-pVDZ basis sets were used for transition metal atoms and other atoms (C, H, N, O and B), respectively.[24] The values of binding enthalpy were calculated using the following equation:[25]

$$\Delta H = H_{MOF/COF+H_2} - \left(H_{MOF/COF} + H_{H_2}\right) \qquad (1)$$

The geometric and physical features of porous COFs and MOFs were calculated using the RASPA suite code.[26] Hydrogen adsorption capacities of porous materials were widely computed via GCMC simulations and implemented by the RASPA package. The nonbonded interactions of H_2-MOF/COF and H_2-H_2 were described by the Lennard-Jones (L-J) potential and electrostatic interaction based on Coulomb's law:[27]

$$U(ij) = 4\varepsilon_{ij}\left[\left(\frac{\sigma_{ij}}{r_{ij}}\right)^{12} - \left(\frac{\sigma_{ij}}{r_{ij}}\right)^{6}\right] + \frac{1}{4\pi\varepsilon_0}\frac{q_i q_j}{r_{ij}} \qquad (2)$$

MOFs and COFs were assumed to have rigid frameworks using Lennard-Jones (LJ) parameters from the Universal Force Field (UFF) and the Dreiding force field.[28][29] Lorentz-Berthelot combination rules were used to calculate Lennard-Jones parameters for intermolecular interactions.[30] The cutoff distance for L-J interactions was set to 12 Å. The partial atomic charges of MOFs were estimated using the charge equilibration method, which is utilized to rapidly and accurately evaluate electrostatic interactions of H_2-MOF via Ewald summation.[31] To validate the accuracy of the H_2 simulation in our work, we have compared the H_2 adsorption capacity at various temperatures and high pressure with experimental data from similar MOFs reported in prior studies.

3. Thesis Objectives

Objective 1. Enhancement of H_2 Physisorption in Covalent Organic Framework's Linkers by Li-decoration [32]

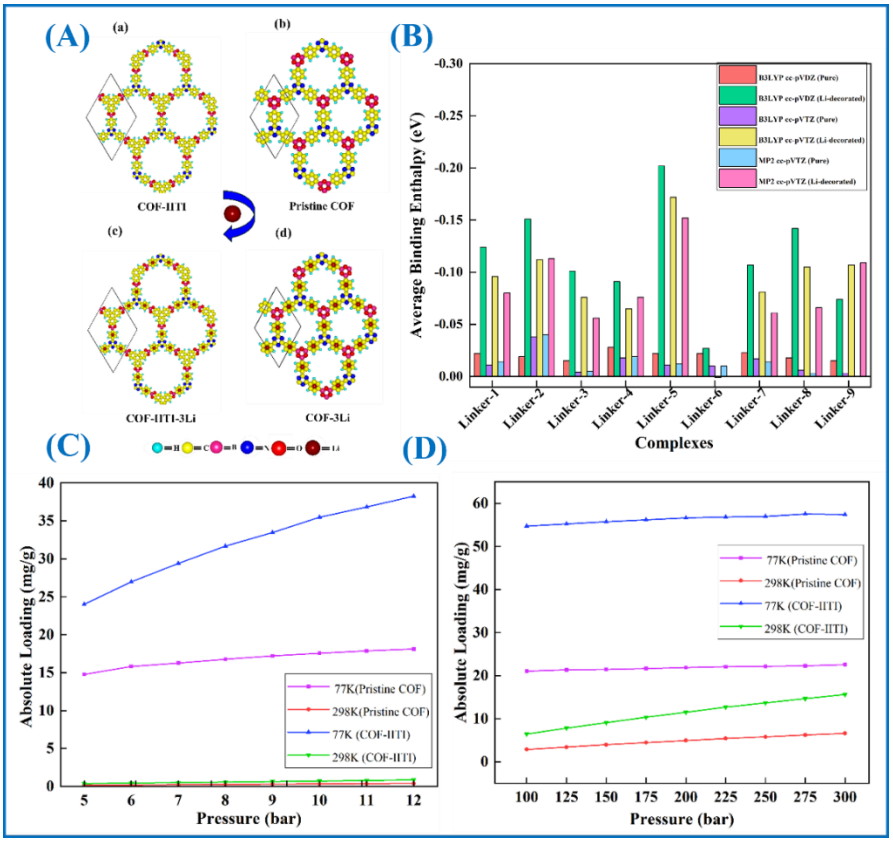

Scheme 1. *(A) Equilibrium structures of pristine and Li-decorated COFs, (B) average binding enthalpy per H_2 for COF linkers, (C) absolute loading for pristine COFs at low pressure, and (D) absolute loading for pristine COFs at high pressure.*

Summary: In the present study, we have employed Li-decorating techniques with nine organic linkers from our designed COFs and have explored their H_2-binding properties and H_2-uptake capacity. The paramount goal of this work is to present an elementary analysis of the mechanism of hydrogen physisorption on Li-decorated COF linkers and to understand the nature of interactions responsible for H_2 adsorption in the COFs.

The theoretical study of the quantum nature of H_2 interactions is the backbone of experimental results and is useful for unravelling the storage properties of porous materials. Our study suggests that decorating the COF with a Li atom is a suitable strategy for practical H_2 storage, potentially achieving the USDOE target. The Li binding energy in the COF linker was in the range of -0.5 to -1.3 eV, computed by both the B3LYP-D3 and MP2 methods, which is a remarkable value for strong binding between the Li atoms and linkers. It was observed that the Li atom prefers to interact with the phenyl rings, with the most negative binding energy (ΔE_b) of -1.11eV. Linker-5 shows the most favorable binding enthalpy value of -0.20 eV, satisfying the optimal binding enthalpy range of -0.15 to -0.25 eV, which is a must for practical H_2 storage at ambient conditions. However, the calculated vibrational frequencies and binding energies indicate that the systems are stable, which can be further integrated into COFs. Thus, we expect these COF model systems to be readily fabricated experimentally and studied for H_2 storage in the near future. We have performed GCMC simulations on pure COFs (Pristine COF and COF-IITI) and found that our designed COFs outperform some previously reported COFs for H_2 uptake at 77 K and 100 bar. We found that the maximum loading is approximately 38.27 mg/g for the COF-IITI at 77K and 12 bar. The isotherms increase approximately linearly when pressure increases from 100 to 300 bars. The H_2 absolute loading is higher at low temperature than at room temperature. COF-IITI shows 57.41 mg/g at high pressure, and the Pristine-COF shows 22.56 mg/g H_2 loading at 300 bars. The COF-IITI appears more effective for H_2 uptake than the pristine COF. This is consistent with the large surface area and pore volume, which increase the H_2 uptake in porous materials. Our calculated H_2 loading results for COF-IITI at 77K and 100 bar are better than those previously reported for COF-1, COF-5, COF-6, COF-8, and COF-10.

Objective 2. Role of the Quantum Interactions in H_2 Adsorption on Late Transition Metal Chelated Linkers of Covalent Organic Frameworks [15]

Summary: Transition-metal (Tm) chelation is an effective strategy to achieve optimal binding enthalpy (ΔH) for H_2 adsorption in the linkers of COFs. The first principle-based DFT method was implemented to determine H_2 adsorption on nine organic linkers and transition-metal chelated linkers. The obtained range of binding enthalpy for single H_2 adsorbed on the pure and chelated complexes is −7 to −20 kJ/mol, which is required for onboard H_2 storage. The Linker-3 chelated with Ni (II) metal exhibits the most favorable binding enthalpy of approximately −18.72 kJ/mol for the single adsorbed H_2 molecule, which falls within the physisorption range.

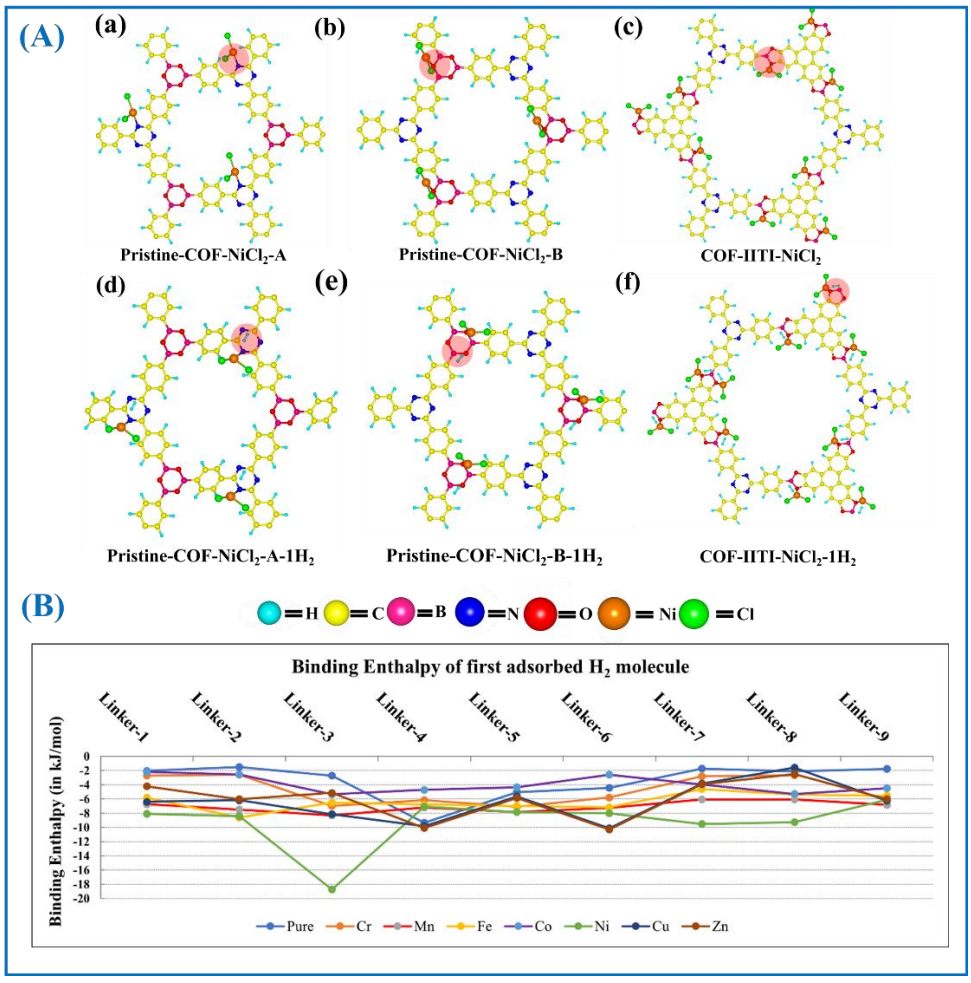

Scheme 2. *(A) Equilibrium structures of Ni-chelated COFs and with adsorbed H_2 molecules, and (B) binding enthalpy of first adsorbed H_2 molecules of pure and chelated COF linkers.*

Some of the complexes have shown binding enthalpies spanning physisorption to chemisorption, and in such cases, H_2 binds via Kubas interactions. However, physisorption-based complexes are preferable to others because physisorption is a reversible process with rapid kinetics. This study reveals that dispersion, polarization, and electrostatic interactions mainly contribute to the binding enthalpy of H_2 adsorption. Molecular surface potential analysis verifies the origin of the induced dipole moment in the H_2 molecule, thereby enhancing hydrogen adsorption in transition-metal-chelated COFs.

Objective 3. Hydrogen Storage Capacities in Nanoporous M_2(*m*-dobdc) Metal-Organic Frameworks at Near Ambient Temperatures [33]

Summary: We selected M_2(*m*-dobdc) MOFs and evaluated their H_2 adsorption properties under conditions applicable to onboard H_2 storage in vehicles. Our results reveal that the Fe_2(*m*-dobdc) MOF exhibits a superior gravimetric capacity value of 4.24 wt.% under cryogenic conditions and an exceptional volumetric capacity value of 12.36 g/L at room temperature compared to other MOFs in the chosen M_2(*m*-dobdc) series. To date, these calculated volumetric H_2 uptake capacities are the highest reported for MOFs at room temperature. This finding indicates that the gravimetric H_2 uptake capacities of M_2(*m*-dobdc) MOFs at 77 K and 100 bar are quite close to the DOE target for 2025, 5.5 wt%. The calculated values of volumetric H_2 uptake in Ni_2(*m*-dobdc) and Co_2(*m*-dobdc) MOFs show good agreement with previously reported experimental values for these MOFs under various temperature and pressure conditions.

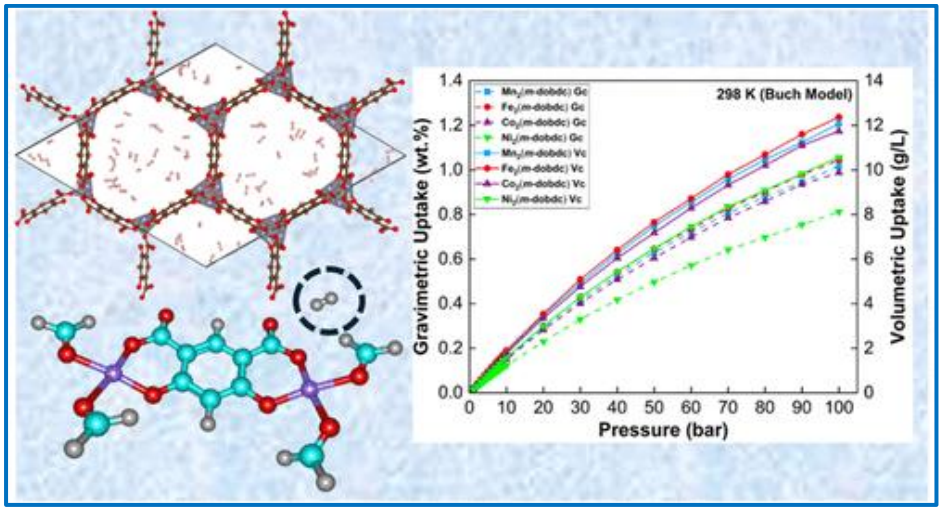

Scheme 3. *H_2 adsorption and uptake capacities at room temperature in M_2(m-dobdc) MOFs.*

The simulated heat of H_2 adsorption of the M_2(*m*-dobdc) MOFs at 298 K and 100 bar ranges from -11.5 to -13.0 kJ/mol at high pressure. The M_2(*m*-dobdc) series MOFs have shown a promising deliverable volumetric H_2 capacity of 36.3 g/L to 40.8 g/L, compared to some well-known MOF materials in the temperature-pressure swing range (77 K/100 bar to 160 K/5 bar). The volumetric H_2 uptake capacity of M_2(*m*-dobdc) outperforms those of leading nanoporous MOFs with open metal sites, such as Cu^I-MFU-4*l* and $V_2Cl_{2.8}$(BTDD), under comparable conditions. Future work will focus on enhancing the density of active M(II) sites in M_2(*m*-dobdc) through targeted ligand modifications and on modifying the geometry of transition-metal centres in MOFs to control the strength of π-back-bonding interactions. This study marks an important step toward the design of next-generation MOFs capable of integrated H_2-storage under industrial conditions. In the case of these specific MOFs, the M_2(*m*-dobdc) MOF series with open metal sites, there is a need to develop more accurate polarized force fields for CO_2 to metal interactions. We believe that future efforts should involve quantum mechanical (QM) calculations to parameterize these interactions. This is a direction we intend to explore in our future studies.

4. Conclusions

The need for lightweight adsorbents that can perform well in ambient conditions is crucial for hydrogen storage in fuel cell vehicles. By carefully selecting COF linkers and adopting strategies to enhance H_2 binding, researchers can focus on designing three-dimensional COF frameworks with high H_2-uptake capacities. Computational simulations can be used to tune the binding enthalpy and to study gas adsorption isotherms under varying temperature and pressure conditions. In our Li-decorated and transition-metal-chelated COF linkers, we found that the dispersion, electrostatic, and polarization interactions mainly contribute to H_2 binding enthalpy. In our Monte Carlo study, we found that the volumetric delivery amount for M_2(*m*-dobdc) MOFs reaches the 2025 DOE target of 40 g/L at 77 K, and the room-temperature volumetric uptakes are also satisfactory. However, none of the MOFs in this series meets the 2025 DOE gravimetric target of 5.5 wt%. The best volumetric uptake is found for the Fe_2(*m*-dobdc) MOF, where the surface area is larger than that of other MOFs of this series.

In summary, four key strategies can be adopted to enhance both the binding enthalpy and hydrogen uptake capacity of porous materials: (a) designing materials with high surface area where

all atomic sites are accessible to adsorbates, (b) optimizing pore volume to achieve an appropriate balance between gravimetric and volumetric storage capacities, (c) improving hydrogen binding affinity by incorporating coordinatively unsaturated or partially charged lightweight metal centers that facilitate electrostatic charge-quadrupole, charge-induced dipole, and occasionally charge transfer interactions, including σ-donation from H_2 to the metal-center, the magnitude of these interactions being strongly dependent on the nature and charge of the metal, and (d) ensuring sufficient polarization of the hydrogen molecule to attain a practical adsorption enthalpy, which largely depends on the geometry of the metal coordination environment and the presence of a strong electrostatic dipole or quadrupole moment.

5. References

[1] US Department of Energy, U.S Drive (2017) 1–29.

[2] S. Pakhira, J.L. Mendoza-Cortes, Journal of Physical Chemistry C 124 (2020) 6454–6460.

[3] A. Vaidyanathan, P. Mane, V. Wagh, B. Chakraborty, Journal of Energy Storage 78 (2024) 109899.

[4] H. Furukawa, O.M. Yaghi, Journal of the American Chemical Society 131(2009) 8875–8883.

[5] M.T. Kapelewski, S.J. Geier, M.R. Hudson, D. Stück, J.A. Mason, J.N. Nelson, D.J. Xiao, Z. Hulvey, E. Gilmour, S.A. Fitzgerald, M. Head-Gordon, C.M. Brown, J.R. Long, Journal of the American Chemical Society 136 (2014) 12119–12129.

[6] N.T. Xuan Huynh, O.M. Na, V. Chihaia, D.N. Son, RSC Advances 7 (2017) 39583–39593.

[7] Y. Pramudya, J.L. Mendoza-Cortes, Journal of the American Chemical Society 138 (2016) 15204–15213.

[8] R. Chakraborty, J.J. Talbot, H. Shen, Y. Yabuuchi, K.M. Carsch, H.Z.H. Jiang, H. Furukawa, J.R. Long, M. Head-Gordon, Physical Chemistry Chemical Physics 26 (2024) 6490–6511.

[9] M. Djokic, J.L. Mendoza-Cortes, Energy and Fuels 38 (2024) 4711–4720.

[10] N.L. Rosi, J. Eckert, M. Eddaoudi, D.T. Vodak, J. Kim, M. O'Keeffe, O.M. Yaghi, Science 300 (2003) 1127–1129.

[11] P. García-Holley, B. Schweitzer, T. Islamoglu, Y. Liu, L. Lin, S. Rodriguez, M.H. Weston, J.T. Hupp, D.A. Gómez-Gualdrón, T. Yildirim, O.K. Farha, ACS Energy Letters 3 (2018) 748–754.

[12] Y. Yabuuchi, H. Furukawa, K.M. Carsch, R.A. Klein, N. V. Tkachenko, A.J. Huang, Y. Cheng, K.M. Taddei, E. Novak, C.M. Brown, M. Head-Gordon, J.R. Long, Journal of the American Chemical Society 146 (2024) 22759–22776.

[13] Z. Ke, Y. Cheng, S. Yang, F. Li, L. Ding, International Journal of Hydrogen Energy 42 (2017) 11461–11468.

[14] A. Mavrandonakis, E. Tylianakis, A.K. Stubos, G.E. Froudakis, Journal of Physical Chemistry C 112 (2008) 7290–7294.

[15] H. Joshi, S. Pakhira, ChemPhysChem 16(2024) e202400237.

[16] N. Sinha, S. Pakhira, Molecular System Design & Engineering 7(2022) 577–591.

[17] H. Joshi, S. Pakhira, International Journal of Hydrogen Energy 79 (2025) 1139–1154.

[18] R.T. Sanderson, Science 114 (1951) 670–672.

[19] S. Pakhira, J.L. Mendoza-Cortes, Physical Chemistry Chemical Physics 21 (2019) 8785–8796.

[20] R. Dovesi, A. Erba, R. Orlando, C.M. Zicovich-Wilson, B. Civalleri, L. Maschio, M. Rérat, S. Casassa, J. Baima, S. Salustro, B. Kirtman, Wiley Interdisciplinary Reviews: Computational Molecular Science 8 (2018) e1360.

[21] D.J. Frisch, M. J.; Trucks, G. W.; Schlegel, H. B.; Scuseria, G. E.; Robb, M. A.; Cheeseman, J. R.; Scalmani, G.; Barone, V.; Petersson, G. A.; Nakatsuji, H.; Li, X.; Caricato, M.; Marenich, A. V.; Bloino, J.; Janesko, B. G.; Gomperts, R.; Mennucci, B.; Hratch, Gaussian, Inc., Wallingford CT, 2019.

[22] A.D. Becke, Journal of Chemical Physics 98 (1993) 5648–5652.

[23] S. Grimme, J. Antony, S. Ehrlich, H. Krieg, Journal of Chemical Physics 132 (2010) 154104.

[24] J. Laun, D. Vilela Oliveira, T. Bredow, Journal of Computational Chemistry 39 (2018) 1285–1290.

[25] S. Pakhira, J.L. Mendoza-Cortes, Journal of Physical Chemistry C 124 (2020) 6454–6460.

[26] D. Dubbeldam, S. Calero, D.E. Ellis, R.Q. Snurr, Molecular Simulation 42 (2016) 81–101.

[27] D. Sengupta, P. Melix, S. Bose, J. Duncan, X. Wang, M.R. Mian, K.O. Kirlikovali, F. Joodaki, T. Islamoglu, T. Yildirim, R.Q. Snurr, O.K. Farha, Journal of the American Chemical Society 145 (2023) 20492–20502.

[28] A. K. Rappi, C. J. Casewit, K. S. Colwell, W. A. Goddard III, W. M. Skiff, Journal of the American Chemical Society 114(1992) 10024–10035.

[29] S.L. Mayo, B.D. Olafson, W.A. Goddard, Journal of Physical Chemistry 94 (1990) 8897–8909.

[30] H.A. Lorentz, Annals of Physics 248 (1881) 127–136.

[31] A.K. Rappé, W.A. Goddard, Journal of Physical Chemistry 95 (1991) 3358–3363.

[32] H. Joshi, S. Pakhira, International Journal of Hydrogen Energy 79 (2024) 1139–1154.

[33] H. Joshi, S. Pakhira, ACS Applied Nanomaterials 8 (2025) 19167-19178.

LIST OF PUBLICATIONS

Publications Related to Thesis:

1. **Himani Joshi** and Srimanta Pakhira** **2024** Enhancement of H_2 Physisorption in Covalent Organic Framework's Linkers by Li-Decoration, *International Journal of Hydrogen Energy*, 79, 1139-1154.
2. **Himani Joshi** and Srimanta Pakhira** **2024** Role of the Quantum Interactions in H_2 Adsorption on Late Transition Metal Chelated Linkers of Covalent Organic Frameworks, *ChemPhysChem*, 25, e202400237.
3. **Himani Joshi** and Srimanta Pakhira** **2025** Hydrogen Storage Capacities in Nanoporous M_2(*m*-dobdc) Metal-Organic Frameworks at Near Ambient Temperatures. *ACS Applied Nanomaterials*, 8, 19167–19178.

Publications other than Thesis:

1. Swapnamoy Pramanik, Suma Das, **Himani Joshi**, Srimanta Pakhira**, Avijit Chowdhury* **2026** Silver Quantum Dots-Mediated Band Engineering in Graphitic Carbon Nitride for Photocatalytic Hydrogen Generation. *ACS Applied Nano Materials*. DOI: https://doi.org/10.1021/acsanm.6c00990
2. Shrish Nath Upadhyay, **Himani Joshi**, Naveen Sharma, Srimanta Pakhira** **2026** Two-Dimensional Materials as Emerging Electrocatalysts for HER, ORR, and OER: Design Strategies, Challenges, and Prospects in Sustainable Energy Conversion. *Physical Chemistry Chemical Physics*. DOI: https://doi.org/10.1039/D6CP00222F
3. Vinay Kumar Sriramadasu[†], **Himani Joshi**[†], Iba Lyngdomh, Naveen Sharma, Srimanta Pakhira* and Santanu Bhattacharyya* **2026** Insight into Multivalent Iron Complex Bounded Oxygen Vacancy-Rich BiOBr Nanodiscs for Photocatalytic Ammonia Synthesis. *Journal of Materials Chemistry A*, 4, 1782-1792.
4. Nageshwarrao Chanda, Bhavya Jaksani, Sukanya Saha, Ashok Singh, **Himani Joshi**, Naveen Sharma, Srimanta Pakhira, Ujjwal Pal*, Mohsen Ahmadipour* **2025** $CaCu_3Ti_4O_{12}$/CNT nanocomposite for enhanced photocatalytic seawater splitting to hydrogen generation, *International Journal of Hydrogen Energy,* 140, 36-44.
5. Vinay Kumar Sriramadasu, **Himani Joshi**, Satish Kumar Patro, Naveen Sharma, Ashok Singh, Srimanta Pakhira*, Santanu Bhattacharyya* **2025** Low Bandgap $NiCo_2S_4$ Nanoparticles Decorated 2D-BiOBr Nano Pallets: Atomic Level Insight into the Active Sites for Photocatalytic H_2O_2 Production, *Small,* 21, 2503321.

6. Vikash Kumar, **Himani Joshi**, Naveen Sharma, and Srimanta Pakhira** **2025** Electrocatalytic Activity of Post Nb-doped 2D $MoSe_2$ TMD Towards Highly Effective H_2 Evolution Reaction, *ChemCatChem*, e00157.
7. Kashika Khatri, Naveen Sharma, **Himani Joshi**, and Srimanta Pakhira** **2025** Unravelling the Electrocatalytic Activity of $LaFeO_3$ Perovskite Towards O_2 Reduction Reaction*, Energy and Fuels,* 39, 9066–9080.
8. **Himani Joshi**†, Nilima Sinha†, Kahkasha Parveen† and Srimanta Pakhira** **2023** Unveiling Electrocatalytic Activity of Cobaloxime Metallolinker in UU-100(Co) Metal-Organic Frameworks towards H_2 Evolution Reaction: A DFT Study, *Energy and Fuels*, 37, 19771–19784.
9. Nilima Sinha, **Himani Joshi** and Srimanta Pakhira**, **2022** Lithium Intercalation in Covalent Organic Frameworks: A Porous Electrode Material for Lithium-Ion Battery, *ACS Applied Electronic Materials*, 4, 6237-6252.

Table of Contents

Introduction and Motivation 32

1.1. Need for Hydrogen Energy 32

1.2. Hydrogen Storage Methods 34

1.3. Porous Materials for H_2 storage 35

1.4. Objectives 45

1.5. Recent Developments in the Field of Porous Materials for Hydrogen Storage 45

1.6. Challenges in the Hydrogen Storage on Porous Materials 49

1.7. References 50

Principles of DFT Methods and Monte Carlo Simulations 55

2.1. Many Body Equations 55

2.2. Born-Oppenheimer Approximation 56

2.3. Slater Determinant 57

2.4. Basis Function 59

2.5. Hohenberg-Kohn Theorem 61

2.6. Kohn-Sham (KS) Method 62

2.7. Classification of Exchange-Correlation Functionals 64

2.8. van der Waals (vdW) Correction 67

2.9. Software used in our DFT and DFT-D Calculations 68

Introduction to Monte Carlo (MC) Simulations 79

2.10. Interatomic Potentials: The Foundation of Molecular Interactions 79

2.11. Specialized Models for Hydrogen 82

2.12. Feynman-Hibbs (FH) Effective Potential 84

2.13. Monte Carlo Simulations: Computational Methodology 84

2.14. Adsorption Fundamentals in Porous Materials 87

2.14.1. Types of Adsorptions in Porous Materials 87
2.14.2. Adsorption Isotherm 87
2.14.3. Geometric Properties of Porous Materials 87
2.14.4. Performance Analysis 89
2.15. RASPA Software 90
2.16. References 92
Enhancement of H_2 Physisorption in Covalent Organic Framework's Linkers by Li-decoration 96
3.1. Introduction 96
3. 2. Methodology, computational details, and material description 98
3.2.1. Computational Details 98
3.2.2. Materials description 101
3.3. RESULTS AND DISCUSSION 103
3.3.1. Li-decoration in linkers 103
3.3.2. H_2 Physisorption in the Li-decorated linkers 105
3.3.3. Dispersion Energy and EDA Analysis 113
3.3.4. Vibrational spectroscopic properties of the adsorbed H_2 116
3.3.5. Highest occupied molecular orbital and lowest unoccupied molecular orbital (HOMO-LUMO) analysis 117
3.3.6. Partial density of states (PDOS) of adsorption of H_2 molecules in both the pure and Li-decorated linkers 119
3.3.7. H_2 Uptake in both the pure and Li-decorated linkers 120
3.3.8. Adsorption isotherms and desorption temperature (T_d) 121
3.4. Conclusions 123
3.5. References 124
Role of the Quantum Interactions in H_2 Adsorption on Late Transition Metal Chelated Linkers of Covalent Organic Frameworks 129

4.1. Introduction 129

4.2. Material design and Computational details 132

4.3. Results and Discussion 134

4.3.1. Chelation of transition metal atoms in the pure organic linkers 134

4.3.2. Interaction of H_2 molecules with chelated COFs 135

4.3.3. Adsorption of the first H_2 molecule in both the pure and transition-metal chelated periodic COFs 143

4.3.4. Adsorption of four H_2 molecules in the pure and transition metal chelated organic linkers 146

4.3.5. H_2 uptake capacities in weight percentage 154

4.3.6. Type of interactions controlling the binding enthalpy value 156

4.3.7. Molecular electrostatic potential mapping 158

4.3.8. Study of global indices of reactivity and HOMO-LUMO gap 159

4.4. Conclusions 162

4.5. References 163

H_2 Storage Capacities in Nanoporous M_2(*m*-dobdc) Metal-Organic Frameworks at Near Ambient Temperatures 168

5.1. Introduction 169

5.2. Theory, Computational Methods, and Material Description 171

5.2.1. Theory and Computational Details 171

5.2.2. Properties of MOF Materials 174

5.3. Results and Discussion 177

5.3.1. Isosteric Heat of Adsorption (Q_{st}) 177

5.3.2. H_2 Adsorption Isotherms 178

5.3.3. Gravimetric and Volumetric H_2 Uptake Capacities of M_2(*m*-dobdc) MOFs 184

5.4. Conclusions 192

5.5. References....193

Future Research Scope....199

6.1. Linker functionalization and node modification....199

6.2. Designing of hybrid materials and MOF-COF composites....199

6.3. High-throughput computational screening and development of force fields for flexible frameworks....201

6.4. Combination of computational insights and theoretical predictions with real-world MOF synthesis....202

6.5. References....203

Appendix-A....205

LIST OF FIGURES

Figure 1.1. (a) Global H_2 demand by sector from 2020 to 2030 and (b) regional distribution of hydrogen demand. The bar chart illustrates the projected increase in hydrogen consumption across various sectors, including industry, refining, transport, synthetic fuels, and others. The pie chart highlights the regional share of hydrogen demand, with China, North America, and the Middle East as major contributors.

Figure 1.2. The assembly of covalent organic frameworks (COFs) and metal-organic frameworks (MOFs) from their constituent building blocks. (a) COF-105, (b) COF-108, (c) MOF-5, (d) MOF-177.

Figure 1.3. Hydrogen storage performance and design strategies in COF-based materials. (a) Excess H_2 uptake of COF-108 at 77 K as a function of pressure. (b) Schematic representation of Li-functionalized COFs showing enhanced H_2 isosteric heat through electrostatic interactions between Li^+ sites and H_2 molecules. (c) Gravimetric H_2 uptake at 298 K for Li-decorated COFs and MOFs, COF102-Li and MOF200-Li.(d) Screening of 240 H_2 COF linker complexes to analyze H_2 interaction mechanisms, including spin coordination, dispersion, electrostatics, and orbital contributions.

Figure 1.4. Hydrogen storage performance of various MOFs under different conditions. (a) Total H_2 uptake of IRMOF-62, MOF-324, and MOF-177 at 77 K as a function of pressure, (b) Structures of Li-functionalized IRMOF derivatives (IRMOF-2-54 and IRMOF-2-96), (c) Total H_2 uptake of different IRMOF-2 series at 77 K and up to 100 bar, (d) Correlation between H_2 storage capacity, surface area, and vibrational shifts for CPO-27-Ni, HKUST-1, and MOF-5, (e) Schematic of Ni_2(m-dobdc) MOF, and (f) Total H_2 uptake of Ni_2(m-dobdc) across a wide temperature range (−75 °C to 100 °C).

Figure 1.5. Metal-organic framework structures and hydrogen storage performance. (a) Schematic illustration of NU-2100 MOF structure, (b) Temperature-dependent hydrogen adsorption isotherms (233-298 K) showing total uptake as a function of absolute pressure up to 100 bar in NU-2100 MOF, (c) Comparison of excess hydrogen uptake at 298 K for bimetallic MOFs, (d) Zn^{II}MFU-4*l*

unit cell structure and $V^{(II)}$MFU-4*l* cluster model, (e) hydrogen adsorption Ti adatom decorated Aza-COF[58] and (f) Net volumetric hydrogen uptake comparison for MSUCOF-3-PtCl, MSUCOF-3-CoCl, MSUCOF-3-PdCl versus bulk H_2.

Figure 2.1. The schematic diagram of the self-consistent field cycle

Figure 2.2. Jacob's Ladder Approach for the Systematic Improvement of DFT Functionals.

Figure 2.3. (a) The schematic diagram of the L-J potential, (b) representation of physisorption and chemisorption, (c) representation of Kubas interaction, (d) schematic diagram of H_2 models.

Figure 2.4. (a) The flowchart of the RASPA 2.0 calculation process, (b) pore-size distribution and Connolly surface.

Figure 2.5. Comparison of experimental and simulated adsorption isotherms. (a) H_2 uptake (g/L) in NU-2100 MOF, (b) CO_2 uptake (mol/kg) in CAU-10 (Al) (The graphs are taken from ref.

Figure 3.1. Equilibrium structures of our designed 3D COFs, (a) COF-IITI, (b) Pristine COF, (c) COF-IITI-3Li, (d) COF-3Li, and (e) Pore-size distribution (PSD) curve for all designed COFs.

Figure 3.2. The equilibrium structures of nine pristine linkers are represented here. The name of these nine linkers is written as (a) Linker-1, (b) Linker-2, (c) Linker-3, (d) Linker-4, (e) Linker-5, (f) Linker-6, (g) Linker-7, (h) Linker-8, and (i) Linker-9.

Figure 3.3. The selected sites in Linker-2 and Linker-7: (a) Site A for the phenyl ring, (b) Site B for the triazine ring, (c) Site C for the boronate ester ring, and (d) Site D for the boroxine ring are shown here.

Figure 3.4. The Li atom decoration in sites A of each linker (a) Linker-1 is decorated by 4 Li atoms in 2 phenyl rings: 2 atoms from the lower side of the ring and two atoms from the upper side of the ring. (b) Linker-2 is decorated by 2 Li atoms in 1 phenyl ring, (c) Linker-3 is decorated by 4 Li atoms in 2 phenyl rings, (d) Linker-4 is decorated by 4 Li atoms in 2 phenyl rings, (e) Linker-5 is decorated by 6 Li atoms in 3 phenyl rings, (f) Linker-6 is decorated by 6 Li atoms in 3 phenyl rings, (g) Linker-7 is decorated by 6 Li atoms in 3 phenyl rings, (h) Linker-8 is decorated by 4 Li atoms in 2 phenyl rings, and (i) Linker-9 is decorated by 2 Li atoms in single one phenyl ring.

Figure 3.5. Hydrogen physisorption in Li-decorated linkers. (a) Linker-1 with 8 adsorbed H_2 molecules, (b) Linker-2 with 4 adsorbed H_2 molecules, (c) Linker-3 with 8 adsorbed H_2 molecules, (d) Linker-4 with 8 adsorbed H_2 molecules, (e) Linker-5 with 12 adsorbed H_2 molecules, (f) Linker-6 with 12 adsorbed H_2 molecules, (g) Linker-7 with 12 adsorbed H_2 molecules, (h) Linker-8 with 8 adsorbed H_2 molecules, and (i) Linker-9 with 4 adsorbed H_2 molecules.

Figure 3.6. Average binding enthalpy per one H_2 molecule physiosorbed in both the pure and Li-decorated linkers. (Units are in eV)

Figure 3.7. The average dispersion energy values of both the pure and Li-decorated linkers are depicted here. The green curve displays the average dispersion energy of the pure linkers, and the red curve shows the average dispersion energy of the Li-decorated linkers. (These curves are plotted using dispersion energy data computed by the B3LYP-D3/cc-pVTZ level of theory).

Figure 3.8. Energy decomposition analysis (EDA) graph of the Li-decorated complexes with a single adsorbed H_2 molecule. The binding enthalpy (ΔH) with dispersion energy (ΔE_{Disp}), electrostatic energy (ΔE_{Elstat}), and Pauli repulsion energy (ΔE_{Pauli}) are shown by black, blue, green, and red colors, respectively.

Figure 3.9. The overlapping of atomic orbitals and HOMO-LUMO in Li-Linker complexes (a) Linker-1 (b) Linker-2; (c) Linker-3. The green circle shows an overlap of the 2s-orbital of Li and the 2p-orbital of the C atom, and the black circle shows an overlap of the 1s-orbital of H_2 and the 2p-orbital of the C atom.

Figure 3.10. The energy of the HOMO and LUMO with their gap for both the pure and Li-decorated linkers. (This graph is plotted using the reference data of the HOMO-LUMO gap obtained by the B3LYP-D3/cc-pVTZ method.)

Figure 3.11. PDOS of the Li-decorated linkers with H_2 molecules adsorbed. (a) PDOS of the Li-Linker-1 with a single adsorbed H_2 molecule. (b) PDOS of the Li-Linker-1 with eight adsorbed H_2 molecules.

Figure 3.12. H_2-uptake in weight percentage (wt.%) in both the pure and Li-decorated linkers.

Figure 3.13. Absolute loading of H_2 in mg/g, (a) at low pressure range (5-12 bar), (b) at high pressure range (100-300 bar).

Figure 3.14. H_2 desorption temperature for all Li-decorated complexes with single and maximum adsorbed H_2 molecules.

Figure 4.1. (a) Bond distance between the transition metal atom and the first adsorbed H_2 molecule; (b) binding enthalpy value of the first adsorbed H_2 molecule on the surface of chelated linkers.

Figure 4.2. The equilibrium structures of the pure and Tm-chelated organics, Linker-1 to Linker-3, with one adsorbed H_2 molecule.

Figure 4.3. The equilibrium structures of both the pure and Tm-chelated organics Linker-4 to Linker-6 with one adsorbed H_2 molecule.

Figure 4.4. The equilibrium structures of the pure and Tm-chelated linkers Linker-7 to Linker-9, each with one adsorbed H_2 molecule.

Figure 4.5. (a) and (b) The equilibrium structures of the Pd and Pt chelated Linker-3, (c) and (d) The equilibrium structures of the Pd and Pt chelated Linker-3 with single adsorbed H_2 molecules.

Figure 4.6. The equilibrium structures of both the pure periodic COFs and with a single adsorbed H_2 molecule. (a) Pristine-COF, (b) COF-IITI, (c) Pristine-COF-A-1H_2, (d) COF-IITI-1H_2, and (e) Pristine-COF-B-1H_2.

Figure 4.7. The equilibrium structures of both the periodic chelated COFs with a single adsorbed H_2 molecule. (a) Pristine-COF-$NiCl_2$-A, (b) Pristine-COF-$NiCl_2$-B, (c) COF-IITI-$NiCl_2$, (d) Pristine-COF-$NiCl_2$-A-1H_2, (e) Pristine-COF-$NiCl_2$-B-1H_2, and (f) COF-IITI-$NiCl_2$-1H_2.

Figure 4.8. The binding enthalpy graph for pure and chelated Linker-1 to Linker-4.

Figure 4.9. The binding enthalpy graph for pure and chelated Linker-5 to Linker-8.

Figure 4.10. The binding enthalpy vs. complexes graph for both the pure and chelated Linker-9.

Figure 4.11. H_2 uptake capacities (in wt.%) and binding enthalpies with maximum adsorbed H_2 molecules in both the pure and transition metal chelated linkers.

Figure 4.12. Energy decomposition analysis and study of interactions contributing to H_2 binding in Tm-chelated linkers.

Figure 4.13. Molecular electrostatic potential mapping of both the pure Linker-3 and Linker-3-$TmCl_x$.

Figure 4.14. HOMO and LUMO of both the pure Linker-3 and transition metal chelated Linker-3. The dotted black circles show the overlapping of the **s**-orbital of the H atom and the 2**p**-orbital of atoms in organic linkers. The dotted red circles show the overlapping of the **s**-orbital of the H atom and the 3**d**-orbital of transition metal atoms in $TmCl_x$.

Figure 5.1. Equilibrium structures of M_2(*m*-dobdc) MOFs and their pore diameter. (a) Mn_2(*m*-dobdc), (b) Fe_2(*m*-dobdc), (c) Co_2(*m*-dobdc), (d) Ni_2(*m*-dobdc) and (e) pore-size distribution (PSD) curve.

Figure 5.2. The calculated heat of H_2 adsorption (Q_{st}) values at 298 K. (a) The simulated Q_{st} values at low pressure, (b) the simulated Q_{st} values at high pressure, (c) DFT calculated Q_{st} value for molecular model system of Mn_2(*m*-dobdc), and (d) DFT calculated Q_{st} value for molecular model system of Ni_2(*m*-dobdc).

Figure 5.3. The H_2 adsorption isotherms of M_2(*m*-dobdc) MOFs at 77 K and 298 K. a) 77 K Buch model, (b) 77 K DL model, (c) 298 K Buch model, and (d) 298 K DL model.

Figure 5.4. Representation of error bars in the adsorption isotherm curves for M_2(*m*-dobdc) for 77 K and 298 K by the DL model. (a) 77 K loading with error bars, (b) 298 K loading with error bars.

Figure 5.5. The H_2 adsorption isotherms of M_2(*m*-dobdc) MOFs at three temperatures: 160 K, 198 K and 233 K. (a) 160 K Buch model, (b) 160 K DL model, (c) 198 K Buch model, (d) 198 K DL model, (e) 233 K Buch model, and (f) 233 K model.

Figure 5.6. The H_2 uptake capacities of M_2(*m*-dobdc) MOFs at cryogenic conditions and room temperature. (a) 77 K Buch model, (b) 77 K DL model, (c) 298 K Buch model, and (d) 298 K DL model.

Figure 5.7. The H_2 uptake capacities of M_2(*m*-dobdc) MOFs at three temperatures. (a) 160 K Buch model, (b) 160 K DL model, (c) 198 K Buch model, (d) 198 K DL model, (e) 233 K Buch model, and (f) 233 K DL model.

Figure 5.8. Comparison of the simulated gravimetric and volumetric H_2 uptake capacities and loading values of M_2(*m*-dobdc) MOFs with experimental uptake capacities/loadings of other MOFs. (a) Simulated vs experimental V_c and G_c values comparison of Ni_2(*m*-dobdc) at 298 K, (b) simulated vs experimental V_c values comparison of Co_2(*m*-dobdc) at 198 K, 233 K and 298 K, (c) G_c values comparison of M_2(*m*-dobdc) with other MOFs at 77 K, and (d) absolute loading comparison of M_2(*m*-dobdc) with other MOFs at 77 K.

Figure 6.1. Fluorinated metal–organic frameworks PCN-222 and UiO-66, (b) MOF/COF hybrid photocatalysts, (c) data-driven design of flexible metal−organic frameworks for gas storage.

LIST OF TABLES

Table 1.1. Comparison of U.S. DOE 2025 hydrogen storage targets with conventional, chemical, and physical storage approaches. Key performance parameters such as gravimetric and volumetric capacities, operating temperature and pressure, reversibility, and system fill time are summarized to highlight the gap between current storage technologies and the DOE targets.

Table 1.2. Hydrogen storage capacities of various COFs and Li-decorated COFs under different temperature and pressure conditions.

Table 1.3. Hydrogen storage capacities of various MOFs under different temperature and pressure conditions.

Table 3.1. Average binding energy per Li atom (ΔE_b in eV) calculated for the Li-decorated complexes.

Table 3.2. The binding enthalpy (ΔH) of a single H_2 molecule adsorbed on the Li-decorated linkers.

Table 3.3. Calculated values of average binding enthalpy per one H_2 molecule physiosorbed on pure and Li-decorated linkers. (Units are in eV)

Table 3.4. Compared the values of the binding enthalpy of H_2 adsorption in various COFs.

Table 3.5. Infrared spectroscopy properties of the adsorbed H_2 molecules on the Li-decorated linkers. (1 $Debye^2$-$angstrom^{-2}$-amu^{-1} (IR intensity unit) = 42.2561 KM/Mole = 5.82573×10^{-3} cm^{-2}-atm^{-1} at STP or a.u.)

Table 3.6. Comparison of H_2 uptake in weight % uptake across different COFs.

Table 4.1. The values of binding enthalpy (ΔH) of the first adsorbed H_2 molecule in both the pure and Tm-chelated linkers.

Table 4.2. A comparative analysis of the values of the binding enthalpy for the first H_2 molecule adsorbed onto Linker-3 chelated with early, late, and precious transition metals.

Table 4.3. A comparative analysis of the values of the binding energy for the first adsorbed H_2 molecule on both the pure and chelated periodic COFs with their cluster models.

Table 4.4. Energy values of frontier orbitals and HOMO-LUMO gap for Linker-3 with maximum adsorbed H_2 molecules. (Units are in eV)

Table 5.1. Calculated partial charges (expressed in electronic charge e^-) and force field (FF) parameters for the chemically distinct atoms in the M_2(m-dobdc) MOFs (M = Mn, Fe, Co and Ni)

Table 1.1. Parameters used to characterize the H_2 potential used in this work: Buch model, Darkrim-Levesque (DL) model. COM corresponds to the center-of-mass site, and H corresponds to the atomic locations of the hydrogen atoms.

Table 5.3. The calculated surface area, pore volume, framework mass, and density of the subject MOF materials, M_2(*m*-dobdc).

Table 5.4. The calculated gravimetric H_2 uptake capacities (G_c) of M_2(*m*-dobdc) MOFs by using the Buch model.

Table 5.5. The calculated volumetric H_2 uptake capacities of M_2(*m*-dobdc) MOFs by using the Buch model.

Table 5.6. The calculated H_2 deliverable capacity in the temperature-pressure range (77 K/100 bar $\rightarrow$160 K/5 bar) and total gravimetric H_2 adsorption capacities at T=298 K and P =100 bars in M_2(*m*-dobdc) MOFs by using the Buch model.

Table 5.7. The calculated Volumetric H_2 deliverable capacity (in g/L) under ambient conditions for M_2(*m*-dobdc) MOFs.

ACRONYMS

COF: Covalent organic frameworks

MOF: Metal-organic frameworks

DOE: Department of Energy

DFT: Density Functional Theory

B3LYP: Becke, 3-parameter, Lee-Yang-Parr

GGA: Generalized gradient approximation

TZVP: Triple zeta valence polarized

MP2: Second-order Møller-Plesset Perturbation Theory

EDA: Energy decomposition analysis

SCF: Self-consistent field

HOMO: Highest occupied molecular orbital

LUMO: Lowest unoccupied molecular orbital

PDOS: Partial density of states

GCMC: Grand Canonical Monte Carlo

UFF: Universal Force Fields

Tm: Transition metals

LJ: Lennard-Jones

wt%: Weight percentage

G_c: Gravimetric uptake

V_c: Volumetric uptake

CHAPTER 1

Introduction and Motivation

This chapter summarizes the need for hydrogen energy, its storage methods and limitations. A detailed description of solid-state hydrogen storage methods is provided, along with recent innovations and developments in porous materials, including covalent organic frameworks (COFs) and metal-organic frameworks (MOFs). We have highlighted the recent developments in hydrogen storage materials and technologies that have shown advantages in H_2 binding enthalpy and storage capacities. The goal of this chapter is to outline key strategies for enhancing the hydrogen binding enthalpy and storage capacities of porous materials. Advanced hydrogen storage technology is crucial for enhancing hydrogen storage, which could help us achieve our environmental and energy goals as we transition from carbon-based energy to cleaner alternatives, such as hydrogen energy.

1.1. Need for Hydrogen Energy

Hydrogen energy is recognized as a remarkable competitor to replace carbon-based fuel cells. It is a promising alternative that can reduce carbon emissions and address the main issues related to global climate change and the depletion of fossil fuels.[1] H_2 is an ideal energy carrier with the potential to reshape industries such as power generation and transportation. H_2, when used as a fuel, releases only water as a byproduct and does not contribute to greenhouse gas emissions like petroleum and other carbon-based fuels. It has an energy density three times that of petroleum, which plays a major role in the global transition to a low-carbon economy.[2] The integration of hydrogen generation, storage, transportation and utilization forms a foundational element of an economic system. However, several barriers stand in the way of efficient H_2 storage in the onboard storage of next-generation fuel cell vehicles, which is the implementation of large-scale infrastructure for its storage and producing H_2 from green energy sources at an affordable cost.[3] Regardless of several advantages of hydrogen energy, the commercialization of H_2 energy is far from being achieved. The global hydrogen energy demand had increased to over 94 million tons (Mt) in 2021, indicating a significant 5% rise

from the previous year's levels, and the worldwide hydrogen production satisfied this demand. The predicted hydrogen demand is expected to be around 115 million tons by 2030.[4]

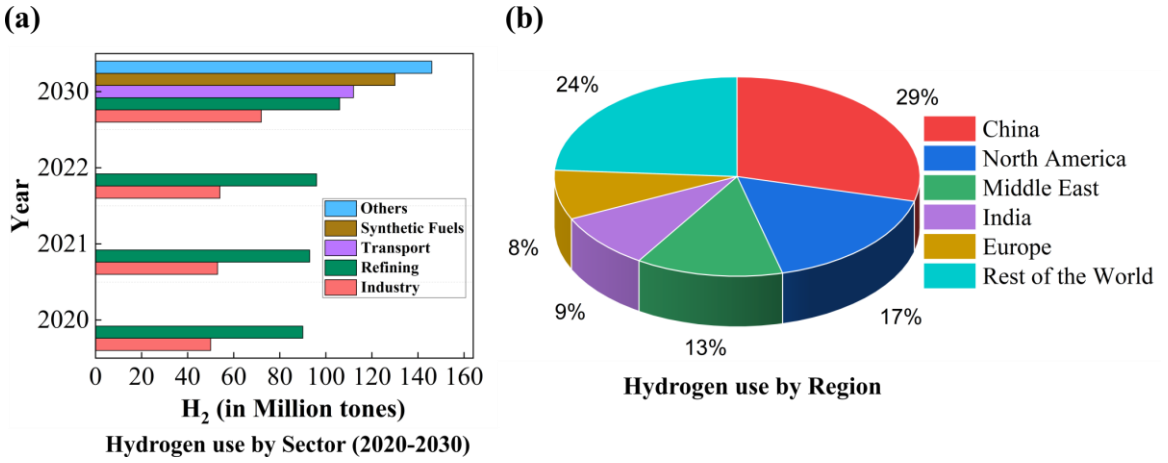

Figure 1.1. *(a) Global H_2 demand by sector from 2020 to 2030 and (b) regional distribution of hydrogen demand. The bar chart illustrates the projected increase in hydrogen consumption across various sectors, including industry, refining, transport, synthetic fuels, and others. The pie chart highlights the regional share of hydrogen demand, with China, North America, and the Middle East as major contributors.[4]*

In addition, H_2 storage techniques suffer from major disadvantages, including infrastructure requirements, high costs, and safety concerns, which limit their use in real-world applications.[5] Various novel techniques have been developed to design materials with enhanced heat of adsorption and reversible H_2 adsorption capacities. Moreover, the proper execution of this H_2 storage technology requires advancements in the development of highly stable materials for H_2 storage, with efficient storage capacity at an affordable cost.[6] To encourage research in the field of H_2 storage technology, the United States Department of Energy (USDOE) set targets for on-board storage systems: 5.5 wt % and 40 g/L for 2025, with an ultimate target of 6.5 wt % and 50 g/L (**See Table 1.1**).[7]

Table 1.1*. Comparison of U.S. DOE 2025 hydrogen storage targets with conventional, chemical, and physical storage approaches. Key performance parameters such as gravimetric and volumetric capacities, operating temperature and pressure, reversibility, and system fill time are summarized to highlight the gap between current storage technologies and the DOE targets.[7]*

Storage Parameters	**DOE Target 2025**	**Conventional Techniques**		**Chemical Storage**	**Physical Storage**
		Compressed H_2	Liquid H_2		

Gravimetric Capacity (wt %)	5.5	100	100	Max 11.4	Max 11.4
Volumetric Capacity (g/L)	40	NA	NA	Max 30	Max 66
Temperature (˚C)	-40/-85	25	-253	>-200	70-400
Pressure (bar)	<100	350-700	1-10	30-100	~1
Reversibility (cycle)	1500	NA	NA	Limited Reversible	Reversible
System fill time (for 5Kg H_2/min)	3-5 min	fast	fast	too slow	fast

1.2. Hydrogen Storage Methods

The most traditional method for storing hydrogen is compressed hydrogen storage. It compresses the gas into a gas tank to a specific density for room temperature. Compressed hydrogen storage has a volumetric capacity of 10-15 g/L and a gravimetric capacity of 1-2 wt %, with an estimated cost ranging from $500 to $1000 per kilogram of stored hydrogen.[8] This compressed hydrogen storage can achieve practical storage capacity with reduced energy use, but it presents challenges: it requires a high-pressure storage tank that increases overall cost and necessitates additional safety measures.[5] The other method is liquification of H_2 gas at extremely low temperatures (-253°C). To minimize the vaporization, high-vacuum adiabatic low-pressure tanks are commonly used for liquid hydrogen storage.[9] This process is energy-intensive and consumes approximately 30% of the overall energy contained in hydrogen. Although liquid hydrogen storage is a viable option for long-term storage and large-scale production, it has the potential to achieve a volumetric density of 8.5 MJ/L, with an approximate cost of $1,500 to $3,000 per kilogram of stored hydrogen.[8] Solid-state H_2 storage is an affordable, reliable, and safest method for H_2 storage in a wide range of materials at varying temperature and pressure conditions.[10] Depending on the binding of H_2 molecules with the materials, H_2 adsorption is divided into two categories: **Physical and Chemical adsorption**. Physisorption is characterized by the absence of new molecular orbital formation between the adsorbate and adsorbent. The interaction is dominated by non-specific van der Waals and electrostatic forces, with no significant perturbation of the electronic structure of either the adsorbate or the surface. The binding is inherently reversible, and the extent of dispersion contribution to the total binding energy is substantial, as can be confirmed by comparing binding energies calculated with and without dispersion corrections.[11]

Chemisorption, in contrast, involves the formation of new molecular orbitals through covalent or ionic bonding between the adsorbate and the surface, resulting in a meaningful reorganization of the electronic structure of the interacting species. This can be identified through molecular orbital visualization or energy decomposition analysis. It is important to note, however, that not all chemisorption is dissociative, a weakly chemisorbed H_2 molecule that retains its molecular identity may still undergo reversible desorption, and it is specifically dissociative chemisorption, where H_2 splits into atomic H, that renders desorption energetically prohibitive and thus undesirable for storage applications.[12]

Physisorption has gained much more attention for storing H_2 in porous materials because it does not require extensive energy to store or desorb hydrogen, and is also cost-effective.[13] Some of the most explored materials for H_2 storage are metal hydrides, activated carbons, Metal-Organic Frameworks (MOFs), and Covalent Organic Frameworks (COFs).[5] Although metal hydrides show high H_2 storage capacity, they also suffer from high desorption temperature and poor cycle performance.[14] Developing a new class of porous materials, namely MOFs and COFs, has provided a new perspective on hydrogen production and storage.[1,3,5,11] Their extraordinary properties, such as high surface area, porosity, and tunable electronic properties, make them suitable for electrocatalysis and gas storage/gas separation applications.[13,15–18] Their high surface area creates a large number of potential binding sites for molecules, enabling high-capacity physical adsorption.

1.3. Porous Materials for H_2 storage

This thesis examines hydrogen adsorption in two classes of porous framework materials: Covalent Organic Frameworks (COFs), composed entirely of organic ligands, and Metal-Organic Frameworks (MOFs), which integrate metal nodes with organic linkers. The study analyzes H_2 adsorption mechanisms in COFs and evaluates hydrogen storage capacities in MOFs.

(a) Covalent Organic Frameworks

Covalent Organic Frameworks (COFs) have become an advantageous class of materials due to their superior structural properties and tunability. COFs are three- or two-dimensional, robust, and stable frameworks designed by covalent bond formation between two or more organic linkers or ligands.[15] COFs consist of light elements such as C, B, N, O and Si, and the covalent bonds B-N, B-O, C-N, and O-Si provide exceptional chemical and thermal stability to these materials.[14] Yaghi and coworkers synthesized a large range of COFs, including

boronate ester linkage, imine linkage, triazine linkage, boroxine linkage, imide linkage, hydrazone linkage and many others. [15,19,20]Their crystalline structure, high surface area, low density, and tunable pores have provided great potential for COF materials in various applications, including gas storage and separation, catalysis, supercapacitors, and biomedicine.[5] Compared with other conventional porous materials, such as activated carbons, zeolites, and silica-supported salts, COFs are attracting increasing attention for gas storage applications due to their unique features, including high surface area and tunable porosity. Based on their spatial structures, the building blocks of COF materials can be classified as 2D or 3D. The uniform expression for 2D COFs is C_n, and using different combinations of symmetric groups,

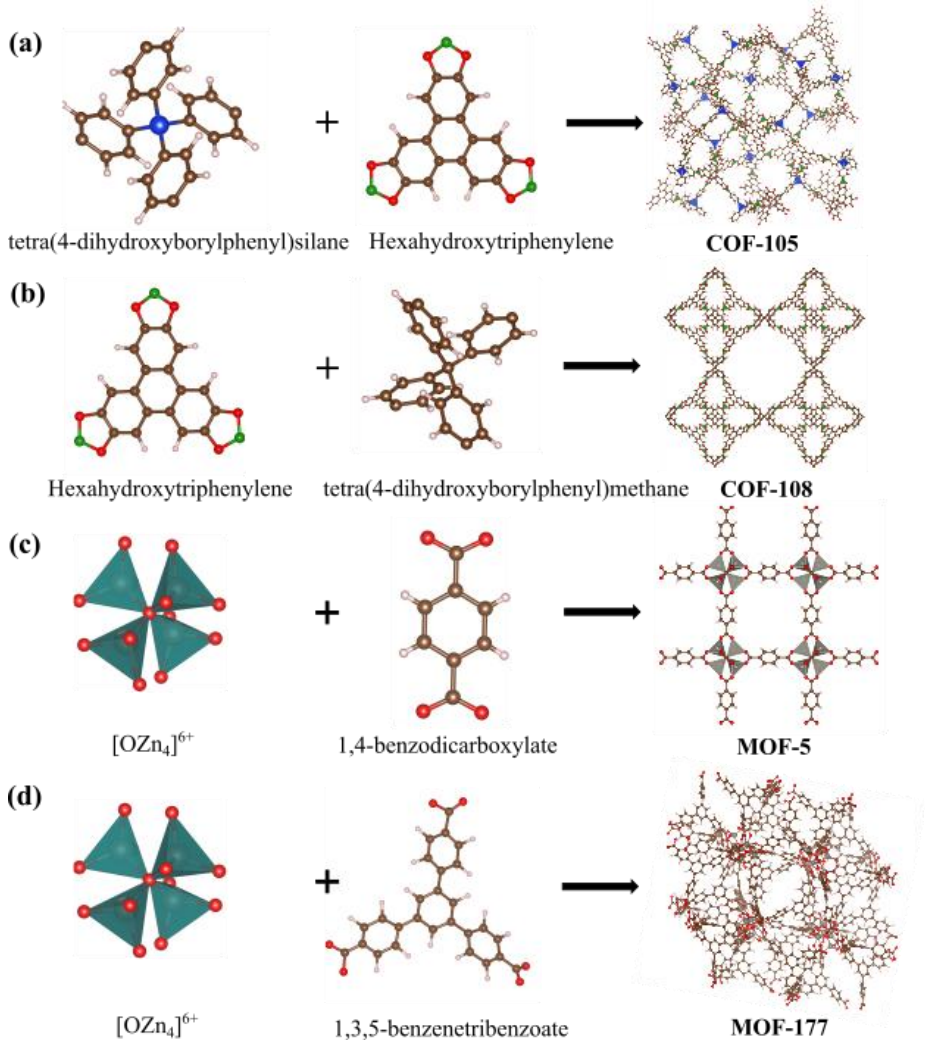

Figure 1.2. *The assembly of covalent organic frameworks (COFs) and metal-organic frameworks (MOFs) from their constituent building blocks. (a) COF-105, (b) COF-108, (c) MOF-5, (d) MOF-177.*

COFs can be described as tetragonal, trigonal or hexagonal. The construction of 3D COFs needs at least one building block with orthogonal symmetry to extend the structure to a 3D framework. The choice of linkage has a major effect on the porosity and crystallinity of the COFs. In addition, functionalization of linkers is crucial for improving the interaction between guest molecules and COFs.[21] Hydrogen bonding and quadrupole interactions, as well as orbital and electrostatic interactions, can be tailored through ligand functionalization in COFs. A wide range of COFs has been reported by modifying functional groups and tuning structural properties.[20–24] COFs can play a transformative role in the hydrogen economy due to their distinct surface characteristics.

In our thesis, we are particularly interested in hydrogen storage on COF and MOF materials. We have strategically enhanced the hydrogen-storage properties of COFs using various techniques, including **alkali-metal doping and chelation of transition-metal atoms**. Detailed research on the hydrogen adsorption properties of doped and chelated COFs will be presented in **Chapters 3 and 4**. However, before that, *we must first explore the history of hydrogen storage in COFs, including its origins and current state in these materials.*

Yaghi *et al.* synthesized both 2D and 3D purely organic ligand-based materials named COF-102, COF-103, COF-105 and COF-108. Their high surface areas are 3472 m^2/g for COF-102 and 4210 m^2/g for COF-103, and their very low density is 0.17 g/cm^3 for COF-108. In this study, COF-105 and COF-108 were identified as the best-performing materials for hydrogen storage with a maximum excess H_2 uptake value of 10 wt % and at T=77 K. **(Figure 1.3a)** The highest volumetric uptake of 40.4 g/L was achieved for COF-102 at T=77 K.[25] Another simulation study of hydrogen storage in COF-102 and COF-103 showed high gravimetric uptake values of 26.7 and 6.5 wt % at 77 K and 300 K, respectively, and reached the DOE target even at room temperature.[26] The hydrogen adsorption of 2D COFs, specifically COF-6, COF-8, and COF-10, has been reported at both 77 K and 298 K (temperatures). The highest hydrogen storage capacity of 4.2 wt % was achieved in COF-10. The gravimetric and volumetric capacities of 2D COFs were observed to be lower than those of 3D COFs. The same behavior was observed at room temperature; the hydrogen storage capacity was half that of the 3D COFs, and 0.8 wt% storage capacity was observed at 298 K and 100 bars.[27]

A 2D mesoporous imine linkage-based COF (ILCOF-1) was synthesized with a high surface area of 2723 m^2/g to explore the gas (H_2, CH_4, and CO_2) storage. The isosteric heat of adsorption was found to be 5.9 kJ/mol for H_2 adsorption at zero coverage. The hydrogen uptake

shows a gradual increase with pressure, reaching 4.7 wt% at T=298 K and 40 bars (pressure). This value is higher than that of most organic polymers but lower than that of 3D COFs with a similar surface area.[28] Then Liu *et al.* have synthesized a new 1,3,5,7-tetraphenyladamantane-based covalent organic framework (adm-COFs) and their computational findings suggested that these COFs possess high surface area (5967-6709 m^2/g) and porosity. The simulated results showed that adm-COF-4 exhibited the highest gravimetric H_2 adsorption capacity of 38.36 wt % and volumetric capacity of 60.71 g/L at T=77 K. The gravimetric H_2 uptake capacity of adm-COF-1 reached up to 5.81 wt % at 298 K and 100 bars, which was close to the DOE criteria.[29] Another study reported a hydrogen spillover mechanism on 3D COFs, including COF-102, COF-103, COF-105, and COF-108, as well as 2D COFs, including COF-8, COF-10, and COF-12. This study revealed that in 3D COFs, high gravimetric hydrogen storage capacities were observed, but their volumetric uptake was very low due to their large unit cell volume. The gravimetric and volumetric capacities of 2D COFs were found to be in the range of 5.13-6.06 wt % and they reached the DOE 2010 target. Then, to observe the H migration, a tetrahedral Pt_4 cluster was chosen as a catalyst and HHTP as a substrate. This study revealed that at most two H atoms can migrate from the Pt_4 cluster to the HHTP substrate, and this reaction was an endothermic process.[30]

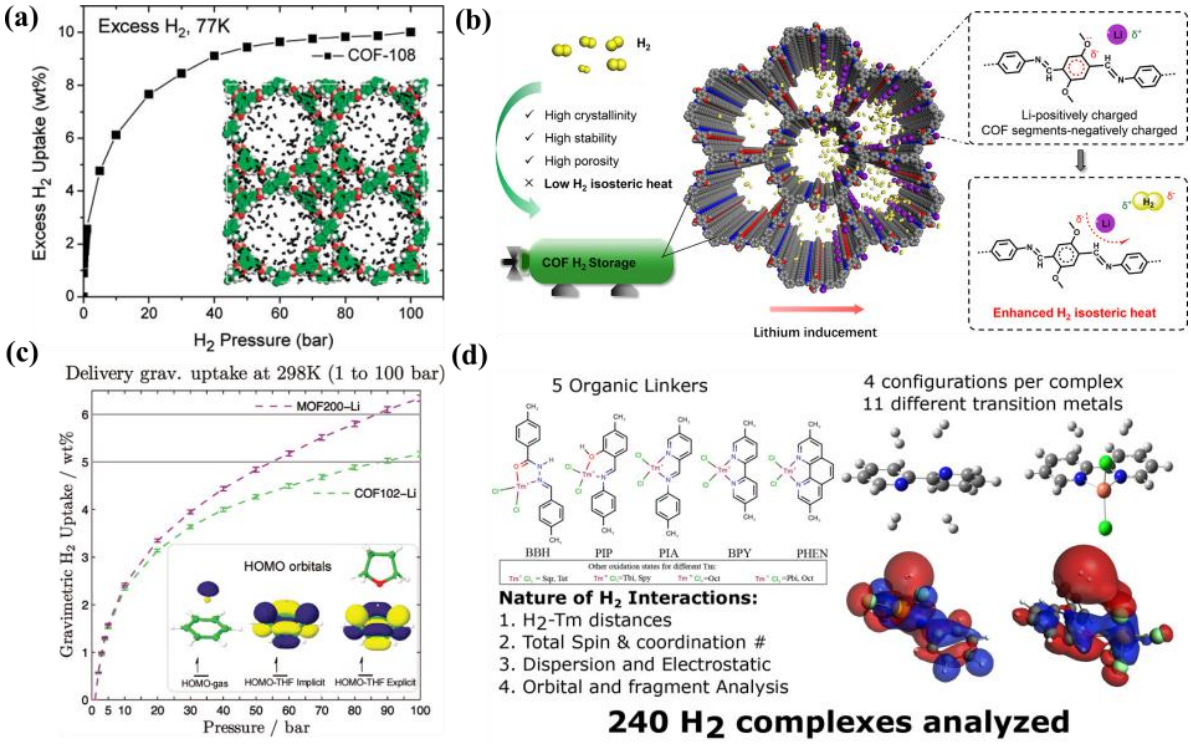

Figure 1.3. *Hydrogen storage performance and design strategies in COF-based materials. (a) Excess H_2 uptake of COF-108 at 77 K as a function of pressure.[25] (b) Schematic representation of Li-functionalized COFs*

showing enhanced H_2 isosteric heat through electrostatic interactions between Li^+ sites and H_2 molecules.[25] (c) Gravimetric H_2 uptake at 298 K for Li-decorated COFs and MOFs, COF102-Li and MOF200-Li.[31] (d) Screening of 240 H_2 COF linker complexes to analyze H_2 interaction mechanisms, including spin coordination, dispersion, electrostatics, and orbital contributions.[32]

Metal doping and chelation were suggested to add active binding sites and enhance hydrogen storage at room temperature. Numerous theoretical investigations have been conducted involving the decoration of alkali-metal ions and clusters, as well as the chelation of transition metal atoms on COFs, to improve H_2 binding and storage capacities. Cao *et al.* performed Monte Carlo (MC) simulations to study the H_2 adsorption isotherms in Li-doped COFs 102, 103, 105 and 108. All four Li-doped COFs achieve an approximately doubled volumetric H_2 storage capacity compared to the pristine COFs. Li-doped COF-102 reached a gravimetric uptake of 4.25 wt % and 21.11 g/L, respectively.[33] Recently, Tang *et al.* experimentally studied the H_2 adsorption performance of Li-doped TPB-DMTP-COF at 77 K and 1 bar. The H_2 uptake increased from 0.84 wt % to 1.16 wt % after Li decoration. The DFT results show that the H_2 adsorption energy reached -19 kJ/mol in Li-doped TPB-DMTP-COF, and it was observed that when H_2 is close to the Li atom, the strong electrostatic interactions of the Li ions will induce electron polarization in H_2 molecules **(Figure 1.3b)**.[25] A multiscale study on hydrogen storage was performed on Li-doped Pc-PBBA COF. The DFT calculations suggested that Li atoms can be doped in this COF with a binding energy value of 1.08 eV, and each Li cation can adsorb three H_2 molecules. The maximum gravimetric density of 5.3 wt % and volumetric uptake of 45.2 g/L was obtained with a maximum adsorbed 24 H_2 molecules. The Kinetic Monte Carlo (KMC) simulations have predicted the gravimetric density of 4.70 wt % at 250 K and 100 bar.[34]

***Table 1.2**. Hydrogen storage capacities of various COFs and Li-decorated COFs under different temperature and pressure conditions.*

COFs	Surface Area (m^2/g)	Temperature (K)	Pressure (bar)	H_2 Storage Capacities (wt %)	Ref
COF-5	1670	77	50	3.58	[14]
COF-10	1760	77	50	3.92	[14]
COF-102	3620	77	35	7.24	[14]
COF-103	3530	77	35	7.05	[14]
Li@COF-202	-	77	100	7.83	[35]

Li@COF-202	-	298	100	4.39	[35]
Li@COF-105	-	298	100	6.84	[33]
Li@COF-108	-	298	100	6.73	[33]

Goddard *and co-workers* predicted the H_2 uptake capacities of pure and Li-, Na-, and K-metalated COFs and MOFs, revealing that Li-metalated materials exhibit better performance than other COFs and MOFs.[31] Their designed 11 structures have reached the 2010 DOE gravimetric uptake target. MOF200-Li showed the highest gravimetric uptake value of 6.34 wt % and CO102-Li achieved high uptake value of 5.16 wt % at 298 K. **(Figure 1.3c)** Additionally, these materials exhibited a high volumetric uptake value of 23.3 g/L for COF102-Na at 298 K and 100 bar. The isosteric heat of adsorption for pure systems ranges from 3.5-5 kJ/mol, while the Li-metalated systems vary from 13 to 21 kJ/mol, the Na-metalated cases vary between 10-17 kJ/mol, and the K-metalated frameworks show values ranging from 8-10 kJ/mol. This study suggested that certain design strategies should be followed to achieve high adsorption capacities, including controlling the pore volume (a smaller pore volume leads to better volumetric delivery), creating multiple strong adsorption sites in materials, and tuning the surface area to accommodate more H_2 molecules.[31]

Mendoza-Cortes *et al.* employed a different strategy, chelating the organic linkers of COFs with first-row transition metal atoms and investigating the H_2 adsorption mechanism. Their quantum mechanical calculations revealed that the long-range nonbonding interactions depend poorly on the geometry of the coordination shell and transition metal oxidation state. Most of these transition metals fall into the ideal binding enthalpy range of 7-15 kJ/mol. Furthermore, they performed Grand Canonical Monte Carlo Simulations (GCMC) to investigate the H_2 adsorption isotherms of the Chelated COFs, specifically COF-300, COF-301, COF-320, COF-322, COF-330, COF-333, COF-340, and COF-350. The cobalt-chelated COF-301 has shown the highest uptake relative to bulk H_2, at 22.2 g/L under 120 bars. The other chelated COF-322, COF-330, COF-33, and COF-350 have shown a wider range of uptake over bulk H_2 between 8-13 g/L at 100-700 bar.[36] Pakhira and Mendoza-Cortes extended this study to explore the quantum nature of H_2 interaction in the same COF linkers. **(Figure 1.3d)** They have designed 240 complexes using those five ligands with different transition metal atoms, spins, oxidation

states and geometrical configurations. Energy decomposition analysis revealed the quantum nature of the H_2 interactions on Tm-chelated COFs, with electrostatic and dispersion interactions being the most significant contributors to the H_2 binding enthalpy.[32] A novel strategy was adopted in a research in which a phthalocyanine-based COF was intercalated by a range of fullerenes (C_{20}, C_{24}, C_{26}, C_{28}, C_{30}, C_{36}, C_{60} and C_{70}), and hydrogen gravimetric and volumetric uptakes were evaluated at pure C_n-PC-PBBA COFs and Li-doped C_n-PC-PBBA COFs. Their GCMC simulations indicated that the hydrogen gravimetric and volumetric uptakes reached 9.4-12 wt % and 4.8-52.2 g/L in pure C_n-PC-PBBA COFs at 77 K and 100 bar. Four Li-doped C_n-PC-PBBA COFs exhibited the gravimetric and volumetric uptake values of 4.2 wt % and 18.2 g/L at 298 K and 100 bar. This study showed that these Li-doped fullerene-based C_n-PC-PBBA COFs are promising materials for H_2 adsorption at ambient conditions.[37] **Table 1.2** summarizes the experimental and simulated results for COFs in hydrogen storage applications. *These findings demonstrate that metal atom doping and chelation in COFs are effective strategies to enhance the heat of hydrogen adsorption and storage capacities, and these techniques have proven their potential for reversible hydrogen storage applications.*

In this section, we provided a comprehensive literature review of hydrogen adsorption in both the pure COFs and metal-doped/decorated COFs. These studies suggest that the COF materials exhibit exceptional performance at both cryogenic and room temperature conditions. However, pristine COFs failed to meet the DOE target; therefore, some strategies should be implemented to improve the hydrogen storage capacities of COF materials. Here, we have analyzed that the metal doping, intercalation, and chelation are effective strategies to enhance the gravimetric and volumetric hydrogen storage capacities and to reach the USDOE target.

(b) Metal-Organic Frameworks

Metal-Organic Frameworks are crystalline nanostructures formed by organic ligands connected by a metallic cluster through coordination bonds. A diverse range of MOFs can be designed by varying the type or length of the organic ligand and also the metal element in the metal node.[5] Professor Susumu Kitagawa, Professor Richard Robson, and Professor Omar Yaghi were awarded the 2025 Nobel Prize in Chemistry for developing highly porous materials: MOFs. These MOF materials show specific characteristics, including high surface area and porosity; these features are appealing for gas adsorption and separation, which is widely used in fuel cell technologies.[5,11,16] MOFs exhibit higher flexibility and tunability, along with good chemical and thermal stability, compared to other well-known materials such

as zeolites. [5] MOFs are also used in the fields of electrocatalysis, battery applications and drug delivery.[16,37–39] Yaghi and coworkers first experimentally reported the MOF-5 with a surface area of 3534 m^2/g. Its building units comprise inorganic $[OZn_4]^{6+}$ units connected with the organic linker 1,4-benzenedicarboxylate (BDC) to form a cubic topology. It showed a high H_2 uptake of 4.5 wt.% at 78 K and 0.8 bar. [40] After that, Wong-Foy *et al.* synthesized a new MOF-177 with a surface area of 4746 m^2/g. It consists of a tetrahedral metal node $[OZn_4]^{6+}$ unit and 1,3,5-benzenetribenzoate (BTB) as an organic ligand; this MOF reported 7.0 wt.% gravimetric capacity and 32 g/L volumetric capacity at 77 K and 70 bar. [41] According to reported results, it is evident that MOFs showed higher H_2 storage capacities than other porous materials. The two large surface area MOFs (MOF-5 and MOF-177) and two catenated MOFs (IRMOF-11 and MOF-14) were selected to study the adsorption isotherms of pure and binary mixtures of hydrogen and methane using GCMC simulations. The catenated frameworks, MOF-14 and IRMOF-11, and the open metal site of MOF-74 showed selectivity values three times higher than those of the noncatenated frameworks. The methane adsorption isotherm starts to saturate as pressure increases.[42]

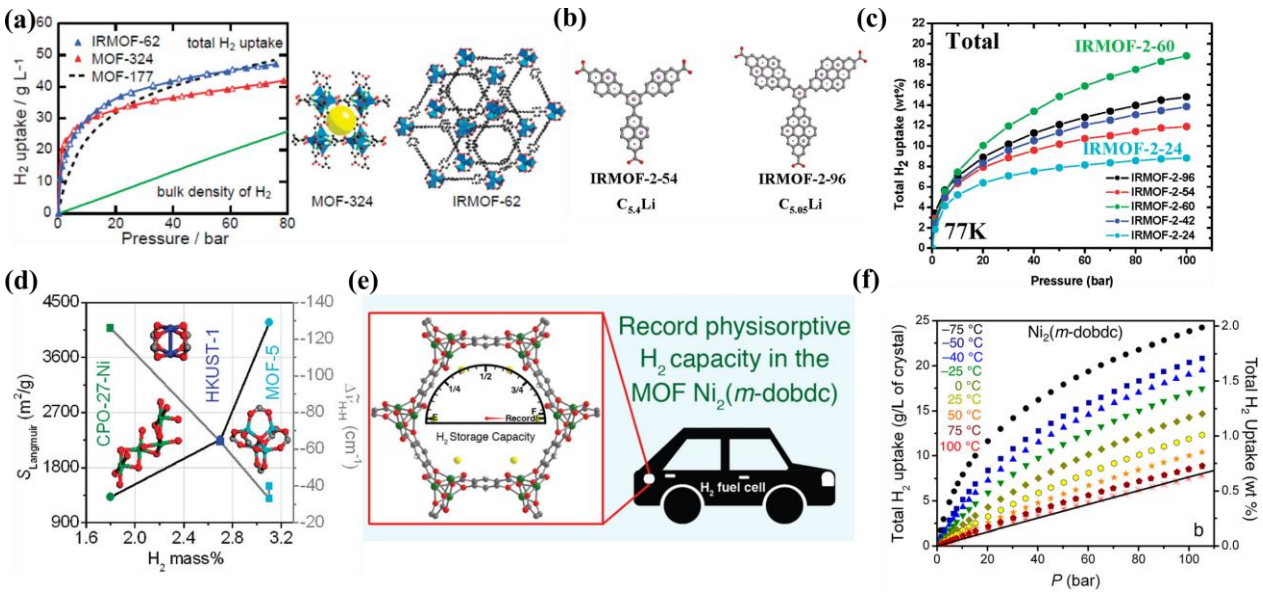

Figure 1.4. *Hydrogen storage performance of various MOFs under different conditions. (a) Total H_2 uptake of IRMOF-62, MOF-324, and MOF-177 at 77 K as a function of pressure[43], (b) Structures of Li-functionalized IRMOF derivatives (IRMOF-2-54 and IRMOF-2-96), (c) Total H_2 uptake of different IRMOF-2 series at 77 K and up to 100 bar[44], (d) Correlation between H_2 storage capacity, surface area, and vibrational shifts for CPO-27-Ni, HKUST-1, and MOF-5[45], (e) Schematic of Ni_2(m-dobdc) MOF, and (f) Total H_2 uptake of Ni_2(m-dobdc) across a wide temperature range (−75 °C to 100 °C).[46]*

Yaghi *et al.* synthesized five metal-organic frameworks (MOF-324, 325, 326 and IRMOF-61 and 62) using short linkers (pyrazolecarboxylate and pyrazaboledicarboxylate) and long linkers (ethyldibenzoate and butadiynedibenzoate) to study the impact of various ligands on hydrogen storage in these MOFs. **(Figure 1.4a)** Their study found an interesting fact: at 77 K and low pressure, there was no specific relationship between H_2 uptake and surface area. MOF-324 outperforms the other designed novel MOFs in a pressure range from 100 to 800 torr and obtained a H_2 loading value of 21 mg/g at 760 torr. [43] This loading value is slightly lower than that of some benchmark MOFs, such as MOF-505 and HKUST-1, which have open metal sites, but higher than those of MOF-5 and MOF-177. High-pressure H_2 storage was investigated for MOF-324 and IRMOF-62 at 77 K and 298 K. The gravimetric excess H_2 uptake values of 33 and 49 mg/g were obtained for MOF-324 and IRMOF-62 at 77 K. At high pressure, the observed uptake capacities were modest and lower compared to the well-known MOF-177 at 70 bar. The hydrogen uptake in MOF-326 indicates that polarizable linkers significantly accelerate hydrogen uptake due to enhanced interactions. Moreover, the long linkers identified in both the IRMOF-61, and IRMOF-62 MOFs demonstrate that highly interpenetrated structures can be designed, allowing for pore control and the regulation of adsorption site density.

The effect of Li doping was also observed in hexagonal MOFs (IRMOF-2-24 and IRMOF-2-60), and the H_2 storage capacities were reported at ambient conditions. Li doping significantly improved the H_2 uptake at 300 K, IRMOF-2-96-Li stored 6.0 wt% at 273 K and 100 bar, reaching the DOE target. **(Figure 1.4b)** The best-performing MOF, based on volumetric uptake, was IRMOF-2-54-Li, which achieved a volumetric uptake of 20.7 g/L at 273 K, lower than the DOE target. Their simulated results were well correlated with the experimental findings and yielded results similar to those obtained in the experiments.[44] Vitillo *et al.* have unraveled the role of exposed metal sites in HKUST-1 and CPO-27-Ni MOF for H_2 storage applications. The value of initial adsorption enthalpy of -13.5 kJ/mol was obtained for the CPO-27-Ni, indicating efficient H_2 storage through physisorption. The total H_2 amount stored in these materials was 1.8 H_2 mass% for CPO-27-Ni, 2.7 H_2 mass% for HKUST-1, and 3.1 H_2 mass% for MOF-5 at 77 K and 45 bar, and these capacities were largely dependent on their surface area and pore volume. The adsorption capacities of these materials were directly correlated with the surface area at higher pressure. **(Figure 1.4c)** This study proposed that the development of porous materials with a high surface density of active sites for hydrogen adsorption could be a potential route for better H_2 storage.[45] A study found that

remarkably enhanced hydrogen storage capacity can be observed in Pd nanocrystals covered with the MOF (HKUST-1). Their experimental findings showed that the 74% increase in hydrogen storage capacity was observed after coating HKUST-1 with Pd nanocrystals. It also improves the kinetics of hydrogen storage by allowing H_2 molecules to interact with these nanocrystals. This study suggested that other earth-abundant transition metals can be used in place of Pd to design cost-effective and accessible H_2 storage materials.[47] **Table 1.3** summarizes the experimental and simulated results for MOFs in hydrogen storage applications.

Table 1.3. *Hydrogen storage capacities of various MOFs under different temperature and pressure conditions.*

MOFs	Surface Area (m^2/g)	Temperature (K)	Pressure (bar)	H_2 Storage Capacities (wt %)	Ref
MOF-5	3510	77	100	7.8	[48]
IRMOF-20	4070	77	100	9.1	[48]
NU-1101	4340	77	100	9.2	[49]
NU-1102	3720	77	100	9.6	[49]
NU-1103	6245	77	100	12.6	[49]
NU-100	6050	77	100	13.9	[50]
UiO-66 (Zr)	1903	77	1	1.36	[5]
Ni-MOF-74	848	298	100	0.8	[51]
Co-MOF-74	797	298	100	0.7	[51]

In our study, we have explored the H_2 adsorption and evaluated the H_2 adsorption capacities in a family of structural isomers of this framework, M_2(*m*-dobdc) (M = Mn, Fe, Co, Ni; *m*-dobdc^{4-} = 4,6-dioxido-1,3-benzenedicarboxylate), featuring exposed M^{2+} cation sites with a higher apparent charge density. In 2014, Long *et al.* synthesized this series and observed the H_2 interaction with metal coordination sites and found greater isosteric heats of H_2 adsorption ranging from -10.3 kJ/mol to -12.3 kJ/mol.[52] In 2018, Long *et al.* extended this study to measure H_2 storage in M_2(*m*-dobdc) and M_2(dobdc) (M = Co, Ni) under conditions most relevant to onboard H_2-storage for practical applications. **(Figure 1.4d)** Based upon the data of the adsorption isotherm, Ni_2(*m*-dobdc) was found to be the top-performing physisorptive

storage material with a usable volumetric capacity between 100 and 5 bar of 11.0 g/L at 25 °C and 23.0 g/L with a temperature swing between −75 and 25 °C.[46]

1.4. Objectives

1. We have studied the H_2 storage mechanism in Li-decorated and late-transition metal (Cr to Zn) chelated COFs. These COFs contain various ligands such as HHTP (2,3,6,7,10,11-hexahydroxytriphenylene), TPT (Triphenyl-1,3,5-triazine), and 2-phenyl-1,3,2-benzodioxaboroles. We have explored the H_2 binding mechanism in both 3D COFs and their molecular organic linkers. The gravimetric capacities and the role of the interactions involved in the H_2 binding were studied and explained in detail. **Chapters 3 and 4** will give a comprehensive view of both research works.
2. We have performed *Grand Canonical Monte Carlo Simulations* (GCMC) to study the H_2 adsorption isotherms in M_2(*m*-dobdc) series at five different temperatures: 77 K, 160 K, 198 K, 233 K, and 298 K. We also performed Density Functional theory (DFT) calculations to verify the binding enthalpies and physisorption phenomena. More details regarding this work will be provided in **Chapter 5** of this thesis.

1.5. Recent Developments in the Field of Porous Materials for Hydrogen Storage

The enhanced H_2 storage in MOF materials can be achieved through effective design strategies, including the functionalization of ligands, the insertion of open metal sites, and alterations to their local environment and coordination geometry. Earlier research was primarily focused on increasing the surface area of porous materials to enhance storage capacities. Due to the weak interactions between H_2 molecules and porous materials, the accepted H_2 uptake capacities that could satisfy the DOE target were mostly observed only at cryogenic temperatures. However, the ambient conditions are required for real-world H_2 storage applications. Introducing several functional groups, such as -OH, -CH_3, -CF_3, and -NH_2, in the organic ligands of COFs and MOFs could play a crucial role in enhancing H_2 storage.

Recently, Ghosal *et al.* employed a dicarboxylate linker containing two -CF_3 groups, which features a pendant polar acylamide (-CONH-) group, and synthesized a mixed-ligand 3D MOF$\{[Zn_2(4\text{-pmi})(hfipbb)_2].(H_2O)_3\}_n$. This synthesized MOF material shows both hydrogen storage and supercapacitance together in a single material. This MOF material achieved maximum H_2 uptake of 128 cc/g at 1 bar pressure.[53] Farha *et al.* have developed a

robust Cu(I)-based MOF, NU-2100, using a mixture of Cu/Zn precursors in which zinc acts as a catalyst to transform an intermediate MOF into NU-2100 without getting incorporated into the final MOF. **(Figure 1.5a)** NU-2100 shows the high isosteric heat of adsorption value of 32 kJ/mol and H_2 deliverable capacity of 10.4 g/L at ambient conditions (233 K/100 bar→296 K/6 bar). **(Figure 1.5b)** The isosteric heat of adsorption in this MOF outperforms some benchmark MOFs with open metal sites.[54] Cu and Zn-based MOFs have been recognized as a potential candidate to improve H_2 adsorption enthalpies. Long *et al.* recently synthesized a series of isostructural frameworks $Cu_{2.7}M_{2.3}X_{1.3}(btdd)_3$ (M = Mn, Cd; X = Cl, I; Cu^IM-MFU-4*l*) and modulated the π-back bonding interactions by tuning the pyramidal geometry of the trigonal Cu^I sites. This strategy enhanced the H_2 binding enthalpy, revealing that a decrease in the ionic radius of the metal atom increases the enthalpy value. The H_2 binding enthalpy values in Cu^IM-MFU-4*l* MOF followed this sequence: −33 kJ/mol for M = Zn^{II} (0.74 Å), −27 kJ/mol for M = Mn^{II} (0.83 Å), and −23 kJ/mol for M = Cd^{II} (0.95 Å). **(Figure 1.5c)** Then, they measured the high-pressure H_2 adsorption isotherms at a temperature range of 223 to 323 K. Cu^ICd-MFU-4*l* showed the highest volumetric usable capacity of 8.5 g/L at 298 K, **(Figure 1.5d)** and Cu^IZn-MFU-4*l* achieved the highest gravimetric usable capacity of 3.5 wt % at 233 K and 170 bar, then decreased to 298 K and 5 bar.[55] Gordon *et al.* computationally studied $M^IM_4^{II}Cl_3(bta)_6$ (bta^- = benzotriazolate) Kuratowski-type clusters as a model for strong binding sites in MFU-4*l* frameworks. **(Figure 1.5e)** They have discovered a linear relationship between enthalpy and the increase in ionic radius. Among the other 3d transition metals selected in their study, Co^I showed the highest strong H_2 binding, with the binding enthalpy ranging from -45 to -41 kJ/mol when the central M^{II} atom is altered from Zn^{II} to Cd^{II}.[56] Additionally, their other findings revealed the H_2 storage in V(II)XMFU-4*l* node containing halogen groups. They found the fluorine ligand-based structure showed the highest binding enthalpy value of -19.3 kJ/mol at 77 K and 1 atm and -21.3 kJ/mol at 228 K and 1 atm for the first adsorbed H_2 molecule. The usable capacity for the fluoride-containing node in MFU-4l was 4.1 g/L pressure swing between 5 and 100 bars at 228 K.[11] Recent studies suggested that tuning the crystal size and shape distribution in MOFs enhances their packing density and volumetric H_2 storage capacity. After tuning the crystal size of the well-known MOF material MIL-53-Al, a 25% enhancement in volumetric uptake was achieved compared to pristine MIL-53-Al. Tuned $(MIL\text{-}53\text{-}Al)_{1:1}$ has achieved volumetric usable capacity of 37 g/L under the pressure swing conditions 70 bar to 5 bar at 77 K.[57]

Current research is primarily focused on machine learning-guided DFT and GCMC simulations to predict the hydrogen capacity of large datasets for MOFs and COFs. Recently, Snurr *et al*. developed a machine learning (ML) model to predict the deliverable capacity of 105,230 MOFs. Their developed ML model reliably identified the top-performing MOFs, as validated by the following GCMC simulations. They suggested that it would be a challenging task to design and develop new MOFs with a deliverable capacity exceeding 51.9 g/L under preferred cryogenic operating conditions. This study also suggested that using lighter and smaller metal clusters and constructing MOFs from denser net platforms could benefit gas storage applications for physisorption-based materials.[17]

In conclusion, this literature review provides compelling evidence that tuning the MOF crystal size, pore sizes, unsaturated metal sites and ligand functionalization will be beneficial to utilize the full potential of MOF materials to meet the USDOE targets and satisfy the global energy demands. These findings suggest that integrating concepts from chemistry, materials science, and mathematics could advance sustainable and efficient H_2 storage in MOF-based technologies.

In addition to this, COFs promote extensive electron delocalization through their π-conjugated frameworks and improve the conductivity. The level of control over their structural features enhances their functionality and allows for optimized H_2 storage performance. Aza-COF is a microporous 2D COF with a periodic structure and well-dispersed pyridinic nitrogen sites. This COF was found to be highly chemically and thermally stable. A recent DFT study suggested that the Ti adatom formed a strong bond with the pyridinic N in Aza-COF and contributed to the charge transfer from the Ti atom to COF.

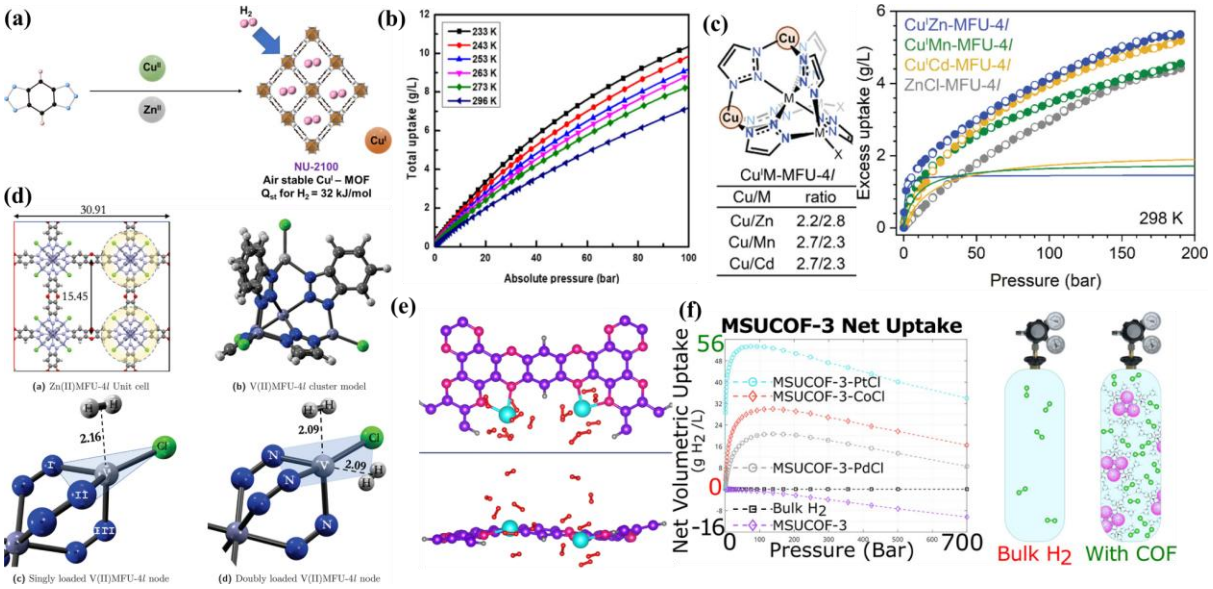

Figure 1.5. *Metal-organic framework structures and hydrogen storage performance. (a) Schematic illustration of NU-2100 MOF structure, (b) Temperature-dependent hydrogen adsorption isotherms (233-298 K) showing total uptake as a function of absolute pressure up to 100 bar in NU-2100 MOF[54], (c) Comparison of excess hydrogen uptake at 298 K for bimetallic MOFs[55], (d) Zn^{II}MFU-4l unit cell structure and V(II)MFU-4l cluster model[11], (e) hydrogen adsorption Ti adatom decorated Aza-COF[58] and (f) Net volumetric hydrogen uptake comparison for MSUCOF-3-PtCl, MSUCOF-3-CoCl, MSUCOF-3-PdCl versus bulk H_2.[59]*

This resulted in an orbital-level interaction between the 3d orbital of the Ti atom and the 2p orbital of N. Each Ti atom can adsorb seven H_2 molecules and show the highest uptake capacity of 9.34 wt % **(Figure 1.5e)**.[58] Mendoza-Cortes *et al.* recently designed novel COF materials (MSUCOF) and chelated these COFs with transition metal atoms (Co, Cu, Fe, Ni, and Mn). The fitted Morse potential force field parameters have been developed to accurately capture the interaction between H_2 molecules and transition metal chelated complexes. The MSUCOF-3 family gave the best volumetric uptake of 73 g/L, and MSUCOF-3-PtCl achieved approximately triple the uptake values of pristine MSUCOF-3. **(Figure 1.5f)** The highest gravimetric uptake of 4.7 wt % was obtained for Pt chelated MSUCOF-1 and Mn chelated MSUCOF-2 at room temperature.[59] Recently, Keskin *et al.* assessed the performance of 69784 COFs for the adsorption of five gas molecules at various pressure conditions using molecular simulations and machine learning models. This study revealed that hypoCOFs performed exceptionally with H_2 adsorption capacities of 1.73 mol/kg at 1 bar. Their selectivity for CO_2/H_2, CH_4/H_2, CO_2/N_2, and CO_2/CH_4 separations outperforms experimentally studied COFs.[60]

1.6. Challenges in the Hydrogen Storage on Porous Materials

Researchers have observed that the cost, stability, and synthesis limitations are the main obstacles to the real-world applications of H_2 storage in MOFs and COFs. The high cost of these materials is mainly linked to the organic linker. However, the linker performs well across various applications; it may be possible to develop methods to produce large numbers of linkers at an affordable cost. Simplifying the complexity of linker synthesis and increasing the overall yield can be achieved through reaction optimization, such as using efficient catalysis. The other major concern is the stability of the MOFs and COFs, which is highly required for H_2 storage applications. In the case of CO_2 capture, the stability of these materials is characterized by their structural retention in the presence of water. Maintaining their stability in humid conditions is very challenging and needs more attention. Theoretically, accurate prediction of hydrogen binding enthalpy and adsorption behaviors highlights their limitations. Despite numerous advances in research, correlating theoretical predictions with experimental outcomes remains challenging. One main concern is the accuracy of computational outcomes, which can be compromised by several factors, including poor selection of exchange-correlation functionals, neglect of zero-point energy effects, and the use of an improper basis set to describe the atomic orbitals of atoms in MOF/COF. These factors often lead to an underestimation or overestimation of the hydrogen binding enthalpy. Addressing these issues is crucial for providing accurate guidance on experimental findings and enhancing the reliability of DFT studies. To overcome this issue, advancements in computational methodologies are needed to improve accuracy for practical hydrogen storage applications. It has been identified that accurate potential parameters for the interaction of hydrogen and other gases with unsaturated metal sites of MOFs are necessary to obtain results that support experimental findings. These potential parameters can be developed using DFT calculations for a simple model system. GCMC simulations are unable to predict the long-term stability of MOFs in the presence of water, air, and other impurities, which represents a significant area for future research. The Universal Force Field (UFF) is unable to provide accurate uptake capacities, generally underestimating H_2 storage capacities. There is an urgent need to develop force fields that describe strong interactions between hydrogen and COFs or MOFs, utilizing quantum mechanical calculations. Neither MOFs nor COFs achieve the DOE 2025 target for usable capacity (6.5 wt % and 40 g/L at ambient conditions). This could be achieved through ligand functionalization and the tuning of pore size or surface area in porous materials.

1.7. References

[1] P. Liu, Y. Jia, Y. Ning, X. Zhang, S. Tian, F. Yang, W. Song, Y. Zhang, International Journal of Hydrogen Energy 56 (2024) 315–322.

[2] M.K. Sarmah, T.P. Singh, P. Kalita, A. Dewan, RSC Advances 13 (2023) 25253–25275.

[3] D. Zhao, X. Wang, L. Yue, Y. He, B. Chen, Chemical Communications 58 (2022) 11059–11078.

[4] Global Hydrogen Review 2021 (2021).

[5] R.A. Alabdulhadi, S. Khan, A. Khan, L.T. Alfuhaid, M.Y. Khan, M. Usman, N. Maity, A. Helal, ACS Applied Energy Materials 8 (2025) 1397–1413.

[6] M.A. Sattar, M.G. Rasul, M.I. Jahirul, M.M. Hasan, Sustainable Energy and Fuels 8 (2024) 3545–3573.

[7] US Department of Energy, U.S Drive (2017) 1–29.

[8] A.S. Mekonnin, K. Wacławiak, M. Humayun, S. Zhang, H. Ullah, Catalysts 15 (2025) 260.

[9] Q. Li, H. Machida, K. Norinaga, Industrial and Engineering Chemistry Research 63 (2024) 19063–19075.

[10] P. Zhou, Q. Zhou, X. Xiao, X. Fan, Y. Zou, L. Sun, J. Jiang, D. Song, L. Chen, Advanced Materials 37 (2025) 2413430.

[11] R. Chakraborty, K.M. Carsch, D.E. Jaramillo, Y. Yabuuchi, H. Furukawa, J.R. Long, M. Head-Gordon, Journal of Physical Chemistry Letters 13 (2022) 10471–10478.

[12] V. Mahamiya, A. Shukla, A.K. Adak, H. Lee, N. Seriani, R. Gebauer, PRX Energy 4 (2025) 022001.

[13] A.M. Varghese, S. Kuppireddy, S. Tsatsos, G. Kyriakou, N. Alamoodi, G.N. Karanikolos, Industrial and Engineering Chemistry Research 64 (2025) 16845–16861.

[14] H. Furukawa, O.M. Yaghi, Journal of the American Chemical Society 131 (2009) 8875–8883.

[15] N. Sinha, H. Joshi, S. Pakhira, ACS Applied Electronic Materials 4 (2022) 6237–6252.

[16] H. Joshi, N. Sinha, K. Parveen, S. Pakhira, Energy and Fuels 37 (2023) 19771–19784.

[17] K. Liu, H. Chen, T. Islamoglu, A.S. Rosen, X. Wang, O.K. Farha, R.Q. Snurr, Molecular Systems Design and Engineering 10 (2025) 817-835.

[18] C. Zhang, F. Formalik, D. Lv, F. Sha, K.O. Kirlikovali, X. Wang, X. Tang, S. Su, H. Xie, Y. Chen, Z. Li, R.Q. Snurr, O.K. Farha, Angewandte Chemie 137 (2025) e202424260.

[19] S. Pakhira, J.L. Mendoza-Cortes, Physical Chemistry Chemical Physics 21 (2019) 8785–8796.

[20] Y. Lan, Y. Gong, X. Pang, Y. Feng, Y. Ran, H. Guo, X. Lu, Chemical Communications 60 (2024) 9534–9537.

[21] Y. Tian, S.Q. Xu, C. Qian, Z.F. Pang, G.F. Jiang, X. Zhao, Chemical Communications 52 (2016) 11704–11707.

[22] A. Garcia-Duran, M. Fumanal, Journal of Materials Chemistry C 13 (2025) 18239–18249.

[23] X. An, K. Zhao, W. Zhang, J. Yang, Y. Liao, L. Wang, D. Fu, Fuel 309 (2022) 122175.

[24] S. Gao, F. Li, T. Yu, L. Wang, Langmuir 41 (2025) 22856–22862.

[25] S.H. Sang, H. Furukawa, O.M. Yaghi, W.A. Goddard, Journal of the American Chemical Society 130 (2008) 11580–11581.

[26] E. Klontzas, E. Tylianakis, G.E. Froudakis, Nano Letters 10 (2010) 452–454.

[27] G. Garberoglio, R. Vallauri, Microporous and Mesoporous Materials 116 (2008) 540–547.

[28] M.G. Rabbani, A.K. Sekizkardes, Z. Kahveci, T.E. Reich, R. Ding, H.M. El-Kaderi, Chemistry - A European Journal 19 (2013) 3324–3328.

[29] X.D. Li, J.H. Guo, H. Zhang, X.L. Cheng, X.Y. Liu, RSC Advances 4 (2014) 24526–24532.

[30] J.H. Guo, H. Zhang, Y. Tang, X. Cheng, Physical Chemistry Chemical Physics 15 (2013) 2873–2881.

[31] J.L. Mendoza-Cortés, S.S. Han, W.A. Goddard, Journal of Physical Chemistry A 116 (2012) 1621–1631.

[32] S. Pakhira, J.L. Mendoza-Cortes, Journal of Physical Chemistry C 124 (2020) 6454–6460.

[33] D. Cao, J. Lan, W. Wang, B. Smit, Angewandte Chemie - International Edition 48 (2009) 4730–4733.

[34] J.H. Guo, H. Zhang, Z.P. Liu, X.L. Cheng, Journal of Physical Chemistry C 116 (2012) 15908–15917.

[35] J. Lan, D. Cao, W. Wang, Journal of Physical Chemistry C 114 (2010) 3108–3114.

[36] Y. Pramudya, J.L. Mendoza-Cortes, Journal of the American Chemical Society 138 (2016) 15204–15213.

[37] Z. Li, X. Feng, Y. Zou, Y. Zhang, H. Xia, X. Liu, Y. Mu, Chemical Communications 50 (2014) 13825–13828.

[38] H.D. Lawson, S.P. Walton, C. Chan, ACS Applied Materials and Interfaces 13 (2021) 7004–7020.

[39] R. Mehek, N. Iqbal, T. Noor, M.Z.B. Amjad, G. Ali, K. Vignarooban, M.A. Khan, RSC Advances 11 (2021) 29247–29266.

[40] N.L. Rosi, J. Eckert, M. Eddaoudi, D.T. Vodak, J. Kim, M. O'Keeffe, O.M. Yaghi, Science 300 (2003) 1127–1129.

[41] A.G. Wong-Foy, A.J. Matzger, O.M. Yaghi, Journal of the American Chemical Society 128 (2006) 3494–3495.

[42] M. Gallo, D. Glossman-Mitnik, Journal of Physical Chemistry C 113 (2009) 6634–6642.

[43] D.J. Tranchemontagne, K.S. Park, H. Furukawa, J. Eckert, C.B. Knobler, O.M. Yaghi, Journal of Physical Chemistry C 116 (2012) 13143–13151.

[44] S.S. Han, W.A. Goddard, Journal of Physical Chemistry C 112 (2008) 13431–13436.

[45] J.G. Vitillo, L. Regli, S. Chavan, G. Ricchiardi, G. Spoto, P.D.C. Dietzel, S. Bordiga, A. Zecchina, Journal of the American Chemical Society 130 (2008) 8386–8396.

[46] M.T. Kapelewski, T. Runčevski, J.D. Tarver, H.Z.H. Jiang, K.E. Hurst, P.A. Parilla, A. Ayala, T. Gennett, S.A. Fitzgerald, C.M. Brown, J.R. Long, Chemistry of Materials 30 (2018) 8179–8189.

[47] G. Li, H. Kobayashi, J.M. Taylor, R. Ikeda, Y. Kubota, K. Kato, M. Takata, T. Yamamoto, S. Toh, S. Matsumura, H. Kitagawa, Nature Materials 13 (2014) 802–806.

[48] A. Ahmed, Y. Liu, J. Purewal, L.D. Tran, A.G. Wong-Foy, M. Veenstra, A.J. Matzger, D.J. Siegel, Energy and Environmental Science 10 (2017) 2459–2471.

[49] D.A. Gómez-Gualdrón, T.C. Wang, P. García-Holley, R.M. Sawelewa, E. Argueta, R.Q. Snurr, J.T. Hupp, T. Yildirim, O.K. Farha, ACS Applied Materials and Interfaces 9 (2017) 33419–33428.

[50] A. Ahmed, S. Seth, J. Purewal, A.G. Wong-Foy, M. Veenstra, A.J. Matzger, D.J. Siegel, Nature Communications 10 (2019) 1568.

[51] S. Xie, Q. Qin, H. Liu, L. Jin, X. Wei, J. Liu, X. Liu, Y. Yao, L. Dong, B. Li, ACS Applied Materials and Interfaces 12 (2020) 48476–48485.

[52] M.T. Kapelewski, S.J. Geier, M.R. Hudson, D. Stück, J.A. Mason, J.N. Nelson, D.J. Xiao, Z. Hulvey, E. Gilmour, S.A. Fitzgerald, M. Head-Gordon, C.M. Brown, J.R. Long, Journal of the American Chemical Society 136 (2014) 12119–12129.

[53] A. Maiti, B. Jana, R. Kumar, K. Das, D. Ghoshal, Inorganic Chemistry 64 (2025) 18332–18345.

[54] D. Sengupta, P. Melix, S. Bose, J. Duncan, X. Wang, M.R. Mian, K.O. Kirlikovali, F. Joodaki, T. Islamoglu, T. Yildirim, R.Q. Snurr, O.K. Farha, Journal of the American Chemical Society 145 (2023) 20492–20502.

[55] Y. Yabuuchi, H. Furukawa, K.M. Carsch, R.A. Klein, N. V. Tkachenko, A.J. Huang, Y. Cheng, K.M. Taddei, E. Novak, C.M. Brown, M. Head-Gordon, J.R. Long, Journal of the American Chemical Society 146 (2024) 22759–22776.

[56] N. V. Tkachenko, Y. Yabuuchi, K.M. Carsch, H. Furukawa, J.R. Long, M. Head-Gordon, Journal of Physical Chemistry C 129 (2025) 167–178.

[57] R. Murugavel, A.A. Rownaghi, F. Rezaei, ACS Applied Nano Materials 7 (2024)

23733–23743.

[58] A. M, U. Jethawa, S.M. Ali, B. Chakraborty, Journal of Energy Storage 136 (2025) 118382.

[59] M. Djokic, J.L. Mendoza-Cortes, Energy and Fuels 38 (2024) 4711–4720.

[60] G.O. Aksu, S. Keskin, ACS Materials Letters 7 (2025) 954–960.

CHAPTER 2

Principles of DFT Methods and Monte Carlo Simulations

This chapter provides a comprehensive overview of Density Functional Theory (DFT) and the Monte Carlo (MC) simulation methods used in our computational studies of H2 storage in both covalent organic frameworks (COFs) and metal-organic frameworks (MOFs). This chapter will help us understand the theory behind quantum-mechanical calculations and MC simulations, and it is essential to establish a solid conceptual foundation before examining the research findings. This chapter is divided into two parts: the first explains the theory of DFT, and the second provides the theoretical background for MC simulations.

2.1. Many Body Equations

Hartree proposed a method after Schrodinger's equation, and he proposed an equation for multiple-electron systems. This equation, based on fundamental physical principles, is known as the *Hartree method*.[1] The equation for the He atom can be written as:

$$\widehat{H} = -\frac{\nabla_1^2}{2} - \frac{\nabla_2^2}{2} + V_{ne}(\mathbf{r}_1) + V_{ne}(\mathbf{r}_2) + V_{ee}(\mathbf{r}_1, \mathbf{r}_2), \qquad (2.1)$$

where $\mathbf{r}_n$ is the position vector of the nth electron and ∇_n is the gradient vector operator for the nth electron. On the right-hand side of this equation, the first two terms are kinetic energy operators, and the next two terms are nuclear-electron electrostatic interaction potentials. The last term is an electron-electron electrostatic interaction potential. Hartree assumed that each electron moves in the averaged potential of the electrostatic interactions with surrounding electrons and suggested the independent electron approximation, which approximates the averaged potential as an effective potential V_{eff}. As a result, the Hamiltonian operator (H) is divided into terms for the different electrons as:

$$\widehat{H} = \left[-\frac{\nabla_1^2}{2} + V_{ne}(r_1) + V_{eff}(\mathbf{r}_1)\right] + \left[-\frac{\nabla_2^2}{2} + V_{ne}(r_2) + V_{eff}(\mathbf{r}_2)\right] \quad (2.2)$$

$$= \hat{h}(\mathbf{r}_1) + \hat{h}(\mathbf{r}_2), \qquad (2.3)$$

where $h(\mathbf{r}_i)$ is the Hamiltonian operator for the i[th] electron. The wave function for this Hamiltonian operator can be represented as the product of different electronic motion wavefunctions,

$$\psi(\mathbf{r}_1, \mathbf{r}_2) = \phi(\mathbf{r}_1)\phi(\mathbf{r}_2) \qquad (2.4)$$

and the expectation value of the Hamiltonian operator is written as:

$$E = \frac{\int d^3\mathbf{r}_1 d^3\mathbf{r}_2 \psi^*(\mathbf{r}_1, \mathbf{r}_2)\, \hat{H}\psi(\mathbf{r}_1, \mathbf{r}_2)}{\int d^3\mathbf{r}_1 d^3\mathbf{r}_2 \psi^*(\mathbf{r}_1, \mathbf{r}_2)\psi(\mathbf{r}_1, \mathbf{r}_2)}$$

$$= \frac{\sum_{i=1}^{2} \int d^3\mathbf{r}_i \phi^*(\mathbf{r}_i)\, \hat{h}(\mathbf{r}_i)\phi(\mathbf{r}_i)}{\sum_{i=1}^{2} \int d^3\mathbf{r}_i \phi_i^*(\mathbf{r}_i)\phi_i(\mathbf{r}_i)} \qquad (2.5)$$

The variation principle states that the Schrodinger equation for obtaining the set of one-electron wavefunctions $\{\phi_i\}$, which makes this expectation value stationary can be written as:

$$\hat{h}(\mathbf{r}_i)\phi(\mathbf{r}_i) = \epsilon_i \phi_i(\mathbf{r}_i) \qquad (2.6)$$

The eigenvalue ϵ_i is explained as the eigenenergy for the motion of the i[th] electron, the total wavefunction can be gained by solving the eigen equation for each electron. This expression in equation (2.6) also suggests that the total eigenenergy is the sum of the orbital energies corresponding to different electronic motions,

$$\hat{H}\psi = (\epsilon_1 + \epsilon_2)\phi_1\phi_2 = \epsilon\psi. \qquad (2.7)$$

This theory is known as the *Hartree method.*

2.2.Born-Oppenheimer Approximation

Now, with the help of the above-mentioned Hartree method, we can write the Hamiltonian operator for the hydrogen molecule as:

$$\hat{H} = \hat{h}(\mathbf{r}_1) + \hat{h}(\mathbf{r}_2) + V_{nn}(R_{AB}), \qquad (2.8)$$

R_{AB} represents the distance between two atomic nuclei A and B.

The behavior of electrons in molecules has been studied using a highly effective simplification called the *Born-Oppenheimer (BO) approximation*, which is also known as the *adiabatic*

approximation.[2] ***The basic principle is that electrons are so much lighter and faster than atomic nuclei that we can treat the nuclei as stationary while electrons are revolving around them.*** It means we can neglect the nucleus's kinetic energy, vibrations, and rotations. This approximation is remarkably accurate for most molecules in their ground states, and it makes quantum chemical calculations much simpler without compromising key chemical aspects. The mathematical equation is now much easier to solve, and this approximation can serve as the standard approach for quantum-chemical calculations. Now the equation becomes:

$$\hat{H} = \hat{h}(\mathbf{r}_1) + \hat{h}(\mathbf{r}_2), \qquad (2.9)$$

This equation is analogous to the Hamiltonian of the He atom. Later, to solve this equation, the concept of molecular orbitals was introduced.

2.3.Slater Determinant

In 1926, Heisenberg and Dirac made a major discovery to explain the behavior of electrons in molecules.[3,4] They realized that to properly follow the Pauli exclusion principle (which states that no two electrons can occupy the exact same quantum state), the mathematical description of electron's wavefunctions must follow an antisymmetric property. To achieve this antisymmetric nature, this wavefunction should be written in the form of a determinant. Later on, John Slater developed a systematic method for solving the Schrodinger equation using these normalized determinants that represent antisymmetric wavefunctions and introduced the concept of the *exchange integral*.[5]

Let us consider the exchange of electrons, using the He atom as an example. The Hamiltonian remains the same by exchanging the coordinates of two electrons:

$$\hat{H}(\mathbf{r}_1, \mathbf{r}_2) = \hat{H}(\mathbf{r}_2, \mathbf{r}_1). \qquad (2.10)$$

This leads to $$\hat{H}(\mathbf{r}_1, \mathbf{r}_2)\psi(\mathbf{r}_2, \mathbf{r}_1) = E\psi(\mathbf{r}_2, \mathbf{r}_1), \qquad (2.11)$$

The Hamiltonian operator is commutative with the exchange operator, replacing the positions of two electrons $\hat{P}_{12}$,

$$\hat{H}(\mathbf{r}_1, \mathbf{r}_2)\, \hat{P}_{12}\psi(\mathbf{r}_1, \mathbf{r}_2) = \hat{P}_{12}\hat{H}(\mathbf{r}_1, \mathbf{r}_2)\psi(\mathbf{r}_1, \mathbf{r}_2), \qquad (2.12)$$

Means; $$\left[\hat{H}, \hat{P}_{12}\right]\psi = \left(\hat{H}\,\hat{P}_{12} - \hat{P}_{12}\,\hat{H}\right)\psi = 0. \qquad (2.13)$$

This indicates that the Hamiltonian and exchange operators have simultaneous eigenstates. Moreover, $\hat{P}_{12}^2 = 1$ is found by considering that the positions of two electrons are reversed by two exchanges. This leads to the eigenvalues of $\hat{P}_{12}$: ± 1. The symmetric wavefunction for +1 eigenvalues is:

$$\psi^{(S)}(\mathbf{r}_1, \mathbf{r}_2) = \frac{1}{\sqrt{2}}\{\psi(\mathbf{r}_1, \mathbf{r}_2) + \psi(\mathbf{r}_2, \mathbf{r}_1)\}, \tag{2.14}$$

and the antisymmetric wavefunction corresponding to the -1 eigenvalue,

$$\psi^{(A)}(\mathbf{r}_1, \mathbf{r}_2) = \frac{1}{\sqrt{2}}\{\psi(\mathbf{r}_1, \mathbf{r}_2) - \psi(\mathbf{r}_2, \mathbf{r}_1)\} = -\psi^{(A)}(\mathbf{r}_2, \mathbf{r}_1), \tag{2.15}$$

where $1/\sqrt{2}$ is the normalization constant.

Now, the symmetric and antisymmetric wavefunctions can be expressed as:

$$\psi^{(S)}(\mathbf{r}_1, \mathbf{r}_2) = \frac{1}{\sqrt{2}}\{\phi_1(\mathbf{r}_1)\phi_2(\mathbf{r}_2) + \phi_1(\mathbf{r}_2)\phi_2(\mathbf{r}_1)\} \tag{2.16}$$

and $$\psi^{(A)}(\mathbf{r}_1, \mathbf{r}_2) = \frac{1}{\sqrt{2}}\{\phi_1(\mathbf{r}_1)\phi_2(\mathbf{r}_2) - \phi_1(\mathbf{r}_2)\phi_2(\mathbf{r}_1)\}, \tag{2.17}$$

respectively. The antisymmetric wavefunction can be expressed by a *Slater determinant*. For a two-electron, this takes the form:

$$\psi(\mathbf{r}_1, \mathbf{r}_2) = \frac{1}{\sqrt{2}}\begin{vmatrix} \phi_1(\mathbf{r}_1) & \phi_1(\mathbf{r}_2) \\ \phi_2(\mathbf{r}_1) & \phi_2(\mathbf{r}_2) \end{vmatrix} \tag{2.18}$$

This ensures that the wavefunction is antisymmetric under partial exchange. When $\mathbf{r}_1 = \mathbf{r}_2$, the determinant equals zero, which directly enforces the Pauli exclusion principle: an electron cannot occupy the same quantum state simultaneously.

For the case of N electrons, the antisymmetric wavefunction can be written in a determinant form,

$$\psi(\mathbf{r}_1, \mathbf{r}_2, \ldots\ldots, \boldsymbol{r}_N) = \frac{1}{\sqrt{N!}}\begin{vmatrix} \phi_1(\mathbf{r}_1) & \phi_1(\mathbf{r}_2) & \cdots & \phi_1(\mathbf{r}_N) \\ \phi_2(\mathbf{r}_1) & \phi_2(\mathbf{r}_2) & \cdots & \phi_2(\mathbf{r}_N) \\ \vdots & \vdots & \ddots & \vdots \\ \phi_N(\mathbf{r}_1) & \phi_N(\mathbf{r}_2) & \cdots & \phi_N(\mathbf{r}_N) \end{vmatrix} \tag{2.19}$$

$$= \frac{1}{\sqrt{N!}} \det|\phi_1(\mathbf{r}_1)\phi_2(\mathbf{r}_2)\cdots\phi_N(\mathbf{r}_N)| \qquad (2.20)$$

This determinant is called the *Slater Determinant.*

2.4.Basis Function

The Roothaan method accelerates Hartree-Fock (HF) calculations by expanding molecular orbitals in a basis set.[6,7] The computational accuracy and speed depend on the quality of basis functions. Gaussian-type functions are the most popular basis functions in quantum chemistry due to their computational advantages. The product rule of Gaussian-type basis functions can be written as:[8]

$$\exp(-\alpha|\mathbf{r}-\mathbf{R}_\mathrm{A}|^2)\exp(-\beta|\boldsymbol{r}-\boldsymbol{R}_B|^2) \qquad (2.21)$$

$$= \left[\frac{2\alpha\beta}{(\alpha+\beta)\pi}\right]^{\frac{3}{4}} \exp\left(-\frac{\alpha\beta}{(\alpha+\beta)}|\mathbf{R}_\mathrm{A}-\mathbf{R}_\mathrm{B}|^2\right)\exp[-(\alpha+\beta)|\mathbf{r}-\mathbf{R}_\mathrm{C}|^2], \qquad (2.22)$$

$$\mathbf{R}_\mathrm{C} = \frac{\alpha}{\alpha+\beta}\mathbf{R}_\mathrm{A} + \frac{\beta}{\alpha+\beta}\mathbf{R}_\mathrm{B}, \qquad (2.23)$$

where $\mathbf{R}_\mathrm{A}$ is the coordinate vector of nucleus A. Based on this definition, the product of two Gaussian functions yields another Gaussian function centred at a different point, significantly accelerating two-electron integral evaluations. Later, Boys *et al*. proposed contracted Gaussian-type basis functions, which are linear combinations of primitive Gaussian functions and achieve high accuracy with fewer basis functions.[9]

$$\chi_p(\mathbf{r}-\mathbf{R}_\mathrm{A}) = \sum_\mu c_{p\mu}\exp\left(-\alpha_{\mu p}\,|\mathbf{r}-\mathbf{R}_\mathrm{A}|^2\right). \qquad (2.24)$$

In this equation (2.24), the original Gaussian-type functions are called primitive functions to distinguish them from the contracted ones. The primitive functions are specified only by the orbital exponent, $\alpha_{\mu p}$, contracted coefficient, $c_{p\mu}$, and the coordinate vector of the center of the function, $\mathbf{R}_\mathrm{A}$. The primitive functions are standardized for *s, p, d and f* orbitals analogous to spherical harmonics. For *d and f* orbitals, linear combinations are used to provide the correct

The most important Gaussian-type basis functions are described as:

a) Minimal basis sets: They contain only the essential contracted functions for each atom. For carbon, this includes five functions for *1s*, *2s* and three *2p* orbitals. Example: STO-*L*G. The

minimal basis functions approximating Slater-type orbitals (STO) corresponding to atomic orbitals with L primitive functions are called STO-*L*G basis functions. [10]

b) Split-valence basis sets: This basis set uses single contracted functions for core orbitals but multiple functions for valence orbitals, since valence electrons primarily participate in bonding. Pople-type notation like "6-31G" indicates 6 primitive functions contracted for core orbitals and double-split valence functions (3 primitives + 1 uncontracted). [11] Dunning-Huzinaga (DZ, TZ, QZ) and Ahlrichs (DZV, TZV, QZV) types follow similar splitting patterns. Examples are: 6-31G, 6-311G and others.

c) Polarization-augmented basis sets: This basis set incorporates bond isotropy by adding higher angular momentum functions of the atomic orbitals. In the Pople notation, "*" indicates *d* functions on heavy atoms, while "**" adds *p* functions to hydrogen. Correlation-consistent basis sets (cc-pVXZ) are designed to provide equivalent treatment of electron correlation across different orbital types. Dunning *et al.* developed these basis functions to account for electron correlations in valence orbitals, such as the *4d* and *4f* orbitals.[12] Furthermore, there are "cc-pCVXZ" basis functions, which incorporate the electron correlations of the core orbitals by adding *s* and *p* orbital functions. Examples are: 6-31G*, cc-pVXZ and cc-pCVXZ.

d) Diffuse-augmented basis sets: This basis set includes diffuse functions for weakly bound electrons, essential for anions and excited states. Adding diffuse functions is shown by a plus "+" in Pople-type basis functions. For correlation-consistent basis functions, augmenting diffuse functions are denoted by "aug-" at the head of the names, and one diffuse function is added to each angular-momentum type of basis function. Example: 6-311+G(d), aug-cc-pVXZ, etc. [13]

e) Effective core potential (ECP) basis set: This replaces core electrons with an effective potential, which reduces computational cost while maintaining accuracy. Relativistic ECPs incorporate relativistic effects for heavy element atoms, making them standard for fourth-period elements and beyond. Example: LanL2DZ and Stuttgart-ECP. [14] These are the most widely used basis functions in quantum chemistry calculations.

2.5.Hohenberg-Kohn Theorem

This theorem consists of the following two auxiliary theorems for nondegenerate ground electronic states:[15]

a) First Theorem: External potentials (nuclear-electron interactions) are uniquely determined by electron density alone, not wavefunctions. This means the ground-state Hamiltonian can be completely defined by electron density.

b) Second Theorem: The energy variational principle applies to the electron density, which ensures that the correct ground-state density minimizes the total energy for a given external potential.

In the early stages of these theorems, they revealed significant conceptual gaps. The first is the *V-representability* problem, which arises because the first theorem suggested an unproven one-to-one correspondence between electron density and wavefunction. Another problem is implicitly assuming the *N-representability* of the electron density.[16] The N-representability of the electron density indicates that the electron density is always greater than or equal to zero, the sum of the electron density is the number of electrons N, and the square of the gradient of the square root of the electron density $\left|\nabla\rho^{\frac{1}{2}}\right|^2$ has a finite total sum. In general, the energy variation principle is violated unless the Hamiltonian operator is written in terms of N-representable variables. In practice, DFT calculations typically employ Slater determinants rather than full-electron wave functions. Since Slater determinants are inherently N-representable, this N-representability problem of variables is rarely seen in practical DFT applications.

In 1979, Levy's *constrained search formulation* solved the V-representability problem.[17] Instead of assuming density-wavefunction correspondence, it defines a universal functional $E_{univ}[\rho]$, as the minimum expectation value of kinetic plus electron-electron interaction energies among all wavefunctions yielding density :

$$E_{univ}[\rho] = \min_{\psi\to\rho} \int d^3\mathbf{r}\, \psi^*(\hat{T} + \hat{V}_{ee})\, \psi. \qquad (2.25)$$

This *constrained search formulation* establishes a one-to-one correspondence between the electron density and wavefunction for every system and solves the *V-representability* problem.

2.6.Kohn-Sham (KS) Method

The Hohenberg-Kohn theorems provide the theoretical foundation for density-based quantum chemistry, but it does not reveal a practical method for calculating electronic states. The famous Kohn-Sham (KS) method represents an exact reformulation of the Hohenberg-Kohn theorem, not an approximation.[18] It rigorously implements the one-to-one correspondence between external potential and electron density through variational principles, ensuring that the method is accurate for determining electronic structures. In practice, the Kohn-Sham method employs a one-electron **self-consistent field (SCF)** equation analogous to Hartree-Fock theory. Both methods apply Slater determinants as trial wavefunctions, use the Lagrange multiplier method for energy minimization under normalization constraints and generate similar Fock-type operators for the resulting nonlinear equations.

$$\hat{F} = \hat{h} + 2\sum_{j}^{n} \hat{J}_j + V_{xc}. \tag{2.26}$$

The difference between this Fock operator and the Hartree-Fock counterpart is only the *exchange-correlation potential functional* (V_{xc}), which substitutes for the exchange operator in the Hartree-Fock operator.[19] Specifically, the Coulomb operator $\hat{J}_j$, remains identical, representing electron density interactions; the exchange operator is substituted with exchange-correlation density functionals, and electron correlation effects, treated as multi-configurational interactions in wavefunction methods, are incorporated simply as potential density functionals.

Using this Fock operator, orbitals ϕ_i, and orbital energies, ϵ_i are calculated by solving the one-electron equation,

$$\hat{F}\phi_i = \epsilon_i \phi_i, \tag{2.27}$$

Orbital energies are represented as,

$$\epsilon_i = \int d^3\mathbf{r}_1 \phi_i^*(r_1)\, \hat{F}\phi_i(\mathbf{r}_1) \tag{2.28}$$

$$= h_i + 2\sum_j^n J_{ij} + \int d^3\mathbf{r}_1 \rho_i(\mathbf{r}_1) V_{xc}\,, \tag{2.29}$$

where ρ_i is the electron density of the i-th orbital, and is summed to be the total electron density,

$$\rho = \sum_{i}^{n} \rho_i = 2\sum_{i}^{n} |\phi_i|^2. \tag{2.30}$$

Unlike the Hartree–Fock method, the Kohn–Sham approach calculates the total electronic energy using the exchange–correlation energy functional rather than the exchange–correlation potential functional,

$$E = \sum_i^n (h_i + 2\sum_j^n J_{ij}) + E_{xc}. \quad (2.31)$$

The exchange-correlation potential functional (V_{xc}), is the first derivative of this exchange-correlation energy functional with respect to electron density,

$$V_{xc} = \frac{\delta E_{xc}}{\delta \rho}. \quad (2.32)$$

The Kohn-Sham method employs a self-consistent field approach identical to Hartree-Fock for solving the nonlinear equations:

a) Initialize the molecular system (nuclear coordinates, charges, electron count) and guess initial molecular orbitals

b) Construct the Fock operator's two-electron components using current reference orbitals

c) Solve the Kohn-Sham equation with the updated Fock operator

d) Calculate the exchange-correlation energy from the orbitals and determine the total electronic energy

e) Check convergence by comparing current orbitals and total energy with previous iteration. If the differences exceed the threshold, return to step (b) with new orbitals; otherwise, accept the solution as converged.

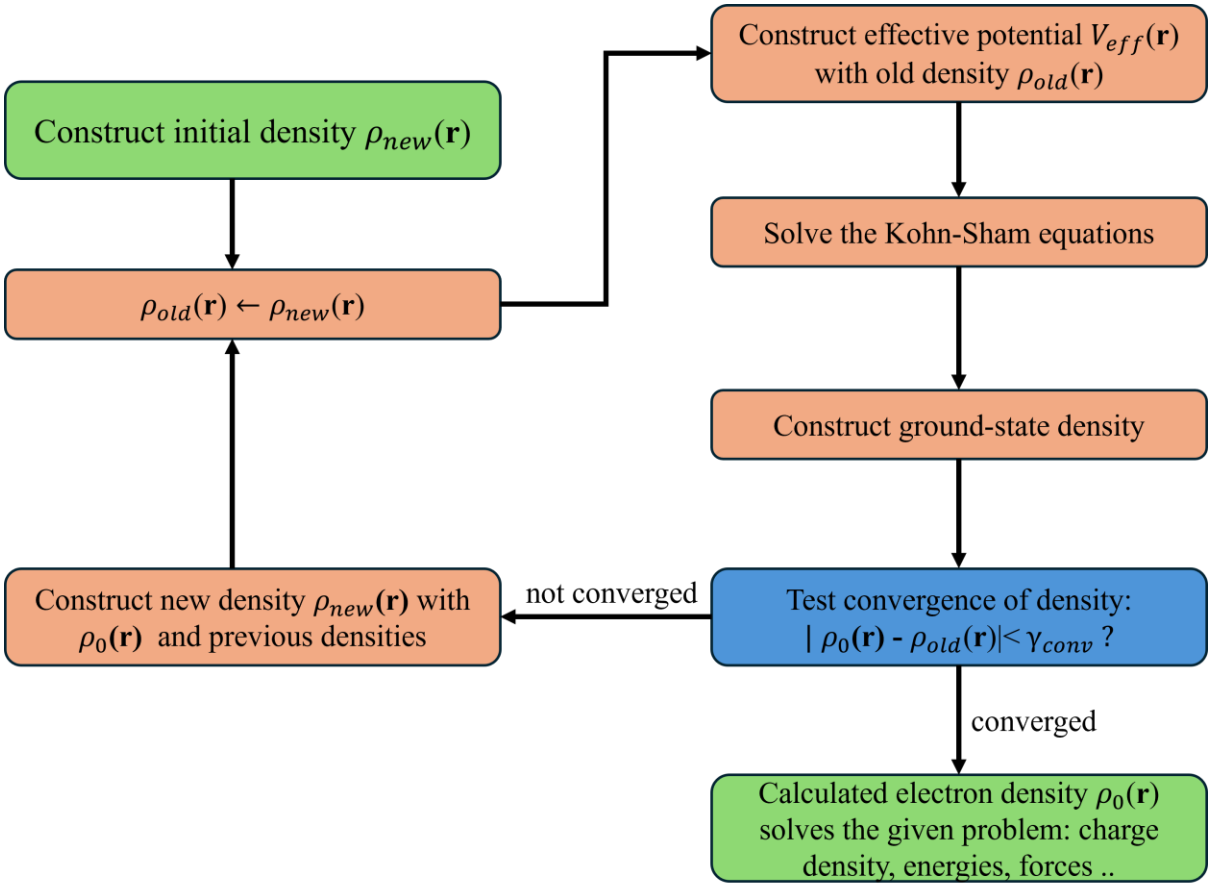

Figure 2.1. The schematic diagram of the self-consistent field cycle

2.7. Classification of Exchange-Correlation Functionals

The Kohn-Sham method relies fundamentally on exchange-correlation functionals, which makes it impossible to evaluate the reliability of methods without examining these functionals specifically. Since the exchange-correlation functional represents the only approximated component in the Kohn-Sham equation, the entire method's accuracy depends on how well this functional approximates reality. Numerous exchange-correlation functionals have been developed in the past years based on different physical models. These can be organized into several categories:

Local density approximation (LDA) functionals depend solely on electron density. **Generalized gradient approximation (GGA) functionals** improve upon LDA by incorporating density gradients $\nabla\rho$. Meta-GGA functionals further enhance GGA by adding kinetic energy density terms.[20] Hybrid functionals combine DFT exchange with a fixed proportion of Hartree-Fock exchange E_x^{HF}. Semiempirical functionals use multiple fitted

parameters to reproduce experimental data accurately. While some functionals do not align in this category, most represent modifications of the standard types to account for specific physical effects. The standard functionals follow a hierarchical structure known as *Jacob's ladder*,[21] as represented in **Figure 2.2**.

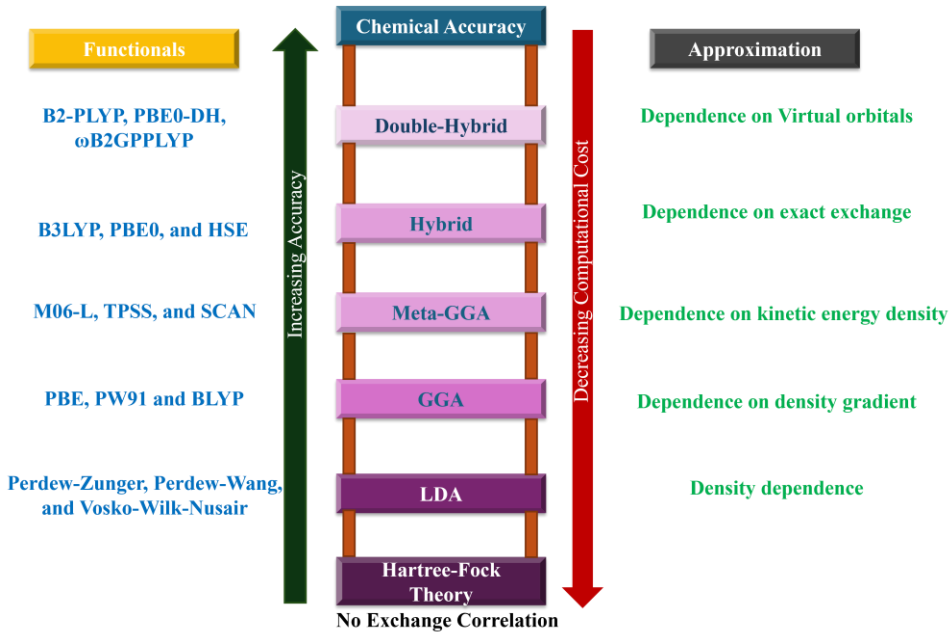

Figure 2.2. *Jacob's Ladder Approach for the Systematic Improvement of DFT Functionals.*

(a) LDA and GGA Exchange Functionals

The LDA exchange functional uses the exact Dirac form, which is the Dirac LDA exchange functional. Similar to the usual exchange integral, this functional is first used as an exchange potential in the Fock operator, and it significantly underestimates the exchange energies. Dirac suggested that the χ_α method means the multiplication of the semiempirical parameter α by the exchange potential, this method improves this underestimation. The exact form of the Dirac LDA exchange functional is usually used in the Kohn-Sham method. Since the Dirac LDA exchange functional is also the exact local density approximation of exchange energy, it is generally used as the local density limit of exchange functionals.

The general form of GGA exchange functionals is defined as:

$$E_x = -\frac{1}{2}\sum_{\sigma} \int \rho_\sigma^{\frac{4}{3}} K_\sigma d^3\mathbf{r}. \qquad (2.33)$$

This K_σ is usually expressed with the dimensionless parameter x_σ,

$$x_\sigma = \frac{|\nabla \rho_\sigma|}{\rho_\sigma^{\frac{4}{3}}} \tag{2.34}$$

Although various forms of GGA exchange functionals have been developed, the differences in the best-known functionals are found only in the dependence of K_σ on x_σ.

(b) Hybrid Functionals

Hybrid functionals are constructed by using a specific theoretical framework that connects exchange functionals (representing exchange energies in independent electron systems) with the Hartree-Fock exchange integral (representing exchange energies in fully interacting systems).

$$E_x = \int_0^1 d\lambda E_x^\lambda \approx E_x^{GGA} + \lambda(E_x^{HF} - E_x^{GGA}), \tag{2.35}$$

This connection involves a coupling strength parameter λ in the above equation, which differs from the standard adiabatic connection because it links both the non-correlated and correlated systems rather than non-interacting and interacting systems. The electron-correlation component in these functionals is calculated separately and does not necessarily follow adiabatic-connection principles. Various hybrid functionals have emerged with different mixing ratios and parameter counts, including the B3LYP,[22] PBE0,[23] and Heyd-Scuseria-Ernzerhof (HSE) functionals.[24]

The B3LYP hybrid functional holds the distinction of being both the first hybrid functional and the most widely used functional in quantum mechanical (QM) calculations. It employs three mixing coefficients to establish adiabatic connections: one between the Hartree-Fock and LDA exchange functionals, another between the LYP-GGA and LDA correlation functionals, and a third to incorporate a modified B88 exchange functional component.

$$E_{xc}^{B3LYP} = E_{xc}^{LDA} + a_1(E_x^{HF} - E_x^{LDA}) + a_2\Delta E_x^{B88} + a_3(E_c^{LYP} - E_c^{VWN-LDA}) \tag{2.36}$$

Besides the parameters in the exchange and correlation functionals, the semiempirical parameters are $a_1 = 0.2, a_2 = 0.72, and\ a_3 = 0.81$.

2.8.van der Waals (vdW) Correction

van der Waals interactions represent one of the most important forms of electron correlation, even though it has been neglected in the development of most correlation functionals. The van der Waals interaction is a collective term that includes dipole-dipole, dipole-induced dipole, and dispersion interactions. Dipole-dipole interactions occur through electrostatic forces between permanent dipoles in polar systems. For interactions between systems A and B, the classical potential follows:

$$V_{\mu-\mu}(r) = -\frac{\mu_A \mu_B}{R_{AB}^3}, \qquad (2.37)$$

where μ_X represents the permanent dipole of each system X and R_{AB} is the inter-system distance. The Kohn-Sham equation already accounts for this interaction within its Coulomb interaction terms.

Dipole-induced dipole interactions arise between polar and nonpolar systems. When a polar system A with a permanent dipole moment μ_A interacts with a nonpolar system B having polarizability α_B, the classical potential becomes:[25]

$$V_{\mu-\alpha}(r) = -\frac{\mu_A \alpha_B}{R_{AB}^6}, \qquad (2.38)$$

This weak interaction explains why polar molecules have limited solubility in nonpolar solvents. Kohn-Sham self-consistent field (SCF) calculations also incorporate this interaction.

Dispersion interactions represent a universal force that operates even between electrically neutral bodies lacking multipole moments. London's perturbation theory provides the classical expression for the potential between two different bodies:[26]

$$V_{disp}^{London}(r) = -\frac{3\alpha_A \alpha_B \ I_A I_B}{2R_{AB}^6 \ \ I_A + I_B}, \qquad (2.39)$$

where I_X is the ionization potential of partial system X.

Dispersion interactions arise from correlations between instantaneous dipole moments created by electron fluctuations and the induced dipole moments they generate. Essentially, electron distributions in two spatially separated systems fluctuate around their equilibrium positions in a correlated manner, creating inter-system attractions. This makes dispersion a pure form of

electron correlation between separate bodies that cannot be captured by one-body mean-field approximations. It represents an explicit long-range correlation acting between distant electrons.

In our DFT calculations, we have used the highest level DFT-D3 functional (i.e., Grimme's 3rd order dispersion correction parameters), which is defined as:

$$E^{DFT-D3} = E^{KS} + E^{(2)}_{disp} + E^{(3)}_{disp} \tag{2.40}$$

$$E^{(2)}_{disp} = -\sum_{A>B}\sum_{n=6,8,10,\dots} \frac{S_n\, C^{AB}_n}{R^n_{AB}}\, f^n_{damp}(R_{AB}), \tag{2.41}$$

$$E^{(3)}_{disp} = -\sum_{A>B>C} \frac{C^{ABC}_9 (3\, cos\theta_a cos\theta_b cos\theta_c + 1)}{(R_{AB}R_{BC}R_{CA})^3} f^{(3)}_{damp}(\bar{R}_{ABC}), \tag{2.42}$$

Where A, B and C are atomic labels, $\theta_a, \theta_b, and\ \theta_c$ are the internal angles of the ABC triangle, and $\bar{R}_{ABC}$ are geometrically averaged radii. The damping functions are given by

$$f^n_{damp}(R_{AB}) = \frac{1}{1 + 6\left(\frac{R_{AB}}{s_{r,n}R^{AB}_0}\right)^{-\alpha_n}}, \tag{2.43}$$

and

$$f^{(3)}_{damp}(\bar{R}_{ABC}) = \frac{1}{1 + 6\left(\frac{\bar{R}_{ABC}}{\left(\frac{4R^{ABC}_0}{3}\right)}\right)^{-16}} \tag{2.44}$$

All the remaining parameters are semiempirical and R^{AB}_0 and R^{ABC}_0 are cutoff radii adjusted to each pair and trio of atoms. Coefficients $s_n (n = 8, 10, \dots)$ are fitted in benchmark calculations depending on the functionals combined, while s_6 is unity or adjusted value less than unity. For dispersion coefficients, C^{AB}_9 and C^{ABC}_9, the time-dependent Kohn-Sham method and recursion relations are used to determine the values for each atomic pair and trio.

2.9. Software used in our DFT and DFT-D Calculations

(a) CRYSTAL17 Suite Code

CRYSTAL17 suite code[27] implements quantum mechanical methods to study the electronic structure and properties of crystalline materials. The theoretical foundation of this suite code rests on Bloch's theorem, which exploits the translational symmetry of periodic crystals by expressing electronic wave functions as Bloch functions-plane waves modulated by functions having the periodicity of the crystal lattice. This fundamental quantum-mechanical principle allows CRYSTAL17 to handle infinite periodic systems by solving the eigenvalue problem only within the first Brillouin zone, with k-point sampling determining the accuracy of the reciprocal-space integration. The approach of the CRYSTAL17 software centers on expanding crystalline orbitals as linear combinations of atom-centered Gaussian-type functions, which provide computational efficiency while maintaining sufficient flexibility to describe both core and valence electron distributions.

i. Basic Structure Parameters

CRYSTAL: Defines the structure as three-dimensional, SLAB: Defines the structure as two-dimensional.

Space Group or Layer number: In the attached input file, 187 corresponds to a specific trigonal space group $P\bar{6}m2$

Lattice parameters: The values a=4.7844 Å and c=7.0775 Å represent the lattice parameters, and γ=120.00˚ shows the angle between the a and b axes.

Number of Atoms: Then the next line indicated the total number of atoms.

ii. Atomic Specifications:

Atomic Number: Element identification (6 for Carbon, and N for Nitrogen)

Fractional Coordinates: x/a, y/b, z/c positions in terms of lattice parameters

iii. Optimization Control Parameters

OPTGEOM: Initiates geometry optimization procedure.

FULLOPTG: Specifies full optimization of both atomic positions and lattice parameters.

MAXCYCLE 800: Sets maximum number of optimization cycles to 800.

ENDOPT: Terminates optimization parameter specification.

iv. Basis Set Structure for Each Element

The first line contains the atomic number, then the number of shells. Each shell begins with parameters *l* value (angular momentum) and n primitives (number of primitive Gaussian functions in this contracted shell). Each contracted shell is "a weighted sum of primitive Gaussians with different exponents". The left column shows exponents (α values), the right column shows contraction coefficients (c values).

v. Density Functional Theory Settings

B3LYP-D3: Hybrid density functional with Grimme's third order dispersion correction.

XLGRID: Specifies an extra-large integration grid for high accuracy DFT calculations.

SPIN: enables spin-polarized calculations.

TOLINTEG 7 7 7 7 14: Coulomb integrals, exchange integrals, Coulomb fitting, and exchange fitting $=10^{-7}$, and bipolar expansion = 10^{-14}.

TOLDEE 7: Total energy convergence criteria (10^{-7}).

SHRINK 0 16: Defines K-POINT sampling in reciprocal space, 0: automatic k-point generation and 16: shrinking factor determining k-point density.

SCFDIR: Enables direct SCF algorithm for memory efficiency.

BIPOSIZE and EXCHSIZE: Memory allocation for bipolar expansion and exchange integrals.

MAXCYCLE: Maximum SCF iterations allowed.

FMIXING: Fock matrix mixing parameter.

ANDERSON: Anderson mixing acceleration technique.

PPAN: Periodic Pulay's DIIS (Direct Inversion of Iterative Subspace) method.

Example Input File for CRYSTAL 17:

```
Title: - g-C3N4 by HIMANI JOSHI
CRYSTAL
0 0 0
```

```
187
4.7844  7.0775   120.0000
6
```

```
6     0.01936   0.50968   0.00000
6     0.15671   0.31343   0.50000
7     0.17009   0.34018   0.00000
7     0.32625   0.16312   0.50000
7     0.33333   0.66667   0.50000
7     0.66667   0.33333   0.00000
```

```
OPTGEOM
FULLOPTG
MAXCYCLE
800
ENDOPT
END
```

```
6 8
0 0 6 2.0 1.0
13575.349682 0.00022245814352
2035.2333680 0.00172327382520
463.22562359 0.00892557153140
131.20019598 0.03572798450200
42.853015891 0.11076259931000
15.584185766 0.24295627626000
0 0 2 2.0 1.0
6.2067138508 0.41440263448000
2.5764896527 0.23744968655000
0 0 1 0.0 1.0
0.4941102000 1.00000000000000
0 0 1 0.0 1.0
0.1644071000 1.00000000000000
0 2 4 2.0 1.0
34.697232244 0.00533336578050
7.9582622826 0.03586410909200
```

2.3780826883 0.14215873329000

0.8143320818 0.34270471845000

0 2 1 0.0 1.0

0.5662417100 1.00000000000000

0 2 1 0.0 1.0

0.2673545000 1.00000000000000

0 3 1 0.0 1.0

0.8791584200 1.00000000000000

7 8

0 0 6 2.0 1.0

19730.800647 0.00021887984991

2957.8958745 0.00169607088030

673.22133595 0.00879546035380

190.68249494 0.03535938260500

62.295441898 0.11095789217000

22.654161182 0.24982972552000

0 0 2 2.0 1.0

8.9791477428 0.4062389614800

3.6863002370 0.2433821717600

0 0 1 0.0 1.0

0.7865398200 1.0000000000000

0 0 1 0.0 1.0

0.2677997200 1.0000000000000

0 2 4 3.0 1.0

49.200380510 0.0055552416751

11.346790537 0.0380523797230

3.4273972411 0.1495367102900

1.1785525134 0.3494930523000

0 2 1 0.0 1.0

0.3780331700 1.0000000000000

0 2 1 0.0 1.0

0.1473661500 1.0000000000000

0 3 1 0.0 1.0

```
 0.3612294900 1.0000000000000
99 0
END
DFT
SPIN
B3LYP-D3
XLGRID
END
TOLINTEG
7 7 7 7 14
TOLDEE
7
SHRINK
0  16
8  8  8
SCFDIR
BIPOSIZE
10000000
EXCHSIZE
10000000
MAXCYCLE
800
FMIXING
80
ANDERSON
PPAN
END
```

(b) Gaussian16 Suite Code

Gaussian 16 [28] is a quantum chemistry suite code that employs computational methods to predict molecular properties, electronic structures, and thermodynamic parameters. The Gaussian 16 input file needs multiple parameters that define the computational methods and

molecular system. The reliability and accuracy of Gaussian 16 calculations depend critically on the convergence criteria employed for various computational procedures. SCF convergence criteria conduct the iterative solution of the electronic structure problem and typically involve multiple matrices that must simultaneously satisfy specified tolerances. Energy convergence requires that successive SCF iterations yield total energies that differ by less than a specified threshold, ranging from 10^{-6} to 10^{-8} Hartree. Root-mean-square density matrix changes are typically required to be less than 10^{-8} for standard calculations. The maximum force and RMS force criteria require that the largest component of the gradient vector should be less than 0.000450 Hartree/Bohr and 0.000300 Hartree/Bohr, respectively. The maximum displacement criterion requires that the largest atomic coordinate change be less than 0.001800 Bohr, while the RMS displacement criterion requires that the root-mean-square coordinate change be less than 0.001200 Bohr. These criteria ensure that the optimization has converged to a stationary point where further coordinate changes would be negligible. The input file of the Gaussian 16 suite code includes the following parameters:

The route section, denoted by the (#) symbol, specifies the level of theory, basis set and job type of the calculation.

Print Level: #P for detailed output, #N for normal output

Memory: %mem directive for RAM allocation

Processors: %nprocshared for parallel computation

Checkpoint: %chk for saving wavefunction data

Method Selection: B3LYP, M06-L, MP2, CCSD(T) for different levels of theory

Basis Set: cc-pVDZ, cc-pVTZ, 6-31G(d,p), def2-TZVP for atomic orbital representation

Job Types: Opt (geometry optimization), Freq (frequency calculation), SP (single point energy), IRC (reaction path)

Keywords: EmpiricalDispersion for van der Waals corrections, Solvent for implicit solvation models

Charge and Multiplicity: It defines the electronic state (0 1 for neutral singlet)

Coordinates: Cartesian (x,y,z) or Z-matrix format for atomic positions

Connectivity: Bond topology specification when automatic detection is insufficient

Output Analysis and Result Interpretation

Zero-point energy corrections account for quantum mechanical vibrational effects that persist even at absolute zero temperature and represent a significant contribution which is essential for accurate thermodynamic calculations. Temperature-dependent thermodynamic corrections help compare theoretical results with experimental calorimetric and spectroscopic data by accounting for how temperature affects the translational, rotational, and vibrational motions of molecules. The thermal correction to enthalpy includes both the zero-point energy and temperature-dependent contributions, providing the total enthalpy change relative to the electronic energy. Gibbs free energy corrections additionally incorporate entropy effects, yielding the thermodynamic quantity used to predict reaction spontaneity and equilibrium positions. Vibrational analysis enables direct comparison with infrared (IR) and Raman spectroscopic data. The real frequencies, or positive frequency values, confirm the true minimum, while negative frequency values indicate saddle points or transition states. Electronic structure analysis provides insight into the nature of chemical bonding and electronic distribution within molecules through molecular orbital analysis, population analysis, and electrostatic properties.

Example input file for Gaussian 16 suite code:

```
%mem=180GB
%nprocshared=20
%NProcLinda=1
#p B3LYP/cc-pVDZ EmpiricalDispersion=GD3 geom=connectivity Opt Freq

Benzene Ring by HIMANI JOSHI

0 1
 C          -6.91032684  -0.45996776  -0.00063400
 C          -5.51516684  -0.45996776  -0.00063400
 C          -4.81762884   0.74778324  -0.00063400
 C          -5.51528284   1.95629224  -0.00183300
 C          -6.91010784   1.95621424  -0.00231200
 C          -7.60770884   0.74800824  -0.00131600
```

H	-7.46008584	-1.41228476	-0.00018400
H	-4.96565884	-1.41248076	0.00068100
H	-3.71794884	0.74786324	0.00000000
H	-4.96508284	2.90843524	-0.00189200
H	-7.46022984	2.90849524	-0.00326500
H	-8.70731284	0.74819124	-0.00149600

1 2 1.5 6 1.5 7 1.0
2 3 1.5 8 1.0
3 4 1.5 9 1.0
4 5 1.5 10 1.0
5 6 1.5 11 1.0
6 12 1.0
7
8
9
10
11
12

(c) GAMESS Suite Code

The General Atomic and Molecular Electronic Structure System (GAMESS)[29] is a quantum chemistry tool designed for electronic structure calculations and molecular property predictions. GAMESS input files are organized using control groups that specify different aspects of the quantum chemical calculation.

I. Primary Control Section

The $CONTRL group defines fundamental calculation parameters and includes several keywords:

SCFTYP: Specifies the self-consistent field method

(a) RHF: Restricted Hartree-Fock for closed-shell systems
(b) UHF: Unrestricted Hartree-Fock for open-shell systems

(c) RKS/UKS: Restricted/Unrestricted Kohn-Sham for DFT calculations

RUNTYPE: Defines the type of calculation to be performed

(a) ENERGY: Single-point energy calculations
(b) OPTIMIZE: Geometry optimization
(c) EDA: Energy Decomposition Analysis for intermolecular interactions
(d) HESSIAN: Second derivative calculation for frequencies

DFTTYP: Specifies exchange-correlation functional for DFT calculations

MULT: Defines spin multiplicity (2S+1 where S is the total spin)

NOSYM: Disables symmetry considerations when needed

MAXIT: Maximum number of SCF iterations allowed

II. Basis Set Specification

GBASIS: Specifies the basis set family

III. Energy Decomposition Analysis

MATOM: Defines which atoms belong to each molecular fragment

MCHARG: Specifies the charge of each fragment

MMULT: Defines the multiplicity of each fragment

Energy decomposition analysis provides a rigorous theoretical framework for understanding intermolecular interactions by systematically decomposing the total interaction energy into physically interpretable components. The methodology begins with isolated molecular fragments and progressively includes different physical effects:

Total Interaction Energy = Electrostatic + Exchange-Repulsion + Polarization + Charge Transfer + Dispersion

Example input file of GAMESS software:

```
$CONTRL SCFTYP=RHF RUNTYP=EDA DFTTYP=B3LYP MAXIT=200
    MULT=1 NOSYM=1 ISPHER=1 $END
```

```
 $CCINP  NCORE=10 $END
 $System mwords=12000  MEMDDI=4500 $end
 $INTGRL NOPK=1 $END
 $BASIS GBASIS=TZV $END
 $lmoeda matom(1)=12,2 mcharg(1)=0,0 mmult(1)=1,1 $end
$DATA
Benzene_1H2 by HIMANI JOSHI
C1
C     6.0          -6.91032684   -0.45996776   -0.00063400
 C     6.0          -5.51516684   -0.45996776   -0.00063400
 C     6.0          -4.81762884    0.74778324   -0.00063400
 C     6.0          -5.51528284    1.95629224   -0.00183300
 C     6.0          -6.91010784    1.95621424   -0.00231200
 C     6.0          -7.60770884    0.74800824   -0.00131600
 H     1.0          -7.46008584   -1.41228476   -0.00018400
 H     1.0          -4.96565884   -1.41248076    0.00068100
 H     1.0          -3.71794884    0.74786324    0.00000000
 H     1.0          -4.96508284    2.90843524   -0.00189200
 H     1.0          -7.46022984    2.90849524   -0.00326500
 H     1.0          -8.70731284    0.74819124   -0.00149600
 H     1.0          -6.07992611    0.72531268    2.28291711
 H     1.0          -6.11345821    0.70087531    1.68435349
$END
```

Introduction to Monte Carlo (MC) Simulations

Molecular simulations enable us to study the properties of many-particle systems at the atomic level. However, most of these quantities do not correspond to properties measured in real experiments. The gap between these two levels can be bridged by methods in statistical mechanics. In statistical mechanics, large systems with many energy states for each energy level can be studied. The assumption is that many microscopic states are compatible with a macroscopic state: a physical system can be arranged in different ways while still having the same energy. A collection of different configurations of a system that share macroscopic properties is called an ensemble.

Depending on the property to be computed, simulations can be performed across several ensembles. Most of the common ensembles are:

a) Microcanonical Ensemble (NVE): In this ensemble, the total energy (E), volume (V), and the number of particles (N) are fixed.
b) Canonical Ensemble (NVT): In this ensemble, the temperature (T), volume (V), and the number of particles (N) are fixed, but the energy (E) is not known.
c) Grand Canonical Ensemble (μVT): In this ensemble, the chemical potential (μ), volume (V), and temperature (T) are fixed, but the energy (E) and the number of particles (N) are not fixed.

2.10. Interatomic Potentials: The Foundation of Molecular Interactions

To perform accurate molecular simulations within the statistical mechanics framework, we need to define how atoms and molecules interact. Classical molecular simulation techniques use the sum of inter- and intra-molecular interactions to describe the energy of a host-guest system, and these interactions are described by force fields. Such classical simulations do not consider the degree of freedom of electrons, and it saves computational effort to model electron interactions by using the Born-Oppenheimer approximation. The interatomic potential is a sum of various terms that can be calculated separately.

$$E_{Total} = E_{stretch} + E_{bend} + E_{torsion} + E_{improper\_torsion} + E_{electroostatic} + E_{vDW} \quad (2.45)$$

$E_{stretch}$ = two-body stretching potential, E_{bend} = three-body bending potential, $E_{torsion}$, $E_{improper\_torsion}$= four body torsional potential. The summation of these four potentials is the bonded potential. The non-bonding interaction is the sum of the electrostatic and van der Waals potentials.

(a) Bonded Interactions

Bond stretching

Bond stretch potential terms are described by Hook's law:

$$E_{stretch} = k_b(r - b_0)^2 \qquad (2.46)$$

This equation describes the energy $E_{stretch}$ changes with the distance r to the force field defined reference b_0.

Angle bending

DRIDING[30] use the harmonic cosine function to show the angle bending:

$$E_{bending} = k[\cos(\theta) - \cos(\theta_0)] \qquad (2.47)$$

k is the bending energy constant and θ and θ_0 are the bond angle and reference bond angle defined in the force field.

Torsional and improper torsional terms

The magnitudes of both bond stretching and angle bending are large, and a significant amount of energy is required to provide deformation from their reference values. Hence, torsional terms can vary the structure. Like the bonding, stretching, and angle bending terms, torsional and improper terms, the four-body dihedral motion is based on the energy barriers of bond rotation. Quantum-mechanical calculations suggest that the rotational barriers result from the antibonding interaction between two opposite atoms in a four-body system.

$$E_{torsion} = \sum_{n=0}^{n=N} \frac{V_n}{2}[1 + \cos(nw - \gamma)] \qquad (2.48)$$

w = angle of the torsion, and V_n stands for the barrier's height, n is the multiplicity that defines the number of minimal points, and γ defines where the minimum points should be located.

The following expression is used to explain the improper torsion angle:

$$E_{improper_{torsion}} = k(1 - \cos(2w)) \qquad (2.49)$$

(b) Non-bonded Interactions

van der Waals Interaction

The weak van der Waals (vdW) interaction is the combination of long-range dispersive and short-range repulsive interactions. The long-range dispersive interaction is responsible for the attractive force between atoms. This interaction is also referred to as the London dispersion force. To model attractive and repulsive interactions, a force field should accurately reproduce the potential energy curve. The 12-6 Lennard-Jones (LJ) interaction can be written as:

$$E_{VDW} = 4\varepsilon[\left(\frac{\sigma}{r}\right)^{12} - \left(\frac{\sigma}{r}\right)^{6}] \qquad (2.50)$$

ε = potential well, and σ = is the collision diameter where the separation energy is zero.

Electrostatic Interactions

Electrostatic interactions between charged sites can be computed in RASPA using the Ewald summation method to account for long-range Coulombic effects under periodic boundary conditions. The electrostatic energy between two partial charges q_i and q_j can be written as the second term in the Equation. The *charge equilibration (Q_{eq}) method* computes partial charges for atoms in a molecule using their geometry as input and three important properties of isolated atoms.[31] The first is the ionization potential, i.e., the energy needed to remove the outer valence electron; the second is the electron affinity, i.e., the energy difference related to the injection of an extra electron; and the last is the atomic radius. These quantities can be obtained from experimental measurements and/or computed by the *ab initio* methods. The Q_{eq} method is based on Sanderson's concept of electronegativity equalization,[32] postulating that two or more atoms combining within a molecule get their electronegativity equalized.

LJ potential and Coulomb potentials:[33]

$$U_{ij}(r_{ij}) = 4\varepsilon_{ij}\left[\left(\frac{\sigma_{ij}}{r_{ij}}\right)^{12} - \left(\frac{\sigma_{ij}}{r_{ij}}\right)^{6}\right] + \frac{1}{4\pi\varepsilon_0}\frac{q_i q_j}{r_{ij}} \qquad (2.51)$$

(c) Mixing Rules

To combine two defined parameters of different types of atoms, there are three mixing rules:[34,35]

(a)Lorentz-Berthelot

$$\varepsilon_{ij} = \sqrt{\varepsilon_i \varepsilon_j},\ \sigma_{ij} = \frac{\sigma_{i+}\sigma_j}{2}$$

(b)Waldman-Hagler

$$\varepsilon_{ij} = \frac{2\sigma_i^3 \sigma_j^3}{\sigma_i^6 + \sigma_j^6} \sqrt{\varepsilon_i \varepsilon_j}\ ,\ \sigma_{ij} = \left(\frac{\sigma_{i+}\sigma_j}{2}\right)^{1/6}$$

The vdW potential needs to be cut off at a certain distance, called the *"cut-off"* distance. In the MC simulation, a cut-off distance can be used because van der Waals potentials are negligible beyond it. However, this cut of energy may lead to force divergence. In general, the vdW potential can be switched to a smooth function.

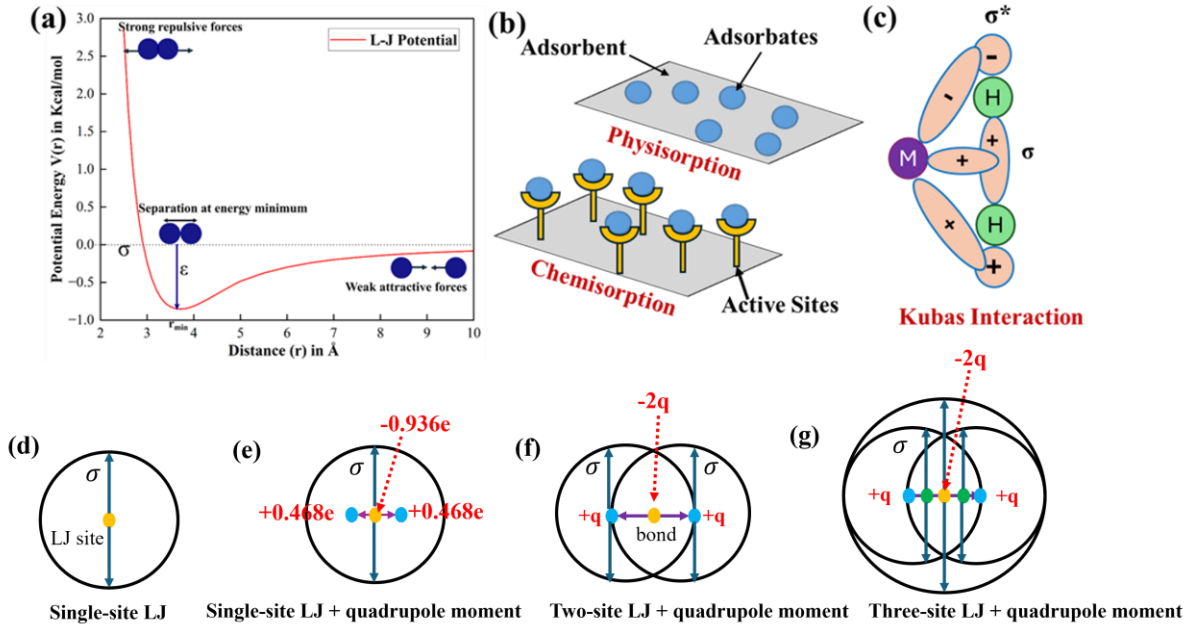

Figure 2.3. *(a) The schematic diagram of the L-J potential, (b) representation of physisorption and chemisorption, (c) representation of Kubas interaction, (d) schematic diagram of H_2 models.*

2.11. Specialized Models for Hydrogen

(a) Single-site LJ Model

The simplest model of diatomic H_2 uses a single-site Lennard-Jones 12-6 potential placed at the COM of the molecule and is generally referred to as a "LJ-1S model" (**Figure 2.3d**). An LJ potential is defined by its well depth ε and the distance σ at which the potential is equal to zero. Buch proposed a value of ε/kB = 34.2 K, with kB being Boltzmann's constant and σ = 2.96 Å for the COM site.[36] In its original form, it was supplemented by a small quadrupole–quadrupole interaction term. However, preliminary tests showed problems attaining equipartition between the different modes due to a slow exchange of kinetic energy between the rotational and translational degrees of freedom, and as done elsewhere, the weak quadrupole interaction was discarded.

(b) Single-site LJ Model + Quadrupole Moment

In the Darkrim-Levesque (DL) model,[37] the H_2 molecules were described with a three-site, rigid model having an H–H bond length of 0.741 Å as represented in **Figure 2.3e**. A Lennard-Jones site (σ_{HH} = 2.958 Å and ε_{HH}/k_B = 36.7 K) was placed at the H_2 centre of mass, and a negative charge of −0.936 on the centre of mass was balanced by positive charges of 0.468 on the H nuclei.

(c) Two-Site LJ + Quadrupole Moment

The two-site LJ model can be further extended by including the quadrupole moment of H2, thereby referred to as a "LJ-2S-q±" model (**Figure 2.3f**). This is the case for Marx and Nielaba,[38] whose model had a quadrupole moment of 54.2 $(KÅ^5)^{1/2}$, along with LJ 12-6 interactions between the H atoms, with ε_{HH}/k_B = 36.7 K and σ_{HH} = 2.958 Å; i.e., they were very close to those of a LJ-1S model.

(d) Three-Sites LJ + Quadrupole Moment

Belof *et al.* have developed both a polarizable and non-polarizable potential for H_2 from first principles.[39] Their non-polarizable model is a "LJ-3S-q± model" (**Figure 2.3g**) combining three LJ 12-6 interaction sites with a quadrupole moment (model Be5 LJ-3S-q±). The masses are placed at atomic positions separated by 0.742 Å. These mass sites carry a charge of q/e = 0.3732 but are not the origin of an LJ interaction. The COM has a charge of −2q placed on it and an LJ interaction with parameters ε/kB = 8.8516 K and σ = 3.2293 Å. Two other massless sites are placed along the H–H bond at 0.329 Å from the COM, and these are also the origin of a LJ interaction with ε/kB = 4.0659 K and σ = 2.3406 Å.

2.12. Feynman-Hibbs (FH) Effective Potential

The accurate representation of hydrogen fluid molecules requires consideration of quantum effects, particularly given the small molecular mass of hydrogen, the low temperatures (typically 77 K), and the significant confinement effects in nanoporous materials. These factors make quantum contributions especially important in both the liquid and adsorbed phases. A widely adopted method to incorporate such effects into molecular simulations is the Feynman-Hibbs (FH) effective potential approach.[40] This method, also known as the effective potential method, modifies the classical intermolecular potential by adding a quantum correction term derived from path-integral formulations. The FH potential estimates quantum effects exactly to first order in $\hbar^2$, retaining the classical potential framework while accounting for the finite de Broglie wavelength of light molecules. Mathematically, the FH effective potential is expressed as:

$$V_{FH}(r) = V_{classical}(r) + \frac{\hbar^2}{24 m_r k_B T}\left(\frac{\partial^2 V(r)}{\partial r^2} + \frac{2}{r}\frac{\partial V(r)}{\partial r}\right) \qquad (2.52)$$

The first term represents the conventional classical interaction, while the second term introduces the quantum correction. The zeroth-order approximation neglects the quantum term, recovering the purely classical description. By including the first-order correction, simulations can more accurately reproduce experimental thermodynamic properties for hydrogen in both bulk and confined states. This method has been applied to predict hydrogen adsorption in MOFs and other nanoporous materials, bridging the gap between experimental data and theoretical predictions.

2.13. Monte Carlo Simulations: Computational Methodology

We now turn to the computational methods used to study these systems, with the interatomic potentials defined. The MC method is a numerical statistical method to approximate mathematical expressions that cannot be evaluated accurately. It operates through an iterative process of randomly sampling points within the space and then averaging the collected data. To calculate the average properties of a system, one needs to reduce the sampling number, as there are a vast number of accessible states. To reduce sampling, importance sampling is employed. The MC scheme exploits the fact that only the relative probability of visiting points in configuration space is needed, not the absolute probability, allowing the estimation of a macroscopic property without accounting for all microstates. The Markov chain Monte Carlo (MCMC) method is a class of algorithms for sampling from a probability distribution. The MCMC method generates compatible configurations of the microstate with a probability

proportional to the Boltzmann weight. This algorithm generates a random trial move from the current state to a new state, which can be accepted or rejected. The movements of MC are designed such that the states are visited with the correct probability. The probability of accepting the trial move from the old state (o) to the new state (n) is the same as accepting the trial move from any state (n) to state (o):

$$P_{eq}(o)\alpha(o \to n)P_{acc}(o \to n) = P_{eq}(n)\alpha(n \to o)P_{acc}(n \to o) \qquad (2.53)$$

For the equilibrium in the Metropolis algorithm:

$$\alpha(o \to n) = \alpha(n \to o) \qquad (2.54)$$

It leads to:

$$\frac{P_{acc}\,(o \to n)}{P_{acc}\,(n \to o)} = \frac{P_{eq}(n)}{P_{eq}(o)} \qquad (2.55)$$

Hence, the Metropolis acceptance rule is written as:

$$P_{acc}(o \to n) = \min\left(1, \frac{P_{eq}(n)}{P_{eq}(o)}\right) \qquad (2.56)$$

Random trial moves help the MC method move the system towards an equilibrium where the average properties can be calculated. Insertion, rotation, translation and swap are some of the random trial moves that can be attempted.

(a) Grand Canonical Ensemble Implementation

The grand canonical (μVT) ensemble is the most used ensemble for adsorption simulation. The partition function of this ensemble is:

$$Q(\mu, V, T) = \sum_{N=0}^{\infty} \frac{V^N e^{\beta\mu N}}{\Lambda^{3N} N!} \int e^{-\beta U(s^N;h)} d^N s \qquad (2.57)$$

And the probability of a configuration is:

$$P(s^N, V) \propto \frac{V^N e^{\beta\mu N}}{\Lambda^{3N} N!} e^{-\beta U(s^N;h)} \qquad (2.58)$$

The acceptance rule for several trials is listed below:

i.Particle moves

$$\frac{acc(o \to n)}{acc(n \to o)} = \frac{\frac{V^N e^{\beta\mu N}}{\Lambda^{3N} N! e^{-\beta U_n(S^N;h)}}}{\frac{V^N e^{\beta\mu N}}{\Lambda^{3N} N! e^{-\beta U_o(S^N;h)}}} e^{-\beta[U_n(S^N;h) - U_o(S^N;h)]} \qquad (2.59)$$

ii.Insertion

$$\frac{acc(o\to n)}{acc(n\to o)} = \frac{\frac{V^{N+1}e^{\beta\mu(N+1)}}{\Lambda^{3(N+1)}(N+1)!e^{-\beta U_n(S^{N+1;h})}}}{\frac{V^N e^{\beta\mu N}}{\Lambda^{3N}N!e^{-\beta U_o(S^{N;h})}}} = \frac{Ve^{\beta\mu}}{\Lambda^{3(N+1)}} e^{-\beta[U_n(S^{N+1;h})-U_o(S^{N;h})]} \quad (2.60)$$

iii.Deletion

$$\frac{acc(o\to n)}{acc(n\to o)} = \frac{\frac{V^{N-1}e^{\beta\mu(N-1)}}{\Lambda^{3(N-1)}(N-1)!e^{-\beta U_n(S^{N-1;h})}}}{\frac{V^N e^{\beta\mu N}}{\Lambda^{3N}N!e^{-\beta U_o(S^{N;h})}}} = \frac{\Lambda^3 N}{Ve^{\beta\mu}} e^{-\beta[U_n(S^{N-1;h})-U_o(S^{N;h})]} \quad (2.61)$$

The pressure P is related to the chemical potential μ and fugacity f, which is written as:

$$\beta\mu = \beta\mu_{IG}^0 + \ln(\beta f) \quad (2.62)$$

The chemical potential μ is defined as:

$$\mu_{IG}^0 \equiv \frac{\ln(\Lambda^3)}{\beta} \quad (2.63)$$

Fugacity is a closely related term to the pressure that describes the activity of a gas. The fugacity coefficient Φ is written as:

$$\Phi = \frac{f}{P} = \exp\left[\frac{g(T,P) - g^{IG}(T,P)}{RT}\right] = \exp\left[\frac{\int_0^P \left(\frac{z-1}{P}\right)_T dP}{RT}\right. \quad (2.64)$$

The $g(T,P)$ is Gibbs free energy and IG indicates the ideal gas, z is the compressibility. For an ideal gas, $f = P$ (P close to 0), and the fugacity and pressure can be converted.

In our work, the Peng-Robinson equation is employed:[41]

$$P = \frac{RT}{V_m - b} - \frac{\alpha\alpha}{V_m^2 + 2bV_m - b^2} \quad (2.65)$$

$$a = \frac{0.45724\, R^2 T_c^2}{P_c}$$

$$b = \frac{0.07780 RT_c}{P_c}$$

$$T_r = \frac{T}{T_c}$$

$$\alpha = (1 + (0.37464 + 1.54226\,\omega - 0.26992\,\omega^2)(1 - T_r^{0.5}))^2 \quad (2.66)$$

Where ω is the acentric factor, P_c is the critical pressure, T_c is the critical pressure, and R is the ideal gas constant.

2.14.Adsorption Fundamentals in Porous Materials

In the previous section, we established a theoretical foundation and computational methods; now, we can apply them to study adsorption phenomena in porous materials.

2.14.1. Types of Adsorptions in Porous Materials

An adsorbate molecule can bind to the surface of porous materials in two ways: chemical adsorption and physical adsorption. Chemical adsorption involves the formation of chemical bonds between adsorbates and the surface of the porous material, and it requires a high (more than 100 kJ) energy. On the other hand, physisorption is an adsorption mechanism based on the weak vdW interaction, and the bonding energy of physisorption is weak (7-32 kJ/mol). Gas adsorption in porous materials is usually quantified through adsorption isotherms, which are the amount of gas adsorbed at a constant temperature as a function of pressure.

2.14.2. Adsorption Isotherm

Adsorption isotherms are the principal performance metric of MOF and COF for gas adsorption. For the same pair of gas and framework atom, the amount of adsorption that occurs (loading) depends on pressure, temperature and the binding energy of the gas molecules with the framework. The amount of adsorption is a function of pressure at a constant temperature. Hence, the gas uptake property in both the MOFs and COFs is studied by varying the applied pressure, and the relationship between the uptake and pressure is called an adsorption isotherm. An adsorption isotherm can be obtained experimentally, but also computationally through GCMC simulations. The adsorption mechanics is a phase equilibrium process, as, at equilibrium, the temperature and chemical potential for all species are equal between the adsorbed phase and bulk fluid. The chemical potential is related to pressure through fugacity, which is a measure of the difference between the chemical potential in a system and that in the hypothetical ideal gas state. Fugacity equals the pressure of an ideal gas. In simulations, the chemical potential is directly obtained from the fugacity.

2.14.3. Geometric Properties of Porous Materials

(a) Pore Size and Surface Area

In simulations, the helium void fraction is calculated, and it corresponds to the empty space of a structure divided by the total volume. It is also used to compute excess adsorption during simulations. Excess adsorption can be substantially lower than the absolute adsorption at high pressure and temperatures. It is the difference between the amount of gas in the system and the amount present at the same temperature and pressure in the absence of adsorption. The surface area of a porous material is one of the most important properties, as it is the base where the adsorption process happens. Experimentally, the BET models and the adsorption isotherm of non-reactive gases such as N_2 and Ar are used to calculate the surface area. Computationally, a geometry-based approach is usually used, which involves rolling a probe molecule over the atoms to compute the surface area. In the figure, as can be seen, the red area is shown as a solvent-accessible surface area, which is closely related to the experimentally obtained surface area.

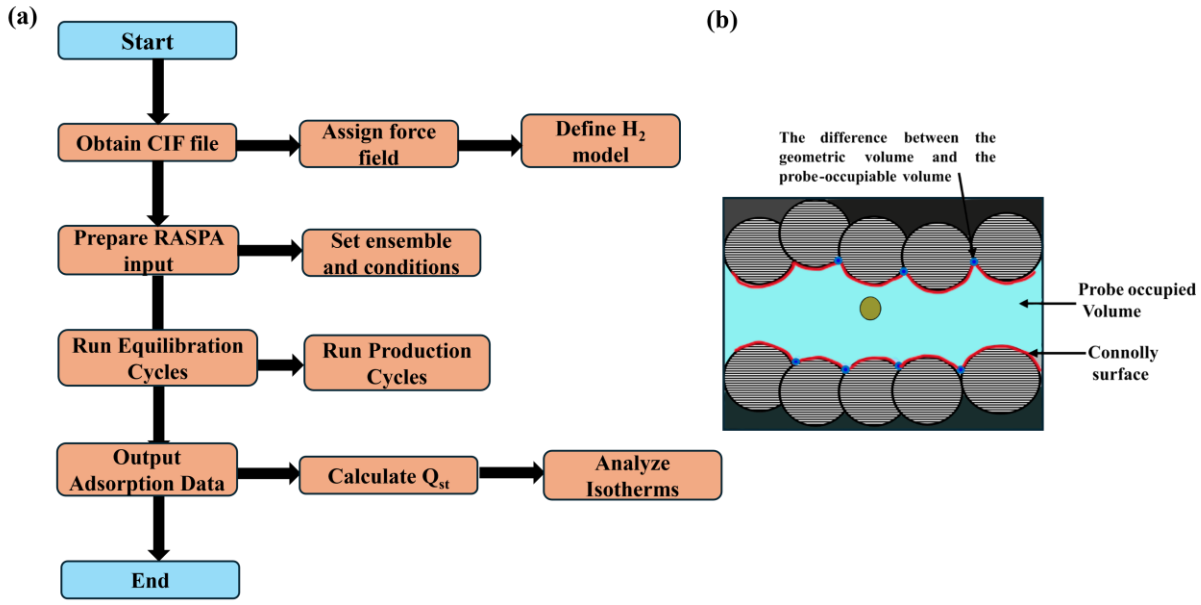

Figure 2.4. *(a) The flowchart of the RASPA 2.0 calculation process, (b) pore-size distribution and Connolly surface.*

The *pore-size distribution (PSD)* can be calculated geometrically in RASPA using the Gelb and Gubbins method.[42] For every point in the void volume, the largest sphere is found that encloses the point but does not overlap with any framework atoms. This yields the cumulative pore volume curve. Let $V_{pore}(r)$ be the volume of the void space 'coverable' by spheres of radius r. A point x is in $V_{pore}(r)$ only if we can construct a sphere of radius r that overlaps x and does not overlap any adsorbent atoms. This volume is equivalent to that enclosed by the pore's "Cannolly surface". $V_{pore}(r)$ is a monotonic decreasing function of 'r' and is easily compared with the "cumulative pore volume" curves often calculated in isotherm-based PSD methods. The PSD is

represented as a histogram with peaks corresponding to the pore sizes present in an MOF. The figure represents the three different sizes of pores that are identified in MOF.

2.14.4. Performance Analysis

i. Deliverable Capacity

To describe the adsorption performance of a porous material for gas storage applications, the deliverable capacity is used as a key descriptor. The deliverable capacity is the difference between the amount of gas adsorbed at the storage and release pressures.

ii. Heat of Adsorption

GCMC simulations can be employed to obtain the isosteric heat of adsorption, which corresponds to the change in energy when one guest molecule is adsorbed and can be calculated using energy/particle fluctuations. The heat of adsorption can be obtained after enough particle insertions and deletions are performed to obtain averages of energy and the number of particles. The heat of adsorption can be written as:

$$Q_{st} = \frac{\langle U \times N \rangle_\mu - \langle U \rangle_\mu \langle N \rangle_\mu}{\langle N^2 \rangle_\mu - \langle N \rangle_\mu \langle N \rangle_\mu} - \langle N_g \rangle - \frac{1}{\beta} \qquad (2.67)$$

$$\langle U \rangle_\mu = average\ total\ energy, \langle N \rangle_\mu = average\ of\ total\ particle\ number,$$
$$\langle N_g \rangle = average\ number\ of\ guest\ molecule\ only,$$
$$and\ \beta = inverse\ temperature\ factor$$

This function gives the heat of adsorption at zero loading, which is also defined as the isosteric heat of adsorption.

iii. Experimental Validation and Simulation Comparison

The comparison between experimentally observed and GCMC adsorption isotherms can help understand the nature of the porous material. Here, some examples are presented which describe how GCMC simulations complement the experimental adsorption findings.

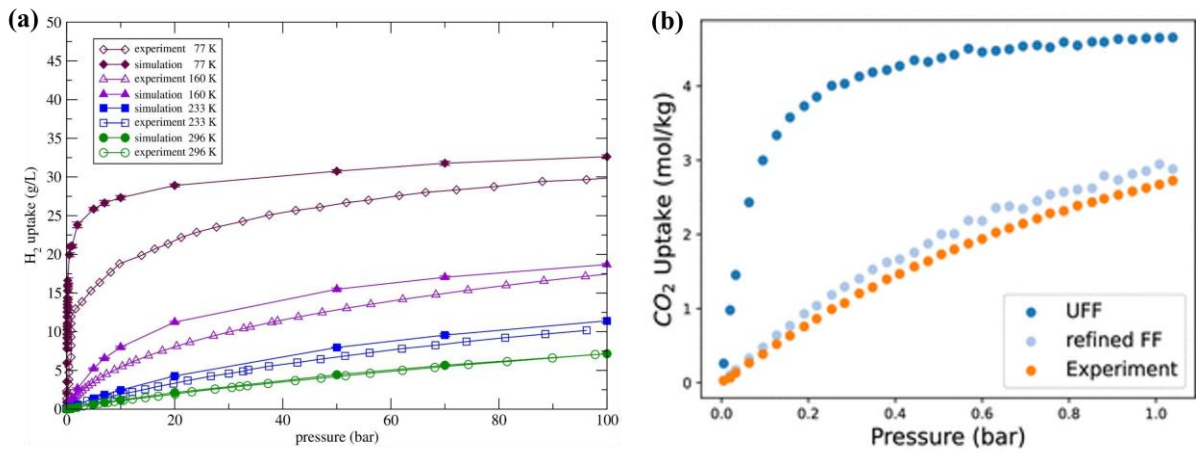

***Figure 2.5**. Comparison of experimental and simulated adsorption isotherms. (a) H_2 uptake (g/L) in NU-2100 MOF, (b) CO_2 uptake (mol/kg) in CAU-10 (Al) (The graphs are taken from ref.* [43,44]

Farha *et.al* have focused on the synthesis of new air-stable Cu(I)-based materials for H_2 storage.[43] They have developed a de novo synthetic strategy to generate a robust Cu(I)-based MOF, denoted NU-2100, using a mixture of Cu/Zn precursors, in which zinc acts as a catalyst to transform an intermediate MOF into NU-2100 without being incorporated into the final MOF structure. Their experimental findings reveal that a combination of adsorption and spectroscopic studies on NU-2100 indicate a very high isosteric heat of adsorption of 30 kJ/mol combined with a good deliverable capacity of 10.4 g/L under practical operational conditions (233 K/100 bar to 296 K/5 bar) at ambient temperature, although only 1% of the Cu(I) species serve as active sites. There is a correlation between the experimental and simulation adsorption isotherms. There is a small difference between isotherm curves as temperature decreases, but at room temperature, both experimental and simulation results are almost identical, as shown in **Figure 2.5a**. Smit *et al.* have developed force fields to address the inaccuracy of UFF[45] caused by different polarizability within different chemical environments. They have observed that their developed refined force fields can give an accurate description of the adsorption isotherm, and follow the experimental curve as represented in **Figure 2.5b**.[44]

2.15.RASPA Software

RASPA is a suite of codes for simulating the adsorption and diffusion of molecules such as H_2, CO_2, CH_4 and other hydrocarbons in porous materials.[46] This code implements the latest state-of-the-art algorithms for Monte Carlo (MC) and Molecular Dynamics (MD) simulations in various ensembles. To run the simulations in RASPA, several input files are required:

a) simulation.input

This input file describes the type of simulation, simulation box size, steps in initialization cycles, production cycle and L-J cutoff.

b) Material_name.cif

The definition of the structure, such as atomic coordinates and lattice parameters, is mentioned in this file.

c) Pseudo_atoms.def

This file lists all the information about pseudo-atoms, such as charges, radii, and atomic masses.

d) Force_field_mixing_rules.def, force_field.def

The force field definition file shows the van der Waals potential (L-J parameters) for atoms involved in the material and molecules, and the rule for mixing the L-J parameters of various atoms.

e) Molecule_name.def

This file includes the atomic coordinates and bond length, and angle of the adsorbate molecule.

Example input file for RASPA 2.0 suite code:

```
SimulationType        MonteCarlo
NumberOfCycles        50000
NumberOfInitializationCycles 50000
PrintEvery            10000
PrintPropertiesEvery  10000
Movies                yes
WriteMoviesEvery      10000

Forcefield            local
UseChargesFromCIFFile yes
ChargeMethod          Ewald
EwaldPrecision        1e-6
CutOffVDW             12.0
CutOffChargeCharge    12.0
```

```
NumberOfSystems          1
Framework 0
FrameworkName            MOF
UnitCells                2 2 2
InputFileType            cif
ExternalTemperature      298.0
ExternalPressure         1e5
NumberOfComponents       1
Component 0 MoleculeName          H2
          MoleculeDefinition      local
          TranslationProbability  1.0
          RotationProbability     1.0
          ReinsertionProbability  1.0
          SwapProbability         1.0
          CreateNumberOfMolecules 0
```

2.16. References

[1] D.R. Hartree, Mathematical Proceedings of the Cambridge Philosophical Society 24 (1928) 89–110.

[2] M. Born, R. Oppenheimer, Annalen Der Physik 389 (1927) 457–484.

[3] W. Heisenberg, Zeitschrift Für Physik 38 (1926) 411–426.

[4] P.A.M. Dirac, Proceedings of the Royal Society of London. Series A, Containing Papers of a Mathematical and Physical Character 112 (1926) 661–677.

[5] J.C. Slater, Physical Review 34 (1929) 1293–1322.

[6] C.C.J. Roothaan, Reviews of Modern Physics 23 (1951) 69–89.

[7] V. Fock, Zeitschrift Für Physik 61 (1930) 126–148.

[8] A. Szabo, N.L. Ostlund, (1996).

[9] S.F. Boys, Proceedings of the Royal Society of London. Series A, Mathematical and

Physical Sciences 200 (1950) 542–554.

[10] E. Davidson, D. Feller, Chemical Reviews 86 (1986) 681–696.

[11] R. Ditchfield, W. J. Hehre, J. A. Pople, The Journal of Chemical Physics 54 (1971) 724–728

[12] D.E. Woon, T.H. Dunning, The Journal of Chemical Physics 103 (1995) 4572–4585.

[13] E. Papajak, H. R. Leverentz, J. Zheng, D. G. Truhlar, Journal of Chemical Theory and Computation 5(2009) 3330.

[14] W. R. Wadt, P. J. Hay, The Journal of Chemical Physics 82(1985) 270.

[15] P. HOHENBERG, Physical Review B 136 (1964) 864–871.

[16] T.L. Gilbert, Physical Review B 12 (1975) 2111–2120.

[17] M. Levy, Proceedings of the National Academy of Sciences of the United States of America 76 (1979) 6062–6065.

[18] J. W. Kohn; L. J. Sham, Physical Review A140 (1965) 1133–1138.

[19] W.. Parr, R.G., Yang, Density-Functional Theory of Atoms and Molecules. Oxford University Press, New York (1994).

[20] E.I. Proynov, E. Ruiz, A. Vela, D.R. Salahub, International Journal of Quantum Chemistry 56 (1995) 61–78.

[21] J.P. Perdew, A. Ruzsinszky, J. Tao, V.N. Staroverov, G.E. Scuseria, G.I. Csonka, Journal of Chemical Physics 123 (2005) 062201.

[22] A.D. Becke, Journal of Chemical Physics 98 (1993) 5648–5652.

[23] C. Adamo, V. Barone, Journal of Chemical Physics 110 (1999) 6158–6170.

[24] J. Heyd, G.E. Scuseria, M. Ernzerhof, Journal of Chemical Physics 118 (2003) 8207–8215.

[25] J.N.. Israelachvili, Intermolecular and Surface Forces, Academic, London, 1992.

[26] F. London, Zeitschrift Für Physik 63 (1930) 245–279.

[27] R. Dovesi, A. Erba, R. Orlando, C.M. Zicovich-Wilson, B. Civalleri, L. Maschio, M. Rérat, S. Casassa, J. Baima, S. Salustro, B. Kirtman, Wiley Interdisciplinary Reviews: Computational Molecular Science 8 (2018) e1360.

[28] D.J. Frisch, M. J.; Trucks, G. W.; Schlegel, H. B.; Scuseria, G. E.; Robb, M. A.; Cheeseman, J. R.; Scalmani, G.; Barone, V.; Petersson, G. A.; Nakatsuji, H.; Li, X.; Caricato, M.; Marenich, A. V.; Bloino, J.; Janesko, B. G.; Gomperts, R.; Mennucci, B.; Hratch, Gaussian, Inc., Wallingford CT, 2019

[29] M. W. Schmidt, K. K. Baldridge, J. A. Boatz, S. T. Elbert, M. S. Gordon, J. H. Jensen, S. Koseki, N. Matsunaga, K. A. Nguyen, S. Su, T. L. Windus, M. Dupuis, J. A. Montgomery, Journal of Computational Chemistry 14(1993) 1347–1363.

[30] S.L. Mayo, B.D. Olafson, W.A. Goddard, Journal of Physical Chemistry 94 (1990) 8897–8909.

[31] A.K. Rappé, W.A. Goddard, Journal of Physical Chemistry 95 (1991) 3358–3363.

[32] R.T. Sanderson, Science 114 (1951) 670–672.

[33] X. Wang, S. Ramírez-Hinestrosa, J. Dobnikar, D. Frenkel, Physical Chemistry Chemical Physics 22 (2020) 10624–10633.

[34] H. A. Lorentz, Annals of Physics 248 (1881) 127-136.

[35] M. Waldman, A.T. Hagler, Journal of Computational Chemistry 14 (1993) 1077–1084.

[36] V. Buch, The Journal of Chemical Physics 100 (1994) 7610–7629.

[37] F.D.D. Levesque, Journal of Chemical Physics 109 (1998) 4981–4984.

[38] D. Marx, P. Nielaba, Physical Review A 45 (1992) 8968–8971.

[39] M. Barraco, S. Neyertz, N.E. Benes, D. Brown, Journal of Physical Chemistry A 127 (2023) 6335–6346.

[40] A. Aasen, M. Hammer, Å. Ervik, E.A. Müller, Ø. Wilhelmsen, Journal of Chemical Physics 151 (2019) 064508.

[41] D.Y. Peng, D.B. Robinson, Industrial and Engineering Chemistry Fundamentals 15

(1976) 59–64.

[42] L.D. Gelb, K.E. Gubbins, Langmuir 15 (1999) 305–308.

[43] Y. Li, X. Jin, E. Moubarak, B. Smit, Journal of Chemical Theory and Computation 20 (2024) 10540–10552.

[44] D. Sengupta, P. Melix, S. Bose, J. Duncan, X. Wang, M.R. Mian, K.O. Kirlikovali, F. Joodaki, T. Islamoglu, T. Yildirim, R.Q. Snurr, O.K. Farha, Journal of the American Chemical Society 145 (2023) 20492–20502.

[45] A. K. Rappe, C. J. Casewit, K. S. Colwell, W. A. Goddard III, W. M. Skiff, Journal of the American Chemical Society 114(1992), 10024–10035.

[46] D. Dubbeldam, S. Calero, D.E. Ellis, R.Q. Snurr, Molecular Simulation 42 (2016) 81-101.

CHAPTER 3

Enhancement of H_2 Physisorption in Covalent Organic Framework's Linkers by Li-decoration

This chapter provides a detailed theoretical analysis of the Li decoration strategy applied to COF materials. In this work, we computationally designed 36 complexes comprising nine pure COF linkers and Li-decorated linkers, demonstrating physisorption of H_2 molecules. The synergy of Li atoms with these linkers shows a Li binding energy of - 0.5 to - 1.3 eV, which enables each Li atom to capture two H_2 molecules with an average ΔH per H_2 molecule about -0.02 to -0.20 eV. We computationally found a significant H_2 uptake weight percentage (wt.%) of 6.5 wt.% for the molecular structure of Linker-3 using the DFT-D method. The true highlight of our work is the average binding enthalpy of -0.20 eV per H_2 molecule in the Li-decorated Linker-5. Our study reveals the intricate interplay between dispersion and electrostatic forces, which play a significant role in determining the binding enthalpy. We performed GCMC simulations on our designed pure COFs to investigate H_2 uptake at 77 K and 298 K over a range of varying low and high pressures. COF-IITI appears more effective in absolute H_2 loading than the pristine COF because of its larger surface area. This groundbreaking research is essential for realizing efficient, secure, compact, and cost-effective hydrogen storage materials. It aligns perfectly with the ambitious goals set by the U. S. Department of Energy (DOE), driving us closer to a sustainable energy future.

3.1. Introduction

The global shift towards utilizing molecular hydrogen (H_2) as a clean, renewable energy source is crucial for reducing reliance on finite, environmentally polluting fossil fuels. However, transitioning to a hydrogen-based economy, particularly for mobile applications, faces significant hurdles, primarily due to technological limitations in economic production and effective fuel storage.[1] While conventional storage methods, such as compressing and liquefying hydrogen, exist, concerns over efficiency, safety, and economic feasibility limit their practicality for widespread use in the future.[2] As an alternative approach, controlling the

interaction between hydrogen and host materials has emerged as a promising approach for hydrogen storage.[3] The fundamental interaction between hydrogen and the storage material dictates sorption properties and reversibility under ambient conditions. Since physisorption, driven by weak van der Waals (vdW) forces, allows reversible, fast hydrogen adsorption and desorption at mild conditions, with an ideal range of heat of adsorption of -0.15 to -0.25 eV at 233-258 K.[4] This work aims to design a new hydrogen storage material with an optimal H_2 adsorption energy that satisfies physisorption. For this purpose, we introduce a Li-decorated COF technique that significantly improves the hydrogen-binding and gravimetric uptake capacities of the COFs.

The US DOE has revised the H_2 storage target to a gravimetric capacity of 5.5 wt.% and a volumetric capacity of 40 g/L at 233-358 K for the year 2025. The ultimate targets are a gravimetric capacity of 6.5 wt.% and a volumetric capacity of 50 g/L for on-board vehicular applications in industries.[5] Various materials, including metallic hydrides, complex hydrides, carbon nanostructures, metal-organic frameworks (MOFs), and zeolites, have been explored for hydrogen adsorption.[6] Several experimental and computational/theoretical studies have recently suggested that COFs can be ideal, compatible hydrogen storage materials for industrial applications in which H_2 storage is primarily based on physisorption.[7,8] Li doping in the organic ligands of the porous COFs is a promising approach to enhance hydrogen storage at near-ambient conditions. Since aromatic rings in their organic linkers have high electron affinity, the sp^2 carbon framework would segregate the charge from the Li atom and stabilize H_2 molecules.[9] Ding *et al.* observed that combining Li-doping with C_{60} impregnation or aromatic ring grafting can significantly enhance the volumetric H_2 adsorption capacity of COF-108.[10] Guo *et al.* theoretically designed an effective hydrogen storage material by doping ILCOF-1 with lithium. Their computational study indicated that the Li-doped ILCOF-1 achieved a high hydrogen storage capacity, with a gravimetric uptake of 7.26 wt.%.[11] The Li decoration technique has been employed in other COFs, such as COF-1,[14] COF-202,[15] and COF-366,[12] for H_2 storage. The main building block of COF-1 is a boroxine ring, the COF-202 has a B-*O*-Si linkage, and the COF-366 consists of tetra (p-amino-phenyl) porphyrin (TAPP) bonded with a terephthaldehyde chain. However, these COF materials have shown poor H_2 storage performance due to weak hydrogen binding. Their results fall short of USDOE targets, hindering their industrial and technological applications.

Our study is crucial because it aims to address this limitation, which is vital to the clean energy transition, economic growth, environmental benefits, and the achievement of global energy goals. In the present study, we have employed Li-decorating techniques with nine different linkers on a COF and have explored its H_2 binding properties and H_2 uptake capacity. The paramount goal of this work is to present an elementary analysis of the mechanism of hydrogen physisorption on Li-decorated COF linkers and to understand the nature of interactions responsible for H_2 adsorption in the COFs. The theoretical study of the quantum nature of H_2 interactions is the backbone of experimental results and is useful for unravelling the storage properties of porous materials.

3. 2. Methodology, computational details, and material description

3.2.1. Computational Details

We have computationally designed 36 new complexes using pure and Li decorated COF linkers. After Li decoration, H_2 physisorption was investigated on these COF linkers. We applied unrestricted hybrid DFT, the B3LYP method [13] i.e., the UB3LYP DFT method, to obtain the equilibrium structures of the Li-decorated COF linkers, and the thermodynamic parameters were calculated using both the B3LYP and MP2 methods.[14] Since B3LYP includes an approximate treatment of electron correlation, the results should be more accurate and economical than those of the Hartree-Fock theory, and it performs well for truly extensive chemical systems and properties. It is generally faster than most post-Hartree-Fock methods and yields results similar to theirs. Next, to account for the weak vdW interactions between gas molecules and the linkers, the semiempirical Grimme's dispersion correction parameters (-D3) were added to the UB3LYP DFT method.[15] Since the MP2 method is free from the self-interaction of electrons, and it naturally takes dispersion into account, the -D3 correction was not included in the MP2 method.

We have used both the double-ζ and triple-ζ quality correlation-consistent polarized Gaussian type basis sets, i.e., cc-pVDZ and cc-pVTZ, for the H, B, N, C, O, and Li atoms in the present computations.[16] All calculations were performed using the Gaussian 16 suite

code.[17] We have used ChemCraft software for designing all the structures, initial geometries and visualization.[18] The PyMOLyze suite code was used to compute the partial density of states (PDOS). An *Energy Decomposition Analysis* (EDA) was performed using the GAMESS-US program.[19] A harmonic vibrational frequencies analysis was carried out, and none of the equilibrium structures has imaginary frequencies, which confirms that all the optimized geometries are energetically stable. Thermodynamic potential, i.e., binding enthalpy and binding energy, is computed at equilibrium structures of the complexes studied here. The average binding energy per Li atom adsorbed on the linkers can be calculated by the following mathematical expression:

$$\Delta E = \frac{E_{Linker\_nLi} - (E_{pure\_linker} + nE_{Li})}{n} \qquad (3.1)$$

The binding enthalpy (ΔH) of adsorbed H_2 molecules on Li-decorated linkers was calculated using the equation below:

$$\Delta H = H_{Linker\_Li+nH_2} - \left(H_{Linker\_Li} + nH_{H_2}\right) \qquad (3.2)$$

The average binding enthalpy (ΔH) per one H_2 molecule adsorbed on linkers decorated by Li can be defined as follows:

$$\Delta H = \frac{\left[H_{Linker\_Li+nH_2} - \left(H_{Linker\_Li} + nH_{H_2}\right)\right]}{n} \qquad (3.3)$$

The following equation has computed the vibrational frequency shift:

$$\Delta \upsilon = \nu_{complex} - \nu_{H_2\ molecule} \qquad (3.4)$$

$\nu_{complex}$ is the value of the vibrational frequency of the Li-linker-H_2 complex, and $\nu_{H_2 molecule}$ is the vibrational frequency of the free H_2 molecule.

The energy gap between the frontier orbitals is defined as

$$E_g = E_{HOMO} - E_{LUMO} \qquad (3.5)$$

The H_2-uptake in terms of weight percentage (wt.%) in the pure and Li-decorated linkers is calculated by the equation given below:

$$wt\% = n * M_{H_2}/(M_{Linker} + n * M_{H_2}) \quad (3.6)$$

The H_2 adsorption isotherms of the pure COFs were studied using the μVT ensemble at 77 K and 298 K and pressures up to 300 bar with the RASPA 2.0 package.[20] The number of initialization cycles was 2.5×10^4 Steps, followed by 5×10^4 Monte Carlo (MC) steps for the random insertion, rotation, swap, and translation of the H_2 molecule in the simulation box. During the simulation, all the atoms of the COF were kept fixed, while the H_2 molecules were free to move within the structure. We used the Lennard-Jones (LJ) 6-12 potential to describe the interaction between the hydrogen molecules and COF atoms (N, B, O, C, and H) presented by:

$$U(ij) = 4\varepsilon_{ij}\left[\left(\frac{\sigma_{ij}}{r_{ij}}\right)^{12} - \left(\frac{\sigma_{ij}}{r_{ij}}\right)^{6}\right] + \frac{1}{4\pi\varepsilon_0}\frac{q_i q_j}{r_{ij}} \quad (3.7)$$

These parameters were determined by using the Lorentz-Berthelot mixing rule for a pair of unlike atoms as follows:

$$\varepsilon_{ij} = \sqrt{\varepsilon_i}\varepsilon_j, \ \sigma_{ij} = \frac{1}{2}(\sigma_i + \sigma_j) \quad (3.8)$$

The potential parameters for the framework atoms in COFs were taken from the standard DREIDING force field implemented in the RASPA 2.0 package,[21] and the cut-off radius for the LJ interaction is 12.0 Å. The DREIDING force field has been widely used to study gas adsorption in nanoporous materials.[22,23]

The desorption temperature T_d is computed utilizing the van't Hoff equation:[24]

$$T_d = \frac{H_B}{k_B}\left(\frac{\Delta S}{R} - ln\, P\right)^{-1} \quad (3.9)$$

where H_B denotes the average adsorption energy, P = 1 atm, ΔS is the entropy change of hydrogen for the gas-to-liquid phase conversion, and R represents the universal gas constant.

3.2.2. Materials description

(a) Periodic 3D COFs

We have represented our designed 3D Pure COFs, named COF-IITI and Pristine COF, in **Figures 3.1a and 3.1b.** The specific surface area (S_A) and pore volume (V_p) of these designed COFs have been reported in our earlier articles.[25,26] Both the COF-IITI and Pristine COF have a high specific surface area of 1555.12 m^2/g [27] and 1081 m^2/g , respectively, and their estimated pore volumes are 0.473 cm^3/g and 0.948 cm^3/g , respectively.

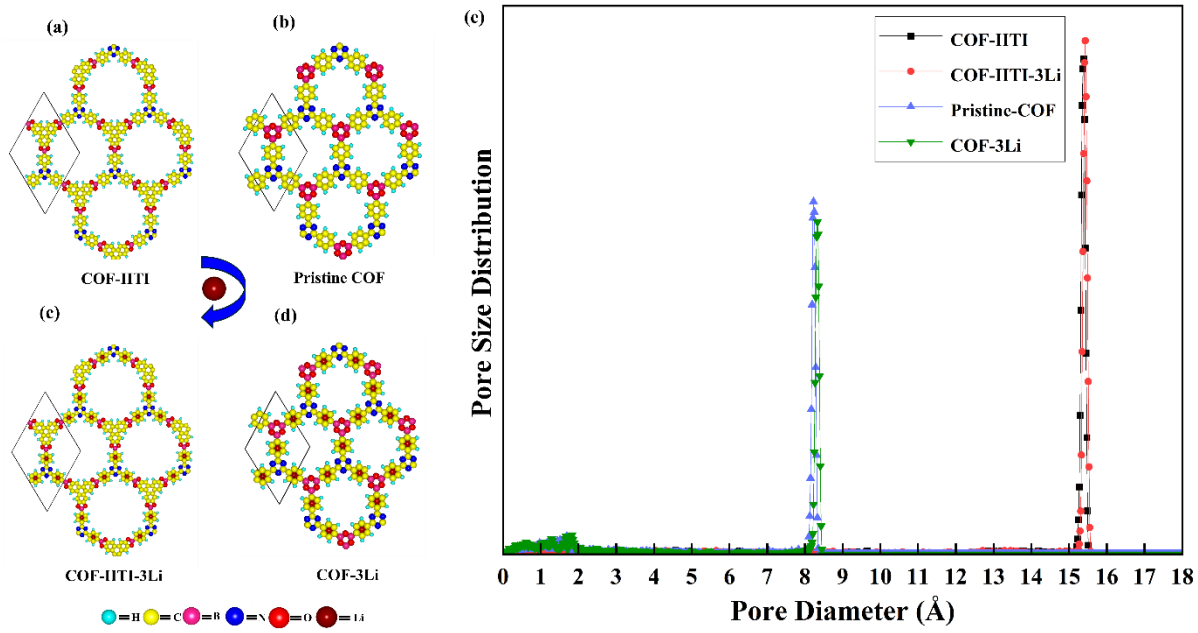

Figure 3.1. *Equilibrium structures of our designed 3D COFs, (a) COF-IITI, (b) Pristine COF, (c) COF-IITI-3Li, (d) COF-3Li, and (e) Pore-size distribution (PSD) curve for all designed COFs.*

Then, we decorated these COFs with Li atoms at the centroids of the phenyl rings, as shown in **Figures 3.1c and 3.1d**. We have estimated the specific surface area and pore volume of these Li-decorated 3D COFs using H_2 as a probe molecule. Both the COF-IITI-3Li and COF-3Li have a high specific surface area of 1583.1 m^2/g and 1228.66 m^2/g, respectively, and their estimated pore volumes are 0.48 cm^3/g and 0.968 cm^3/g, respectively. The extraordinary framework properties (high surface area and pore volume) of our designed COFs can contribute to efficient H_2 storage, making them a potential material for practical H_2 storage applications.

The pore-size distribution (PSD) can be calculated geometrically using the Gelb and Gubbins method [28], implemented in RASPA-2.0. For every point in the void volume, the

largest sphere is found that encloses the point but does not overlap with any framework atoms. This yields the cumulative pore volume curve. Our calculated pore size distribution curve is represented in **Figure 3.1(e)**, which illustrates that both the COF-IITI and COF-IITI-3Li have pore diameters between 15-16 Å, and both the Pristine-COF and COF-3Li have pore diameters about 8-9 Å. These values fall within the microporous range, and some previously reported articles suggest that a porous material with a pore diameter of approximately 9 Å is the most suitable for enhanced H_2 uptake.[29] Some microporous MOFs have already demonstrated extraordinary H_2 storage properties. These findings indicate that the COFs we designed could serve as effective adsorbents for H_2 storage.[30]

(b) Non-periodic organic linkers of the designed COFs

We have considered nine pristine organic linkers from our previously designed covalent organic frameworks, as represented in **Figure 3.2**.[25–27] Various experimental works have been reported on synthesizing several porous materials using these kinds of organic linkers for various applications. These nine linkers are fundamental building units of the pristine COFs, which contain phenyl (C_6H_5),[31] triazine ($C_3H_3N_3$),[32] boroxine (B_3O_3),[33] and boronate ester rings (BO_2C_2).[34] The electronic properties of these pristine COFs were earlier reported by using the DFT-D method.[25] The metal-decorated BO_2C_2 rings have already proven to be superior for H_2 adsorption and enhanced hydrogen uptake capacity.[1][35] These linkers have the potential to provide desirable results in gas storage, energy storage, and CO_2 capture in porous frameworks.[36][37] Linker-3, also known as **2-phenyl-1,3,2-benzodioxaboroles**, is a fundamental building block for various COFs. This Linker-3 can modify the reactivity and structural properties of porous materials. [38] **2,4,6-Tripheny-l-1,3,5-triazine (TPT)** linker is noted as Linker-5, and it is also a main building block of various previously synthesized COFs like COF105, COF108, COF-IITI-0, etc.[25][39] Linker-6 is a widely used organic linker for the design of porous materials, commonly known as **2,3,6,7,10,11-hexahydroxytriphenylene (HHTP)**. Many COFs have been synthesized using the condensation of various linkers with HHTP. Some of them are COF6, COF7, and COF8.[34]

3.3. RESULTS AND DISCUSSION

3.3.1. Li-decoration in linkers

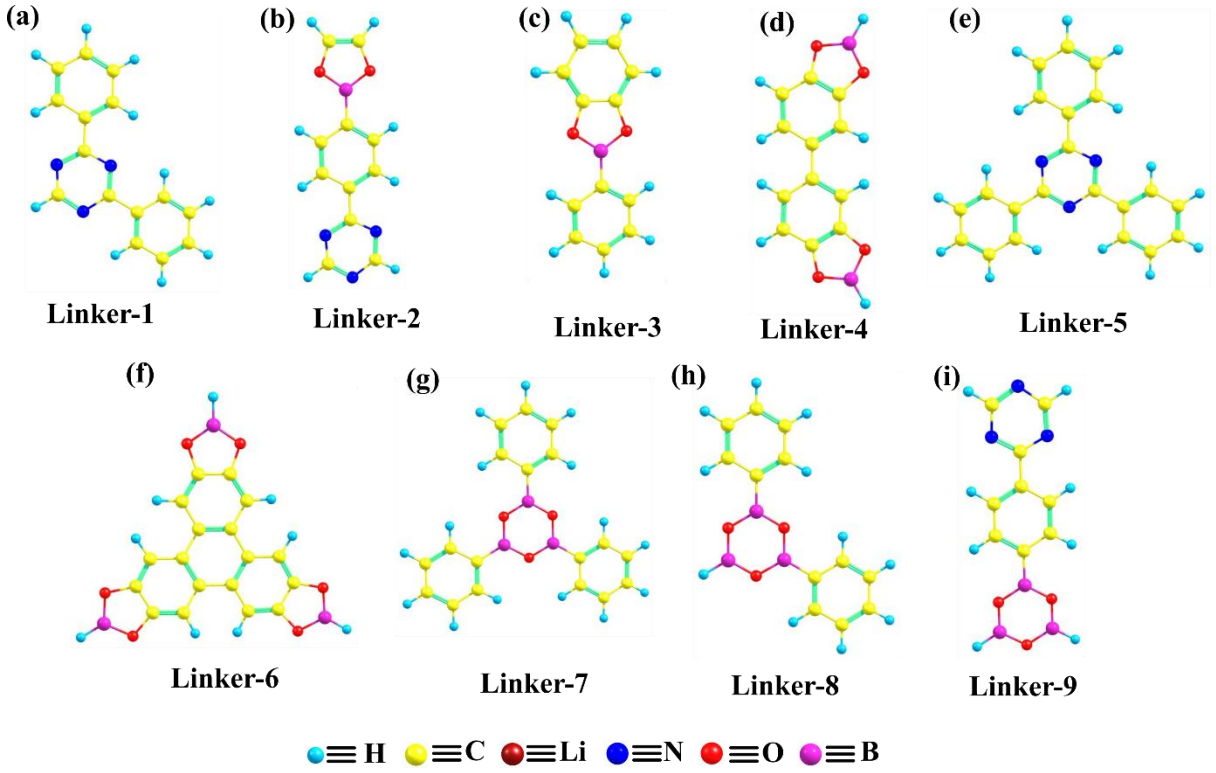

Figure 3.2. *The equilibrium structures of nine pristine linkers are represented here. The name of these nine linkers is written as (a) Linker-1, (b) Linker-2, (c) Linker-3, (d) Linker-4, (e) Linker-5, (f) Linker-6, (g) Linker-7, (h) Linker-8, and (i) Linker-9.*

We have explored various Li adsorption sites in the equilibrium structure of the organic ligands studied here, namely Linker-1 to Linker-9. Linker-2 and Linker-7 are the most suitable linkers for selecting favorable locations for Li adsorption, as Linker-2 has all three phenyl, triazine, and boronate ester rings, and Linker-7 has a boroxine ring. The terminology of our chosen sites is "Site A" for the top of the phenyl ring, "Site B" for the top of the triazine ring, "Site C" for the top of the boronate ester ring and "Site D" for the top of the boroxine ring. The Li atom is placed at the centroid of sites A, B, C, and D, as depicted in **Figure 3.3.** Triazine and boroxine rings, i.e., B and D configurations, have an uneven electron density distribution that causes the Li atom to experience a slight displacement from the centroid. The Mulliken

charge analysis of both the B and D configurations reveals distinctive charge distributions among the constituent atoms.

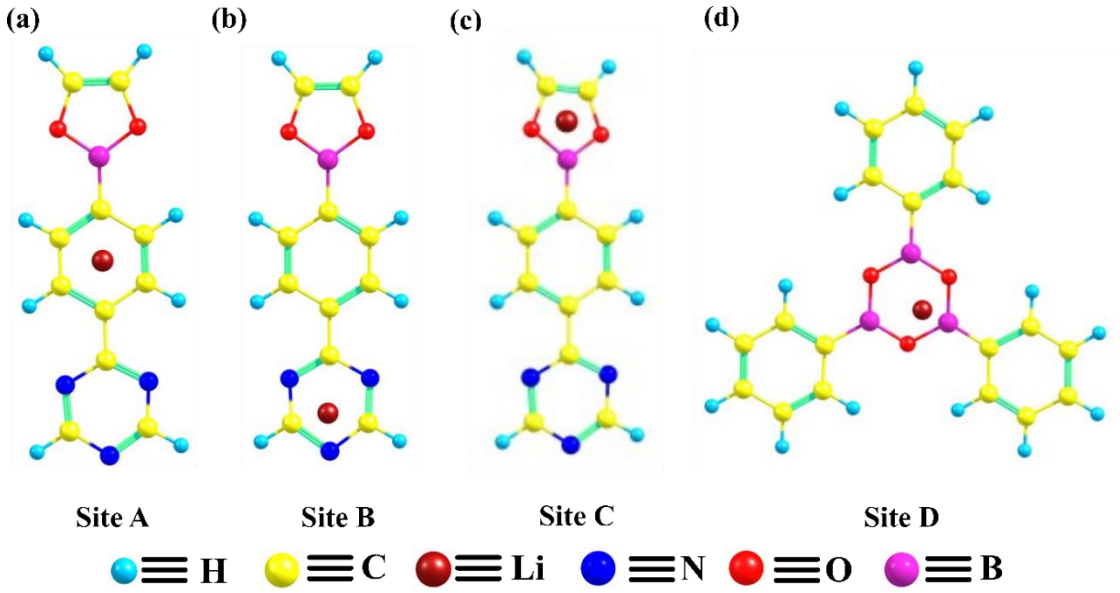

Figure 3.3. *The selected sites in Linker-2 and Linker-7: (a) Site A for the phenyl ring, (b) Site B for the triazine ring, (c) Site C for the boronate ester ring, and (d) Site D for the boroxine ring are shown here.*

In configuration B, nitrogen (N) atoms exhibit a negative charge of -0.17 a.u., while carbon (C) atoms possess a smaller negative charge of -0.04 a.u. Conversely, lithium (Li) atoms in this configuration demonstrate a positive charge of +0.18 a.u. This unequal charge distribution suggests an electron transfer from Li to N, likely influenced by interactions with neighbouring atoms. Conversely, oxygen (O) atoms acquire a negative charge of -0.11 a.u. in the D configuration, whereas boron (B) atoms exhibit a slightly larger positive charge of +0.20 a.u. Li atoms in this setup exhibit a smaller positive charge of +0.03 a.u., indicating less electron transfer than in the B configuration. These unequal charge distributions highlight electron redistribution within the molecules, potentially impacting the positioning of Li atoms relative to the surrounding atoms. The value of binding energy ($\Delta \mathbf{E}$) of the Li atom adsorption in each selected site of the Linker-2 and Linker-7 was calculated by using both the B3LYP-D3 and MP2 methods with two different basis sets (i.e., cc-pVDZ and cc-pVTZ). According to our results, Site A has the most negative binding energy, with values of -1.11 eV, -1.20 eV, and -0.70 eV obtained with the B3LYP-D3/cc-pVDZ, B3LYP-D3/cc-pVTZ, and MP2-cc-pVTZ methods, respectively. It reveals that the phenyl ring is energetically more favorable for the Li

binding. Sites B, C, and D show binding energies of approximately -0.59, -0.39, and -0.62 eV, respectively, as computed by the B3LYP-D3/cc-pVDZ method. Additionally, previous studies have shown that the phenyl ring provides greater Li-binding energy than the triazine, boroxine, and boronate ester rings in COFs.[40][41]

Now, we have decorated phenyl rings with Li atoms in the designed organic linkers. Linker-1, Linker-3, Linker-4, and Linker-8 have two phenyl rings in their structures, so we have decorated them with two Li atoms per ring, one located on the upper side and the other on the lower side of the linker. It is shown that both the Linker-2 and Linker-9 are decorated by two Li atoms because of single phenyl rings in their structure in **Figure 3.4b and Figure 3.4i**. Since Linker-5, Linker-6, and Linker-7 have three phenyl rings, they are decorated by six Li atoms. This phenomenon, in which several Li atoms are absorbed on both sides of the linkers, is studied because these Li atoms could play a significant role as an active site for H_2 binding by expanding the adsorption surface area for H_2 molecules.[42] Linker-5, Linker-6, and Linker-7 have absorbed a maximum of six Li atoms near the centroid of the phenyl rings. It was observed that a slight distortion in the structures occurred after the addition of Li atoms.

We have then calculated the average binding energy (ΔE_b) per Li atom, using **equation 3.1**, since each linker has a different number of Li-atom adsorption sites. The calculated values of average binding energy per Li atom absorbed on both sides of the linkers are shown in **Table 3.1**. The Linker-9 shows the most favorable value of average binding energy about -1.21 eV, -1.31 eV and -1.31 eV computed by the B3LYP-D3/cc-pVDZ, B3LYP-D3/cc-pVTZ and MP2/cc-pVTZ levels of theory, respectively. The range of average binding energy is between -0.5 to -1.3 eV. These results are remarkable for the Li atom adsorption in all the linkers considered in the present study.[43][44]

3.3.2. H_2 Physisorption in the Li-decorated linkers

To develop a feasible solid adsorbent for high hydrogen uptake, solid porous materials typically require three key parameters: a high surface area, low density, and strong binding enthalpy for H_2 physisorption. The first two parameters are the average surface area and volume per unit of the host material, typically obtained from its structural properties. Whereas the binding enthalpy of adsorption is tunable, and various techniques can enhance it. To enhance the H_2

storage capacity of any porous material, it is recommended to optimize the thermodynamics of H_2 binding within the host material.[6]

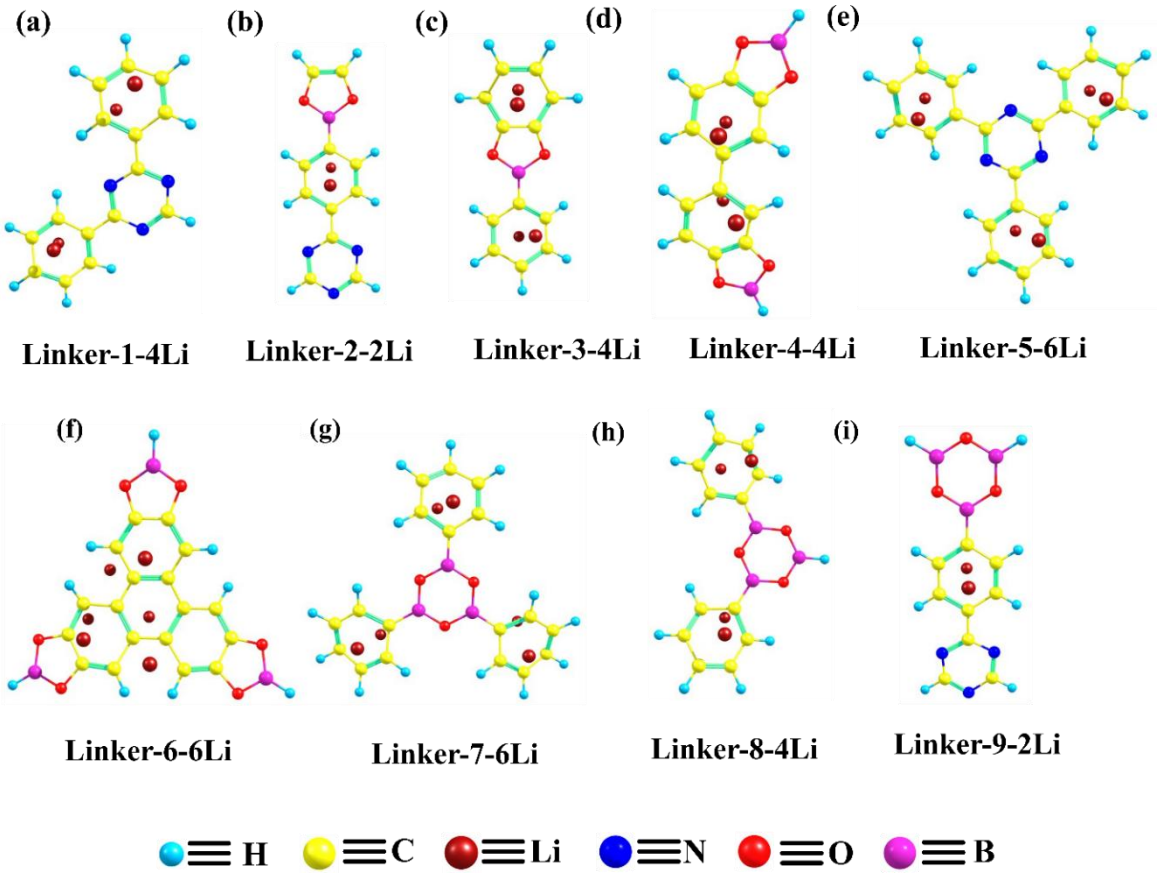

Figure 3.4. *The Li atom decoration in sites A of each linker (a) Linker-1 is decorated by 4 Li atoms in 2 phenyl rings: 2 atoms from the lower side of the ring and two atoms from the upper side of the ring. (b) Linker-2 is decorated by 2 Li atoms in 1 phenyl ring, (c) Linker-3 is decorated by 4 Li atoms in 2 phenyl rings, (d) Linker-4 is decorated by 4 Li atoms in 2 phenyl rings, (e) Linker-5 is decorated by 6 Li atoms in 3 phenyl rings, (f) Linker-6 is decorated by 6 Li atoms in 3 phenyl rings, (g) Linker-7 is decorated by 6 Li atoms in 3 phenyl rings, (h) Linker-8 is decorated by 4 Li atoms in 2 phenyl rings, and (i) Linker-9 is decorated by 2 Li atoms in single one phenyl ring.*

Table 3.1*. Average binding energy per Li atom (ΔE_b in eV) calculated for the Li-decorated complexes.*

Linkers	**Average Binding energy per one Li atom ΔE_b (eV)**

	Number of Sites A	Number of adsorbed Li atoms	B3LYP-D3/cc-pVDZ	B3LYP-D3/cc-pVTZ	MP2/cc-pVTZ
Linker-1	2	4	-0.77	-0.82	-0.90
Linker-2	1	2	-1.11	-1.20	-1.21
Linker-3	2	4	-0.55	-0.58	-0.68
Linker-4	2	4	-0.57	-0.58	-0.68
Linker-5	3	6	-0.72	-0.77	-0.87
Linker-6	3	6	-0.81	-0.83	-0.94
Linker-7	3	6	-0.70	-0.75	-0.81
Linker-8	2	4	-0.74	-0.79	-0.89
Linker-9	1	2	-1.21	-1.31	-1.31

We first applied Li-decorating techniques to the equilibrium structures of the organic linkers and then further investigated H_2 physisorption on Li-decorated linkers. We studied the adsorption of a single hydrogen molecule on the Li-decorated linkers, which is essential for understanding the interactions responsible for H_2 adsorption on the linker surface. Then, we calculated the binding enthalpy of single H_2 adsorption in the Li-Linker complexes. **Table 3.2** presents the binding enthalpy value of a single H_2 molecule adsorbed on the Li-decorated linkers studied here. The maximum binding enthalpy of Linker-5 is approximately -0.19 eV, as computed using the B3LYP-D3/cc-pVDZ method. This value lies in the range of -0.05 to -0.19 eV for all the Li-decorated linkers or complexes, which satisfies the ideal range of hydrogen physisorption (-0.15 to -0.25 eV) and is also comparable to the previously reported values of ΔH for COFs.[3][45][46]

Table 3.2. *The binding enthalpy (ΔH) of a single H_2 molecule adsorbed on the Li-decorated linkers.*

Linkers	Number of Li atoms adsorbed	Binding Enthalpy (kJ/mol) $1H_2$		
		B3LYP-D3/cc-pVDZ	B3LYP-D3/cc-pVTZ	MP2/cc-pVTZ

Linker-1	4	-0.17	-0.15	-0.14
Linker-2	2	-0.15	-0.12	-0.10
Linker-3	4	-0.13	-0.12	-0.08
Linker-4	4	-0.18	-0.16	-0.17
Linker-5	6	-0.19	-0.18	-0.18
Linker-6	6	-0.05	-0.04	-0.05
Linker-7	6	-0.10	-0.07	-0.06
Linker-8	4	-0.11	-0.07	-0.09
Linker-9	2	-0.11	-0.08	-0.08

The range of calculated binding enthalpy of H_2 adsorption is about -0.07 to -0.18 eV obtained by the B3LYP-D3/cc-pVTZ method, and in this case, the complexes also satisfy the ideal range of heat of physisorption except Linker-6. Using the MP2/cc-pVTZ method, we observed that the H_2 molecule binds to all the complexes studied here via weak van der Waals (vdW) interactions, and the Linker-5 complex exhibits the most negative binding enthalpy of -0.18 eV. We conclude that both the B3LYP-D3 and MP2 methods yield similar results for the H_2 binding enthalpy, and that significant variations in enthalpies are observed with changes in basis set quality from double-ζ to triple-ζ quality.

Table 3.3. *Calculated values of average binding enthalpy per one H_2 molecule physiosorbed on pure and Li-decorated linkers. (Units are in eV)*

Linkers	**No. of Li atoms**	**No of H_2 molecules adsorbed**	**Average binding enthalpy per one H_2 molecule ΔH**					
			Pure			**Li decorated**		
			B3LYP-D3/cc-pVDZ	**B3LYP-D3/cc-pVTZ**	**MP2/cc-pVTZ**	**B3LYP-D3/cc-pVDZ**	**B3LYP-D3/cc-pVTZ**	**MP2/cc-pVTZ**
Linker-1	4	8	-0.02	-0.01	-0.01	-0.12	-0.10	-0.08
Linker-2	2	4	-0.02	-0.04	-0.04	-0.15	-0.11	-0.11
Linker-3	4	8	-0.01	-0.004	-0.005	-0.10	-0.08	-0.06

Linker-4	4	8	-0.03	-0.02	-0.02	-0.09	-0.06	-0.08
Linker-5	6	12	-0.02	-0.01	-0.01	-0.20	-0.17	-0.15
Linker-6	6	12	-0.02	-0.01	-0.01	-0.03	0.001	0.00
Linker-7	6	12	-0.02	-0.02	-0.01	-0.10	-0.08	-0.06
Linker-8	4	8	-0.02	-0.006	-0.003	-0.14	-0.10	-0.07
Linker-9	2	4	-0.01	-0.003	-0.00	-0.07	-0.10	-0.10

The discrepancy in binding enthalpies between the cc-pVDZ and cc-pVTZ basis sets can be attributed to differences in basis set completeness and accuracy. The cc-pVDZ basis set, of double-zeta quality, includes fewer basis functions and therefore provides a less accurate description of the molecular system than the cc-pVTZ basis set, which is of triple-zeta quality and includes additional basis functions to represent the electronic structure more accurately, making it computationally more precise.[47][48] As a result, calculations with the cc-pVTZ basis set tend to yield more accurate results than those with the cc-pVDZ basis set. We have further studied the maximum hydrogen-molecule adsorption in both the pure and Li-decorated linkers and calculated the average binding enthalpy per hydrogen molecule. According to previous reports, one Li atom can stably and strongly interact with $2H_2$ or $3H_2$ molecules.[49]

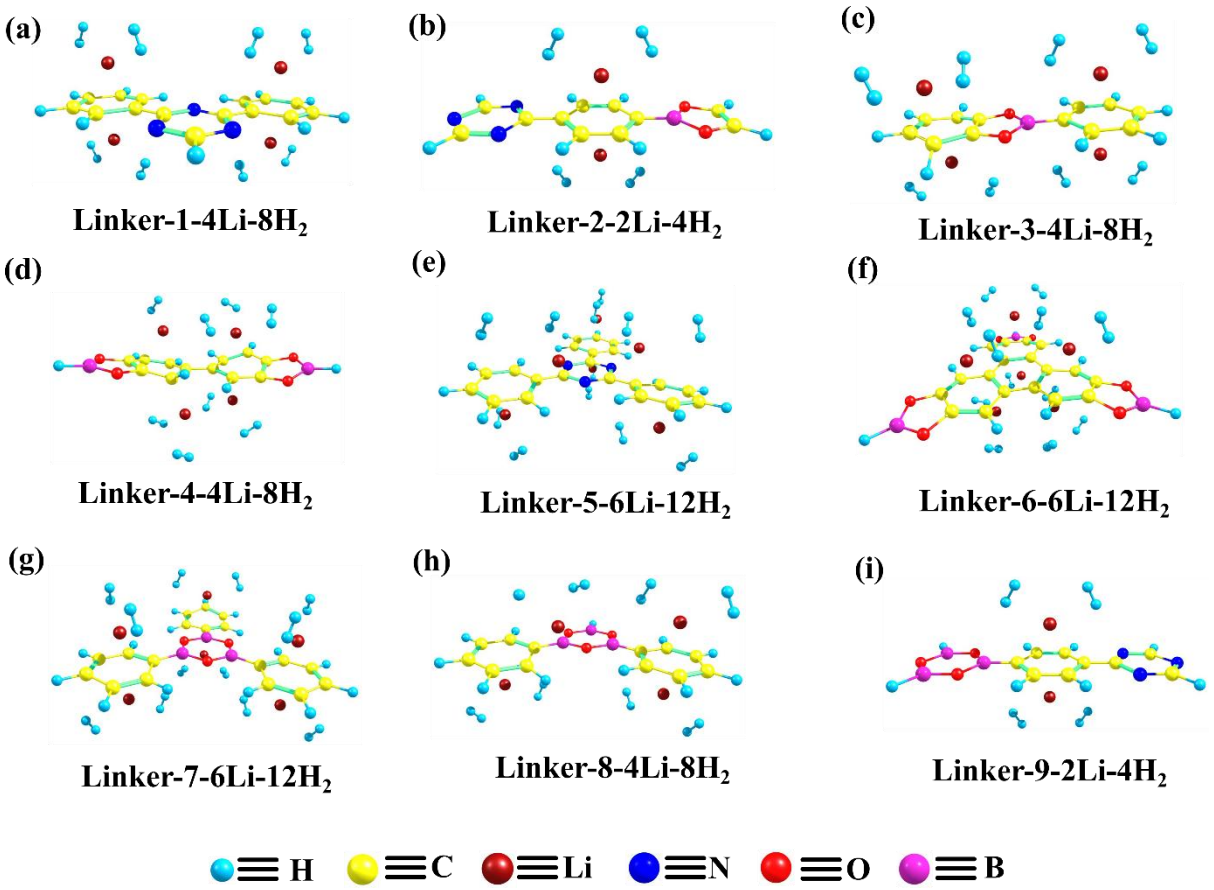

Figure 3.5. *Hydrogen physisorption in Li-decorated linkers. (a) Linker-1 with 8 adsorbed H_2 molecules, (b) Linker-2 with 4 adsorbed H_2 molecules, (c) Linker-3 with 8 adsorbed H_2 molecules, (d) Linker-4 with 8 adsorbed H_2 molecules, (e) Linker-5 with 12 adsorbed H_2 molecules, (f) Linker-6 with 12 adsorbed H_2 molecules, (g) Linker-7 with 12 adsorbed H_2 molecules, (h) Linker-8 with 8 adsorbed H_2 molecules, and (i) Linker-9 with 4 adsorbed H_2 molecules.*

Figure 3.5 shows the equilibrium structures of the Li-decorated linker complexes with the maximum adsorbed H_2, and all H_2 molecules retain their molecular form in each complex. The values of the average binding enthalpy of H_2 molecules in the Li-decorated linkers are tabulated in **Table 3.3**. Linker-5 can bind 12 H_2 molecules, with a maximum binding enthalpy of -0.20 eV. Here, the range of average binding enthalpy for these linkers lies between -0.02 to -0.20 eV. Both the B3LYP-D3 and MP2 methods provide approximately similar values of the binding enthalpy of the systems considered in the present study. Linker-6 shows the least favorable value (-0.02 eV) of binding enthalpy computed by the B3LYP-D3/cc-pVDZ method, and slightly positive values obtained by both the B3LYP-D3/cc-pVTZ and MP2 methods. The binding enthalpy in the last two cases indicates that Linker-6 is unstable, with a maximum

adsorbed H_2 molecules, suggesting saturation of the active site and repulsion between H_2 molecules. **Table 3.4** compares the binding enthalpy for single H_2-molecule adsorption with those of other previously designed COFs.

Table 3.4. *Compared the values of the binding enthalpy of H_2 adsorption in various COFs.*

COF	Binding Enthalpy	Computational Method
Li doped COF-105 and COF-108	-0.13 eV	MP2 [52]
COF-1	-0.02 eV	MP2[53]
COF-102	-0.05 eV	GCMC simulations[7]
COF-103	-0.06 eV	GCMC simulations[7]
Li doped COF-1	-0.25 eV	M.D. simulations[49]
Li doped Linker-5	**-0.20 eV**	**DFT (This work)**

Figure 3.6 shows the average binding enthalpy (ΔH in eV) for all complexes. It was found that the Li-decorated linkers have a higher average binding enthalpy value than the pristine linkers. It means that decorating linkers with Li alkali metal atoms is a good approach to enhance the binding enthalpy during H_2 physisorption, as the alkali metal atoms can act as acidic nodes to attract H_2 molecules.[50][51] The high electron affinity of a π-conjugated aromatic ring in the linkers enables it to accept charge from the Li atom, providing strong stability to adsorbed H_2 molecules. Therefore, the Li-decorated linkers significantly improve H_2 binding compared to the pure linkers.[6] We have also examined the increase in binding enthalpy with the increase in adsorbed H_2 molecules. The enthalpy of adsorption depends on the surface coverage and the interaction between two adsorbed H_2 molecules. If H_2 molecules attract each other, they will form small clusters, and the average binding enthalpy will increase. If the adsorbed H_2 molecules repel each other, the average binding enthalpy becomes less negative as the fractional coverage increases.[50]

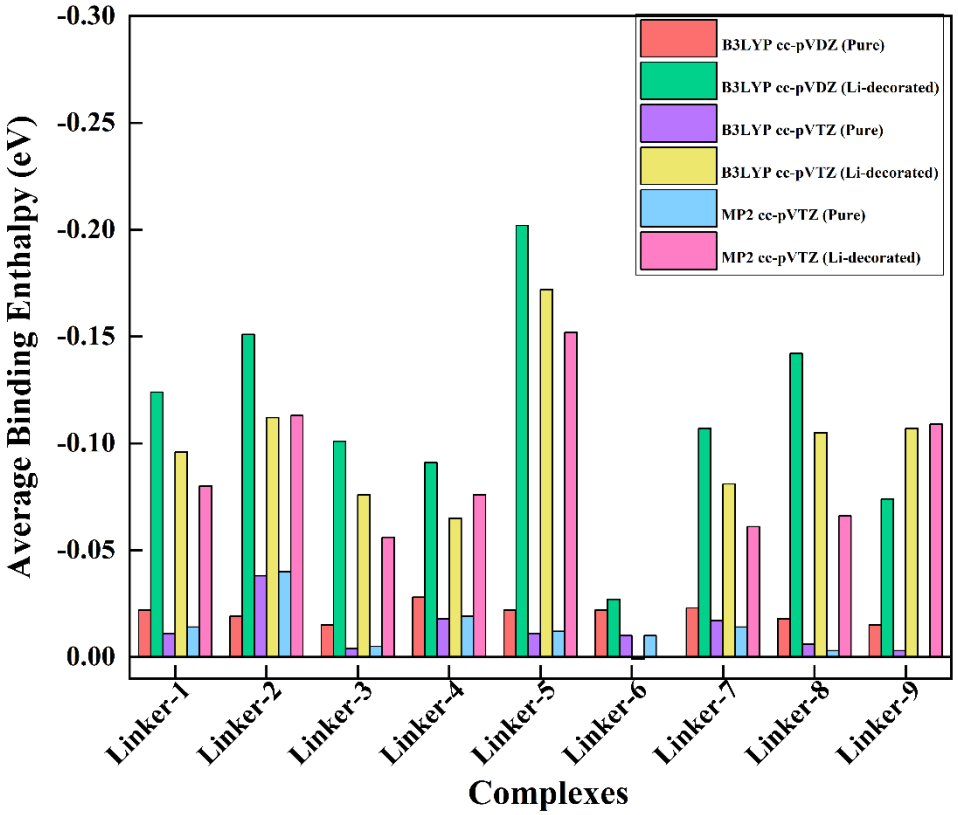

Figure 3.6. *Average binding enthalpy per one H_2 molecule physiosorbed in both the pure and Li-decorated linkers. (Units are in eV)*

When H_2 molecules are adsorbed onto the surface, they maintain their molecular integrity without undergoing dissociation, with the H-H bond distance between the hydrogen atoms slightly increasing to 0.76 Å compared to the 0.74 Å observed in free H_2 molecules. Meanwhile, the average spacing between these adsorbed H_2 molecules ranges from approximately 2.7 to 3.2 Å. This indicates that the Li atoms effectively capture and confine the H_2 molecules, ensuring that they remain closely packed. When the H_2 molecule adsorbs on the surface of Li-decorated linkers, there is a strong correlation between the average binding enthalpy and d_{HH}, which can be used to guide the optimal design of H_2 storage materials.[41]

Suppose the H_2-H_2 interactions cause Li metal atoms to promote charge transfer, then electron polarization plays a significant role in enhancing the binding enthalpy of H_2 molecules.[54] After the saturation of active sites, there will be some steric hindrance, which causes Pauli's repulsion between the H_2 molecules.[55] Consequently, it decreases the average

binding enthalpy of H_2 adsorption. In our case, the average binding enthalpy increases with the number of adsorbed H_2 molecules, consistent with previous studies.[50,56] It is also important to mention here that the maximum number of H_2 molecules that can be stably adsorbed in any metal-decorated/doped materials is limited by the 18-electron rule for metal-based complexes.[57] Recently, Gao *et al.* used the 18-electron rule in their Ca intercalated COF and observed that one Ca metal-doped benzene ring could adsorb a maximum of five H_2 molecules stably and satisfy the 18-electron rule.[41] According to the 18-electron rule, the total number of electrons participating in the H_2-metal complexes must be equal to or less than 18, and this criterion is satisfied by our designed Li-decorated complexes. If we attempt to adsorb 6 H_2 molecules on a single Li-decorated phenyl ring, it will violate the 18-electron rule, and the average binding enthalpy could decrease.

3.3.3. Dispersion Energy and EDA Analysis

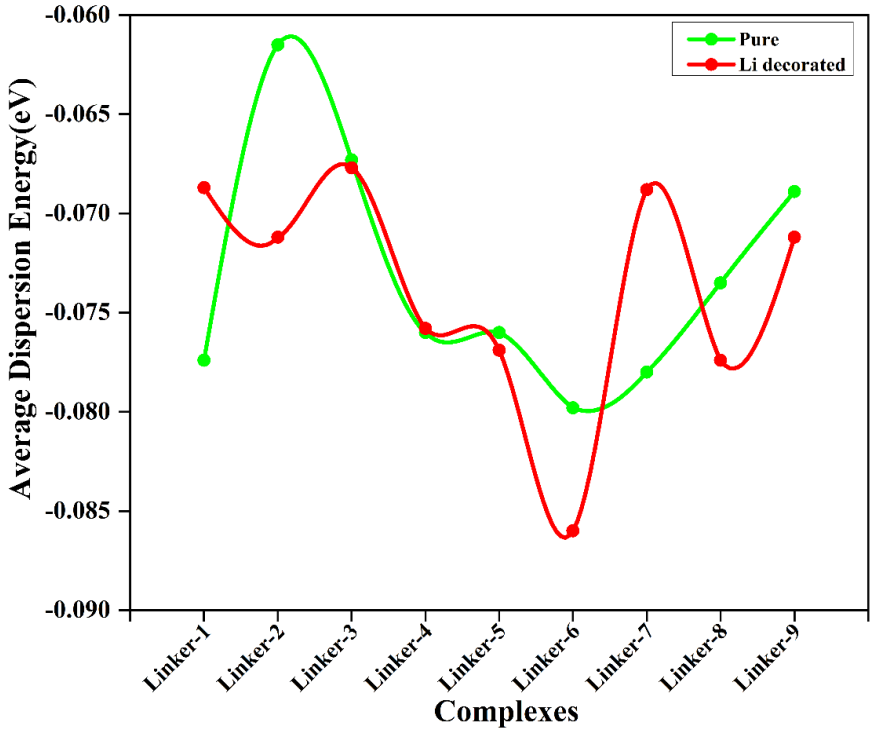

Figure 3.7. *The average dispersion energies of both the pure and Li-decorated linkers are shown here. The green curve displays the average dispersion energy of the pure linkers, and the red curve shows the average dispersion energy of the Li-decorated linkers. (These curves are plotted using dispersion energy data computed by the B3LYP-D3/cc-pVTZ level of theory).*

The dispersion energy is one of the most critical components in explaining the physisorption phenomena for H_2 storage and adsorption. The overlapping electron clouds indicate a stronger dispersion interaction. Still, weak dispersion attractions between atomic orbitals do not always overlap. Dispersion interactions are long-range forces inversely proportional to the interatomic distance's sixth power (~ $1/R^6$).[58] The short distance between the metal atom and the H_2 molecules indicates a strong interaction, which increases the dispersion energy. Since there is a correlation between binding enthalpy and dispersion interaction, the maximum dispersion interaction contributes to the increased value of binding enthalpy of H_2 physisorption in the linkers.[56,59]According to our calculations, the Li-decorated organic linkers have a slightly higher average dispersion energy than the pure linkers, indicating better H_2 physisorption. To enhance dispersion interactions between H_2 and the complex, it is recommended to position the H_2 molecules near the aromatic ring's central region. In the present study, the E_{Disp} was calculated separately by using Grimme's semi-empirical "-D3" dispersion correction implemented in the B3LYP method. The MP2 method naturally accounts for dispersion; therefore, it is excluded from the separate dispersion-energy study.[56]

Previous studies of hydrogen physisorption in organic linkers reported that both dispersion and electrostatic energies dominate other interactions. **Figure 3.7** represents the dispersion energy curves of both the pure and Li-decorated complexes considered in the present investigation. The Li-decorated complexes exhibit more dispersion energy than the pure linkers in most cases. This increase in dispersion energy upon decoration of the Li atoms results in a more negative binding enthalpy for hydrogen physisorption.

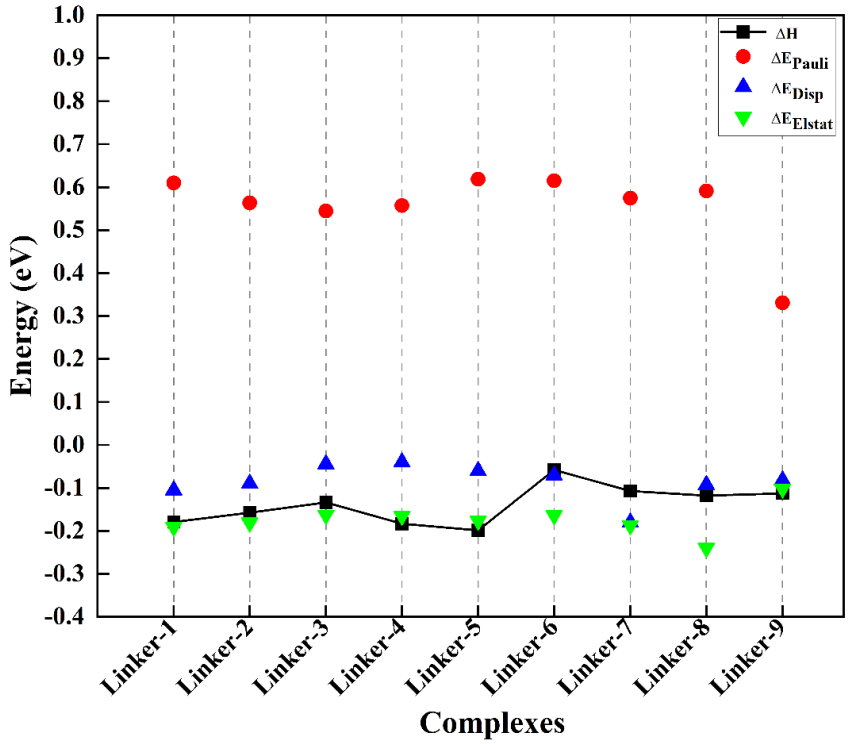

Figure 3.8. *Energy decomposition analysis (EDA) graph of the Li-decorated complexes with a single adsorbed H_2 molecule. The binding enthalpy (ΔH) with dispersion energy (ΔE_{Disp}), electrostatic energy (ΔE_{Elstat}), and Pauli repulsion energy (ΔE_{Pauli}) are shown by black, blue, green, and red colours, respectively.*

To further understand both the contribution of dispersion and electrostatic energies in terms of the magnitude of binding enthalpy of H_2 physisorption, we have performed energy decomposition analysis using the same B3LYP-D3 method, since this method provides the most favorable value of H_2 binding enthalpy than the other methods.[56,59] **Figure 3.8** illustrates the contributing components: Pauli repulsions, electrostatics, and dispersion energy, which comprise the total binding enthalpy of H_2 physisorption in the Li-decorated complexes. It is observed that both the electrostatics and dispersion energy values follow the binding enthalpy curve, whereas the values of repulsion energy have a totally different route. This study proved that both dispersion and electrostatic interactions are the primary factors contributing to the total binding enthalpy. The adsorbed H_2 molecule does not create a bond with the Li-decorated complexes through chemical interactions. It is a weak attractive interaction between the Li cation and the induced H_2 dipole, which is solely responsible for the adsorption of H_2 molecules on the Li-decorated complexes.

3.3.4. Vibrational spectroscopic properties of the adsorbed H_2

Vibrational spectroscopy provides a bridge between theory and experiment. It verifies theoretically calculated adsorption characteristics of the systems. For a particle to be infrared (IR) active, there is a requirement for a change in the dipole moment. When any molecule absorbs infrared radiation, it becomes active. The H_2 molecule has a zero-dipole moment in neutral conditions and is inactive in the IR region. However, our study has found that the adsorbed H_2 molecules can be activated in the IR region. **Table 3.5** shows the estimated values of vibrational frequencies, redshift, and IR intensities.

Table 3.5. *Infrared spectroscopy properties of the adsorbed H_2 molecules on the Li-decorated linkers. (1 Debye^2-angstrom^{-2}-amu^{-1} (IR intensity unit) = 42.2561 KM/Mole = 5.82573 × 10^{-3} cm^{-2}-atm^{-1} at STP or a.u.)[56]*

Parameters	Isolated H_2	Linker-1	Linker-2	Linker-3	Linker-4	Linker-5	Linker-6	Linker-7	Linker-8	Linker-9
υ (H−H) [cm^{-1}]	4368.38	4055.98	4135.98	3964.41	3909.97	4071.36	4016.75	4052.86	4016.92	4154.31
Intensity [KM/Mole or a.u.]	0	68.12	728.95	1132.64	924.49	760.96	530.31	687.76	1012.54	53.70
Δυ red shift in cm^{-1}	0	-312.4	-232.39	-403.97	-458.40	-297.02	-351.62	-315.52	-351.45	-214.07

There is a slight change in the stretch modes of the H-H in the H_2-Li-linker complexes compared to an isolated H_2 because the H_2-Li-linker complexes are bound mainly through weak van der Waals (vdW) interaction and charge transfer forces. Therefore, the shift in vibrational frequency can be probed by IR spectroscopy to confirm the successful synthesis of the complexes predicted here. Due to the transfer of electrons from the σ-bonding orbital to the metal atom, there is a significant amount of robust redshift in the range of 214-377 cm^{-1} of the H-H stretching mode of vibration in the H_2-Li-complexes. So, the important question now is how the H_2-Li-linker complexes achieve a dipole moment and become IR-active? In the H_2-Li-complexes, when a hydrogen molecule oscillates, one of the H atoms goes near the atomic

orbitals of the Li-doped linkers, gaining some partial negative charge; consequently, the dipole moment tends to a non-zero quantity. Therefore, the vibrational induction process is responsible for activating the dipole moment of H_2 molecules in the Li-decorated complexes in the IR region.[60]

3.3.5. Highest occupied molecular orbital and lowest unoccupied molecular orbital (HOMO-LUMO) analysis

Since physisorption is a very weak interaction, explaining H_2 physisorption in the Li-linker complexes requires estimating the energy gap between the highest occupied molecular orbital (HOMO) and the lowest unoccupied molecular orbital (LUMO). The HOMO is associated with bonding orbitals (σ) with more electrons, and the LUMO is associated with the anti-bonding orbitals (σ*) that do not have any electrons at the ground state. A large HOMO-LUMO gap always indicates greater stability for a system.[60] We have calculated the HOMO and LUMO energies for all pristine and Li-decorated linkers, and the HOMO-LUMO gap for all complexes. It was observed that the H_2 molecule has a stronger interaction with the phenyl ring compared to the others. So, we observed a feasible overlapping of the electron clouds between the H_2 and Li-decorated phenyl rings. All the Li-decorated linkers have a smaller HOMO-LUMO gap than the pure linkers.

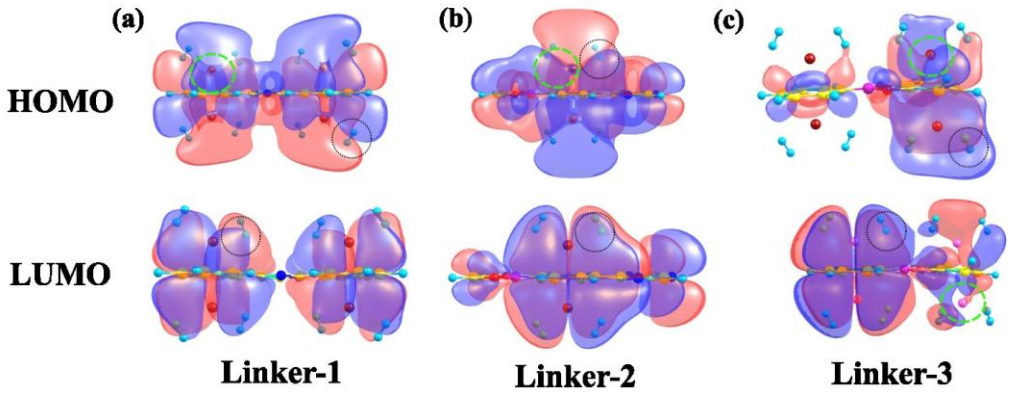

Figure 3.9. *The overlapping of atomic orbitals and HOMO-LUMO in Li-Linker complexes (a) Linker-1 (b) Linker-2; (c) Linker-3. The green circle shows an overlap of the 2s-orbital of Li and the 2p-orbital of the C atom, and the black circle shows an overlap of the 1s-orbital of H_2 and the 2p-orbital of the C atom.*

We have observed that there is no overlapping of electron clouds between the ***s***-orbitals of H_2 and Li. It means there is no covalent bonding between the Li and H atoms, so they are not

forming a Lithium hydride compound. The calculated energy gap of the HOMO-LUMO of the pure linkers-H_2 lies in the range of 4 - 6 eV obtained by the DFT-D3 method with both the cc-pVDZ and cc-pVTZ basis sets. The comparison of the energy gap between the pure and Li-

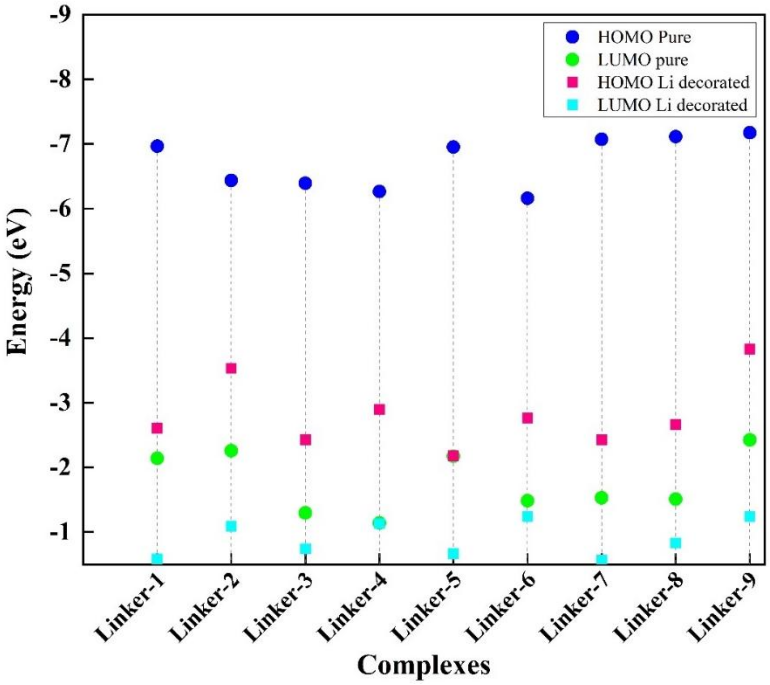

Figure 3.10. *The energy of the HOMO and LUMO with their gap for both the pure and Li-decorated linkers. (This graph is plotted using the reference data of the HOMO-LUMO gap obtained by the B3LYP-D3/cc-pVTZ method.)*

decorated linkers, as calculated using B3LYP-cc-pVTZ, are represented in **Figure 3.10**. In the MP2 method, the energy gap lies in the range of 9 to 11 eV, indicating a large HOMO-LUMO energy gap in the complexes. The calculated HOMO-LUMO energy gap of the Li-linkers-H_2 complexes lies in the range of 1.5–2.5 eV, as determined by the DFT-D3 method using the cc-pVDZ and cc-pVTZ basis sets. Using the MP2 method, the estimated HOMO-LUMO energy gap of the Li-decorated linkers is approximately 1.1–5.9 eV. Both the DFT and MP2 methods were already explored for the HOMO-LUMO calculations, and both methods successfully predicted the energies of the frontier orbitals without any limitations.[56,59,60]

3.3.6. Partial density of states (PDOS) of adsorption of H_2 molecules in both the pure and Li-decorated linkers

PDOS of both the pure and Li-decorated linkers with the first H_2 molecule adsorbed in Linker-1, Linker-2, and Linker-3 are shown in **Figure 3.11**. The PDOS of the Li atoms in all the complexes is broadened above the Fermi level E_f. There is no overlapping of H_2 1s, Li 2s, and C 2p orbitals in the pure linkers with a single H_2 molecule.

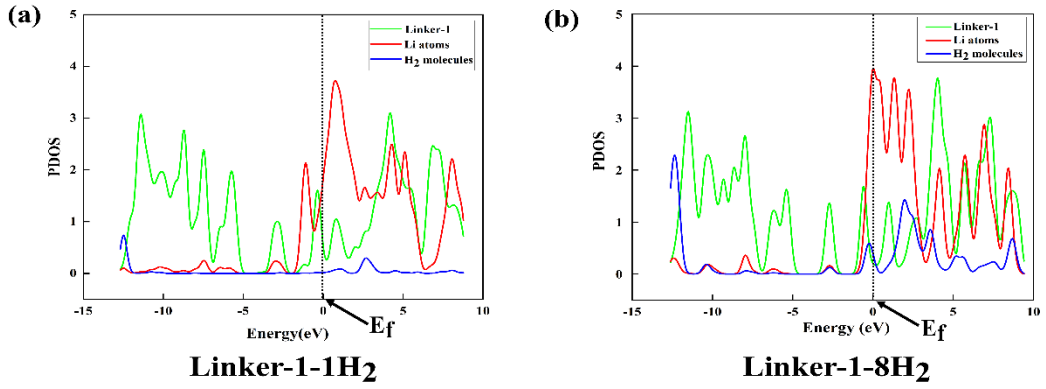

***Figure 3.11**. PDOS of the Li-decorated linkers with H_2 molecules adsorbed. (a) PDOS of the Li-Linker-1 with a single adsorbed H_2 molecule. (b) PDOS of the Li-Linker-1 with eight adsorbed H_2 molecules.*

The present study found that there are still overlaps in the prominent peaks of the H2 1s, Li 2s, and C 2p orbitals, spanning 2-5 eV, in the Li-decorated Linker-1 and Linker-2, indicating a strong interaction among H_2, Li, and the linkers. There is more overlap between the orbitals of Li and the linkers above the Fermi energy level. Li can strongly bind to a linker because of its distinct binding mechanism and relatively low ionization energy. This strong hybridization can impressively intercept the Li atoms from clustering on the surface of the linkers. Mullikan charge analysis also confirmed that each H_2 molecule gained a slight negative charge, and the Li atom became more positive with the H_2 molecule adsorption. This indicates that charge transfer is occurring from the Li atom to the H_2 molecules and polarizes the H_2 molecule. In **Figure 3.11**, it is visible that as the adsorbed H_2 molecules increase in the Li-decorated linkers, the sigma orbital (σ) of the H_2 molecule is shifted towards the right-hand side and splits into several peaks.

3.3.7. H_2 Uptake in both the pure and Li-decorated linkers

The H_2-uptake properties of both the pure COF linkers and Li-decorated linkers were calculated using **equation 3.6** and expressed in weight percentage (% wt.). The values lie in the range of 1–7 wt.%, which is comparable to those previously reported for Li-doped COFs, as represented in **Table 3.6**.

Table 3.6. *Comparison of H_2 uptake in weight % uptake across different COFs.*

COF	H_2 weight % uptake	Temperature and Pressure
Li doped COF-105	6.84 wt.%	298 K and 100 bar[35]
Li doped COF-108	6.73 wt.%	298 K and 100 bar[35]
Li-doped COF-202	4.39 wt.%	298 K and 100 bar[61]
Li-doped COF-102	4.25 wt.%	298 K and 100 bar[35]
Li doped COF-1	5.2 wt.%	300 K[49]
Li doped Linker-3	6.3 wt.%	298 K and 1 bar (This work)

The calculated H_2-uptake capacities in our research closely matched the previously reported data and were close to the USDOE target of 2025. **Figure 3.12** illustrates the difference in uptake capacities between the pure and Li-decorated linkers considered in the present study. It is evident that the uptake capacity is inversely proportional to the molecular weight of the complex. The pure linker complexes have the lowest molecular weight and show greater gravimetric H_2 uptake than the pure linkers. Pristine Linker-3 showed the highest uptake of 7.06 wt.%. Lithium decorated linkers have lower uptake capacity than pristine ones due to their greater mass. It should be noted that the calculations were performed for non-porous, non-periodic organic linkers. For this calculation, we used 298 K and 1 bar, the default temperature and pressure conditions of the Gaussian 16 suite.

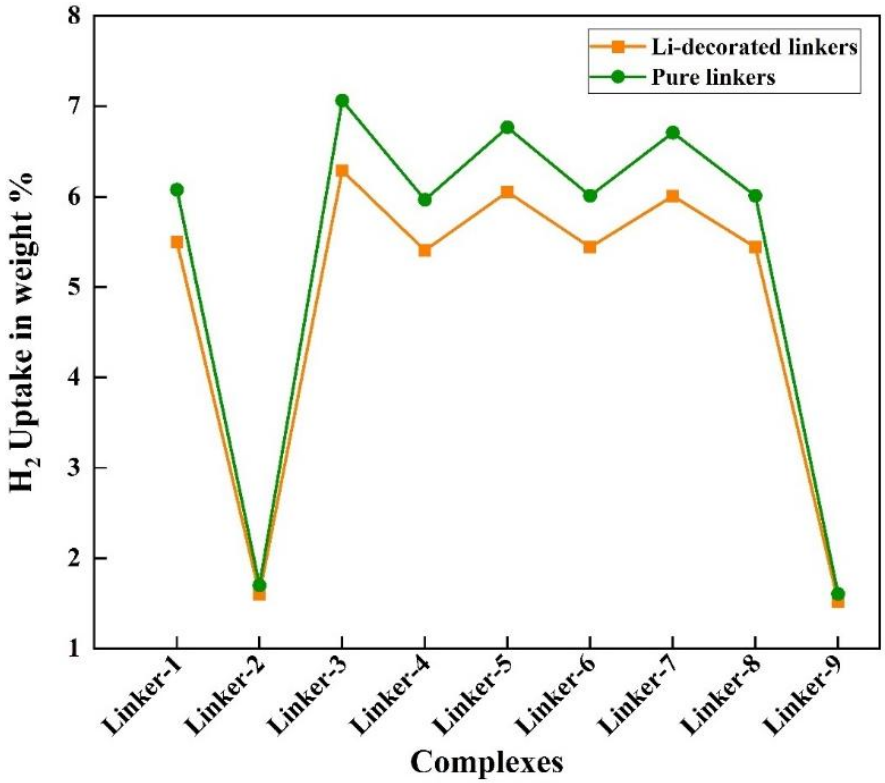

Figure 3.12. *H_2-uptake in weight percentage (wt.%) in both the pure and Li-decorated linkers.*

3.3.8. Adsorption isotherms and desorption temperature (T_d)

Figure 3.13 represents the H_2 absolute loading isotherms in mg/g. Both the COFs show similar adsorption behavior, and the H_2 loading in the COF-IITI is slightly higher than that of the Pristine-COF. The pressure range from 5 to 12 bar indicates that the H_2 loading increases very slowly. We found that the maximum loading is approximately 38.27 mg/g for the COF-IITI at 77K and 12 bar. The isotherms increase approximately linearly when pressure increases from 100 to 300 bars. The H_2 absolute loading is higher at low temperature than at room temperature. COF-IITI shows 57.41 mg/g at high pressure, and the Pristine-COF shows 22.56 mg/g H_2 loading at 300 bars. The COF-IITI appears more effective for H_2 uptake than the pristine COF. This is consistent with the large surface area and pore volume, which increase the H_2 uptake in porous materials.[62] Our calculated results for H_2 loading in COF-IITI at 77K and 100 bar are better than some previously reported COF-1, COF-5, COF-6, COF-8, and COF-10.[63] Even our computationally designed pristine COF is outperforming COF-1. In this article, we have studied the H_2 adsorption isotherms for pure COFs. While we are currently unable to simulate

our computationally designed Li-decorated COFs due to the lack of appropriate force fields, we are actively exploring methods to either generate or adapt force fields from previous reports to accurately represent Li-COF interactions.

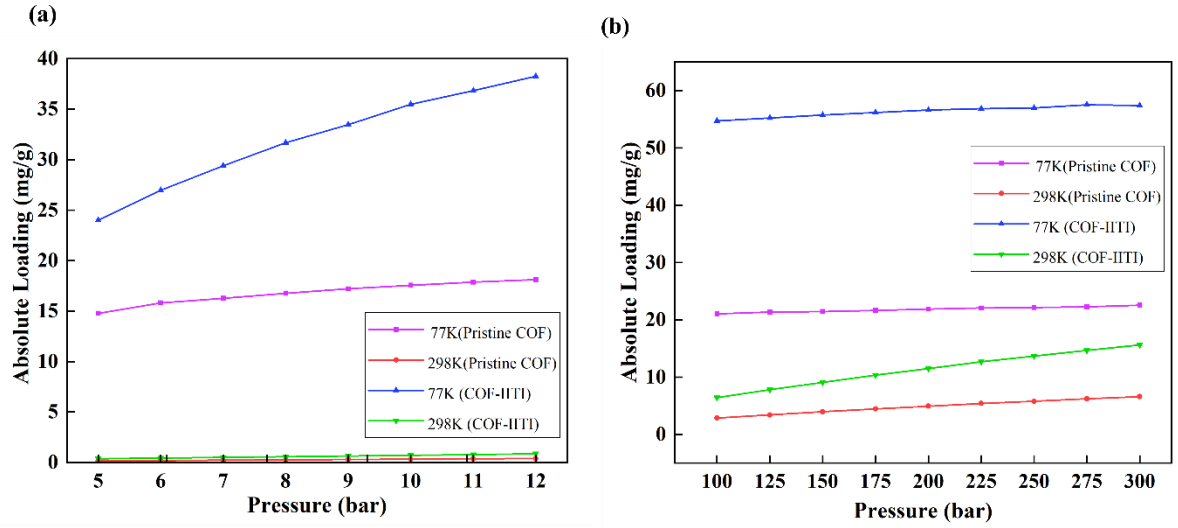

Figure 3.13. *Absolute loading of H_2 in mg/g, (a) at low pressure range (5-12 bar), (b) at high pressure range (100-300 bar).*

We are committed to overcoming this challenge, and this work is left for our future studies. The desorption temperature, calculated using a specific **equation 3.9**, is summarized in **Figure 3.14**. Our calculated desorption temperature range for the maximum number of adsorbed H_2 molecules lies between 20K and 152K. The desorption temperature range for single adsorbed H2 molecules lies in the range of 45K – 154 K. These values suggest H_2 desorption is easy in our Li-decorated COF linkers, as it satisfies the ideal range of desorption temperature, which is $T_d < 433.15$ K.[64]

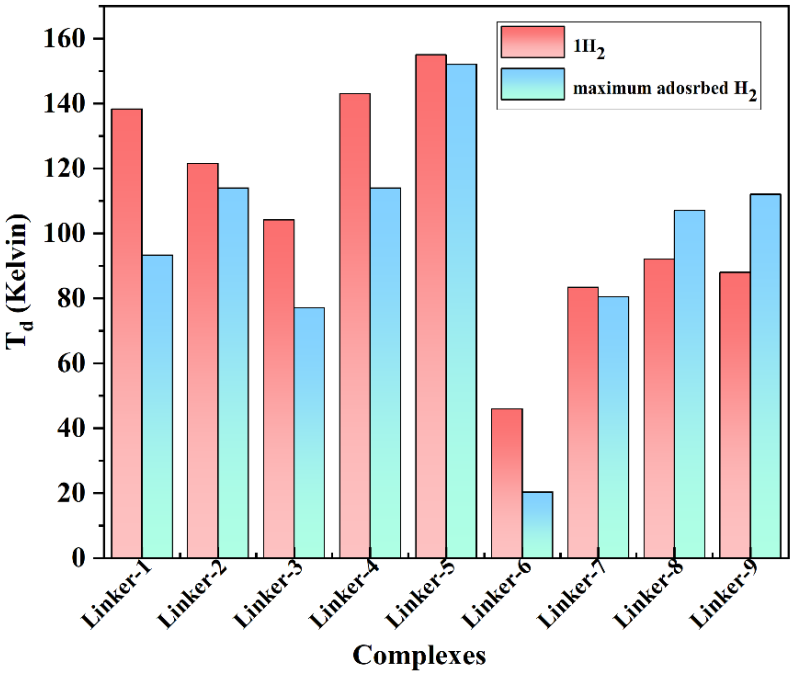

Figure 3.14. *H_2 desorption temperature for all Li-decorated complexes with single and maximum adsorbed H_2 molecules.*

3.4. Conclusions

Our study suggests that decorating the COF/MOF with a Li atom is a suitable strategy for practical H_2 storage, potentially achieving the USDOE target. The Li binding energy in the COF linker was in the range of -0.5 to -1.3 eV, computed by both the B3LYP-D3 and MP2 methods, which is a remarkable value for strong binding between the Li atoms and linkers. It was observed that the Li atom prefers to interact with the phenyl rings, with the most negative binding energy (ΔE_b) of -1.11eV. Linker-5 shows the most favorable binding enthalpy value of -0.20 eV, satisfying the optimal binding enthalpy range of -0.15 to -0.25 eV, which is a must for practical H_2 storage at ambient conditions. However, the calculated vibrational frequencies and binding energies indicate that the systems are stable, which can be further integrated into COFs. Thus, we expect these COF model systems to be readily fabricated experimentally and studied for H_2 storage in the near future. We have performed grand canonical Monte Carlo (GCMC) simulations on pure COFs and found that our designed COFs outperform some previously reported COFs for H_2 uptake at 77 K and 100 bar. The next target of our study is to perform Monte Carlo (MC) simulations of Li-decorated COFs and to investigate hydrogen adsorption isotherms at various pressures and temperatures.

3.5. References

[1] Y.J. Choi, J.W. Lee, J.H. Choi, J.K. Kang, Applied Physics Letters 92 (2008) 2006–2009.

[2] H.R. Abid, A. Hanif, A. Keshavarz, J. Shang, S. Iglauer, Energy and Fuels 37 (2023) 7260–7267.

[3] D.E. Jaramillo, H.Z.H. Jiang, H.A. Evans, R. Chakraborty, H. Furukawa, C.M. Brown, M. Head-Gordon, J.R. Long, Journal of the American Chemical Society 143 (2021) 6248–6256.

[4] S.K. Bhatia, A.L. Myers, Langmuir 22 (2006) 1688–1700.

[5] US Department of Energy, U.S Drive (2017) 1–29.

[6] Y. Xia, Z. Yang, Y. Zhu, Journal of Materials Chemistry A 1 (2013) 9365–9381.

[7] S.H. Sang, H. Furukawa, O.M. Yaghi, W.A. Goddard, Journal of the American Chemical Society 130 (2008) 11580–11581.

[8] E. Klontzas, E. Tylianakis, G.E. Froudakis, Nano Letters 10 (2010) 452–454.

[9] W.Q. Deng, X. Xu, W.A. Goddard, Physical Review Letters 92 (2004) 166103.

[10] Z. Ke, Y. Cheng, S. Yang, F. Li, L. Ding, International Journal of Hydrogen Energy 42 (2017) 11461–11468.

[11] J.H. Guo, Computational Materials Science 143 (2018) 360–367.

[12] P. Srepusharawoot, E. Swatsitang, V. Amornkitbamrung, U. Pinsook, R. Ahuja, International Journal of Hydrogen Energy 38 (2013) 14276–14280.

[13] A.D. Becke, Journal of Chemical Physics 98 (1993) 5648–5652.

[14] P. Matczak, S. Wojtulewski, Journal of Molecular Modeling 21 (2015) 41.

[15] S. Grimme, J. Antony, S. Ehrlich, H. Krieg, Journal of Chemical Physics 132 (2010) 154104 .

[16] J.G. Hill, International Journal of Quantum Chemistry 113 (2013) 21–34.

[17] D.J. Frisch, M. J.; Trucks, G. W.; Schlegel, H. B.; Scuseria, G. E.; Robb, M. A.; Cheeseman, J. R.; Scalmani, G.; Barone, V.; Petersson, G. A.; Nakatsuji, H.; Li, X.; Caricato, M.; Marenich, A. V.; Bloino, J.; Janesko, B. G.; Gomperts, R.; Mennucci, B.; Hratch, Gaussian, Inc., Wallingford CT, 2019.

[18] Zhurko, G. A.; Zhurko DA. ChemCraft, Tool for Treatment of the Chemical Data. http://www.chemcraftprog.com.

[19] Gordon, M. S.; Schmidt, M.W.; Theory and applications of computational chemistry, Elsevier, Amsterdam (2005) 1167-1189.

[20] D. Dubbeldam, S. Calero, D.E. Ellis, R.Q. Snurr, Molecular Simulation 42 (2016) 81–101.

[21] S.L. Mayo, B.D. Olafson, W.A. Goddard, Journal of Physical Chemistry 94 (1990) 8897–8909.

[22] T. Düren, L. Sarkisov, O.M. Yaghi, R.Q. Snurr, Langmuir 20 (2004) 2683–2689.

[23] L. Sarkisov, T. Düren, R.Q. Snurr, Molecular Physics 102 (2004) 211–221.

[24] A. Vaidyanathan, P. Mane, V. Wagh, B. Chakraborty, Journal of Energy Storage 78 (2024) 109899.

[25] N. Sinha, S. Pakhira, ACS Applied Electronic Materials 3 (2021) 720–732.

[26] S. Pakhira, J.L. Mendoza-Cortes, Physical Chemistry Chemical Physics 21 (2019) 8785–8796.

[27] N. Sinha, H. Joshi, S. Pakhira, ACS Applied Electronic Materials 4 (2022) 6237–6252.

[28] L.D. Gelb, K.E. Gubbins, Langmuir 15 (1999) 305–308.

[29] Z. Yang, Y. Xia, R. Mokaya, Journal of the American Chemical Society 129 (2007) 1673–1679.

[30] L. Pan, M.B. Sander, X. Huang, J. Li, M. Smith, E. Bittner, B. Bockrath, J.K. Johnson, Journal of the American Chemical Society 126 (2004) 1308–1309.

[31] S. Pakhira, K.P. Lucht, J.L. Mendoza-Cortes, Journal of Physical Chemistry C 121 (2017) 21160–21170.

[32] X. Wang, S. Zhang, X. Li, Z. Zhan, B. Tan, X. Lang, S. Jin, Journal of Materials Chemistry A 9 (2021) 16405–16410.

[33] X. Zou, G. Zhou, W. Duan, K. Choi, J. Ihm, Journal of Physical Chemistry C 114 (2010) 13402–13407.

[34] A.P. Côté, H.M. El-Kaderi, H. Furukawa, J.R. Hunt, O.M. Yaghi, Journal of the American Chemical Society 129 (2007) 12914–12915.

[35] D. Cao, J. Lan, W. Wang, B. Smit, Angewandte Chemie - International Edition (2009) 4730–4733.

[36] B. Assfour, G. Seifert, Chemical Physics Letters 489 (2010) 86–91.

[37] Y. Zeng, R. Zou, Y. Zhao, Advanced Materials 28 (2016) 2855–2873.

[38] C. Savino, R.P. Ryan, J.L. Knee, C.A. Jiménez-Hoyos, B.H. Northrop, Journal of Physical Chemistry A 124 (2020) 529-537.

[39] M.E.K. Hani, R.H. Joseph, L.M.C. José, P.C. Adrien, E.T. Robert, O. Michael, M.Y. Omar, Science, 316 (2007), 268-272.

[40] H. Furukawa, M.A. Miller, O.M. Yaghi, Journal of Materials Chemistry 17 (2007) 3197–3204.

[41] F. Gao, Z. Ding, S. Meng, Scientific Reports 3 (2013) 1882.

[42] A. Ghosh, T. Debnath, T. Ash, A.K. Das, RSC Advance 7(2017) 9521–9533.

[43] Q. Sun, P. Jena, Q. Wang, M. Marquez, Journal of American Chemical Society 128 (2006) 9741–9745.

[44] C. Xiao, K. Deng, E. Kan, W. Deng, Journal of Physical Chemistry C 116 (2012) 21291–21296.

[45] S.K. Bhatia, A.L. Myers, Langmuir 22 (2006) 1688–1700.

[46] Y. Bae, R.Q. Snurr, Microporous and Mesoporous Materials 132 (2010) 300–303.

[47] T.H. Dunning, Journal of Chemical Physics 90 (1989) 1007–1023.

[48] R.A. Kendall, T.H. Dunning, R.J. Harrison, Journal of Chemical Physics 96 (1992) 6796–6806.

[49] H. Zhao, Y. Guan, H. Guo, R. Du, C. Yan, Materials Research Express 7 (2020) 035506.

[50] T. Liu, Y. Chen, H. Wang, M. Zhang, L. Yuan, C. Zhang, Materials 10 (2017) 1399.

[51] S.J. Kolmann, B. Chan, M.J.T. Jordan, Chemical Physics Letters 467 (2008) 126–130.

[52] Y.J. Choi, J.W. Lee, J.H. Choi, J.K. Kang, Applied Physics Letters 92 (2008) 173102.

[53] P. Srepusharawoot, R.H. Scheicher, C. Moyse, A. Blomqvist, Journal of Physical Chemistry C 113(2009) 8498–8504.

[54] D. Cao, J. Lan, W. Wang, B. Smit, Angewandte Chemie - International Edition 48 (2009) 4730–4733.

[55] Y. Y. Sun, Kyuho Lee, Yong-Hyun Kim, S. B. Zhang, Applied Physics Letters 95(2009) 033109.

[56] N. Sinha, S. Pakhira, Molecular Systems Design & Engineering 7 (2022) 577-591.

[57] B. Kiran, A.K. Kandalam, P. Jena, Journal of Chemical Physics 124 (2006) 224703.

[58] R.C. Lochan, M. Head-Gordon, Physical Chemistry Chemical Physics 8 (2006) 1357–1370.

[59] S. Pakhira, J.L. Mendoza-Cortes, Journal of Physical Chemistry C 124 (2020) 6454–6460.

[60] E. Tsivion, J.R. Long, M. Head-Gordon, Journal of the American Chemical Society 136 (2014) 17827–17835.

[61] J. Lan, D. Cao, W. Wang, Journal of Physical Chemistry C 114 (2010) 3108–3114.

[62] B. Assfour, G. Seifert, Microporous and Mesoporous Materials 133 (2010) 59–65.

[63] H. Furukawa, O.M. Yaghi, Journal of the American Chemical Society 131 (2009) 8875–8883.

[64] N. Patelli, M. Calizzi, A. Migliori, V. Morandi, L. Pasquini, Journal of Physical Chemistry C 121(2017) 11166-11177.

CHAPTER 4

Role of the Quantum Interactions in H_2 Adsorption on Late Transition Metal Chelated Linkers of Covalent Organic Frameworks

Transition-metal (Tm) chelation is an effective strategy to achieve optimal binding enthalpy (ΔH) for H_2 adsorption in the linkers of Covalent Organic Frameworks (COFs). The first principle-based DFT method was implemented to determine H_2 adsorption on nine organic linkers and transition-metal chelated linkers. The obtained range of binding enthalpy for single H_2 adsorbed on the pure and chelated complexes is −7 to −20 kJ/mol, which is required for onboard H_2 storage. The Linker-3 chelated with Ni (II) metal exhibits the most favorable binding enthalpy of approximately −18.72 kJ/mol for the single adsorbed H_2 molecule, which falls within the physisorption range. Some of the complexes have shown binding enthalpies spanning physisorption to chemisorption, and in such cases, H_2 binds via Kubas interactions. However, physisorption-based complexes are preferable to others because physisorption is a reversible process with rapid kinetics. This study reveals that dispersion, polarization, and electrostatic interactions mainly contribute to the binding enthalpy of H_2 adsorption. Molecular surface potential analysis verifies the origin of the induced dipole moment in the H_2 molecule, thereby enhancing hydrogen adsorption in transition-metal-chelated COFs.

4.1. Introduction

Metal-organic frameworks (MOFs) and Covalent organic frameworks (COFs) are emerging solid-state hydrogen storage materials due to their high surface areas, fast adsorption-desorption kinetics, and large pore volumes.[1–3] In these porous materials, H_2 is generally adsorbed via weak intermolecular forces, specifically van der Waals (vdW) interactions, with binding enthalpies ranging from -7 kJ/mol to -20 kJ/mol.[4,5] MOFs have metal nodes or clusters within their framework, and these metal clusters contribute to the weight of the

structures without increasing the storage capacity. In 2005, Yaghi and coworkers synthesized a new class of lightweight porous materials that are known as covalent organic frameworks (COFs). These materials exhibit organic linkers having solid covalent bonds (C-C, C-O, C-B, and B-O) and large surface areas (4210 m^2g^{-1} for COF-103 and 3472 m^2g^{-1} for COF-102).[6] These COF materials have a high gas storage capacity due to their lower densities, large micropore volumes, suitable pore sizes, and moderate adsorption enthalpies.[7,8] A porous material with the optimal H_2 binding enthalpy in the range of physisorption is required to obtain favorable and high H_2 storage at ambient conditions.[4,9]

Computer simulations, including Density Functional Theory (DFT) methods,[10] play a crucial role in uncovering the various applications of MOFs and COFs by predicting their structural and electronic properties. Furthermore, simulations provide invaluable insights into the mechanisms of gas adsorption, separation,[11–13] and catalysis[14] within these frameworks, thereby facilitating the development of novel porous materials. Earlier DFT studies have highlighted the remarkable versatility of transition metal-based MOFs across various applications. Yang *et al.* demonstrated the CO_2 adsorption properties of functionalized M_2(dobpdc) MOFs by incorporating different ligands, showing that performance can be tuned through the selection of metal (M^{2+}) types and ligand structures.[15,16] They also proposed new transition metal-based MOFs, labeled X_4Y−MOF-5, which exhibit band gaps ranging from 1.7 to 3.6 eV, indicating the potential for visible-light photocatalysis due to their tunable electronic states.[17] These findings emphasize the diverse capabilities of transition metal-based porous materials in gas storage, separation, and other energy storage technologies.[18,19]

Additionally, Various approaches have been implemented to increase the number of active sites and improve H_2 binding in both COF and MOF materials using DFT simulations. Some effective strategies include doping alkali metals or chelating transition metals (Tm) into porous materials. Enhancement of H_2 binding has been explored through the intercalation of metal atoms [20,21] and COF impregnation.[22] Transition metals incorporated into porous materials have been recognized as an effective strategy for balancing the binding strength between the materials and H_2 molecules.[23–25]

Searching for H_2 storage materials with high gravimetric and volumetric densities, low cost, and safety is the primary goal for achieving the US Department of Energy (USDOE) set target.[26] To achieve this target, the chelation of transition metals (Tm) into organic linkers of COF material shows great promise. However, this technique has not been extensively studied. Some reports have described enhancements in the H_2 adsorption energy through the chelation of transition metals in the organic ligands of COFs.[5,23] Chelation is an appealing method for modifying metal sites on COFs, introducing unsaturated sites without compromising the COF framework and structural integrity. To chelate TM complexes into porous materials, the COF framework requires the presence of certain heteroatoms in its organic building blocks.

Many previous studies have found doping of transition metals into porous materials as a promising approach for achieving satisfactory H_2 storage.[27,28] Zou *et al.* have investigated hydrogen storage in scandium and titanium-doped COF-1 using the DFT method. The H_2 molecules adsorbed around the Sc and Ti metal atoms achieved binding enthalpy values of approximately -0.32 eV/H_2 and -0.40 eV/H_2, respectively. As a result, their gravimetric hydrogen storage capacity exceeded 6.5 wt.%.[29] Klontzas *et al.* have synthesized MOFs based on transition metals (Co, Ni, and Zn), and the binding enthalpy value ranged from 6 to 13.5 kJ/mol. They noted that the introduction of transition metal atoms enhanced electrostatic and Kubas interactions between the H_2 molecule and the adsorbent.[30] The combination of optimal binding enthalpy values, a high surface area, and a high pore volume in a porous material could meet the onboard H_2 storage target for light-duty vehicles. Recently, Pakhira *et al.* studied H_2 adsorption in computationally designed Sc-, Ti-, and V-chelated COF linkers. Their study revealed that the Sc-, Ti-, and V-chelated linkers exhibit optimal binding enthalpies for H_2 adsorption, and these transition-metal chelated complexes showed physisorption.[5]

Our primary objective is to chelate the COF linkers with late first-row transition-metal atoms ranging from Cr to Zn and to study the enhancement in H_2 binding enthalpy. Our work has adopted a novel approach using transition-metal complexes with halogens, specifically $TmCl_x$. The nature of the interaction between H_2 molecules and the d-subshell of the chelated transition metal within a porous material has not been extensively studied. Therefore, our

secondary goal is to elucidate the nature of the interaction between H_2 molecules and COF linkers, identifying the predominant interactions that contribute to the H_2 binding in linkers.

4.2. Material design and Computational details

(a) Non-Periodic DFT calculations

We have used the same nine organic linkers of COFs as in our earlier study. More details on the non-periodic models of these pure linkers are provided in **Section 3.3.2(b) of Chapter 3.** We computationally designed nine pure organic linkers and chelated them with late transition metals ranging from Cr to Zn. Subsequently, we investigated H_2 adsorption in these pure and transition-metal-chelated complexes by sequentially adsorbing 4 H_2 molecules. The first principle-based unrestricted hybrid density functional theory (B3LYP) method was used to obtain the stable equilibrium structures of the complexes with real vibrational frequencies.[10] We have included Grimme's dispersion correction (-D3) in the U-B3LYP method to incorporate the effect of long-range ordered van der Waals (vdW) forces between the surface of chelated organic linkers and H_2 molecules.[31] In the present DFT calculations, a double-ζ quality Gaussian-type basis set, cc-pVDZ, was used for C, H, B, N, O, and the transition metals Cr and Zn.[32] The LANL2DZ basis set was used for Pd and Pt metal atoms.[33] The threshold for convergence of maximum force and displacement, RMS force and velocity, energy, and electronic density was 10^{-8} a.u. The Gaussian16 suite code[34] was used for all the non-periodic DFT calculations, and the ChemCraft software[35] for molecular designing and visualization. GAMESS-US was used to perform the energy decomposition analysis (EDA).[36] Harmonic vibrational frequency analysis was performed to demonstrate the stability of the complexes.

(b) Periodic DFT calculations

We computationally designed two 2D periodic COFs, namely Pristine COF and COF-IITI, and chelated them to a transition-metal complex, $TmCl_x$ (here, $NiCl_2$). The equilibrium atomic configuration, structures, and energetics were determined by using the spin-unrestricted B3LYP DFT method[10] implemented in the CRYSTAL17 suite code.[37] To enhance the accuracy of the hybrid functionals, Grimme's "-D3" dispersion correction was incorporated to account for the weak van der Waals (vdW) interactions between H_2 molecules and COF

layers.[31] For the C, N, O, H, B, Ni, and Cl atoms, a triple-ζ valence polarized (TZVP) Gaussian basis set was employed in the present calculations.[38] We have employed a full optimization process, i.e., all atomic coordinates and lattice parameters were allowed to relax during geometry optimization. The self-consistent field (SCF) convergence criterion was set to a total energy difference of 10^{-7} a.u. between successive iterations. To achieve precise 2D SLAB calculations with the CRYSTAL17 suite code, a separation of 500 Å in the Z-direction was used to avoid interactions between periodic images. For Brillouin zone integration, a 3 × 3 × 1 k-mesh in the Monkhorst-Pack scheme was utilized for both pure and chelated COFs during geometry optimization.[39] The designed 2D equilibrium structures were displayed using the VESTA code.[40]

(c) Equations and formulas used in the calculations

The binding enthalpy of H_2 adsorption in the Tm-chelated complexes considered in the present investigation:

$$\Delta H = H_{Linker\_Tm+nH_2} - \left(H_{Linker\_Tm} + nH_{H_2}\right) \qquad (4.1)$$

This binding enthalpy is the sum of electronic energies (E_{elec}) and thermal correction in enthalpy (H_{corr}):

$$H = E_{elec} + H_{corr} \qquad (4.2)$$

The following equation was used to calculate the binding energy of H_2 adsorption in the Tm-chelated complexes considered in the present investigation:

$$\Delta E = E_{Linker\_Tm+nH_2} - \left(E_{Linker\_Tm} + nE_{H_2}\right) \qquad (4.3)$$

The energy difference between the HOMO and LUMO levels is calculated as:

$$E_g = E_{LUMO} - E_{HOMO} \qquad (4.4)$$

E_{LUMO} is the energy of the lowest unoccupied molecular orbitals, and E_{HOMO} is the energy of the highest occupied molecular orbitals (HOMO).

The H_2-uptake in terms of weight percentage (wt.%) of both the pure and transition metal chelated linkers was calculated using this equation:

$$wt\% = n * M_{H_2}/(M_{Linker} + n * M_{H_2}) \quad (4.5)$$

Where M_{H_2} is the molecular weight of H_2, n is the number of adsorbed H_2 molecules, and M_{Linker} is the molecular weight of the organic linker.

4.3. Results and Discussion

4.3.1. Chelation of transition metal atoms in the pure organic linkers

Chelating ligands are complexes with one central metal ion attached to a large organic molecule. To maintain oxidation number balance in transition metal ions, halogen atoms were used in the design of $TmCl_x$-type complexes. We have explored two expected geometries, tetrahedral (Tet) and trigonal planar (Tpl), for chelated compounds and the most common oxidation number of the transition metal atoms: Cr (III), Mn (III), Fe (II), Co (II), Ni (II), Cu (II) and Zn (II) to achieve the ideal value of binding enthalpy of H_2 adsorption in chelating ligands. The possible spin states for transition metals were proposed, and these values can be calculated using selected oxidation numbers. We have investigated the following spin states for late-transition metals:

1. Cr (III), geometry = Tetrahedral with s = 1/2 and 3/2.
2. Mn (III), geometry = Tetrahedral with s = 0, 1,2.
3. Fe (II), geometry = Trigonal planar with s = 0, 1,2.
4. Co (II), geometry = Trigonal planar with s = 1/2, 2/2, 3/2.
5. Ni (II), geometry = Trigonal planar with s = 0 and 1.
6. Cu (II), geometry = Trigonal planar with s = 1/2.
7. Zn (II), geometry = Trigonal planar with s = 0.

Hence, our transition metal complexes ($TmCl_x$) are $CrCl_3$, $MnCl_2$, $FeCl_2$, $CoCl_2$, $NiCl_2$, $CuCl_2$ and $ZnCl_2$.

Subsequently, we have attached heteroatoms (N or O) to the organic linkers of these $TmCl_x$ compounds and analyzed the vibrational frequencies of the resulting equilibrium structures. The presence of electron-rich atoms in the framework of COFs promotes additional π-bonds between transition metals and heteroatoms, thereby increasing the hydrogen adsorption strength.

3.3.2. Interaction of H_2 molecules with chelated COFs

(a) Adsorption of the first H_2 molecule in both the pure and transition-metal chelated linkers

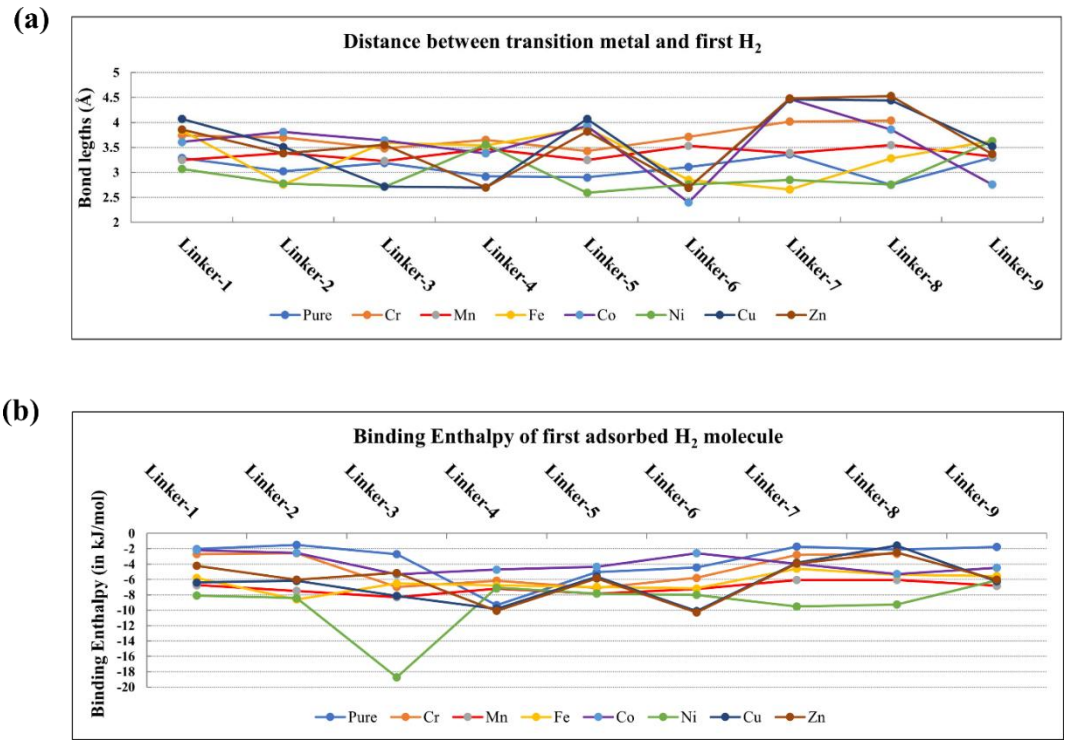

Figure 4.1. *(a) Bond distance between the transition metal atom and the first adsorbed H_2 molecule; (b) binding enthalpy value of the first adsorbed H_2 molecule on the surface of chelated linkers.*

We chelated our designed nine organic linkers to transition-metal complexes ranging from Cr to Zn. Next, to investigate hydrogen adsorption on the chelated ligands, we sequentially adsorbed up to four hydrogen molecules onto the linker surface. It was observed that hydrogen

adsorption in proximity to the chelated complex enhances the adsorption energy. However, it is crucial to maintain a distance between the H_2 molecules and $TmCl_x$ to prevent hydrogen from creating a covalent bond with the Cl atom. The clustering of H_2 molecules on the surface of chelated linkers could compromise material quality by forming HCl, consequently reducing H_2 adsorption capacity.

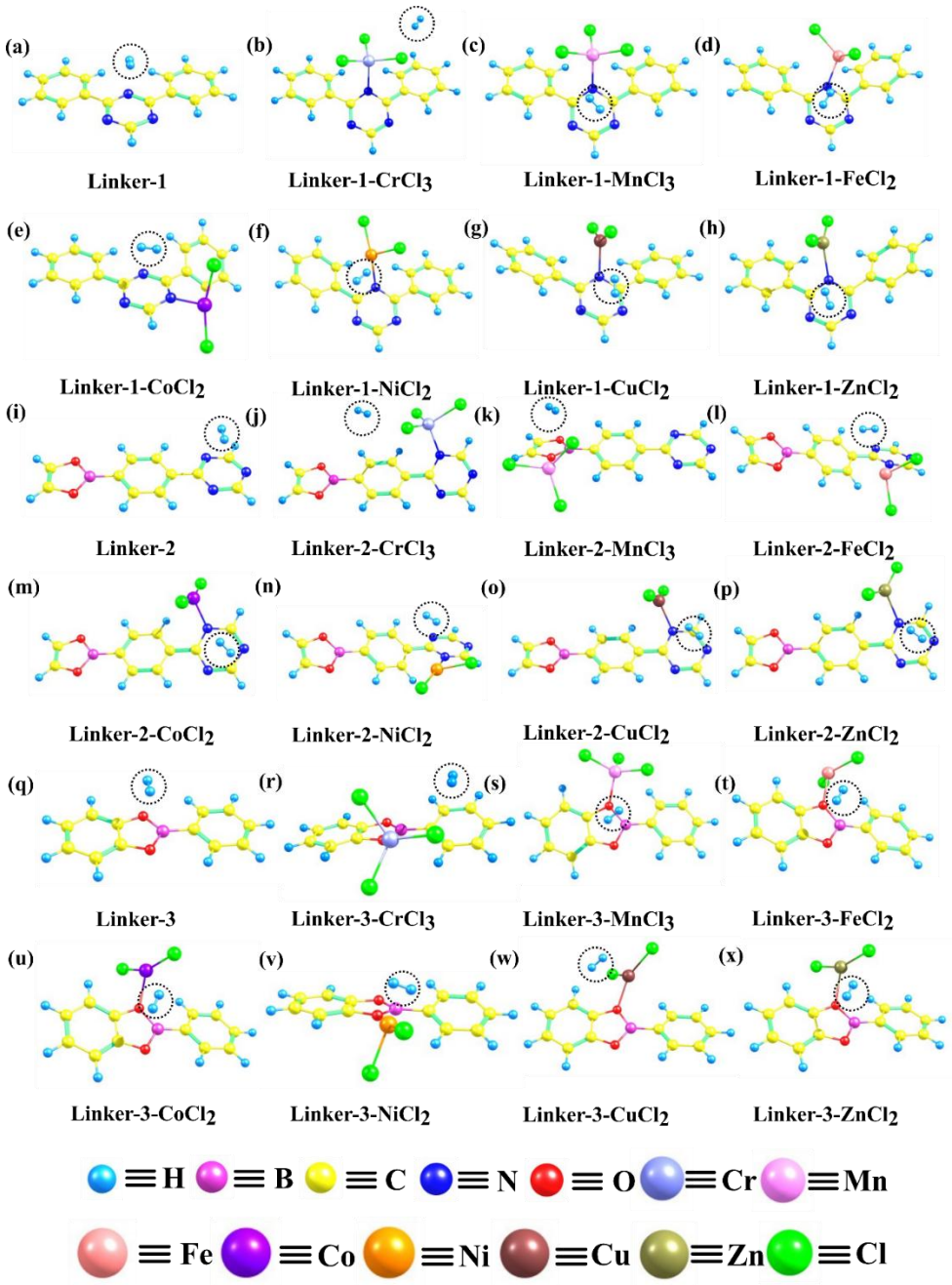

Figure 4.2. *The equilibrium structures of the pure and Tm-chelated organics, Linker-1 to Linker-3, with one adsorbed H_2 molecule.*

With these considerations in mind, we have carefully positioned H_2 molecules near the chelated complex one by one, ensuring proper bond distances between the Cl atom and H_2 molecules. We have computed the first structural parameter: the bond length between the transition-metal atom and the initially adsorbed H_2 molecule. Our calculations reveal that the bond length ranges from approximately 3.0 Å for all the pristine ligands, with Linker-5 exhibiting the shortest bond length at 2.75 Å between the centroid of the host site/chelated site and the H_2 molecule. In the case of chelated ligands, the bond distances change slightly. All transition metals exhibit a bond length range between 2.5 Å and 4.5 Å, with Ni (II) demonstrating the shortest distance between the first adsorbed H_2 molecule and the transition metal.

Subsequently, we have computed the most significant thermodynamic parameter for hydrogen adsorption: H_2 binding enthalpy. **Table 4.1** displays the assessed binding enthalpy values for the first adsorbed H_2 molecule in both pure and chelated linkers, calculated using **equation 4.1**. The value of binding enthalpy (ΔH) of the first adsorbed H_2 molecule in the chelated linkers correlates with the bond length between the H_2 molecule and Tm.

Table 4.1. *The values of binding enthalpy (ΔH) of the first adsorbed H_2 molecule in both the pure and Tm-chelated linkers.*

	Binding enthalpy ΔH of the first adsorbed H_2 molecule (kJ/mol)							
Linkers	Pure	Cr	Mn	Fe	Co	Ni	Cu	Zn
Linker-1	-2.04	-2.69	-6.73	-5.80	-2.19	-8.10	-6.39	-4.21
Linker-2	-1.50	-2.55	-7.49	-8.59	-2.55	-8.41	-6.17	-6.03
Linker-3	-2.69	-6.96	-8.31	-6.51	-5.34	-18.72	-8.13	-5.14
Linker-4	-9.35	-6.15	-7.17	-6.77	-4.71	-7.07	-9.82	-10.07
Linker-5	-5.02	-7.10	-7.83	-6.98	-4.36	-7.83	-5.62	-5.83
Linker-6	-4.41	-5.78	-7.21	-7.16	-2.57	-8.00	-10.12	-10.26
Linker-7	-1.72	-2.77	-6.06	-4.57	-3.94	-9.51	-3.81	-3.92
Linker-8	-2.09	-2.66	-6.06	-5.37	-5.28	-9.26	-1.56	-2.48
Linker-9	-1.74	32.64	-6.81	-5.56	-4.47	-6.10	-6.23	-6.02

Our study reveals no dissociation of H_2 molecules into two H atoms during adsorption, and the required barrier energy for H_2 dissociation is very high. It requires an energy of ~4.5 eV (430.53 kJ/mol) to dissociate the H_2 molecule into two H atoms. Therefore, it is next to impossible to dissociate H_2 molecules into two H atoms during physisorption.

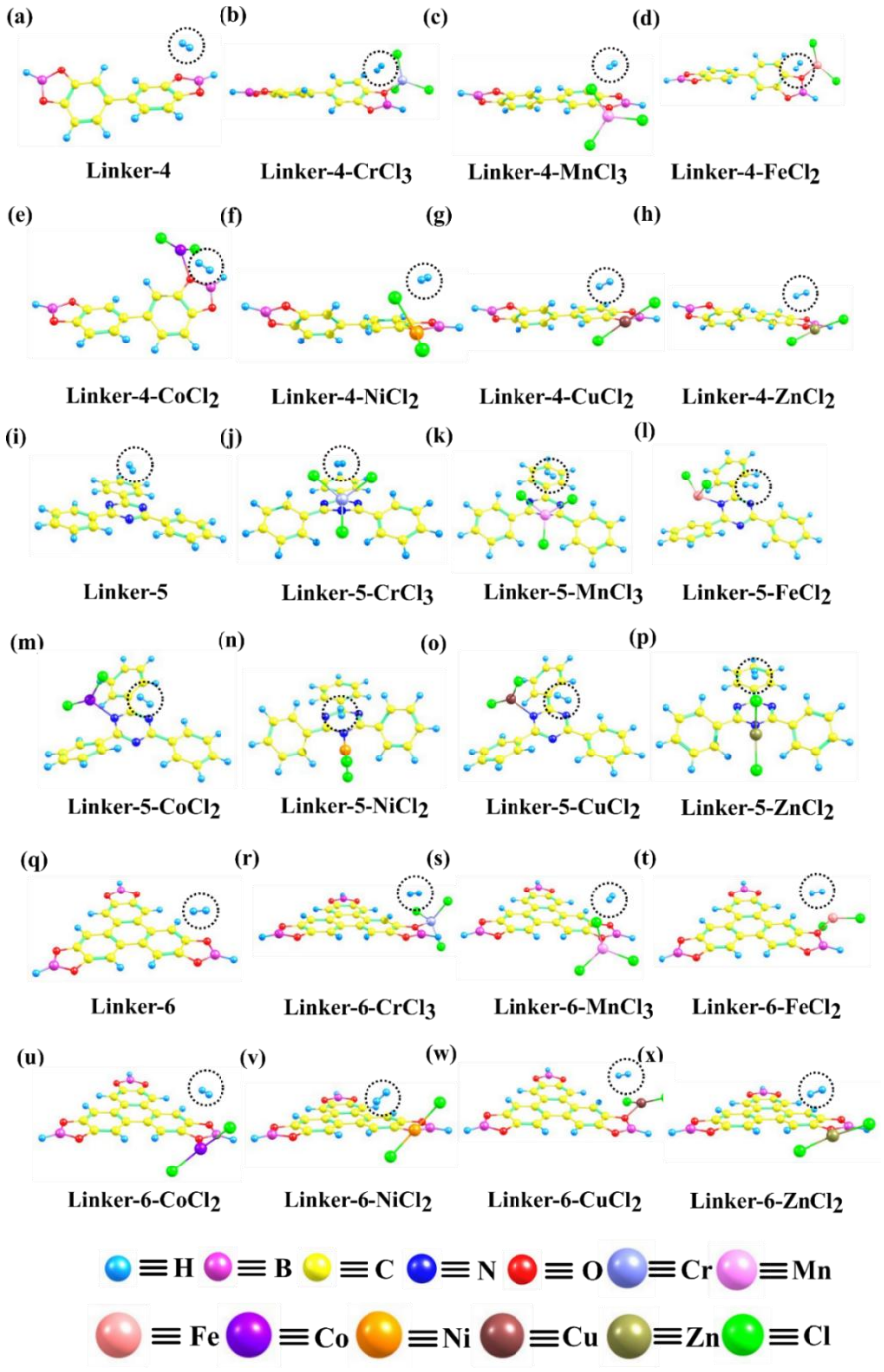

Figure 4.3. *The equilibrium structures of both the pure and Tm-chelated organics Linker-4 to Linker-6 with one adsorbed H_2 molecule.*

Then, we checked the bond distance between two H atoms of the adsorbed H_2 molecules in the relaxed structure of Tm-chelated linkers with a single adsorbed H_2 molecule. We have observed that the H-H bond length varies from 0.75 Å in free hydrogen molecules to 0.77 Å upon adsorption.

Table 4.2. *A comparative analysis of the values of the binding enthalpy for the first H_2 molecule adsorbed onto Linker-3 chelated with early, late, and precious transition metals.*

Linker	**Binding enthalpy ΔH of the first adsorbed H_2 molecule (kJ/mol)**											
	Sc	Ti	V	Cr	Mn	Fe	Co	Ni	Cu	Zn	Pd	Pt
Linker-3	- 9.59	- 2.88	- 3.27	- 6.96	- 8.31	- 6.51	- 5.34	- 18.72	- 8.13	- 5.14	- 9.78	- 59.36

The slight elongation of bond length indicates a binding interaction between the transition metals and H_2 molecules, which lies midway between physisorption and dissociative chemisorption because only H-H bond lengths beyond 1.6 Å are considered to be dissociated.[41] For the pure linkers, the binding enthalpy range falls between -1.5 to -9.3 kJ/mol. Linker-4 exhibits the highest binding enthalpy value of -9.3 kJ/mol, which falls within the ideal range for the heat of physisorption. However, other pure linkers did not yield reasonable binding enthalpies, rendering them unsuitable materials for efficient hydrogen storage. Transition metal chelation has notably improved the values of binding enthalpy, with the most chelated complexes displaying favorable values within the ideal range of heat of physisorption (-7 to -20 kJ/mol). Among our designed complexes, the Ni (II)-chelated Linker-3 exhibits the most negative binding enthalpy of -18.72 kJ/mol. However, a positive binding enthalpy was observed for Linker-9 with Cr (III), suggesting that this structure is unsuitable for H_2 binding, as adsorption would be endothermic and require substantial energy.

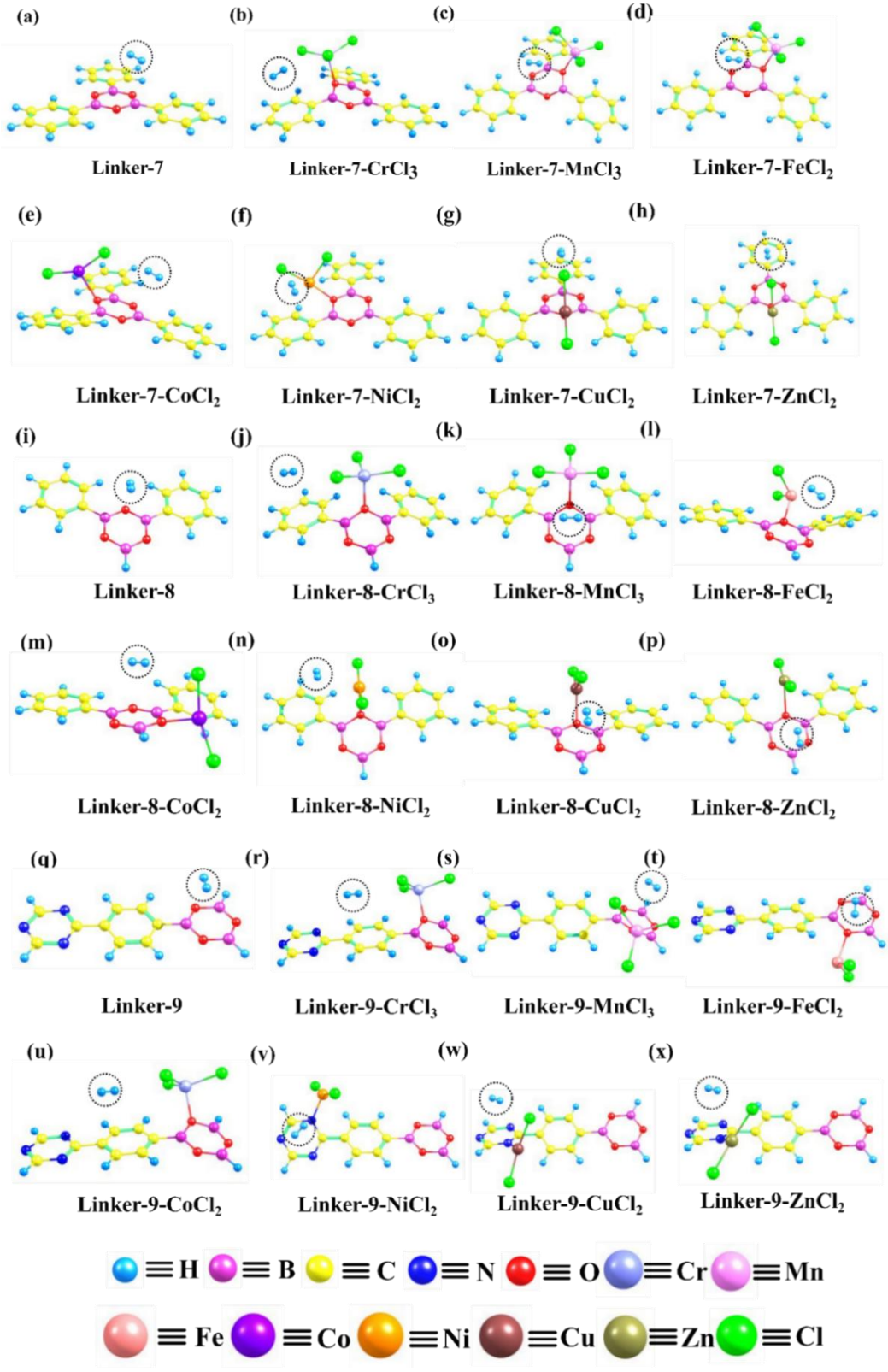
(a)
(b)
(c)
(d)
Linker-7
Linker-7-CrCl3
Linker-7-MnCl3
Linker-7-FeCl2
(e)
(f)
(g)
(h)
Linker-7-CoCl2
Linker-7-NiCl2
Linker-7-CuCl2
Linker-7-ZnCl2
(i)
(j)
(k)
(l)
Linker-8
Linker-8-CrCl3
Linker-8-MnCl3
Linker-8-FeCl2
(m)
(n)
(o)
(p)
Linker-8-CoCl2
Linker-8-NiCl2
Linker-8-CuCl2
Linker-8-ZnCl2
(q)
(r)
(s)
(t)
Linker-9
Linker-9-CrCl3
Linker-9-MnCl3
Linker-9-FeCl2
(u)
(v)
(w)
(x)
Linker-9-CoCl2
Linker-9-NiCl2
Linker-9-CuCl2
Linker-9-ZnCl2
≡H ≡B ≡C ≡N ≡O ≡Cr ≡Mn
≡Fe ≡Co ≡Ni ≡Cu ≡Zn ≡Cl

Figure 4.4. *The equilibrium structures of the pure and Tm-chelated linkers Linker-7 to Linker-9, each with one adsorbed H_2 molecule.*

Consequently, Linker-9 with Cr (III) was excluded from further binding enthalpy calculations. The comparative analysis of H_2 binding enthalpy for early-, late-, and precious-metal chelated linkers was presented using Linker-3, which had a slightly higher H_2 binding enthalpy than the other designed linkers. Then, we conducted additional calculations to investigate the nature of interactions involving early- and late-transition-metal atoms, as well as Pt and Pd. The equilibrium geometries of both the Pd and Pt-chelated Linker-3 are presented in **Figure 4.5**. **Table 4.2** presents a comparative analysis of the binding enthalpy values for the first H_2 molecule adsorbed onto Linker-3, which was chelated to early-, late-, and precious-metal (Pt and Pd) transition metals.

For early transition metals, Sc-chelated Linker-3 shows physisorption, while Ti and V show very weak interactions.[5] Among late transition metals, Mn, Cu, and Ni chelated Linker-3 display physisorption, with other metals in this group showing similarly weak interactions. A distinct behavior was observed in precious transition metals: Pd-chelated Linker-3 results in physisorption, relying more on van der Waals (vdW) forces for H_2 binding. In contrast, Pt-chelated Linker-3 exhibits Kubas-type interactions. Platinum, with its fully filled ***d***-orbitals, engages in back-donation interactions where its valence ***d***-electrons are donated to the anti-bonding orbitals of the H_2 molecule. This interaction stabilizes the H_2 molecule through partial electron density sharing, leading to a more stable and stronger binding complex.

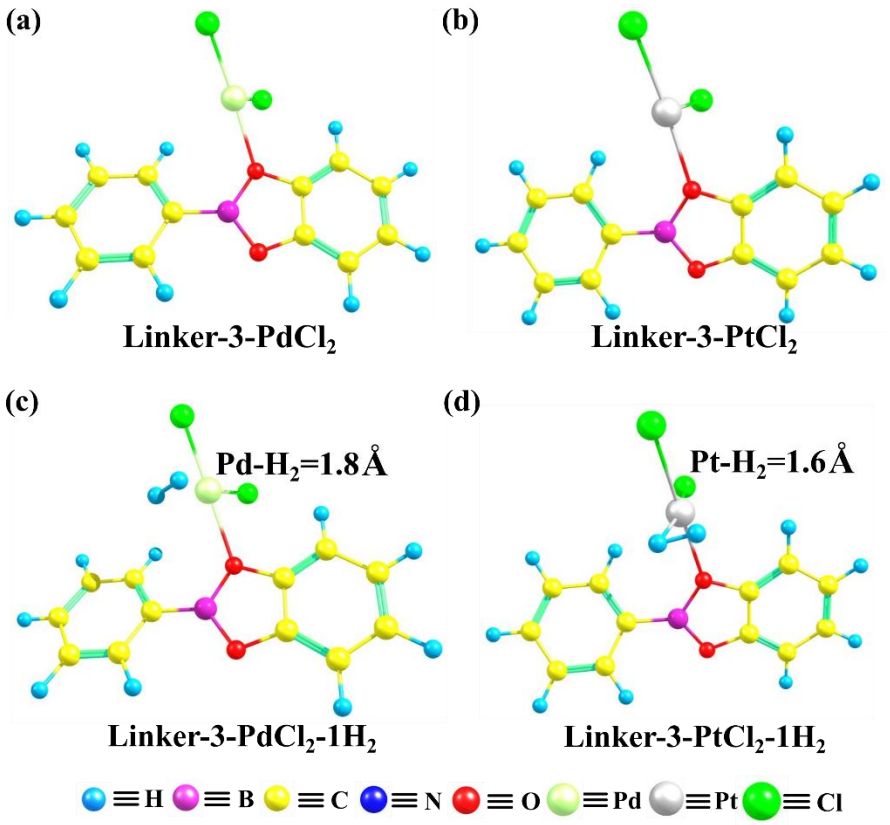

Figure 4.5. *(a) and (b) The equilibrium structures of the Pd and Pt chelated Linker-3, (c) and (d) The equilibrium structures of the Pd and Pt chelated Linker-3 with single adsorbed H_2 molecules.*

The equilibrium structures of both the pure and Tm-chelated linkers with the first adsorbed H_2 molecule are represented in **Figures 4.2 to 4.4**. After chelating them with transition-metal complexes, there is slight stress and tension in the structures of Linker-5 and Linker-7. Some previous studies have shown that the introduction of metal atoms can cause structural distortions in both the triazine and boroxine rings of the materials. An earlier study has found that the Sc-decoration on the g-C_3N_4 plane results in a loss of planarity, changing the C-N-C bond angles from 116.15˚ in pristine g-C_3N_4 to 113.94˚ and 106.23˚ in the doped structure.[41] These examples illustrate that aromatic rings in which N and O heteroatoms are present can bear significant tension and distortions due to metal doping, which aligns with the computed tension in the Linker-5-Tm and Linker-7-Tm of COFs caused by buried N/O atoms. These findings suggest that real materials with similar connections can exhibit analogous structural changes upon metal doping.

4.3.2. Adsorption of the first H_2 molecule in both the pure and transition-metal chelated periodic COFs

As we know, COFs have periodic crystalline structures composed of well-defined repeated building units, i.e., organic linkers. The periodic structure of transition-metal-chelated COFs is complex and requires substantial computational resources. Even though cluster models are not very different from an extended COF, one must remember that the H_2 molecule bond length is only 74 pm long, shorter than a typical C−H bond. Hence, H_2 adsorption is a local interaction mainly sensitive to the immediate environment of the adsorption sites.[42] Therefore, cluster models should accurately describe adsorption interactions and provide valuable insights. Numerous successful previous studies support the reliability of H_2 adsorption in cluster models.[43,44] To evaluate the reliability of cluster models for COF linkers, we performed periodic DFT calculations and designed two 2D periodic COFs: Pristine COF and COF-IITI, as shown in **Figures 4.6a and 4.6b**, respectively. We have compared their H_2 adsorption results with those of cluster models.

Figure 4.6c-4.6e displays the equilibrium structures of the 2D Pristine COF and COF-IITI, with single adsorbed H_2 molecules at different sites. In the previous section, we observed that the Ni-chelated complexes gained the most favorable binding enthalpy among the other complexes. Given the computational resources and time constraints of current DFT calculations, the computational calculations and result analysis for all late transition-metal-chelated periodic COFs may not be feasible.

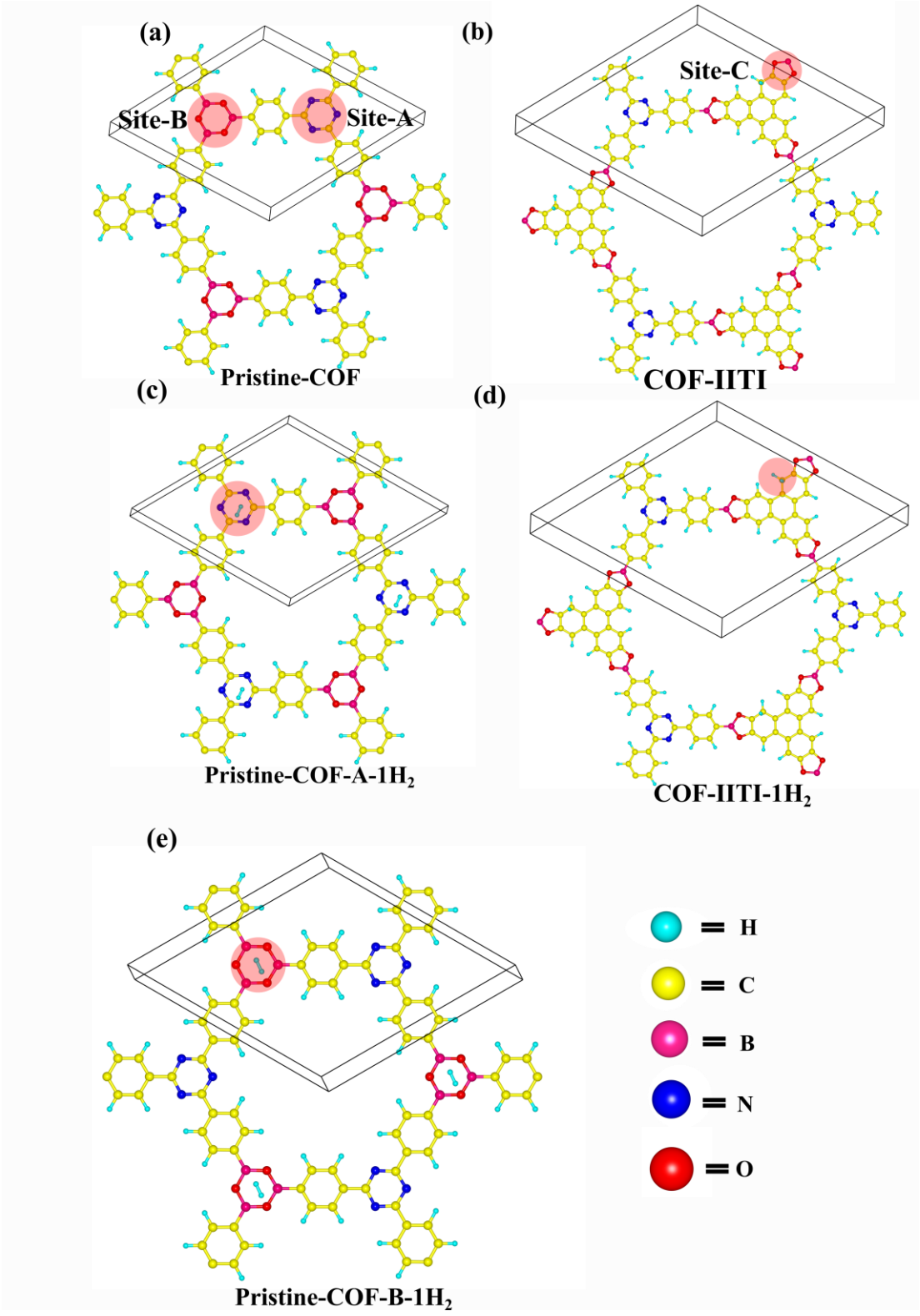
(a)
Site-B
Site-A
Pristine-COF
(b)
Site-C
COF-IITI
(c)
Pristine-COF-A-1H2
(d)
COF-IITI-1H2
(e)
Pristine-COF-B-1H2
= H
= C
= B
= N
= O

Figure 4.6. *The equilibrium structures of both the pure periodic COFs and with a single adsorbed H_2 molecule. (a) Pristine-COF, (b) COF-IITI, (c) Pristine-COF-A-1H_2, (d) COF-IITI-1H_2, and (e) Pristine-COF-B-1H_2.*

Therefore, we have chelated the designed 2D COFs with Ni metal complexes ($NiCl_2$). It is evident from **Figure 4.7** that these COFs have three main building units (Linker-5, Linker-6, and Linker-7), represented in the cluster models (**see Figure 3.2** i**n Chapter 3**). We initially chelated all three sites (A, B, and C) in the COFs, which contain heteroatoms (either N or O), as shown in **Figure 4.7a-4.7c**. Subsequently, we have conducted the adsorption of a single H_2 molecule at all three sites in these chelated COFs, as displayed in **Figure 4.7d-4.7f**. Using **equation 4.3**, we have calculated the H_2 binding energies of a single adsorbed H_2 molecule on periodic COFs. For consistency, we have reported the H_2 binding energies of the chelated linkers in **Table 4.3**.

Table 4.3*. A comparative analysis of the values of the binding energy for the first adsorbed H_2 molecule on both the pure and chelated periodic COFs with their cluster models.*

COFs	**Sites**	**Binding Energy ΔE in kJ/mol of single adsorbed H_2**	
		Periodic system	**Cluster model**
Pristine COF	Linker-5=Site A	-3.32	-5.02
	Linker-6=Site B	-19.96	-11.18
Pristine COF-$NiCl_2$	Linker-5-$NiCl_2$-A	-11.45	-17.04
	Linker-6-$NiCl_2$-B	-25.23	-15.38
COF-IITI	Linker-7=Site C	-17.02	-11.15
COF-IITI-$NiCl_2$	Linker-7-$NiCl_2$-C	-19.10	-16.07

The values of H_2 binding energy reported in **Table 4.3** indicate a significant enhancement after chelation with a Ni metal atom. In the 2D Pristine-COF, Site B (Linker-6) exhibits the most negative binding energy in both pure and chelated cases, indicating it has the most stable geometry. While there is a slight discrepancy in the H_2 binding energy values between the periodic COFs and the cluster models, this minor difference does not undermine the reliability

of our designed cluster models. The data in **Table 4.3** clearly demonstrate that the cluster models are as reliable as the periodic system, providing accurate and acceptable results for H_2 binding energies.

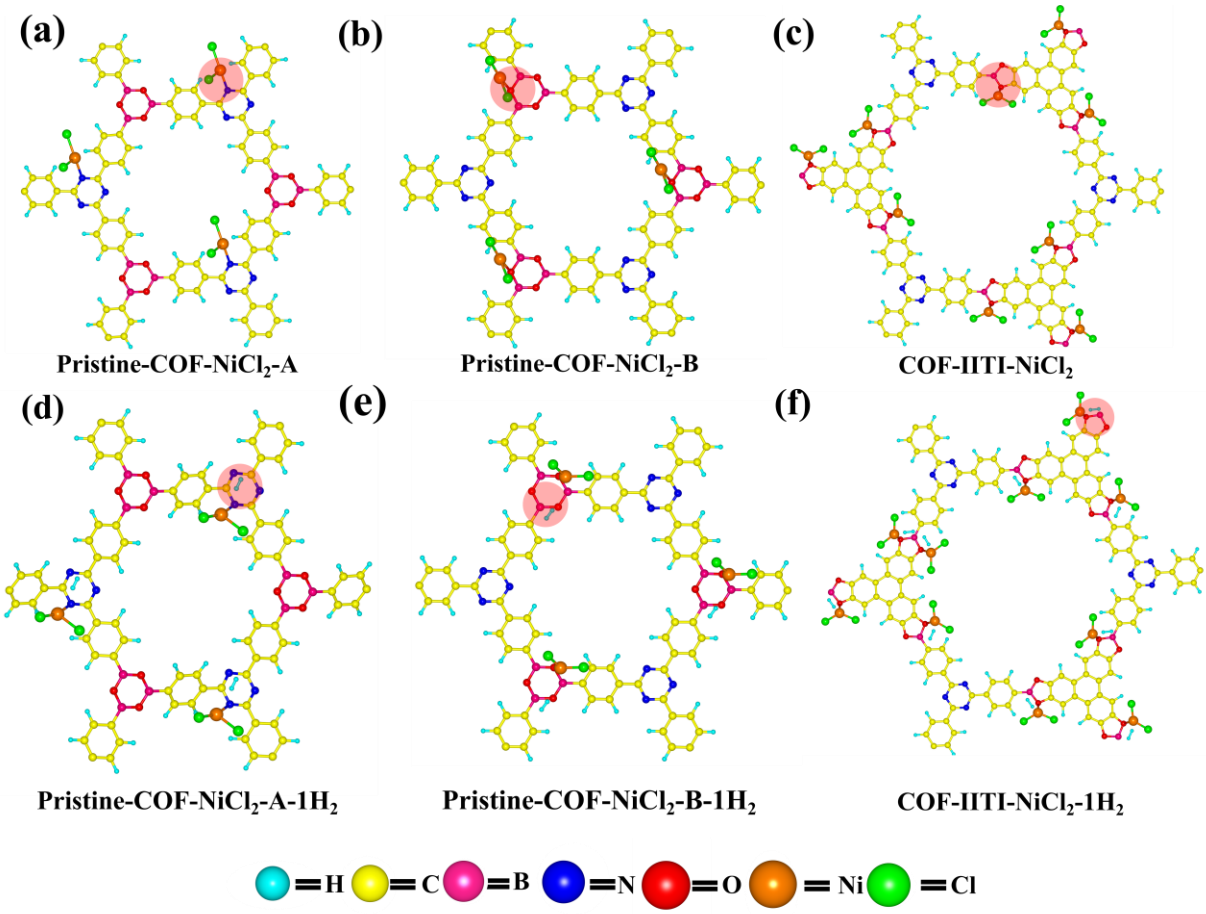

Figure 4.7. *The equilibrium structures of both the periodic chelated COFs with a single adsorbed H_2 molecule. (a) Pristine-COF-$NiCl_2$-A, (b) Pristine-COF-$NiCl_2$-B, (c) COF-IITI-$NiCl_2$, (d) Pristine-COF-$NiCl_2$-A-1H_2, (e) Pristine-COF-$NiCl_2$-B-1H_2, and (f) COF-IITI-$NiCl_2$-1H_2.*

4.3.3. Adsorption of four H_2 molecules in the pure and transition metal chelated organic linkers

Pramudya *et al*. recently used the Langmuir Toy Model to evaluate the delivery and uptake of H_2 molecules at varying pressures. They observed that the adsorption energy directly affects the delivery amount of H_2 at room temperature. They have used a simple approximation (ΔH_{ads}

~ ΔH_{bind}) in this model.[23] This suggests that the ideal range of binding enthalpy, from -7 to -20 kJ/mol, helps achieve the desired H_2 delivery amount for the DOE setup targets. Our next target is to study the pattern of binding enthalpy as the number of adsorbed H_2 molecules increases. For this purpose, we studied the hydrogen adsorption phenomena using both the pure and chelated linkers at 298 K. The estimated binding enthalpies for all complexes are calculated using **equation 4.1.**

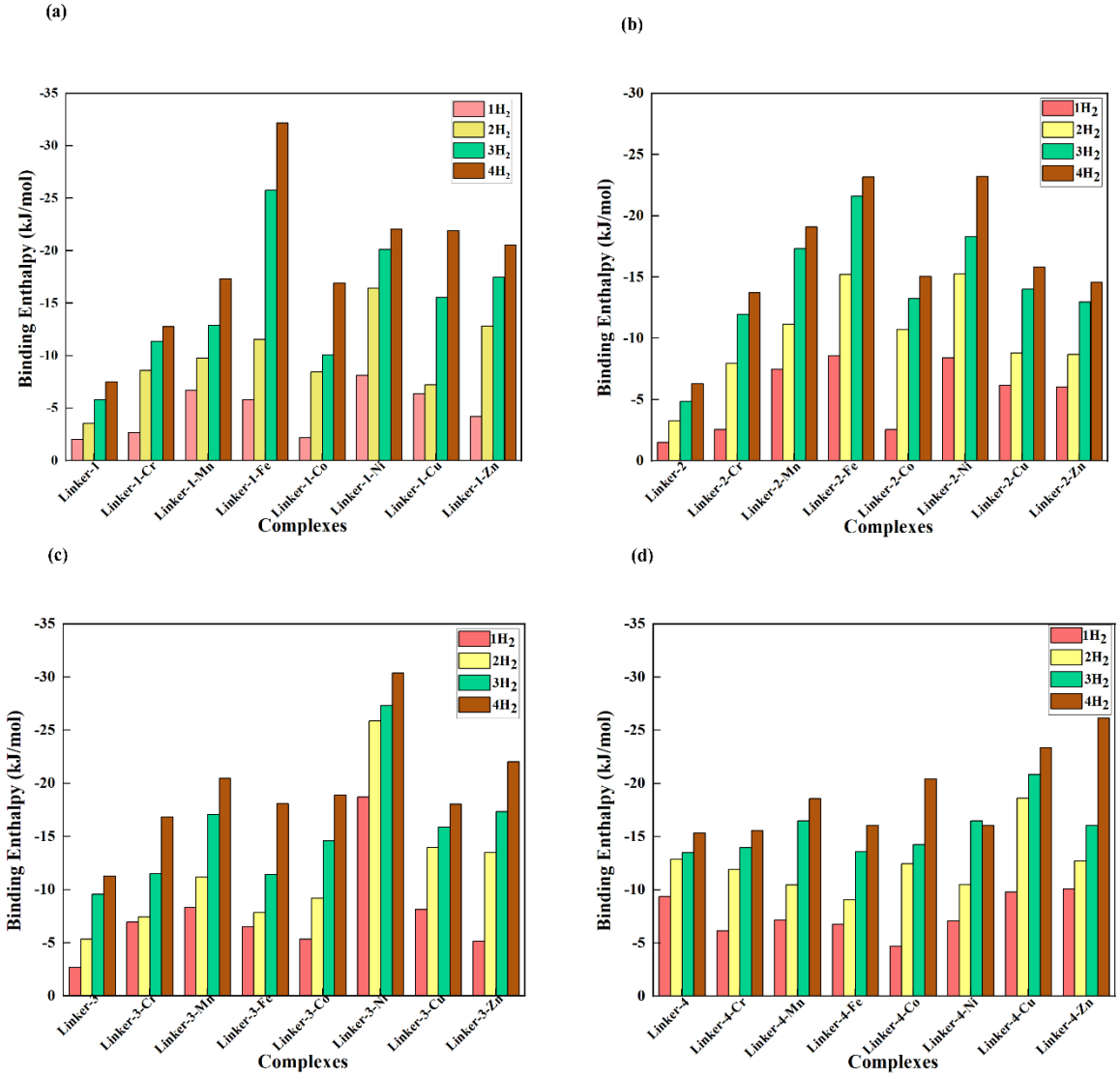

Figure 4.8. *The binding enthalpy graph for pure and chelated Linker-1 to Linker-4.*

According to our results, the binding enthalpy has increased gradually as the adsorbed H_2 molecules become more intense in all chelated complexes. The enthalpy of H_2 adsorption

depends on the surface coverage and the interaction between two adsorbed H_2 molecules on the surface. When a single H_2 molecule adsorbs, the binding enthalpy is mainly influenced by the interaction of the H_2 molecule with the linkers. As additional H_2 molecules adsorb, electrostatic and van der Waals interactions strengthen, increasing the overall adsorption and the binding enthalpy.[45] However, when the adsorption sites become saturated and the coverage is very high, the reduced distance between adjacent H_2 molecules can introduce repulsive interactions and steric hindrance. This can lead to a decrease in the H_2 binding enthalpy.

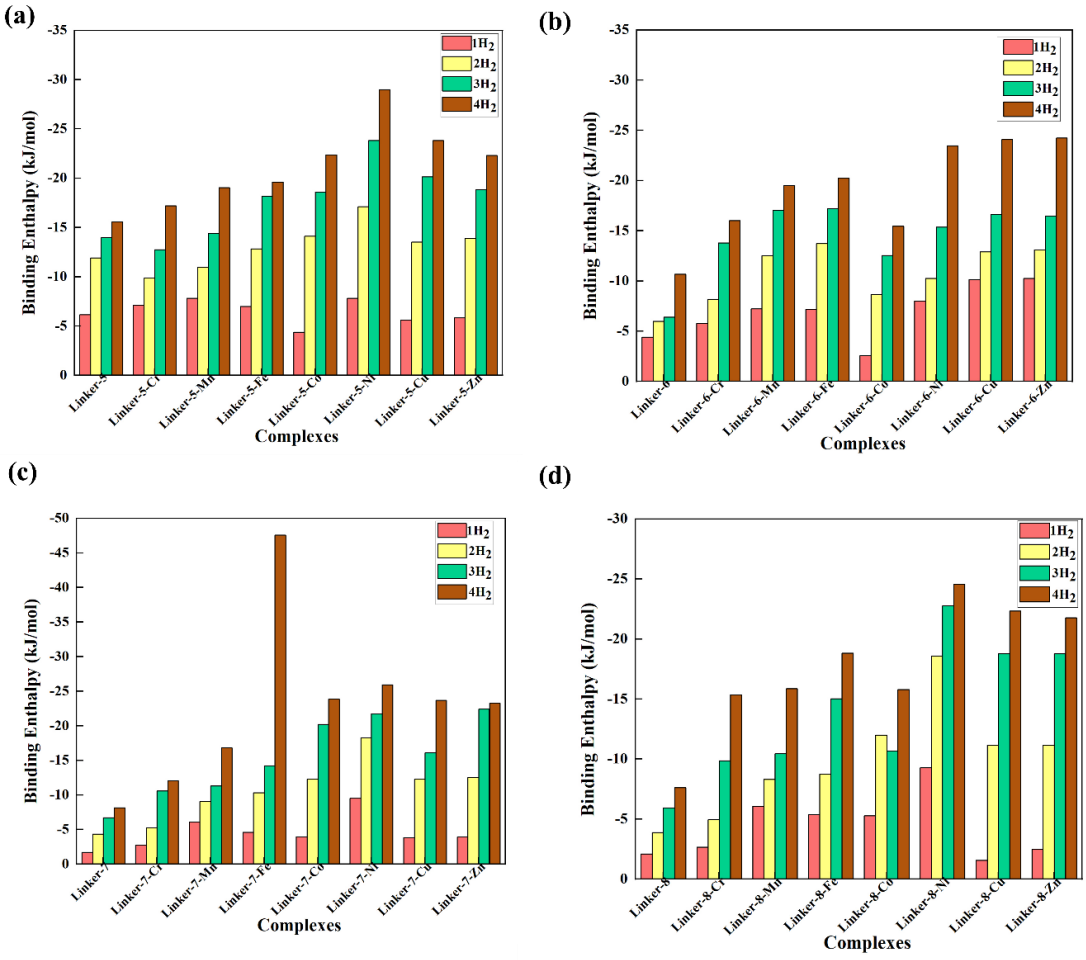

Figure 4.9. *The binding enthalpy graph for pure and chelated Linker-5 to Linker-8.*

The 18-electron rule can predict the maximum number of H_2 molecules that can be adsorbed stably on a transition-metal complex without causing repulsion.[46] This rule suggests that the

sum of the total number of electrons should be 18 within any H_2-adsorbed transition metal complexes. Based on the 18-electron rule, we can predict that the maximum number of H_2 molecules that could be bound to the Linker-$TmCl_x$ complex should be 4 or 5, as this would correspond to the total number of electrons equal to 18. In our designed complexes, either three electrons are contributed by the transition metal in the +3 oxidation state, or two electrons are contributed by the transition metal in the +2 oxidation state. The chelated aromatic ring contributes six electrons, and the four adsorbed H_2 molecules contribute a total of eight electrons. Hence, the $TmCl_x$ complex satisfies the 18-electron rule.

Figures 4.8-4.10 show the enthalpy graphs for both the pure and chelated linkers. Five types of interactions could be responsible for H_2 binding in porous materials. Our research primarily investigates hydrogen physisorption phenomena in both the pure and chelated linkers, focusing on selecting the best complexes based on hydrogen physisorption criteria. In this context, interactions with a binding enthalpy value around -3.5 kJ/mol are termed charge-quadrupole interactions. In comparison, charge-induced dipole interactions exhibit a binding enthalpy value of approximately -6.8 kJ/mol. Interactions with a value of binding enthalpy less than -1 kJ/mol are characterized as dipole-induced dipole interactions. Van der Waals (vdW) interactions typically have a binding enthalpy of around -7 kJ/mol, while those exceeding -20 kJ/mol are Kubas interactions. Generally, the values of binding energy between -7 and -20 kJ/mol indicate physical adsorption, whereas those surpassing -100 kJ/mol signify chemical adsorption. As physisorption is reversible, hydrogen desorption from physiosorbed materials is feasible because the required desorption energy is minimal. Most of the designed complexes have successfully met the criteria for H_2 binding by physical adsorption. However, some linkers bind H_2 molecules through weak charge-induced and quadrupole interactions, which are notably weak and indicative of poor H_2 adsorption in such complexes. Additionally, a few complexes exceed the typical enthalpy range of H_2 adsorption and bind H_2 molecules through Kubas interactions. In these cases, the binding enthalpy exceeds- 20 kJ/mol but remains below -100 kJ/mol.

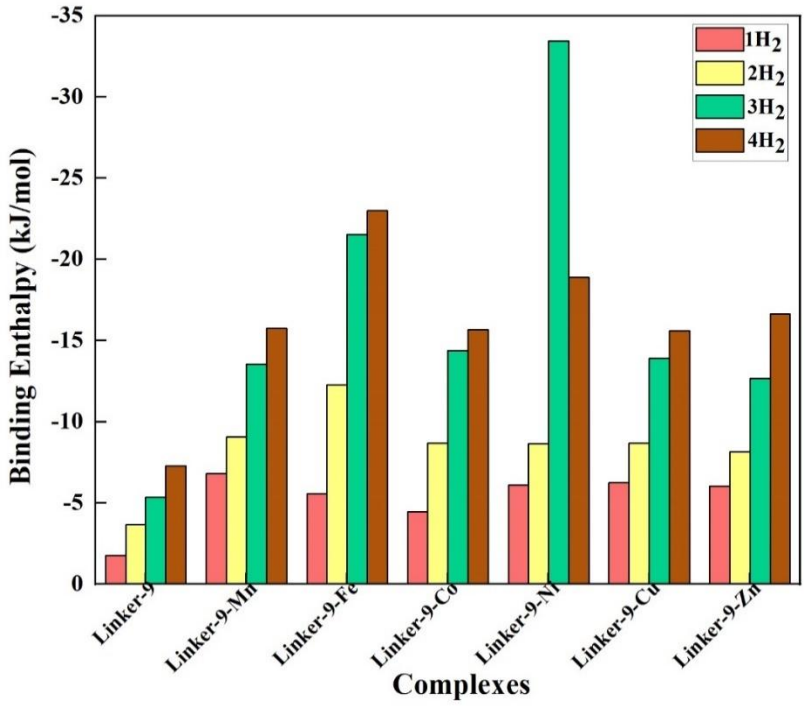

***Figure 4.10**. The binding enthalpy vs. complexes graph for both the pure and chelated Linker-9.*

Linker-1: The computed values of enthalpy (ΔH) for the pure Linker-1 range from approximately -2.04 to -7.48 kJ/mol. This indicates that H_2 molecules were adsorbed via weak van der Waals (vdW) interactions in the pure linker, consistent with physisorption. For the chelated Linker-1-$TmCl_x$, these values span from -2.19 to -32.18 kJ/mol. Linker-1 with Cr (III), Mn (II), Co (II), Ni (II), Cu (II), and Zn (II) exhibit optimal values of heat of physisorption for all four adsorbed H_2 molecules. Only the Linker-1-$FeCl_2$ displays binding enthalpy values of approximately -26 kJ/mol and -32 kJ/mol for 3 H_2 and 4 H_2 molecules, respectively. This suggests that for the Linker-1-$FeCl_2$, there is an interaction responsible for the adsorption of three or more H_2 molecules, and the strength of this interaction falls between physisorption and chemical adsorption. Linker-1-$ZnCl_2$ has attained the most negative value of binding enthalpy, -17.47 kJ/mol, within the range of physisorption with the third adsorbed H_2 molecule.

Linker-2: The pure Linker-2 adsorbs 1 to 4 H_2 molecules via very weak interactions, ranging from a binding enthalpy of -1.5 kJ/mol to -6.2 kJ/mol. This suggests that the charged quadrupole and charge-induced dipole interactions are responsible for H_2 binding in the pure

Linker-2. [Mn (II), Co (II), Cu (II), and Zn (II)] chelated Linker-2 exhibits binding enthalpy values in the range of about -2.55 kJ/mol to -19.10 kJ/mol. In these complexes, H_2 molecules bind with the chelated linkers through physisorption except for Linker-2 [Cr (III), Co (II), Cu (II), and Zn (II)] complexes with a single adsorbed H_2 molecule. Linker-2 [Cr (III), Co (II), Cu (II), and Zn (II)] demonstrates binding energy values of < -7 kJ/mol with single adsorbed H_2 molecules, but upon increasing the number of H_2 molecules, their values align with the ideal range of the heat of physisorption. In Linker-2-$FeCl_2$, favorable values of heat of physisorption are observed for two adsorbed H_2 molecules, but adding more H_2 molecules shifts this interaction towards Kubas interaction with a binding energy value exceeding -20 kJ/mol. A similar phenomenon was observed with Linker-2-$NiCl_2$. At the same time, its hydrogen adsorption energy value is more satisfactory with three adsorbed H_2 molecules. The energy value for the fourth H_2 molecule is more indicative of a Kubas interaction than of van der Waals interactions. Linker-2 chelated $MnCl_2$ exhibits a superior adsorption energy of -19.10 kJ/mol with the fourth adsorbed H_2 molecule.

Linker-3: The calculated hydrogen adsorption energy value for the pristine Linker-3 ranges from approximately -2.68 kJ/mol to -11.29 kJ/mol. For the first and second adsorbed H_2 molecules, the range of binding enthalpy values is below -7 kJ/mol. However, after the third molecule adsorbs, this value increases slightly to -11.29 kJ/mol, indicating that the third and fourth H_2 molecules interact with the pure linkers via van der Waals forces. After the chelation of transition metals, most complexes exhibit values of ideal adsorption energy. Linker-3 with [Cr (III), Fe (II), Co (II), Cu (II), and Zn (II)] demonstrates the values of binding enthalpy exceeding -7 kJ/mol after the adsorption of a second hydrogen molecule. Mn (II) chelated Linker-3 exhibits exceptional binding enthalpy with each adsorbed H_2 molecule. Linker-3 with Ni (II) displays a favorable binding enthalpy value with only a single adsorbed H_2 molecule. Still, as the number of adsorbed H_2 molecules increases, the values tend towards the range of Kubas interactions. Similarly, Mn (II) and Zn(II) chelated Linker-3 exhibit binding enthalpies exceeding -20 kJ/mol for the fourth adsorbed H_2 molecule. The linker-3-$CoCl_2$ complex with four adsorbed H_2 molecules is the most stable and promising, with an enthalpy of approximately -18.89 kJ/mol.

Linker-4: The pure Linker-4 exhibits a binding enthalpy for hydrogen adsorption ranging from about -9.35 kJ/mol to -15.37 kJ/mol, meeting the required enthalpy of adsorption for all the complexes considered in the present investigation. After the second adsorbed H_2 molecule, the Linker-4 with Cr (III), Fe (II), and Co (II) demonstrates a favorable value of enthalpy of adsorption. However, the first H_2 molecule is adsorbed via charge-induced and quadrupole interactions. Upon adsorption of the third H_2 molecule, Cu (II), Co(II), and Zn(II)- chelated Linker-4 exhibit H_2 binding in the materials via Kubas interactions. The present study indicates that upon adsorption of the fourth hydrogen molecule in the Linker-4-$MnCl_2$, the binding enthalpy becomes -18.57 kJ/mol, indicating strong physisorption and high thermodynamic stability of the system.

Linker-5: In the pure Linker-5, a weak charge-induced and quadrupole interaction exists between the linker and the first adsorbed H_2 molecule, with a value of ΔH approximately -5.02 kJ/mol, computed by the DFT method. From the adsorption of 2 to 4 molecules, H_2 shows weak vdW interactions with a change of ΔH about -11.5 kJ/mol to -15.5 kJ/mol. Linker-5, chelated with Cr (III) and Mn (III), makes weak vdW bonds to all four H_2 molecules with a favorable value of heat of physisorption. The Linker-5 chelated by Fe (II) exhibits the binding enthalpy of -7 kJ/mol after the adsorption of the second H_2 molecule. In Linker-5-$CoCl_2$, the first adsorbed H_2 molecule has a value of ΔH less than -7 kJ/mol, but the second and third H_2 molecules were adsorbed on the surface via physisorption. The fourth H_2 molecule exhibits a Kubas interaction, with ΔH around -20 kJ/mol. Linker-5 chelated by Ni (II) shows the value of Ni (II) approximately -20 kJ/mol after the adsorption of the first and second H_2 molecules, with the subsequent adsorption of the other two H_2 molecules via Kubas interactions. Linker-5 chelated by the Cu (II) and Zn (II) exhibits weak charge-induced and quadrupole interactions with the first adsorbed H_2 molecule. In contrast, the second and third H_2 molecules exhibit physisorption. However, the fourth H_2 molecule in both the Cu(II) and Zn(II) chelated complexes forms weak interactions with the linker's surface via Kubas interactions. The best complex was determined to be Linker-5-$FeCl_2$, with a value of ΔH approximately -19.61 kJ/mol for 4 H_2 molecules.

Linker-6: The Linker-6 chelated by the Tm exhibits a feasible value of binding enthalpy for physisorption during the adsorption of third and fourth H_2 molecules, whereas the first and second H_2 molecules interact via weak interactions, with the value of ΔH less than -7 kJ/mol. The Cr(III) and Co(II) chelated complexes show H2 physical adsorption, with 2-4 H_2 molecules. Mn (II) chelated complexes have ΔH values ranging from -7 to -20 kJ/mol for all adsorbed H_2 molecules. The Linker-6 chelated by the Fe (II), Ni (II), Cu (II), and Zn (II) metal atoms display a favorable value of enthalpy of adsorption after the adsorption of 2 H_2 molecules. In contrast, prior to this, H_2 molecules interact with the complexes via weak charge-induced and quadrupole interactions. Among them, Linker-6-$MnCl_2$ with four adsorbed H_2 molecules exhibits the most negative H_2 binding enthalpy value of -19.51 kJ/mol.

Linker-7: In the pristine Linker-7, only the fourth H_2 molecule interacts through physisorption; the other H_2 molecules display a binding enthalpy of less than -7 kJ/mol. Cr(III) chelated Linker-7 shows that the ΔH for the first and second adsorbed H_2 molecules is less than -7 kJ/mol. However, the third and fourth H_2 molecules exhibit an ideal value of enthalpy of adsorption. In the Mn (III) chelated complex, only the first H_2 molecule is adsorbed with a binding enthalpy of less than -7 kJ/mol. In contrast, the other three H_2 molecules exhibit weak vdW interactions with the linker. The Linker-7 chelated by the Fe (II) and Cu (II) demonstrates weak charge-induced and quadrupole interactions with the first H_2 molecule and vdW interactions with the second and third H_2 molecules. The binding enthalpy for the fourth H_2 molecule exceeds -20 kJ/mol. In Linker-7, chelated by the Co (II) and Zn (II), only the second H_2 molecule is adsorbed with the desired value of binding enthalpy. Ni (II) chelated Linker-7 exhibits the value of ΔH approximately -7 to -20 kJ/mol in the case of the first and second H_2 molecules, which exceeds -20 kJ/mol for the third and fourth H_2 molecules. Among them, Linker-7-$NiCl_2$ with the second adsorbed H_2 molecule demonstrates the most favorable enthalpy value of -18.24 kJ/mol for H_2 physisorption.

Linker-8: The pure Linker-8 exhibits the value of ΔH ranging from approximately -2.09 kJ/mol to -7.61 kJ/mol. In the case of Cr (III) chelated Linker-8, all four H_2 molecules interact with weak vdW forces. Mn (II), Fe(II), and Co(II) chelated complexes exhibit an ideal enthalpy of adsorption range of approximately -7 to -20 kJ/mol. In Linker-8-$NiCl_2$, only the first and

second H_2 molecules interact via physical adsorption. Cu (II) and Zn (II) chelated Linker-8 demonstrate favorable values of ΔH for only the second and third adsorbed H_2 molecules; the first and fourth H_2 molecules exhibit binding enthalpies of less than -7 kJ/mol and more than -20 kJ/mol, respectively. Linker-8-$FeCl_2$ with four adsorbed H_2 molecules demonstrates an optimal binding enthalpy value of -18.82 kJ/mol.

Linker-9: In the pristine Linker-9, only the fourth H_2 molecule physiosorbed on the surface, while others also have weak charged interactions with the values of ΔH less than -7 kJ/mol. The structure of Cr (III) chelated Linker-9 is thermodynamically unstable, so we have not studied H_2 adsorption in this system. Mn (III), Co(II), Cu(II), and Zn(II) chelated Linker-9 demonstrates an ideal enthalpy of adsorption for all three H_2 molecules, except for the first. Linker-9-$FeCl_2$ exhibits less than -7 kJ/mol adsorption energy for the first H_2 molecule and more than -20 kJ/mol for the fourth H_2 molecule. Only the third and fourth H_2 molecules show a weak interaction with the Fe (II)- chelated Linker-9. Linker-9-$FeCl_2$ with maximum adsorbed H_2 molecules showed a binding enthalpy value of -16.64 kJ/mol.

None of our complexes followed chemisorption, indicating that H_2 desorption will be facile in late-transition-metal-chelated complexes that require only a small amount of energy to separate H_2 from porous materials. Our theoretically calculated values of binding enthalpy are promising, suggesting the potential to synthesize practical H_2 storage materials with good volumetric and gravimetric H_2 uptake capacities.

3.3.3. H_2 uptake capacities in weight percentage

We can predict the H_2-uptake capacities of both the pure and transition-metal-chelated linkers using **equation 4.5**. The hydrogen uptake capacities of the pure linkers range from approximately 2.2 to 4 wt.%. Linker-3 has the highest H_2 uptake capacity of ~ 4 wt.%. The weight percentage H_2 uptake capacity is inversely proportional to the molecular weight of the complex with adsorbed H_2 molecules, and it is directly proportional to the number of adsorbed H_2 molecules. Consequently, the higher molecular weight of Tm-chelated linkers results in lower H_2 uptake capacities for the complexes.

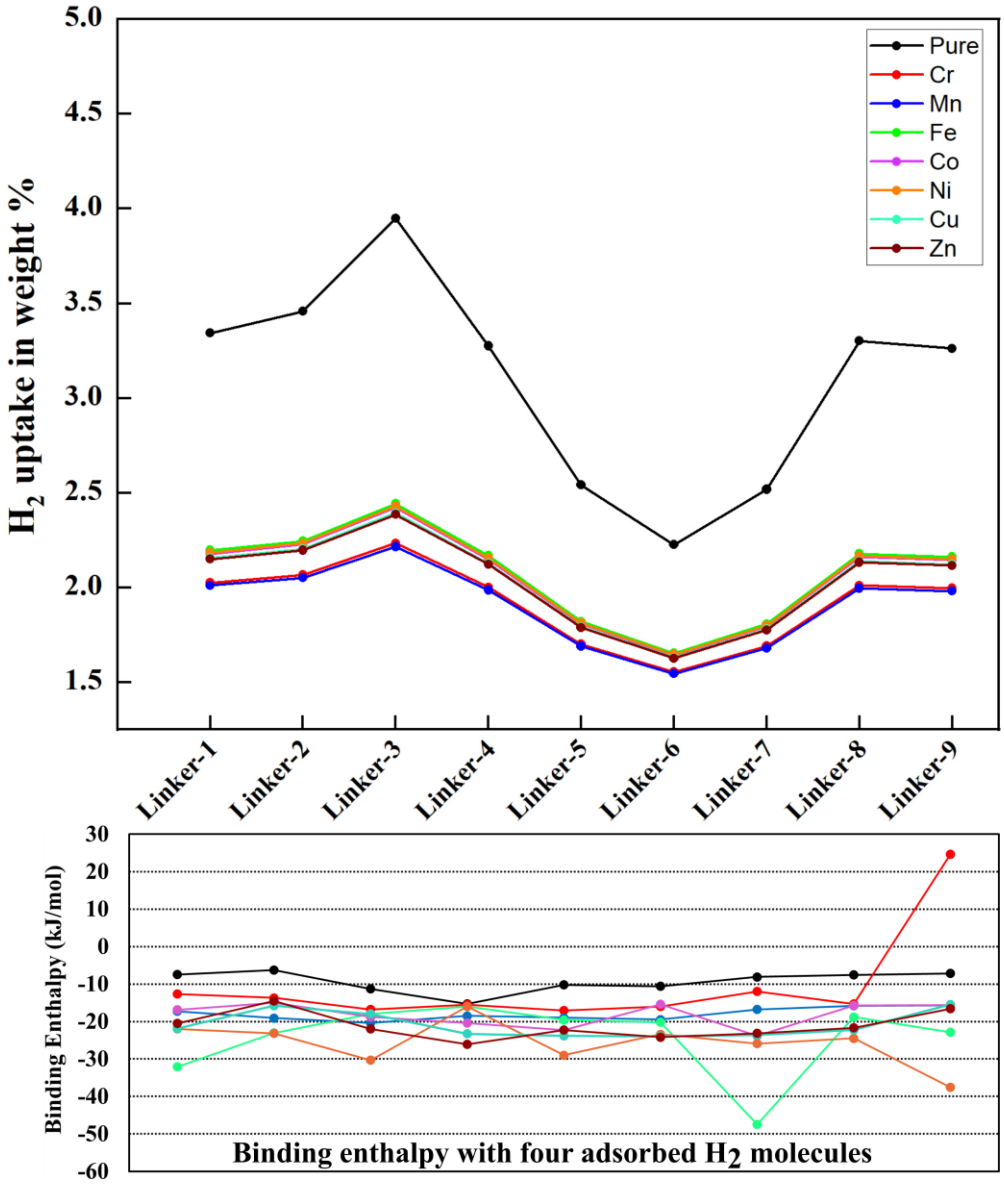

Figure 4.11. *H_2 uptake capacities (in wt.%) and binding enthalpies with maximum adsorbed H_2 molecules in both the pure and transition metal chelated linkers.*

Due to the relatively high atomic masses of transition metals, which result in higher molecular-weight complexes than the pure linkers, we have observed a significant difference in the uptake capacities of the pure and chelated linkers. The range of H_2 uptake capacities for transition-metal-chelated linkers is 1.5-2.5 wt.%. Linker-3 chelated with Cr (III), Mn (III), Fe (II), Co

(II), Ni (II), Cu (II), and Zn (II) has the highest H_2 uptake capacity ~ 2.5 wt.% among the other chelated complexes. The calculated uptake capacities of the pure complexes (4 wt.%) are close to the DOE target (gravimetric uptake of 5.5 wt.%) for 2020. Here, we have considered the adsorption of up to 4 H_2 molecules to calculate the binding enthalpy and the weight percentage uptake for both the pure and Tm-chelated linkers. **Figure 4.11** shows the calculated H_2 uptake capacities and binding enthalpies for the maximum number of adsorbed H_2 molecules in both the pure and transition-metal-chelated linkers considered in the present calculations.

The H_2 uptake capacities and binding enthalpies of our late-transition metal-chelated COF linkers surpass those of the early-transition metal complexes under the same conditions. The pure linkers have a binding enthalpy of -6.2 to -15.3 kJ/mol, and Fe-chelated Linker-7 has obtained a maximum binding enthalpy of -47.5 kJ/mol. Most of the designed complexes follow physisorption phenomena. Hence, late-transition metal-chelated COFs could be promising materials for practical H_2 storage. Zr-doped psi-graphene has set the benchmark for the highest H_2 uptake capacity at 11.3 wt.% as determined by DFT.[47] In the future, we plan to enhance our model by incorporating psi-graphene-conjugated COFs and to investigate H_2 adsorption phenomena and uptake capacities under varying temperature and pressure conditions. Our method provides theoretically calculated H_2 uptake values based on the maximum number of adsorbed H_2 molecules per chelated complex, which may differ from experimental results and practical applications of H_2 storage in COFs. However, it remains a widely used formula for predicting theoretical H_2 uptake in porous materials and generally yields results that are accurate and comparable to experimental findings.[48,49]

3.3.4. Type of interactions controlling the binding enthalpy value

We have considered five types of interactions that contribute to the binding enthalpy. EDA analysis has confirmed that electrostatic, polarization, exchange interactions, and dispersion energy are the main factors that affect the H_2 binding in organic linkers. Still, Pauli repulsions have a positive energy value and do not follow the binding enthalpy curve.

Role of electrostatic and polarization energy: Electrostatic potential is an indirect consequence of non-polar atoms. Since the H_2 molecule has no dipole moment but has a

quadrupole moment of about 2.21 × 10^{-40} cm^2. The dipole moment can be induced in the H_2 molecule by polarizing the bonding σ orbital towards one end, and it becomes moderately polarized. In transition metal cations, the H_2 molecule shows bond stretching caused by charge polarization. In this case, if H_2 coverage increases, binding enthalpy decreases. In this mechanism, the quasi-molecular form of H_2 is stored by transition metal cations.

Role of dispersion energy: Dispersion interactions are long-range forces inversely proportional to the interatomic distance. The short distance between the transition metal atom and the centroid of the H_2 molecules corresponds to the strong interaction, which increases the value of dispersion energy, and this high value of dispersion energy directly correlates with the binding enthalpy of H_2 adsorption.

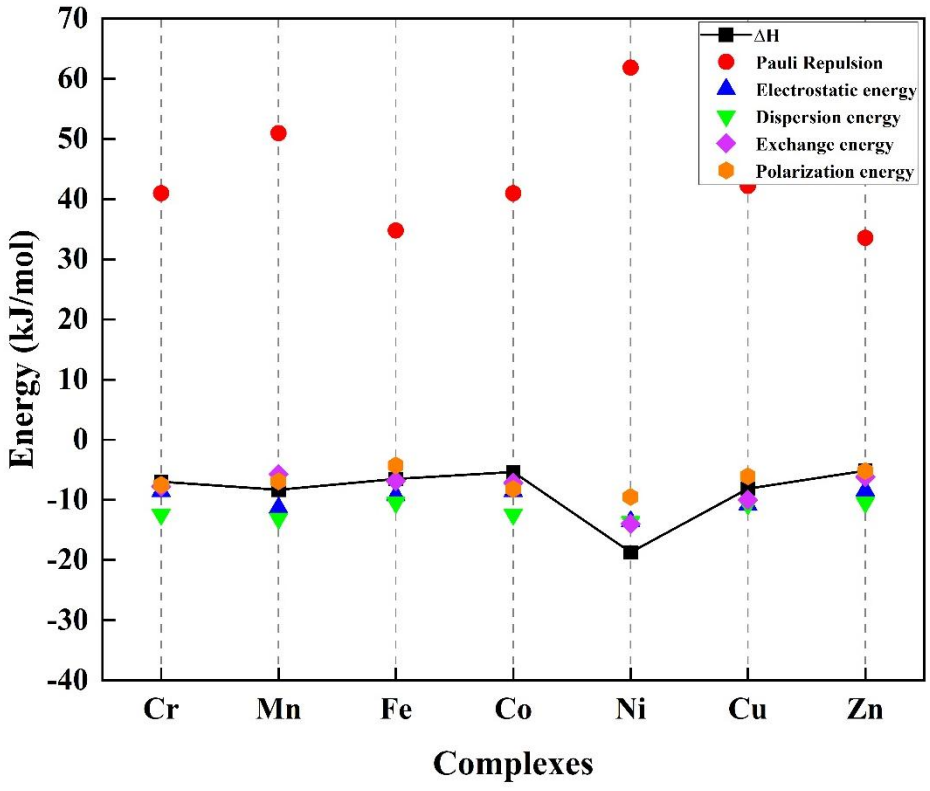

Figure 4.12. *Energy decomposition analysis and study of interactions contributing to H_2 binding in Tm-chelated linkers.*

We can conclude from **Figure 4.12** that the electrostatic, polarization, and dispersion interactions are the leading factors in the binding enthalpy of H_2 adsorption.

3.3.5. Molecular electrostatic potential mapping

Molecular electrostatic potentials (MEPs) are useful for identifying the adsorption sites. Electrophilic and nucleophilic processes involving charge transfer between adsorbed H_2 molecules and organic linkers are interpreted from MEP contours. **Figure 4.13** depicts the charge transfer phenomena from the linkers to the adsorbed H_2 molecules in Linker-3.

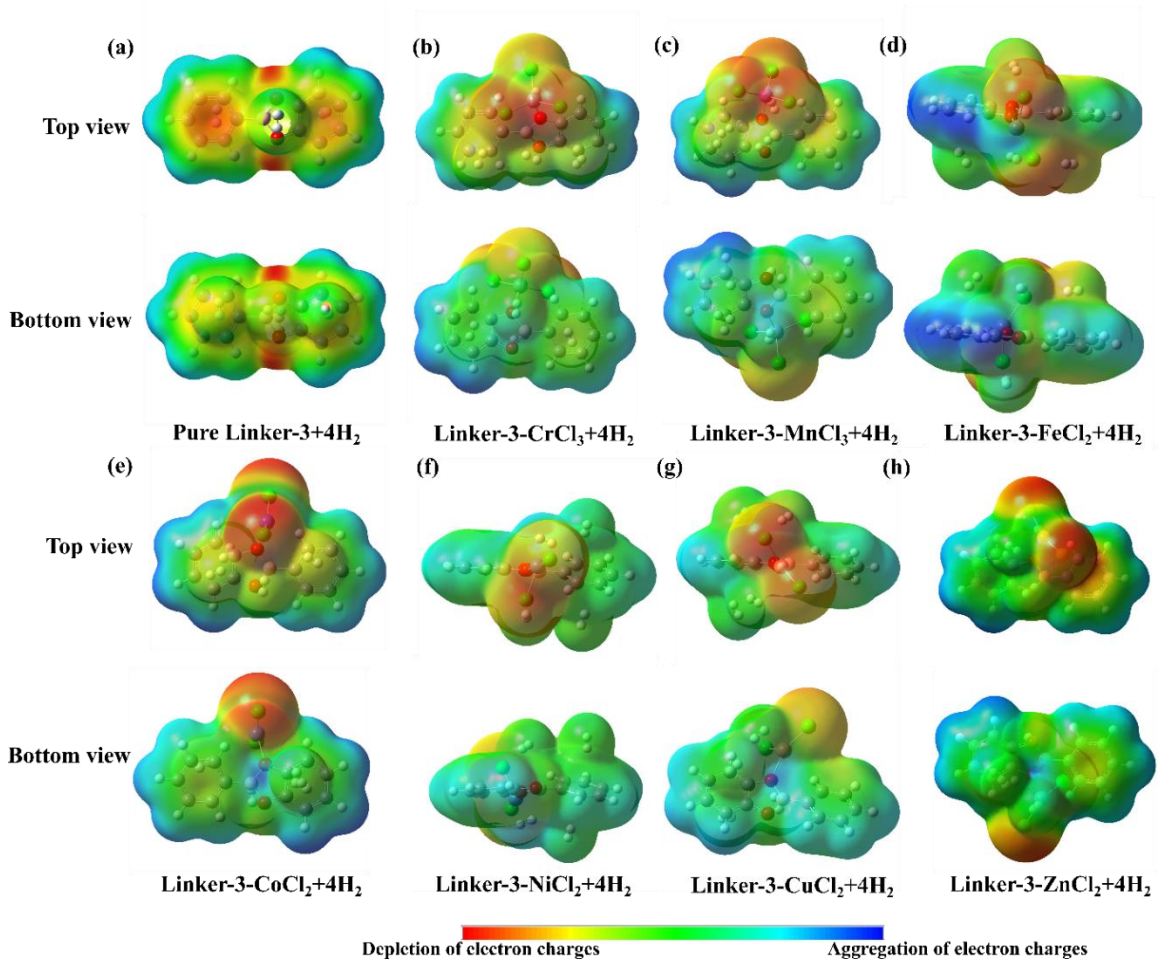

***Figure 4.13**. Molecular electrostatic potential mapping of both the pure Linker-3 and Linker-3-$TmCl_x$.*

Since electrostatic interactions play a significant role in the H_2 storage in COF materials, the potential difference reveals the presence of electrostatic or polarization interactions in H_2

binding. As COF linkers contain π-electrons and C-H bonds within their aromatic rings, they exhibit polarity. Consequently, vdW forces govern the interaction between non-polar H_2 molecules and these linkers. However, when H_2 molecules approach the linker surface, charge separation can induce a dipole moment in the H_2 molecule, leading to its adsorption. This polarization phenomenon results in a shift in the charge density within the H_2 molecule.[50]

Using Mulliken population analysis, we observed that one H atom acquired a positive charge, while the other acquired a negative charge. The positively charged atom tends to migrate towards the surface of the organic linkers. This polarization effect arises from the more electronegative heteroatoms attracting electrons from the less electronegative carbon atoms. Consequently, H_2 molecules become easily polarized by these heteroatoms. This induced polarization phenomenon confirms the weak binding of H_2 molecules with Tm-chelated organic linkers, which means that there is no chemisorption.

3.3.6. Study of global indices of reactivity and HOMO-LUMO gap

Analysis of frontier orbitals is fundamental in determining the electronic properties of any molecular framework. The electron-donating ability of any orbital is defined by the highest occupied molecular orbitals (HOMO), and the electron-withdrawing capacity is obtained by the lowest occupied molecular orbitals (LUMO). The energy gap between HOMO and LUMO helps determine the stability of any molecular structure.

***Table 4.4**. Energy values of frontier orbitals and HOMO-LUMO gap for Linker-3 with maximum adsorbed H_2 molecules. (Units are in eV)*

Complexes	E_{HOMO}	E_{LUMO}	E_g	μ	Ƞ	σ	ω
Linker-3	-6.298	-1.166	5.131	-3.732	2.565	1.282	2.715
Linker-3-$CrCl_3$	-6.717	-3.432	3.284	-5.075	1.642	0.821	7.841
Linker-3-$MnCl_3$	-6.935	-3.596	3.339	-5.266	1.669	0.834	8.304
Linker-3-$FeCl_2$	-6.759	-3.369	3.390	-5.064	1.695	0.847	7.566
Linker-3-$CoCl_2$	-7.024	-4.243	2.780	-5.633	1.390	0.695	11.413
Linker-3-$NiCl_2$	-6.947	-3.486	3.460	-5.217	1.730	0.865	7.864
Linker-3-$CuCl_2$	-7.087	-1.817	5.269	-4.452	2.635	1.317	3.762
Linker-3-$ZnCl_2$	-6.907	-1.651	5.256	-4.279	2.628	1.314	3.484

The larger HOMO-LUMO energy gap indicates greater stability in the complexes. In other words, a smaller HOMO-LUMO gap means more effortless electron transfer and less stability of the complexes. According to our study, Linker-3 shows the most favorable value of H_2 adsorption energy. Hence, we have represented the HOMO-LUMO gaps for both the pure Linker-3 and the Tm-chelated Linker-3. **Table 4.4** shows the energy values of frontier orbitals and the HOMO-LUMO gap of Linker-3 with maximum adsorbed H_2 molecules. The higher the value of E_g, the greater the electron donor capacity and the greater the charge transfer at the molecular surface. Linker-3 with Cu (II) chelation has a maximum energy gap of 5.26 eV. Similar results were obtained with Linker-3 chelated to Zn (II). The high value of the HOMO-LUMO gap showed the conductivity of the material because conductivity is directly proportional to $e^{-E_g/kT}$, where E_g is the HOMO-LUMO gap. Linker-3-$CuCl_2$ is the most stable, and Linker-3-$CoCl_2$ is the least stable complex. **Figure 4.14** represents the HOMO and LUMO in both the pure Linker-3 and Tm-chelated Linker-3. There is a significant overlap of the ***s***-orbital of H_2 molecules with ***d***-orbitals of Tm atoms in the linker-$TmCl_x$ complexes, proving the strong binding of H_2 molecules on the surface of chelated linkers.

By employing Koopman's theorem[51]Global indices of reactivity like global hardness (Ƞ), softness parameter (σ), ionization potential (μ), and electrophilicity (ω) were calculated using the energy of frontier orbitals.[52]

$$\mu = \frac{HOMO+LUMO}{2} \quad (4.6)$$

$$\eta = \frac{HOMO-LUMO}{2} \quad (4.7)$$

$$\omega = \frac{\mu^2}{2\eta} \quad (4.8)$$

$$\sigma = \frac{1}{2\eta} \quad (4.9)$$

The calculated values of global reactivity indices are provided in **Table 4.4**. Chemical hardness (η) and softness (σ) are the essential parameters for predicting the behavior of complexes. This value suggests that computationally designed molecular complexes are stable, exhibit high electrophilicity, and exhibit minimal softness. The excellent value of the chemical potential indicates that these computationally designed Tm-chelated linkers might participate in charge-transfer reactions.

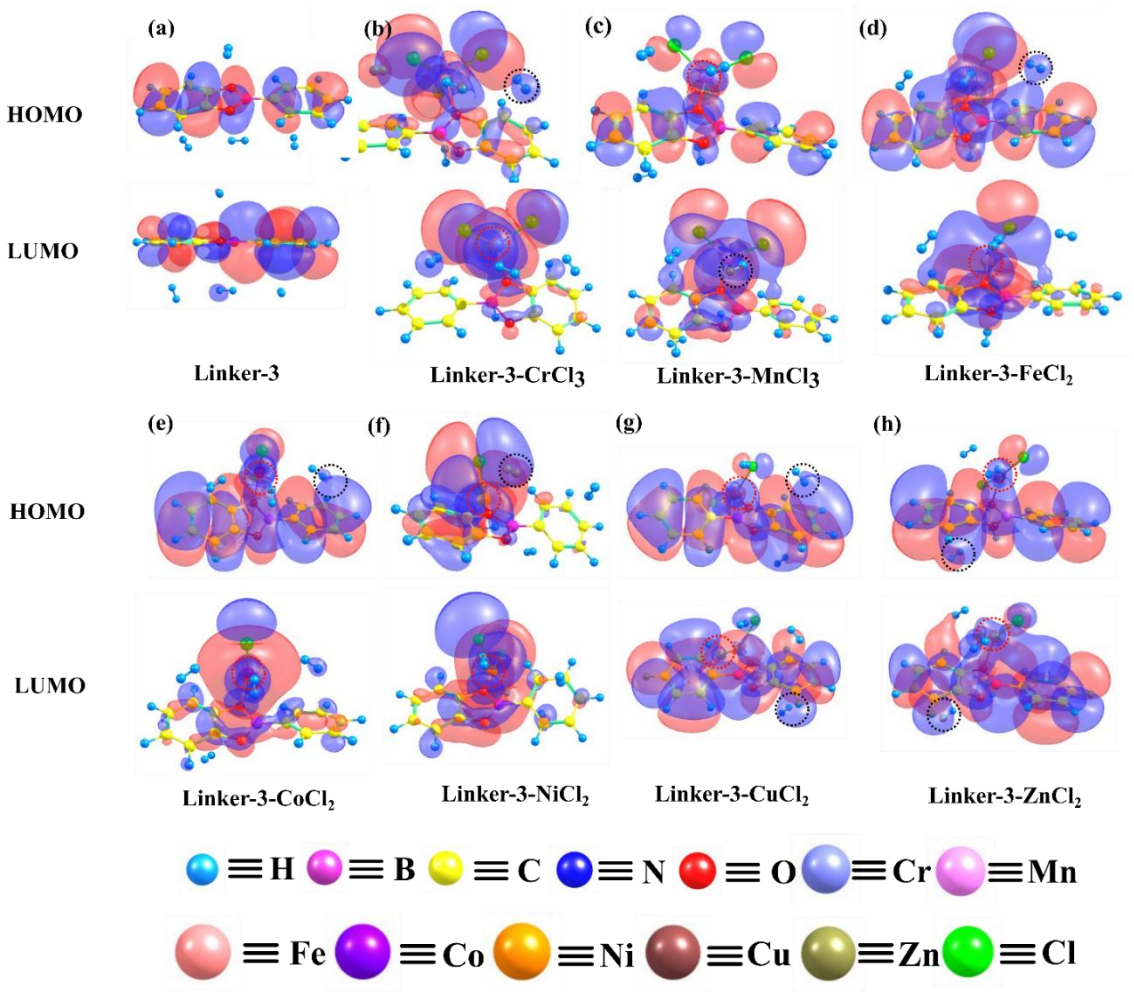

Figure 4.14. *HOMO and LUMO of both the pure Linker-3 and the transition metal chelated Linker-3. The dotted black circles show the overlapping of the* ***s****-orbital of the H atom and the 2****p****-orbital of atoms in organic linkers. The dotted red circles show the overlapping of the* ***s****-orbital of the H atom and the 3****d****-orbital of transition metal atoms in* $TmCl_x$.

4.4. Conclusions

Our study has employed non-periodic molecular modeling to explore H_2 adsorption in the transition metal (Cr to Zn) chelated ligands of COF materials. We have thoroughly examined the intermolecular interactions that contribute to hydrogen binding. The EDA approach reveals that dispersion, electrostatic, and polarization interactions contribute to binding enthalpy. The theoretically calculated H_2 uptake capacity was approximately 1.5-4 wt% for both the pure and chelated linkers. These Tm-chelated COF linkers exhibit promising potential to meet the

USDOE target for safe, cost-effective H_2 storage. Our findings suggest that the induced dipole moment in the H_2 molecule arises from charge transfer between the transition metal and the linkers, which accounts for the weak binding of H_2. Most of the Tm-chelated complexes exhibit ideal values of heat of physisorption, with some falling between physisorption and chemisorption ranges. Notably, Mn (III), Ni (II), and Fe (II) chelated complexes display the most negative values of heat of physisorption. This study concludes that the late-transition-metal-chelated COF linkers hold promise as H_2 storage materials under ambient conditions.

4.5. References

[1] S. Bordiga, J.G. Vitillo, G. Ricchiardi, L. Regli, D. Cocina, A. Zecchina, B. Arstad, M. Bjørgen, J. Hafizovic, Journal of Physical Chemistry B 109(2005) 18237–18242.

[2] J.L.C. Rowsell, O.M. Yaghi, Journal of the American Chemical Society 128(2006) 1304–1315.

[3] D. Cao, J. Lan, W. Wang, B. Smit, Angewandte Chemie International Edition 48(2009) 4730–4733.

[4] S. Pakhira, J.L. Mendoza-Cortes, Journal of Physical Chemistry C 124(2020) 6454–646.

[5] N. Sinha, S. Pakhira, Molecular System Design & Engineering 7(2022) 577–591.

[6] H. M. El-Kaderi, J. R. Hunt, J. L. Mendoza-Cortés, A. P. Côté, R. E. Taylor, M. O'Keeffe, O. M. Yaghi, Science 316(2007) 268–273.

[7] S. K. Bhatia, A. L. Myers, Langmuir 22(2006) 1688–1700.

[8] M. Jordá-Beneyto, F. Suárez-García, D. Lozano-Castelló, D. Cazorla-Amorós, A. Linares-Solano, Carbon 45(2007) 293–303.

[9] A. A. Aduenko, A. Murray, J.L. Mendoza-Cortes, ACS Applied Materials & Interfaces 10(2018) 13244–13251.

[10] A. D. Becke, Journal of Chemical Physics 98(1993) 5648–5652.

[11] H. Zhang, X. Zheng, L. Yang, E. Ganz, Inorganic Chemistry 60(2021) 2656–2662.

[12] H. Zhang, L. Yang, E. Ganz, Langmuir 36(2020) 14104–14112.

[13] H. Zhang, L. Yang, E. Ganz, ACS Sustainable Chemical & Engineering 8(2020) 14616–14626.

[14] H. Joshi, N. Sinha, K. Parveen, S. Pakhira, Energy and Fuels 37(2023) 19771–19784.

[15] H. Zhang, L. M. Yang, H. Pan, E. Ganz, Physical Chemistry Chemical Physics 22(2020) 24614–24623.

[16] H. Zhang, L. M. Yang, E. Ganz, ACS Applied Materials & Interfaces 12(2020) 18533–18540.

[17] LL. M. Yang, G. Y. Fang, J. Ma, E. Ganz, S. S. Han, Crystal Growth & Designing 14(2014) 2532–2541.

[18] L. M. Yang, P. Vajeeston, P. Ravindran, H. Fjellvåg, M. Tilset, Inorganic Chemistry 49(2010) 10283–10290.

[19] L. M. Yang, G. Y. Fang, J. Ma, R. Pushpa, E. Ganz, Physical Chemistry Chemical Physics 18(2016) 32319–32330.

[20] S. Pakhira, J. L. Mendoza-Cortes, Physical Chemistry Chemical Physics 21(2019) 8785–8796.

[21] S. Pakhira, K. P. Lucht, J. L. Mendoza-Cortes, Journal of Physical Chemistry C 121(2017) 21160–21170.

[22] Z. Ke, Y. Cheng, S. Yang, F. Li, L. Ding, International Journal of Hydrogen Energy 42 (2017) 11461–11468.

[23] Y. Pramudya, J.L. Mendoza-Cortes, Journal of the American Chemical Society 138(2016) 15204–15213.

[24] M. El Khatabi, M. Bhihi, S. Naji, H. Labrim, A. Benyoussef, A. El Kenz, M. Loulidi,

International Journal of Hydrogen Energy 41 (2016) 4712–4718.

[25] F. Bakhshi, N. Farhadian, International Journal of Hydrogen Energy 43 (2018) 8355–8364.

[26] US Department of Energy, U.S Drive (2017) 1–29.

[27] L. Yuan, D. Wang, J. Gong, C. Zhang, L. Zhang, M. Zhang, Chemical Physics Letters 726 (2019) 57–61.

[28] L. Yuan, L. Kang, Y. Chen, D. Wang, J. Gong, C. Wang, M. Zhang, X. Wu, Applied Surface Science 434 (2018) 843–849.

[29] X. Zou, G. Zhou, W. Duan, K. Choi, J. Ihm, Journal of Physical Chemistry C 114(2010) 13402–13407.

[30] E. Klontzas, E. Tylianakis, G.E. Froudakis, Journal of Physical Chemistry Letters 2(2011) 1824–1830.

[31] S. Grimme, J. Antony, S. Ehrlich, H. Krieg, Journal of Chemical Physics 132 (2010) 154104.

[32] J.G. Hill, International Journal of Quantum Chemistry 113 (2013) 21–34.

[33] P.J. Hay, W.R. Wadt, Journal of Chemical Physics 283(1985) 270–283.

[34] D.J. Frisch, M. J.; Trucks, G. W.; Schlegel, H. B.; Scuseria, G. E.; Robb, M. A.; Cheeseman, J. R.; Scalmani, G.; Barone, V.; Petersson, G. A.; Nakatsuji, H.; Li, X.; Caricato, M.; Marenich, A. V.; Bloino, J.; Janesko, B. G.; Gomperts, R.; Mennucci, B.; Hratch, Gaussian, Inc., Wallingford CT, 2019.

[35] Zhurko, G. A.; Zhurko D. A. ChemCraft, Tool for Treatment of Chemical Data. http://www.chemcraftprog.com.

[36] M. W. Schmidt, K. K. Baldridge, J. A. Boatz, S. T. Elbert, M. S. Gordon, J. H. Jensen, S. Koseki, N. Matsunaga, K. A. Nguyen, S. Su, T. L. Windus, M. Dupuis, J. A.

Montgomery, Journal of Computational Chemistry 14(1993) 1347–1363.

[37] R. Dovesi, A. Erba, R. Orlando, C. M. Zicovich-Wilson, B. Civalleri, L. Maschio, M. Rérat, S. Casassa, J. Baima, S. Salustro, B. Kirtman, Wiley Interdisciplinary Reviews: Computational Molecular Science 8(2018) 1–27.

[38] M.F. Peintinger, D.V. Oliveira, T. Bredow, Journal of Computational Chemistry 34 (2013) 451–459.

[39] H. J. M. J. D. Pack, Physical Review B 13(1976) 5188–5192.

[40] K. Momma, F. Izumi, Journal of Applied Crystallography 44 (2011) 1272–1276.

[41] B. Chakraborty, P. Mane, A. Vaidyanathan, International Journal of Hydrogen Energy 47 (2022) 41878–41890.

[42] R.C. Lochan, M. Head-gordon, Physical Chemistry Chemical Physics 8(2006) 1357–1370.

[43] R. Chakraborty, K.M. Carsch, D.E. Jaramillo, Y. Yabuuchi, H. Furukawa, J.R. Long, M. Head-gordon, Journal of Physical Chemistry Letters 13(2022) 10471–10478.

[44] R. Chakraborty, J.J. Talbot, H. Shen, Y. Yabuuchi, K.M. Carsch, H.Z.H. Jiang, H. Furukawa, J.R. Long, M. Head-gordon, Physical Chemistry Chemical Physics 26(2024) 6490–6511.

[45] H. Joshi, S. Pakhira, International Journal of Hydrogen Energy 79 (2025) 1139–1154.

[46] B. Kiran, A. K. Kandalam, P. Jena, Journal of Chemical Physics 124(2006) 224703.

[47] H.T. Nair, P.K. Jha, B. Chakraborty, International Journal of Hydrogen Energy 48 (2022) 37860–37871.

[48] L. Wang, Y. Sun, H. Sun, Faraday Discussions 151(2011) 143–156.

[49] I. Cabria, International Journal of Hydrogen Energy 50 (2025) 160–177.

[50] Y. Zhang, X. Cheng, International Journal of Hydrogen Energy 43 (2018) 15338–15347.

[51] A. Mubarik, N. Rasool, M.A. Hashmi, A. Mansha, M. Zubair, M.R. Shaik, M.A.F. Sharaf, E.M. Awwad, A. Abdelgawad, Crystals 11 (2021) 211.

[52] M.R.S.A. Janjua, Journal of Physics and Chemistry of Solids 160 (2022) 110352.

CHAPTER 5

H_2 Storage Capacities in Nanoporous M_2(*m*-dobdc) Metal-Organic Frameworks at Near Ambient Temperatures

Green hydrogen presents a cleaner alternative to petroleum-based energy, with onboard storage challenges addressed by Metal-Organic Frameworks (MOFs). This chapter describes the study of M_2(m-dobdc) MOFs (M = Mn, Fe, Co, and Ni) towards H_2-storage by using Grand Canonical Monte Carlo simulations (GCMC) at five distinct temperatures (77 K, 160 K, 198 K, 233 K, and 298 K) and pressures 1–100 bar. The Fe_2(m-dobdc) MOF achieves a promising volumetric H_2 storage capacity of 51.2 g/L under cryogenic conditions, meeting the target of the Department of Energy, United States of America (USDOE), while the calculated value of the gravimetric uptake is 4.2 wt.%, which approaches the USDOE 2025 target of 5.5 wt.%. The M_2(m-dobdc) MOF series reflects exceptional volumetric uptake capacities at room temperature, ranging from 11.0-12.3 g/L, while gravimetric capacities are moderate, indicating key challenges in physisorption-based nanoporous materials at ambient conditions. Density functional theory (DFT) calculations reveal the enthalpy of H_2 adsorption ranging from -15 to -18 kJ/mol in this M_2(m-dobdc) MOFs series, confirming the reversible physisorption phenomenon. Our results highlight the potential of M_2(m-dobdc) MOFs for mobile H_2-storage applications, with deliverable volumetric capacities ranging from 36.3 g/L to 40.8 g/L and gravimetric uptake ranging from 2.7 to 3.4 wt.% under a temperature-pressure swing range (77 K/100 bar to 160 K/5 bar). The present investigation indicates that the M_2(m-dobdc) MOFs have advanced toward the USDOE target and promise to meet the practical onboard hydrogen storage requirements for automobile applications. Their balanced gravimetric and volumetric capacities make them promising candidates for near-future implementation in green energy systems.

5.1. Introduction

Carbon-based fossil fuels are recognized as the primary contributors to climate change and environmental pollution, and these fossil fuels satisfy most of the human energy requirements for several decades. Their combustion results in the release of carbon into the Earth's atmosphere (carbon that was stored hundreds of millions of years ago), and climate change and its primary root cause, the burning of fossil fuels, are arguably the leading cause of avoidable morbidity and mortality worldwide, emitting greenhouse gases during the combustion of fossil fuels. Replacing carbon-based fossil fuels like coal and petroleum with eco-friendly fuels is essential to reducing CO_2 levels in the atmosphere.[1] Green hydrogen is a clean energy carrier with high energy density and zero toxic gas emissions.[2,3] However, its volumetric energy density is very low compared to conventional fuels, which challenges its feasibility.[4] H_2 gas can be compressed to very high pressure or liquified at cryogenic temperature for storage and practical applications. Liquid and gaseous state H_2-storage requires extra safety measures, and it is costly for storage and transportation.[5–7]

H_2 adsorption is a potential high-density solid-state H_2-storage strategy at ambient conditions.[8] The structure and properties of the adsorbent material influence the efficiency of H_2-storage. Traditionally, metal oxides and activated carbons have been used for H_2-storage as they are relatively easy to synthesize commercially.[8] However, a new efficient H_2 adsorbent material is required to achieve a satisfactory volumetric energy density. In this context, MOFs are known for their excellent potential as gas storage and separation materials.[9,10] MOFs are composed of linking metal ions or clusters with organic molecules;[8] and they are highly tunable in terms of surface area, pore geometry, and volume.[8] The precise crystalline structure of MOFs enables computational studies of host-guest interactions, which provide fundamental insights into rational material design.[11]

In 2003, Yaghi and coworkers experimentally studied H_2 adsorption in MOF-5 at high pressures of up to 20 bar.[12] Since then, numerous MOFs have been explored for H_2-storage and gas separation, and significant progress has been made in this field.[13–16] The usable storage capacities of some highly porous MOFs, such as MOF-5 and IRMOF-20, are 4.5 wt.% and 5.7 wt.%, respectively, at 77 K with the pressure swing between 5 and 100 bars.[17] These observed H_2 uptake capacities outperform conventional porous materials such as activated

carbons and zeolites.[17] In fuel cell vehicles, the minimum usable pressure for onboard hydrogen storage is 5 bar, and the adsorption capacity between 5 and 100 bar is considered a usable working capacity or deliverable capacity.[8] The US Department of Energy (USDOE) has set gravimetric and volumetric uptake capacity targets of 5.5 wt.% and 40 g/L for 2025, with an ultimate target of 6.5 wt.% and 50 g/L.[18] While many nanoporous MOFs have achieved a high gravimetric working capacity that meets the DOE target, reaching a high volumetric working capacity remains a significant challenge.[19,20]

Recently, Long and co-workers experimentally synthesized two types of metal-organic frameworks, M_2(*m*-dobdc) and M_2(dobdc), where (M = Ni and Co) and [*m*-dobdc^{4-}) refer to 4,6-dioxido-1,3-benzenedicarboxylate]. The most notable finding was the exceptional hydrogen storage capacity of Ni_2(*m*-dobdc), achieving a deliverable volumetric capacity of 11.0 g/L between 100 and 5 bar at 298 K.[4] In their study, they experimentally observed the H_2 adsorption isotherms at different conditions by varying temperature and pressure. Similar MOF structures with different metal atoms (Fe and Mn) were synthesized by Yadav *et al.,* and they experimentally studied H_2 adsorption isotherms in Fe_2(*m*-dobdc) and Mn_2(*m*-dobdc).[21] Their experimental study revealed that the Fe_2(*m*-dobdc) MOF can store 4.31 wt.% of hydrogen at 77 K and 100 atm. pressure. At the same time, Yadav *et al.* claimed that the Mn_2(*m*-dobdc) MOF has a higher hydrogen storage capacity of 8.21 wt.% under identical temperature and pressure conditions.[21] Both experimental works suggested that the nanoporous M_2(*m*-dobdc) MOFs are the most efficient material for high H_2-storage, and their exceptional volumetric and gravimetric uptake capacities are close to the USDOE target for 2025.

These findings highlight the necessity of in-depth research and further investigation through GCMC simulations. Relying on experiments can be challenging due to the complex interplay of various properties, which affects the synthesis or modification of adsorbents and their gas storage properties. Hence, we employed Grand Canonical Monte Carlo (GCMC) simulations to overcome these limitations. We studied the H_2 adsorption isotherms and reported the storage and deliverable capacities in the M_2(*m*-dobdc) MOFs at different temperature-pressure conditions. GCMC is a suitable approach for simulating the equilibrium state of hydrogen physisorption when MOF structures are attached to a hydrogen reservoir with well-defined pressure and temperature. We also performed the Density Functional Theory (DFT)

calculations to reveal the H_2 binding mechanism at the open metal sites present in these nanoporous MOFs.

5.2. Theory, Computational Methods, and Material Description

5.2.1. Theory and Computational Details

Grand Canonical Monte Carlo Simulations were conducted to predict the H_2 adsorption isotherms at 77 K, 160 K, 198 K, 233 K, and 298 K in M_2(*m*-dobdc) MOFs by using the RASPA 2.0 package.[22] The simulations used insertion, rotation, swap, and translation moves with equal probability. The number of initialization cycles was 5×10^4 steps, followed by 5×10^4 production steps. During the simulation process, all MOF atoms remained stationary, while H_2 molecules could move freely within the framework structure. The partial atomic charges for the framework atoms were calculated by using the Charge Equilibration (QE_q) method[23] as implemented in RASPA 2.0. This QE_q method is widely used in studies to calculate the partial atomic charges and ensures self-consistent charge distributions by minimizing the electrostatic energy of the system under periodic boundary conditions, with Ewald summation, which handles long-range interactions.[24,25] The calculated partial charges for each atom type are provided in

***Table 5.1**. Calculated partial charges (expressed in electronic charge e^-) and force field (FF) parameters for the chemically distinct atoms in the M_2(m-dobdc) MOFs (M = Mn, Fe, Co and Ni)*

Atom	Mn_2(*m*-dobdc)	Fe_2(*m*-dobdc)	Co_2(*m*-dobdc)	Ni_2(*m*-dobdc)	ε (K)	σ (Å)
Metal (M4)	1.062	0.922	0.901	1.235	Mn=Fe=6.54 Ni=7.54, Co=7.04	Mn=2.63 Fe=2.59 Co=2.55 Ni=2.52
C1	0.396	0.352	0.383	0.393	47.85	3.47
C2	-0.386	-0.336	-0.359	-0.409	47.85	3.47
C3	0.523	0.493	0.475	0.558	47.85	3.47
O5	-0.530	-0.462	-0.496	-0.590	48.15	3.03
O6	-0.584	-0.544	-0.502	-0.632	48.15	3.03
O7	-0.474	-0.437	-0.416	-0.551	48.15	3.03

C8	-0.366	-0.317	-0.321	-0.35	47.85	3.47
H9	0.133	0.128	0.117	0.126	7.64	2.84
C10	0.245	0.212	0.239	0.263	47.85	3.47
H11	-0.014	-0.001	-0.007	-0.016	7.64	2.84

A Lennard-Jones (LJ) 6-12 potential[26] plus Coulomb potential was used to describe the interactions between the hydrogen molecules and MOF atoms (Mn, Fe, Co, Ni, O, C, and H) presented by:

$$U(ij) = 4\varepsilon_{ij}\left[\left(\frac{\sigma_{ij}}{r_{ij}}\right)^{12} - \left(\frac{\sigma_{ij}}{r_{ij}}\right)^{6}\right] + \frac{1}{4\pi\varepsilon_0}\frac{q_i q_j}{r_{ij}} \qquad (5.1)$$

Where r_{ij} is the distance between 'i^{th}' and 'j^{th}' atoms in the system, q_i is the partial charge of the i^{th} atom, ε_0 is the dielectric constant of free space, ε_{ij} is the potential well depth and σ_{ij} is the potential well diameter.

The mixing of force field parameters was done by using the Lorentz-Berthelot mixing rule for a pair of unlike atoms as follows:[27]

$$\varepsilon_{ij} = \sqrt{\varepsilon_i}\varepsilon_j, \ \sigma_{ij} = \frac{1}{2}(\sigma_i + \sigma_j) \qquad (5.2)$$

Where ε_i and σ_i for H, C, O, and B were taken from the DREIDING force field parameters available in the RASPA 2.0 package[22], and the cut-off radius for the LJ interaction is 12.0 Å. The potential parameters for the framework atoms in MOFs were taken from the standard UFF force fields.[27–29] Universal Force Field (UFF) remains one of the most widely adopted force fields in the literature for H_2 adsorption studies in nanoporous MOFs[30–32], especially when dealing with transition metals such as Ni, Fe, Co, and Mn, for which specialized force fields like UFF4MOF, or MOF-FF have not been comprehensively developed non-bonded parameters.[33,34] We included the Feynman-Hibbs (FH) quantum correction[35] in our simulations at cryogenic temperatures. This semi-classical correction appropriately modifies the LJ potential to account for the delocalized nature of the H_2 molecule at low temperatures.

We used two well-established H_2 models: the Buch model[36] and the Darkrim-Levesque model (DL)[37] to ensure accurate and reliable modelling of H_2 adsorption. In the DL model, the H_2 molecules were described using a three-site rigid model with an H–H bond length of 0.741 Å. A Lennard-Jones site (σ = 2.958 Å and ε = 36.7 K) was placed at the H_2 center of mass, and a negative charge of −0.936 on the center of mass was balanced by positive charges of 0.468 on the H nuclei. These models have been widely applied in classical GCMC simulations for H_2 storage applications in nanoporous MOFs.[38] The LJ parameters for these H_2 models are explicitly listed in **Table 5.2.**

Table 5.2. *Parameters used to characterize the H_2 potential used in this work: Buch model, Darkrim-Levesque (DL) model. COM corresponds to the center-of-mass site, and H corresponds to the atomic locations of the hydrogen atoms.*

Model	Atomic Site	r (Å)	ε (K)	σ (Å)	q (e-)
Buch	COM	0.00	34.200	2.960	0.00
DL	COM	0.00	36.70	2.958	-0.936
	H	0.37	0.00	0.00	0.468

All the simulations were carried out on unit cells using 3D periodic boundary conditions, and the adsorption isotherm curves were derived from GCMC simulation data. All 3D equilibrium structures of MOFs were visualized by VESTA software.[39] The snapshots of H_2 adsorption in MOFs were captured by iRASPA software.[40]

The conversions from loading (mg of H_2 per g of framework) to wt.% were performed by using the standard expression:

$$\text{Gravimetric Uptake (in wt.\%)} = \frac{\text{mass of adsorbed } H_2}{\text{mass of framework}} \times 100 \qquad (5.3)$$

This equation number (5.3) expresses that the denominator includes only the mass of the adsorbent. This is the conventional practice in both experimental and simulation-based H_2 storage studies in porous materials.[19]

The volumetric uptake capacity in g/L is defined as:[41]

$$V_c = \frac{n_{ads\,mH_2}}{V_{MOF}} \qquad (5.4)$$

Molecular models of M_2(*m*-dobdc) MOFs were designed to calculate the values of enthalpy of adsorption. Geometry optimizations were performed using the B3LYP functional[42] with Grimme's -D3 dispersion correction[43] incorporated to account for weak van der Waals (vdW) interactions. B3LYP functional with the -D3 correction has been widely used to study H_2 binding in transition-metal molecular complexes.[44] The cc-pVTZ basis set[45] was used to define the atomic orbitals in the molecular models of subject MOFs. Gaussian 16 suite code[46] was used to perform DFT calculations, and ChemCraft software[47] was used to visualize the equilibrium molecular structures. The enthalpy of adsorption ΔH was calculated by employing the following expression:[2]

$$\Delta H = H_{MOF+H_2} - \left(H_{MOF} + H_{H_2}\right) \qquad (5.5)$$

where H_{MOF+H_2}, H_{MOF}, H_{H_2} are the binding enthalpies of the MOF with adsorbed H_2, pristine MOF, and free H_2 molecules, respectively.

5.2.2. Properties of MOF Materials

We selected transition metal cluster-based MOFs with transition metal atoms (Mn, Fe, Co, and Ni) with a ligand structure [*m*dobdc^{4-}) means 4,6-dioxido-1,3-benzenedicarboxylate]. These MOFs were already experimentally synthesized, and H_2 adsorption isotherms have been observed experimentally at varying temperature and pressure conditions.[4,21,22] In the present manuscript, we used computational methods to investigate the equilibrium structures of the MOFs and investigated their H_2 adsorption isotherms, H_2 storage capacities, deliverable capacities and compared them with the previously obtained experimental findings. We utilized CRYSTAL17[48] software to perform structural relaxation and to get the equilibrium structures of the 3D M_2(*m*-dobdc) MOFs. **The crystallographic information files (.cif) of these MOFs are provided in the Appendix.** Our computational approach employed Density Functional Theory (DFT) calculations using the B3LYP exchange-correlation functional,[44] complemented by Grimme's dispersion correction parameters.[43] To accurately represent the

electronic structure, we implemented a triple-zeta valence polarizable (TZVP) basis set, which precisely defined the atomic orbital characteristics of all atoms present in the MOF structure.[49] **Figure 5.1** represents the equilibrium structures of M_2(*m*-dobdc) MOF materials. The pore-size distribution can be calculated geometrically in RASPA-2.0 [22] using the Gelb-Gubbins method.[50,51] The cumulative pore volume curve is obtained by enclosing each point in the void volume with the largest sphere that does not intersect with framework atoms. Our calculated pore size distribution curve is represented in Figure 1(e), which illustrates that the Mn_2(*m*-dobdc), Fe_2(*m*-dobdc), Co_2(*m*-dobdc), and Ni_2(*m*-dobdc) MOFs have pore diameters 10.73, 10.87, 10.77, and 10.73 Å, respectively.

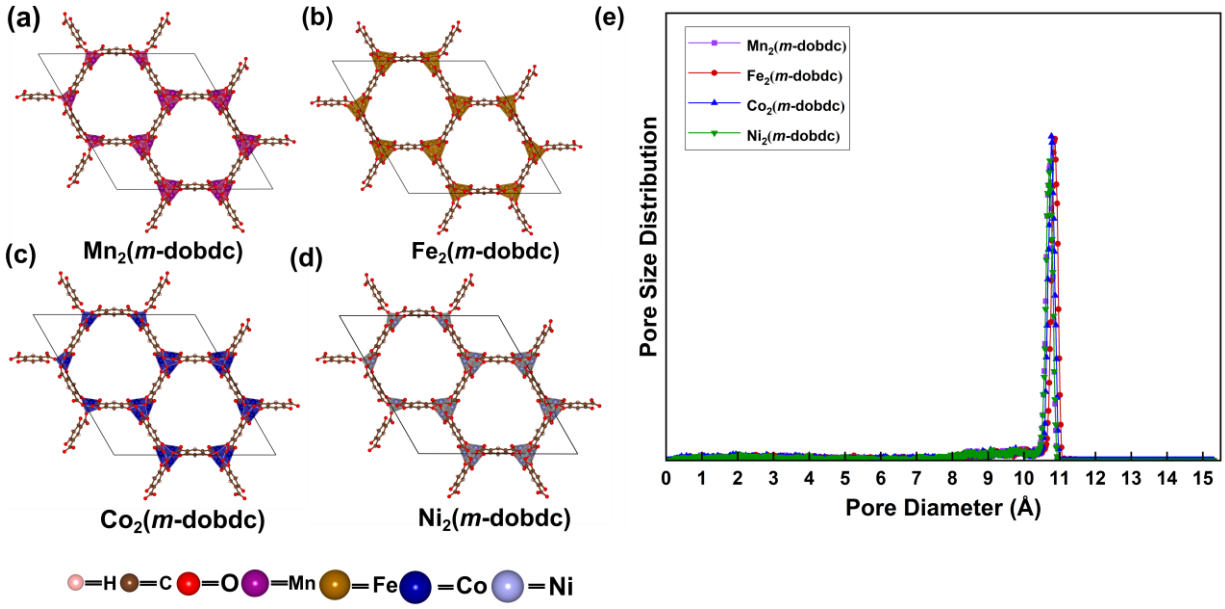

Figure 5.1. *Equilibrium structures of M_2(m-dobdc) MOFs and their pore diameter. (a) Mn_2(m-dobdc), (b) Fe_2(m-dobdc), (c) Co_2(m-dobdc), (d) Ni_2(m-dobdc) and (e) pore-size distribution (PSD) curve.*

The cumulative pore volume curve is obtained by enclosing each point in the void volume with the largest sphere that does not intersect with framework atoms. Our calculated pore-size distribution curve is shown in Figure 5.1(e), which indicates that the Mn2(m-dobdc), Fe_2(*m*-dobdc), Co_2(*m*-dobdc), and Ni_2(*m*-dobdc) MOFs have pore diameters of 10.73, 10.87, 10.77, and 10.73 Å, respectively. Previous studies have reported that hydrogen storage at 77 K predominantly depends on micropores in the material.[52] Earlier, various microporous 3D MOFs have been synthesized, and H_2 adsorption isotherms were observed for those MOFs.

Experimental findings suggest that these 3D MOFs performed exceptionally well towards H_2-storage due to their microporous nature.[12,53,54] M_2(*m*-dobdc) series is also categorized in the microporous range, so these M_2(*m*-dobdc) MOFs could be expected to adsorb more H_2 at 77 K and high pressures.

Table 5.3. *The calculated surface area, pore volume, framework mass, and density of the subject MOF materials, M_2(m-dobdc). (The bold values in the surface area represent the experimentally calculated surface area taken from literature sources)[13]*

MOF	Surface Area (m^2/g)	Pore Volume (cm^3/g)	Framework Mass (g/mol)	Density (cm^3/g)
Mn_2(*m*-dobdc)	1444.62/**1741**	0.53	2735.76	0.85
Fe_2(*m*-dobdc)	1500.03/**1624**	0.54	2751.32	0.87
Co_2(*m*-dobdc)	1423.90/**1504**	0.52	2806.90	0.84
Ni_2(*m*-dobdc)	1410.33/**1592**	0.51	2803.36	0.83

Earlier, the BET surface areas of M_2(*m*-dobdc) were measured experimentally using H_2 as a probe molecule at 77 K.[13] In our study, the geometric area of MOFs was calculated using the Monte Carlo method with a 2.958 Å probe (in the present investigation), which is equal to the diameter of a hydrogen atom at 77 K. We observed that the Ni_2(*m*-dobdc) MOF has the lowest value of surface area about 1410.33 m^2/g and similarly, the Fe_2(*m*-dobdc) MOF has the highest value of surface area about 1500.03 m^2/g. It was found that Fe_2(*m*-dobdc) MOF has the highest pore volume, about 0.54 cm^3/g. The lowest calculated pore volume was 0.51 cm^3/g for Ni_2(*m*-dobdc). We observed that our calculated surface areas are in accord with the experimental observation wherever available.[13,55] We calculated the void fraction for M_2(*m*-dobdc) MOFs and determined their pore volumes. **Table 5.3** indicates that the calculated surface area and pore volumes of our selected M_2(*m*-dobdc) MOFs are higher, which means these MOF materials must be excellent H_2-storage materials.

5.3. Results and Discussion

5.3.1. Isosteric Heat of Adsorption (Q_{st})

The DL model was selected for H_2 heat of adsorption calculations due to its better representation of electrostatic interactions through partial charge distributions, which are essential for accurately modelling H_2-metal binding energetics at open metal sites in the M_2(*m*-dobdc) MOFs. The Ni_2(*m*-dobdc) MOF material shows the highest Q_{st} value of -7.72 kJ/mol at low pressure, as shown in **Figure 5.2a**. At high pressure, we obtained the value of Q_{st} about -12.33 kJ/mol for the Ni_2(*m*-dobdc), -11.54 kJ/mol for Co_2(*m*-dobdc), -13.08 kJ/mol for Mn_2(*m*-dobdc) and -13.04 kJ/mol for Fe_2(*m*-dobdc) as represented in **Figure 5.2b.** Our simulated heat of adsorption (Q_{st}) values are consistent with the previously reported Q_{st} values of -13.0 kJ/mol for the Ni_2(dobdc) and -11.9 kJ/mol for Co_2(dobdc)[38] and also matched the earlier-reported Q_{st} values for the same M_2(*m*-dobdc) MOFs.[13] Additionally, to further validate our computational approach, we performed DFT calculations using molecular modelling and calculated the enthalpy of adsorption (ΔH) , which gives ΔH values of -17.6 kJ/mol for Ni_2(*m*-dobdc), -19.6 kJ/mol for Fe_2(*m*-dobdc), -17.2 kJ/mol for Co_2(*m*-dobdc) and -15.4 kJ/mol for Mn_2(*m*-dobdc) MOFs. The two quantities (Q_{st} and ΔH) become comparable in magnitude, though they are not formally equivalent, the DFT value reflects a specific minimum energy configuration while the RASPA value retains its ensemble-averaged character. The comparison here is intended as a qualitative validation of the DFT-derived adsorption enthalpies rather than a strict quantitative equivalence. The heat of adsorption/enthalpies calculated by both the DFT method and GCMC simulations indicate strong physisorptive interactions between H_2 molecules and metal ions in the M_2(*m*-dobdc) series. The molecular models of Mn_2(*m*-dobdc) and Ni_2(*m*-dobdc) are shown in **Figures 5.2c and 5.2d**, respectively.

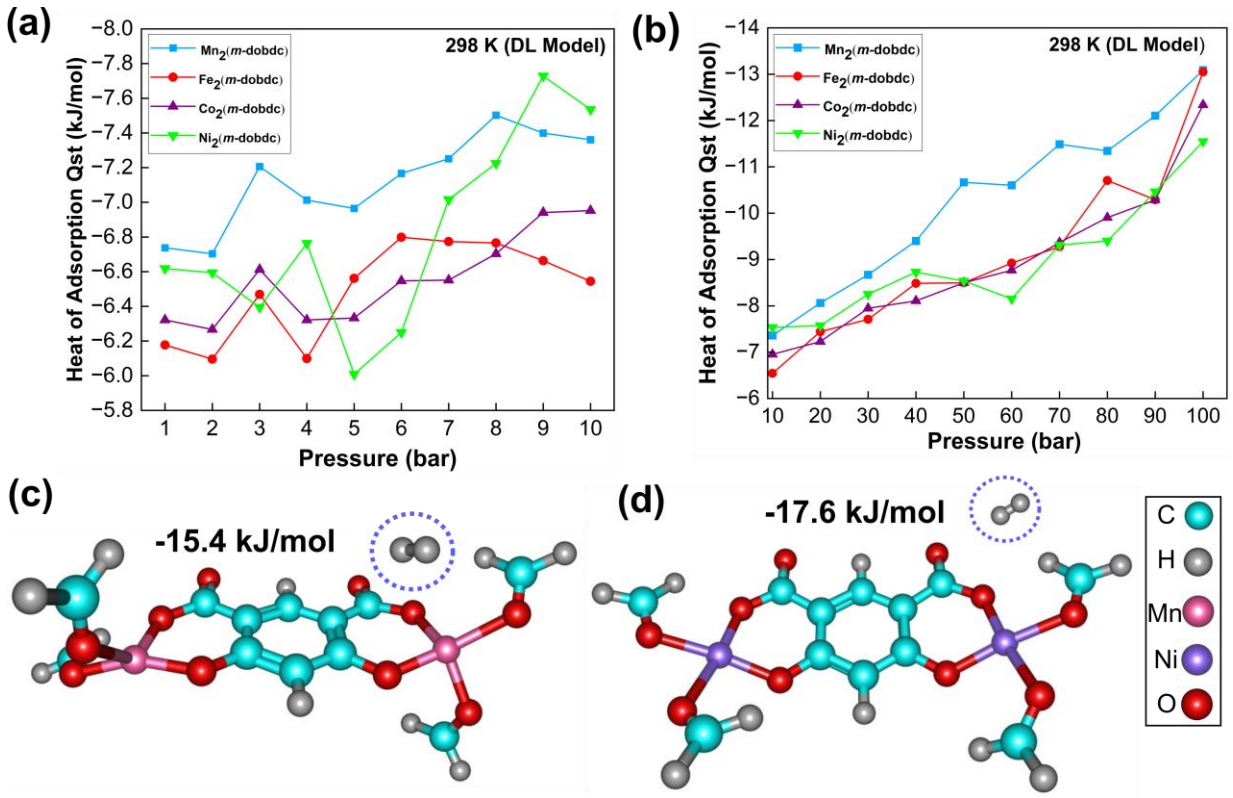

Figure 5.2. *The calculated heat of H_2 adsorption (Q_{st}) values at 298 K. (a) The simulated Q_{st} values at low pressure, (b) the simulated Q_{st} values at high pressure, (c) DFT calculated ΔH value for molecular model system of Mn_2(m-dobdc), and (d) DFT calculated ΔH value for the molecular model system of Ni_2(m-dobdc).*

5.3.2. H_2 Adsorption Isotherms

We calculated the absolute H_2 loading at five different temperatures: 77 K, 160 K, 198 K, 233 K, and 298 K. While numerous computational investigations have been reported for H_2 adsorption in other MOF materials, only a limited number of MOFs have been correlated with experimental data.[16,56–59] Keskin *et al*. proposed that one should not expect a close match between simulated results and experimental data at low pressures for H_2 adsorption in MOFs.[60] These studies found that simulations can significantly differ from experiments at high pressure, even though they align well with experiments at low pressure.[60] Hence, to evaluate the H_2-storage potential of the M_2(*m*-dobdc) MOFs, high-pressure adsorption isotherms were collected over 1-100 bar.

(a) H_2 adsorption isotherms at 77 K and 298 K

We reported the absolute loading and weight percentage with respect to pressure by both models: DL and Buch. At cryogenic temperature (77 K), all MOFs show excellent absolute loading ranging from 34-42 mg/g (3.4-4.2 wt.%) using the Buch model and 35-40 mg/g (3.5-4.0 wt.%)

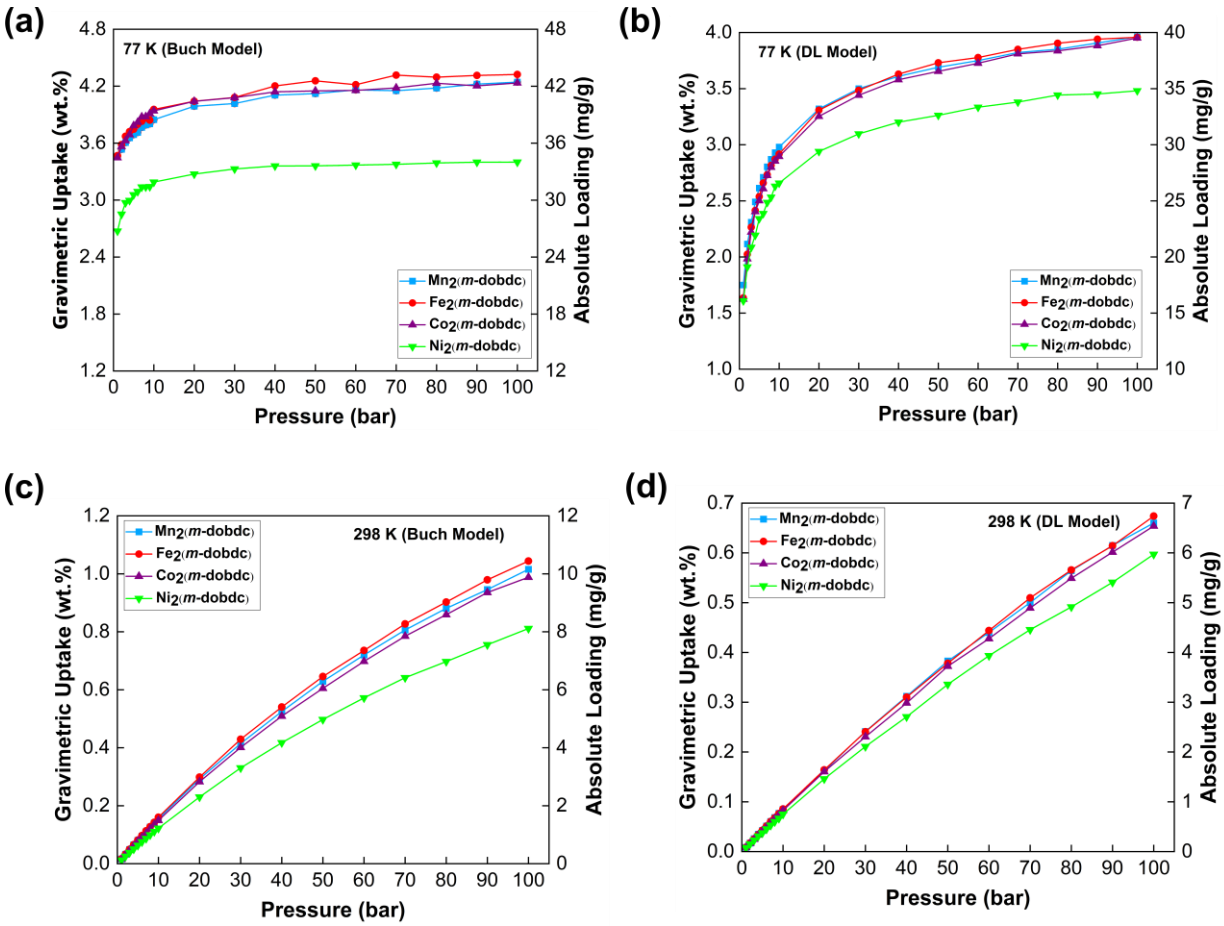

Figure 5.3. *The H_2 adsorption isotherms of M_2(m-dobdc) MOFs at 77 K and 298 K. a) 77 K Buch model, (b) 77 K DL model, (c) 298 K Buch model, and (d) 298 K DL model.*

with the DL model as represented in **Figures 5.3a and 5.3b**. Fe_2(*m*-dobdc) and Mn_2(*m*-dobdc) show the highest performance, followed by Co_2(*m*-dobdc), and the Ni_2(*m*-dobdc) MOF shows the lowest loading values among the series. Even at low-pressure (1 bar) conditions, adsorption isotherms show about 16.08 mg/g H_2 loading for Ni_2(*m*-dobdc) and 16.23 mg/g for Co_2(*m*-dobdc) with the DL model, which are comparable to the previous reported values of approximately 21 mg/g for Ni_2(dobdc) and 22 mg/g for Co_2(dobdc).[38] Our results show reasonable agreement with the literature, given the structural differences between these two MOF series. The H_2 adsorption capacities increased with greater surface area and pore volume, following the order:

Fe_2(*m*-dobdc) > Mn_2(*m*-dobdc) > Co_2(*m*-dobdc) > Ni_2(*m*-dobdc). The Buch model consistently predicts capacities 15-20% higher than those of the DL model. However, at 298 K, performance drops, and loading values range from 8-10 mg/g with the Buch model and 6-7 mg/g with the DL model, as shown in **Figure 5.3c** and **Figure 5.3d**, highlighting the critical issues with physisorption-based hydrogen storage materials at ambient conditions.

We conducted a comprehensive statistical analysis and sensitivity assessment of our simulation results at 77 K and 298 K using the DL model. We performed multiple independent GCMC simulations with different random seeds at both cryogenic (77 K) and ambient (298 K) conditions, with each data point representing the average of these independent runs. The figure showing error bars for the adsorption isotherm curves of Mn_2(*m*-dobdc) at 77 K and 298 K is provided in **Figures 5.4a and 5.4b**.

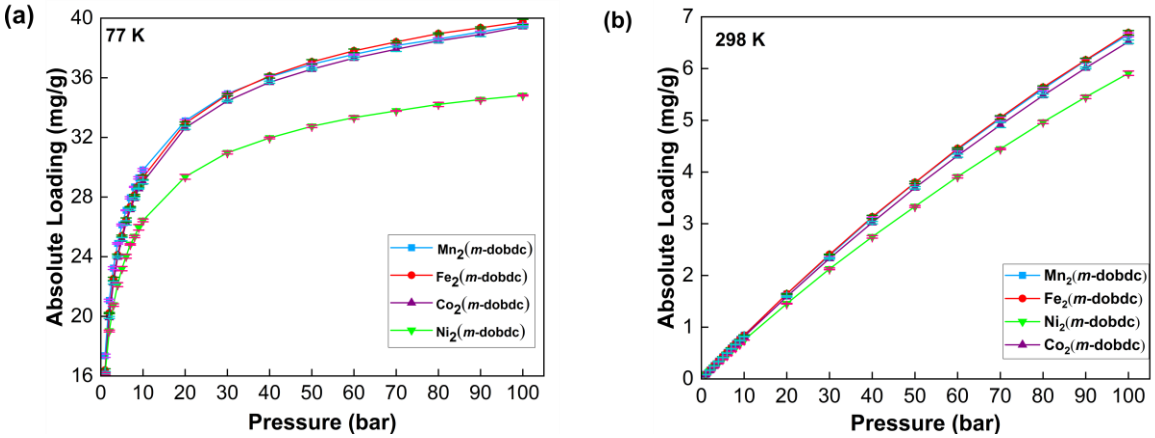

Figure 5.4. *Representation of error bars in the adsorption isotherm curves for M_2(m-dobdc) for 77 K and 298 K by the DL model. (a) 77 K loading with error bars, (b) 298 K loading with error bars.*

Our statistical analysis shows good reproducibility with standard deviation values ranging from 0.025 to 0.17 mg/g and the values of coefficient of variation (CV) lies between 0.001-0.006 (0.1-0.6%) at 77 K, and the standard deviation values from 0.001 to 0.04 mg/g with CV values between 0.004-0.01 (0.4-1.0%) at 298 K across all the studied MOFs. These consistently low statistical measures confirm high simulation precision and minimal data scatter.

(b) H_2 adsorption isotherms at 160 K, 198 K and 233 K

Next, we extended our H_2 adsorption study at T=160 K to a pressure range of 1-100 bars using the same GCMC simulation technique. We observed absolute H_2 loading values for Fe_2(*m*-dobdc) at 5 bar of 8.7 mg/g (0.87 wt.%) by using the Buch model and 2.61 mg/g (0.26 wt.%) by using the DL model. The Ni_2(*m*-dobdc) MOF material shows the minimum absolute H_2 loading value of 6.1 mg/g (0.61 wt.%) by the DL model under the same conditions. The shapes of the isotherms are well consistent across all the MOFs investigated, but the loadings vary because of differences in their pore sizes, as seen in **Figure 5.5a and Figure 5.5b.** The Fe_2(*m*-dobdc) MOF shows the highest absolute loading at the Buch model, and the Mn_2(*m*-dobdc) MOF performs best at the DL model. We obtained the absolute H_2 loading of 27.7 mg/g for Fe_2(*m*-dobdc) at 160 K and 100 bar, using the Buch model, which aligned well with previously reported loading values for MOFs under similar temperature and pressure conditions.[61] We found that the absolute H_2 loading values increased rapidly at low pressure (below 50 bar), then increased slowly to a maximum at 100 bar, as illustrated in **Figures 5.5a and 5.5b**. Our study reveals that H_2 molecules preferentially accumulate around the metal nodes within the framework, which confirms that the metal node site serves as a specific binding site for H_2 in these M_2(*m*-dobdc) MOFs. In an earlier study, DFT-based quantum calculations verified that the metal nodes are the leading active sites for H_2 binding, and the charge transfer and dispersion with the polarization interactions are the most dominating factors in the H_2 binding energy.[7,62]

At low pressure, H_2 molecules in MOFs occupy sites near the organic linkers due to π-π interactions with the organic ligands. As pressure rises, the molecules fill the empty spaces within the MOF channels. The absolute H_2 loadings were subsequently evaluated at 198 K over a pressure range of 1 to 100 bars. The study of H_2 uptake capacities at 198 K is critical for hydrogen storage applications as this temperature represents a practical intermediate condition between cryogenic (77 K) and ambient (298 K) environments. The value of data collected at 198 K provides essential insights for developing viable hydrogen storage systems that could operate with more economical and energy-efficient cooling technologies for practical mobile and stationary applications. The H_2 adsorption isotherms of M_2(*m*-dobdc) MOFs at 198 K with a pressure of 1-100 bars are displayed in **Figure 5.5c and Figure 5.5d.**

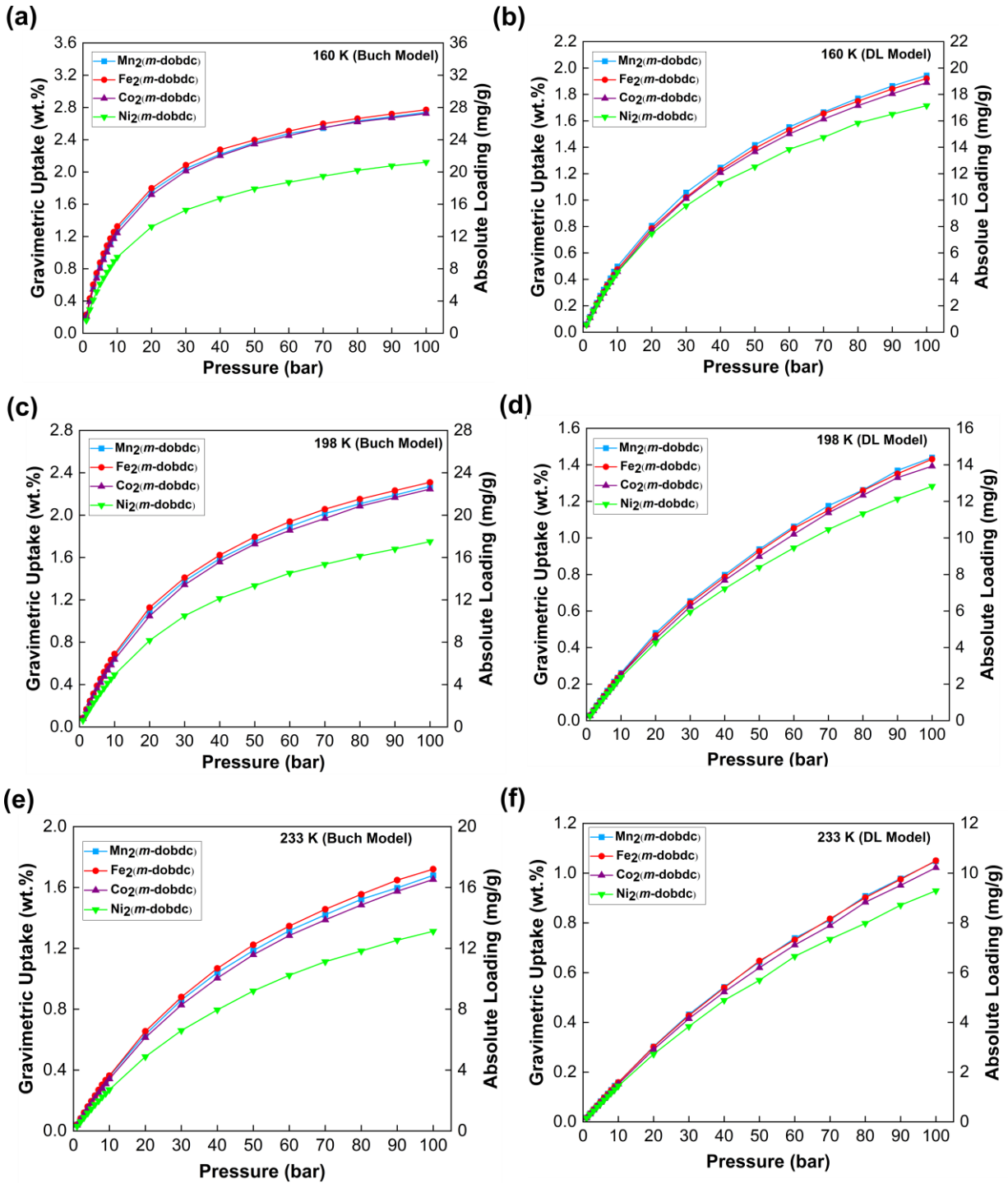

Figure 5.5. *The H_2 adsorption isotherms of M_2(m-dobdc) MOFs at three temperatures: 160 K, 198 K and 233 K. (a) 160 K Buch model, (b) 160 K DL model, (c) 198 K Buch model, (d) 198 K DL model, (e) 233 K Buch model, and (f) 233 K model.*

Our simulations reveal that the Fe_2(*m*-dodbc) MOF reaches a H_2-loading of 23.1 mg/g (2.3 wt.%) in the Buch model and 14.3 mg/g (1.4 wt.%) in the DL model at 100 bars. The Mn_2(*m*-dodbc) MOF material shows the H_2-uptake capacity about 22.7 mg/g (2.2 wt.%) by using the Buch model and 14.4 mg/g (1.4 wt.%) by employing the DL model at 100 bars. Similarly, the Co_2(*m*-dodbc) MOF reveals the H_2-storage capacity about 24.4 mg/g (2.4 wt.%) in the Buch model and 13.9 mg/g (1.3 wt.%) in the DL model. In the case of the Ni_2(*m*-dobdc) MOF, the H_2 loading value was found to be 17.5 mg/g (1.7 wt.%) computed by employing the Buch model and 12.8 mg/g (1.2 wt.%) at the DL model.

Now, we extended our GCMC simulations to investigate H_2 adsorption at a comparable high temperature, T = 233 K, over a pressure range of 1-100 bars to understand the effects of high temperature on H_2 uptake. The adsorption isotherms of M_2(*m*-dobdc) MOFs at 233 K from 1 bar to 100 bars are shown in **Figures 5.5e and 5.5f**. The GCMC simulations reveal that the absolute H_2 loading in the subject MOFs grows gradually with the pressure up to 100 bar at 233 K. As depicted in **Figure 5.5e and 5.5f**, the absolute H_2 loading in M_2(*m*-dobdc) series obeys the sequence of Fe_2(*m*-dobdc) > Mn_2(*m*-dobdc) > Co_2(*m*-dobdc) > Ni_2(*m*-dobdc). This sequence of absolute loading is consistent with their surface area and pore volume. Our analysis reveals that the Fe_2(*m*-dobdc) framework achieves the value of absolute H_2 loading around 17.2 mg/g (1.7 wt.%) computed by using the Buch model and 10.5 mg/g (1.0 wt.%) using the DL model at 233 K and 100 bar, surpassing the maximum storage capacities reported for leading MOFs under identical temperature-pressure conditions.[63] This performance sets a new benchmark for H_2 adsorption in porous materials at moderate temperatures.

Frost *et al.* outlined three phases of adsorption: at low pressures, H_2 loading is always governed by Q_{st}; at intermediate pressures, it depends on surface area; and at high pressures, H_2 uptake is influenced by the free volume in MOFs.[64] Frost and Snurr discovered that the absolute H_2 adsorption at 298 K primarily relates to free volume across the entire pressure range.[65] Using the concept, we quantitatively correlated our simulation results (obtained using the DL model) with the outlined phases of adsorption at both cryogenic and ambient conditions. At 160 K and in the low-pressure regime (1-10 bar), for example, the Co_2(*m*-dobdc) MOF shows a significant increase in H_2 loading of 0.56 mg/g to 4.5 mg/g, which represents strong binding of H_2 at open metal sites, which is supported by the reduced temperature. In **Figure 5.5b**, the

medium-pressure phase (10-50 bar) shows a more gradual increase in loading from 4.5 mg/g to 13.6 mg/g for the Co_2(*m*-dobdc) MOF, which indicates filling of secondary sites with intermediate binding energies. Finally, in the high-pressure regime (50-100 bar), a slight increase from 13.6 to 18.8 mg/g, reflecting pore saturation and the occupation of the weakest physisorption sites. In contrast, at 233 K, the van der Waals (vdW) forces support completely different behavior of the physisorption sites; in the low-pressure regime, only a minimal loading rise from 0.16 to 1.5 mg/g in the Co_2(*m*-dobdc) MOF indicates weaker H_2 binding at open metal sites as represented in **Figure 5.5f**. The medium-pressure regime contributes a moderate increase up to 6.2 mg/g, while the high-pressure regime contributes an additional 4.0 mg/g in the case of Co_2(*m*-dobdc) MOF. This temperature dependent analysis shows that the simulation results generated in this work agree with concepts of the three phase mechanism (low, medium and high pressure ranges) proposed by Frost *et al.,* (1) at cryogenic conditions, the loading is steeped at beginning with a strong initial adsorption at open metal site followed by gradual filling of weaker sites, (2) at ambient conditions, the uptake is more continuous and gradual, reflects that the gas molecules first fill the strongest adsorption sites, and then gradually move to weaker sites as pressure increases.

5.3.3. Gravimetric and Volumetric H_2 Uptake Capacities of M_2(*m*-dobdc) MOFs

Gravimetric H_2 uptake capacity (G_c) and volumetric H_2 uptake capacity (V_c) are related to adsorbed H_2 molecules in MOFs, which directly means the porosity of materials. The hydrogen storage performance of M_2(*m*-dobdc) MOFs was comprehensively evaluated by calculating gravimetric uptake capacities in (wt.%) and volumetric capacities in (g/L) at multiple temperatures. **Figure 5.6** shows the gravimetric and volumetric capacities of the M_2(*m*-dobdc) MOFs as a function of pressure at cryogenic conditions and room temperature using both the Buch model and the DL model. Additional H_2 uptake capacity data (G_c and V_c) of the M_2(*m*-dobdc) MOFs at intermediate temperatures 160 K, 198 K and 233 K are provided in **Figure 5.7a-f**. The total gravimetric H_2 uptake for M_2(*m*-dobdc) MOF series varies from 3.4 to 4.24 wt.% at 77 K and 100 bars by using the Buch model as represented in **Figure 5.6a**. The present study indicates that Fe_2(*m*-dobdc) and Mn_2(*m*-dobdc) have the highest gravimetric uptake capacity, about 4.24 wt.% (at T = 77 K and P =100 bars), compared to the other M_2(*m*-dobdc) MOFs.

Similarly, the total gravimetric H_2 uptake for the M_2(*m*-dobdc) MOF series varies from 2.7 to 4.10 wt.% at 77 K and 100 bar, as shown in **Figure 5.6b** using the DL model.

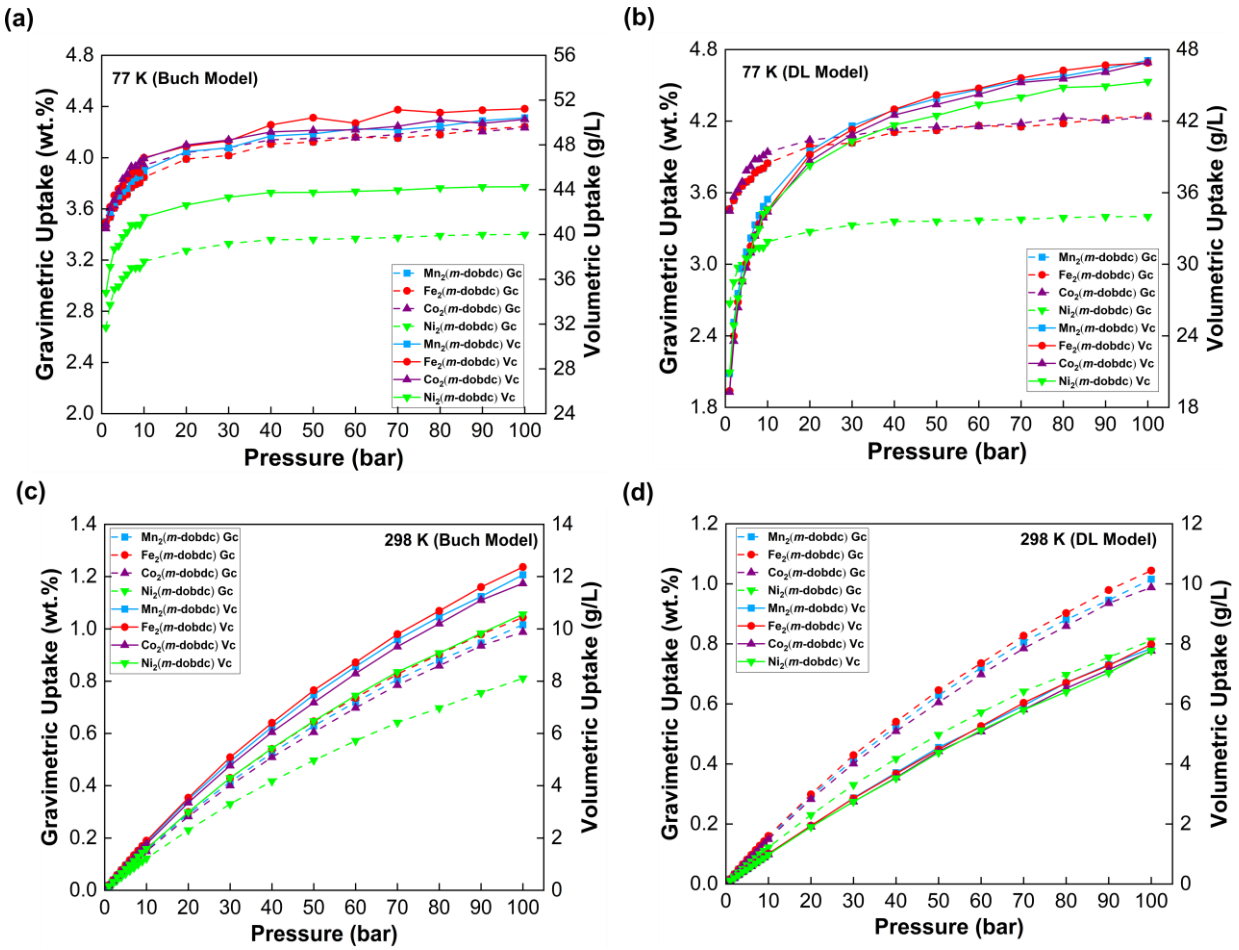

***Figure 5.6**. The H_2 uptake capacities of M_2(m-dobdc) MOFs at cryogenic conditions and room temperature. (a) 77 K Buch model, (b) 77 K DL model, (c) 298 K Buch model, and (d) 298 K DL model.*

This high uptake is expected, as a larger surface area provides more free space within the framework, allowing more bulk H_2 to occupy the empty spaces and boosting the overall capacity. Experimental investigations have consistently demonstrated that MOFs typically exhibit limited hydrogen storage capacities at room temperature and moderate pressures, with gravimetric H_2 uptake capacities generally remaining below 2 wt.%. However, when subjected to elevated pressures of 80-200 bar, these materials exhibit enhanced storage capacity, with gravimetric H_2 capacities increasing from 0.4 to 4 wt.%.[66]

Table 5.4. *The calculated gravimetric H_2 uptake capacities (G_c) of M_2(m-dobdc) MOFs by using the Buch model. (Bold values indicate the experimental values of Gravimetric H_2 uptake have been taken from literature sources)*

MOFs	Gravimetric H_2 Uptake in wt.%				
	T=77 K/ P=100 bars	T=160 K/ P=100 bars	T=198 K/ P=100 bars	T=233 K/ P=100 bars	T=298 K/ P=100 bars
Mn_2(*m*-dobdc)	4.24/**8.21**[21]	2.74	2.27	1.67	1.01/**1.38**[21]
Fe_2(*m*-dobdc)	4.24/**4.31**[21]	2.77	2.31	1.72	1.04/**0.10**[21]
Co_2(*m*-dobdc)	4.23	2.72	2.24/**1.8**[4]	1.65/**1.5**[4]	0.98/**0.9**[4]
Ni_2(*m*-dobdc)	3.4	2.12	1.75/**2.0**[4]	1.31/**1.6**[4]	0.81/**1.0**[4]
MOF-5	8.34[67]/**9.8**[68]	-	-	-	1.15[67]/**0.82**[68]

The present GCMC simulation shows that total gravimetric uptake ranges from 0.60 to 0.67 wt.% by the DL model and from 0.81 to 1.04 wt.% by the Buch model at 298 K, as shown in **Figure 5.6c and Figure 5.6d**. We compared our simulated gravimetric and volumetric uptake capacities with previously reported experimental data for the same MOF series and the benchmark MOF-5. **Table 5.4** summarizes the total hydrogen gravimetric uptake capacities of the M_2(*m*-dobdc) MOFs with pore diameters in the range of 7-15 Å. The predictions of the Buch model showed better agreement with experimental H_2-uptake capacities than those of the DL model. Therefore, we used the Buch model data for tabulation and comparative analysis. As temperature increases, the differences in gravimetric H_2-uptake capacity between the various MOFs become minimal. Therefore, total gravimetric capacity is not a suitable metric for comparing H_2-storage performance among different adsorbents. As porosity increases, the framework mass within a given volume decreases to zero, leading to an infinite total gravimetric capacity.[68] Thus, volumetric H_2 storage capacity represents a more reliable parameter for evaluating the practical utility of MOFs.

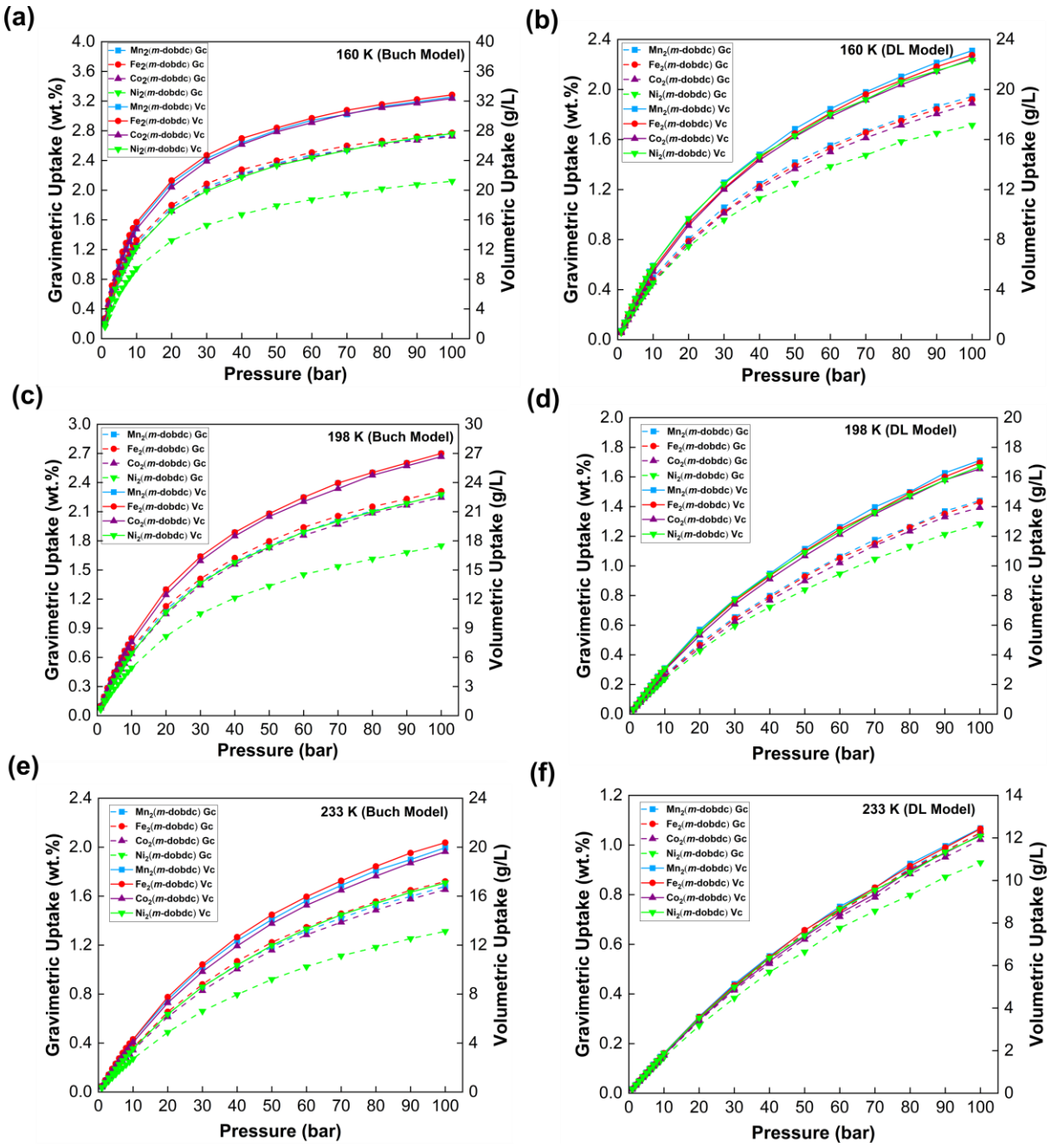

Figure 5.7*. The H_2 uptake capacities of M_2(m-dobdc) MOFs at three temperatures. (a) 160 K Buch model, (b) 160 K DL model, (c) 198 K Buch model, (d) 198 K DL model, (e) 233 K Buch model, and (f) 233 K DL model.*

Table 5.5. *The calculated volumetric H_2 uptake capacities of M_2(m-dobdc) MOFs by using the Buch model. (Bold values indicate the experimental values of Volumetric H_2 uptake have been taken from literature sources)[4]*

MOFs	**Volumetric H_2 Uptake in g/L**				
	77 K/100 bars	160 K/100 bars	198 K/100 bars	233 K/100 bars	298 K/100 bars
Mn_2(*m*-dobdc)	50.41	32.55	26.99	19.95	12.06
Fe_2(*m*-dobdc)	51.22	32.84	27.35	20.36	12.36
Co_2(*m*-dobdc)	50.28	32.35	26.66/**23.0**	19.62/**17.3**	11.73/**11.0**
Ni_2(*m*-dobdc)	44.26	27.61	22.78/**23.8**	17.08/**18.2**	10.55/**11.9**
MOF-5	-	-	**15.8**	**12.8**	**8.8**

When considering volumetric uptake, the amount of hydrogen adsorbed is primarily determined by the density and strength of H_2-binding sites rather than by the volumetric surface area alone. As a result, materials with high surface area and high gravimetric capacity but weak binding sites exhibit significantly lower volumetric capacity than frameworks with smaller surface area but stronger binding sites. The presence of unsaturated metal sites in M_2(*m*-dobdc) makes it the best choice for onboard H_2-storage, as it has a relatively low volumetric surface area compared to some reference MOFs like MOF-5, which have both exceptional gravimetric and volumetric surface areas. M_2(*m*-dobdc) MOF achieve volumetric uptake of 26.7-34.7 g/L at 77 K and 1 bar, with potential to exceed the DOE target of 40 g/L at higher pressure. Among the M_2(*m*-dobdc) series, the Fe_2(*m*-dobdc) MOF achieves an outstanding V_c value of 51.22 g/L under cryogenic conditions (77 K, 100 bar) as reported in **Table 5.5**. At room temperature, the MOFs delivered V_c values ranging from 10.55 to 12.36 g/L, with Fe_2(*m*-dobdc) showing maximum uptake of 12.36 g/L, marginally outperforming MOF-5. This dual performance capability demonstrates the potential of M_2(*m*-dobdc) MOFs for practical H_2 storage applications.

Table 5.6. *The calculated H_2 deliverable capacity in the temperature-pressure range (77 K/100 bar →160 K/5 bar) and total gravimetric H_2 adsorption capacities at T=298 K and P =100 bars in M_2(m-*

dobdc) MOFs by using the Buch model. (The experimental data for other MOFs have been taken from literature sources)

MOFs	77 K/100 bar →160 K/5 bar		H_2 total adsorption at T=298 K, P=100 bars	
	G_c(wt.%)	V_c(g/L)	G_c(wt.%)	V_c(g/L)
HKUST-1[61]	5.2	46	1.2	10.8
Cu-MOF-74[61]	3.0	39	0.8	10.1
NU-1000[61]	8.3	48	1.7	10.0
UiO-67[61]	6.0	41	1.2	8.0
PCN-250[61]	5.2	47	1.2	10.4
Mn_2(*m*-dobdc) This work	3.4	40.3	1.01	12.06
Fe_2(*m*-dobdc) This work	3.3	40.8	1.04	12.36
Co_2(*m*-dobdc) This work	3.4	40.7	0.98	11.73
Ni_2(*m*-dobdc) This work	2.8	36.3	0.81	10.55

Additionally, an optimal MOF structure for hydrogen tank storage should offer both high hydrogen storage capacity and high deliverable capacity.[61] To further investigate gas storage performance, we calculated the theoretical H_2 deliverable capacities of the studied MOFs under two distinct combined temperature-pressure swing systems ranges from (77 K/100 bar →160 K/5 bar) at cryogenic conditions, and (198 K/100 bar → 298 K/5 bar, 233 K/100 bar → 298 K/5 bar and 298 K/100 bar → 298 K/5 bar) at ambient conditions. We reported the calculated H_2 deliverable capacity in the temperature-pressure range (77 K/100 bar →160 K/5 bar) and total gravimetric H_2 adsorption capacities at T=298 K and P =100 bars in M_2(*m*-dobdc) MOFs in **Table 5.6**. The calculated H_2 deliverable capacity (in g/L) for other temperature-pressure swing systems is provided in **Table 5.7.**

The hydrogen deliverable capacities (in g/L) of the M_2(*m*-dobdc) MOFs match or exceed those of leading frameworks like UiO-67 and Cu-MOF-74 under cryogenic temperature-pressure swing conditions (77 K/100 bar → 160 K/5 bar). Their volumetric performance remains competitive with established benchmark materials reported in prior studies, demonstrating their versatility across temperature regimes.[61] The Fe_2(*m*-dobdc) MOF shows the highest gravimetric H_2-storage capacity of 1.04 wt.%, and volumetric H_2 uptake of 12.36 g/L at 298 K and 100 bars. To the best of our knowledge, this simulated volumetric H_2 uptake capacity is the highest measured H_2 volumetric uptake capacity of any MOF under the same temperature-

pressure conditions.

Table 5.7. *The calculated volumetric H_2 deliverable capacity (in g/L) under ambient conditions for M_2(m-dobdc) MOFs. (The uptake values are taken from Buch model simulations.)*

MOFs	198 K/100 bar →298 K/5 bar	233/100 bar →298 K/5 bar	298/100 bar →298 K/5 bar
	v_c(g/L)	v_c(g/L)	v_c(g/L)
Mn_2(*m*-dobdc) This work	26.03	18.99	11.10
Fe_2(*m*-dobdc) This work	26.39	19.40	11.39
Co_2(*m*-dobdc) This work	25.73	18.70	10.81
Ni_2(*m*-dobdc) This work	21.95	16.25	9.73

To test the accuracy of our chosen force field parameters, we compared our simulated results for the H_2-adsorption of the Ni_2(*m*-dobdc) MOF with the previously reported experimental H_2 adsorption isotherms by Long and coworkers of the Ni_2(*m*-dobdc), MOF-5 and Ni_2(dobdc) at 298 K.[4]For instance, the values of RMSE between the simulated and experimental gravimetric uptake of the Ni_2(*m*-dobdc) MOF is 0.153 wt.%, and for volumetric uptake, it is 0.507 g/L, which shows consistency with reported experimental data. The close match between our simulated gravimetric (G_c) and volumetric uptake (V_c) capacities of the H_2-adsorption of the Ni_2(*m*-dobdc) MOF with the experimentally calculated uptake values of the same MOF, as represented in **Figure 5.8a**, reflects that Generic force fields reliably captured the interactions between gas molecules and open metal sites under ambient conditions. The small root mean square error (RMSE) values (<1) derived from these statistical distributions validate the robustness of the chosen force field parameters. The gravimetric capacity of Ni_2(*m*-dobdc) MOF is comparable to that of MOF-5, with a low RMSE value of 0.013 wt.% between MOF-5 (experimental) and Ni_2(*m*-dobdc) (simulated) values for gravimetric uptake. However, the volumetric uptake of the Ni_2(*m*-dobdc) exceeds the corresponding values of the MOF-5, which is an essential metric for practical H_2 storage. This difference is reflected in a higher RMSE value of the volumetric uptake of the MOF-5 (experimental) vs Ni_2(*m*-dobdc) (simulated).

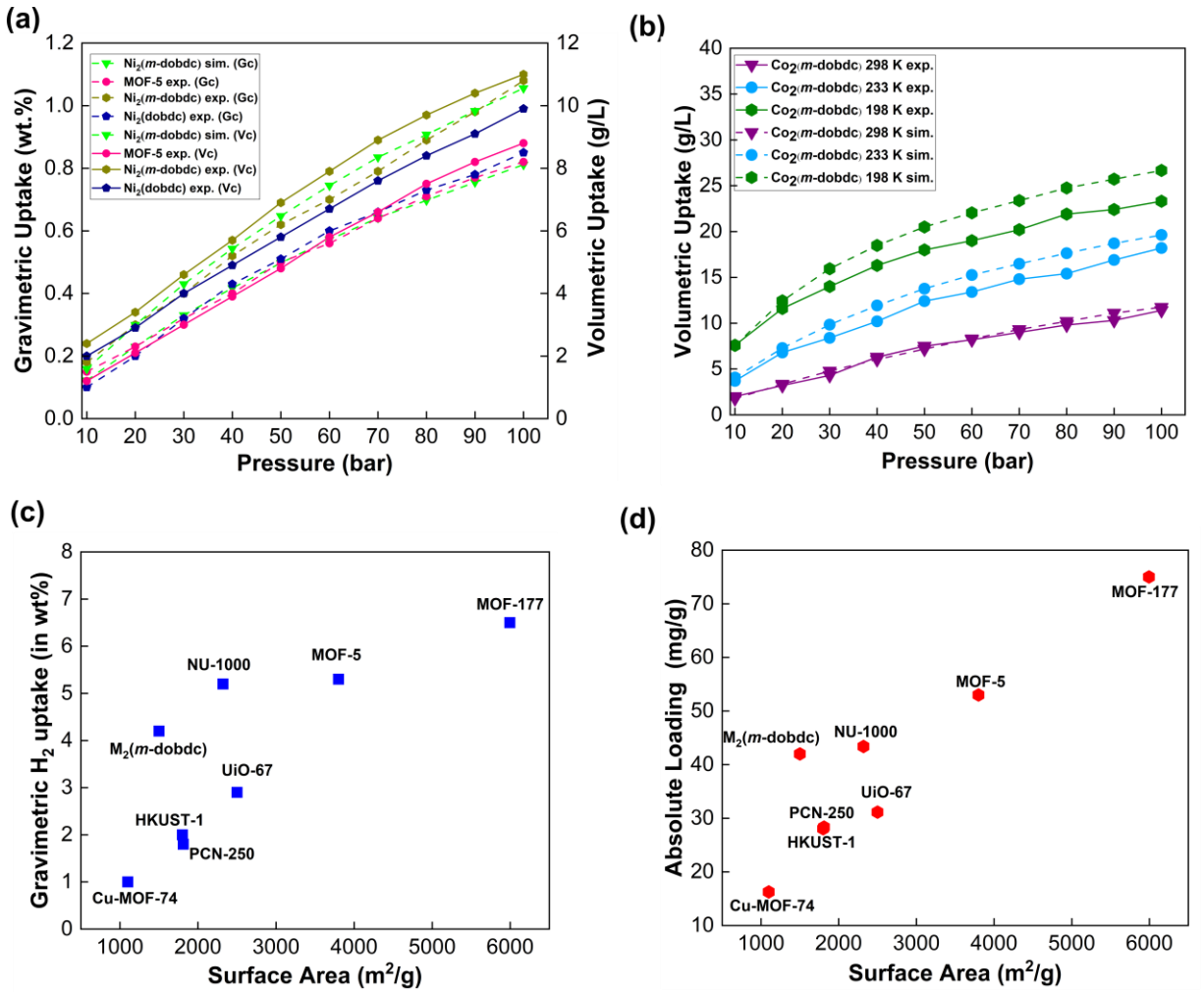

Figure 5.8. *Comparison of the simulated gravimetric and volumetric H_2 uptake capacities and loading values of M_2(m-dobdc) MOFs with experimental uptake capacities/loadings of other MOFs. (a) Simulated vs experimental V_c and G_c values comparison of Ni_2(m-dobdc) at 298 K, (b) simulated vs experimental V_c values comparison of Co_2(m-dobdc) at 198 K, 233 K and 298 K, (c) G_c values comparison of M_2(m-dobdc) with other MOFs at 77 K, and (d) absolute loading comparison of M_2(m-dobdc) with other MOFs at 77 K. (Data was taken for 77 K and 100 bars)*[8,69,70] *(Experimental data of V_c and G_c at 298 K were extracted from the literature.[4])*

Figure 5.8b represents a comparison of the simulated volumetric uptake of the Co_2(*m*-dobdc) with experimentally calculated volumetric uptake of the same MOF at 298K, 233K and 198K.[4]

Our simulation results of the Co_2(*m*-dobdc) MOF show close correlation with the experimental data at 298 K, with a value of RMSE about 0.385 g/L, indicating very small prediction errors. At 233 K, the calculated RMSE for the Co_2(*m*-dobdc) MOF is 1.4 g/L, whereas at 198 K it reaches 2.5 g/L. The increasing error at lower temperatures is expected because molecular

interactions become stronger and more complex, making accurate prediction of uptakes more difficult. Overall, all RMSE values are within acceptable limits for molecular simulation using Generic force fields. As shown in **Figures 5.8c and 5.8d**, our simulated results align with the reported data from both experiments and simulations,[8,61,69,70] at cryogenic conditions. Hence, we conclude that the GCMC method and the chosen force field parameters are sufficiently stable to predict hydrogen adsorption in the M_2(*m*-dobdc) series.

5.4. Conclusions

We selected M_2(*m*-dobdc) MOFs and evaluated their H_2 adsorption properties under conditions applicable to onboard H_2 storage in vehicles. Our results reveal that Fe_2(*m*-dobdc) exhibits a superior gravimetric capacity value of 4.24 wt.% under cryogenic conditions and an exceptional volumetric capacity value of 12.36 g/L at room temperature compared to other MOFs in the chosen M_2(*m*-dobdc) series. To date, these calculated volumetric H_2 uptake capacities are the highest reported for MOFs at room temperature. This finding indicates that the gravimetric H_2 uptake capacities of M_2(*m*-dobdc) MOFs at 77K and 100 bar are quite close to the DOE target for 2025, 5.5 wt%. The calculated values of volumetric H_2 uptake in Ni_2(*m*-dobdc) and Co_2(*m*-dobdc) MOFs show good agreement with previously reported experimental values of volumetric uptake for these MOFs under various temperature and pressure conditions. The simulated heat of H_2 adsorption of the M_2(*m*-dobdc) MOFs at 298 K and 100 bar ranges from -11.5 to -13.0 kJ/mol at high pressure. The M_2(*m*-dobdc) series shows a promising deliverable volumetric H_2 capacity of 36.3 g/L to 40.8 g/L, compared to some well-known MOF materials in the temperature-pressure swing range (77 K/100 bar to 160 K/5 bar). The volumetric H_2 uptake capacity of M_2(*m*-dobdc) outperforms those of leading nanoporous MOFs with open metal sites, such as Cu^I-MFU-4*l* and $V_2Cl_{2.8}$(BTDD), under comparable conditions. Future work will focus on enhancing the density of active M(II) sites in M_2(*m*-dobdc) through targeted ligand modifications and on modifying the geometry of transition-metal centres in MOFs to control the strength of π-back-bonding interactions. This study marks an important step toward the design of next-generation MOFs capable of integrated H_2-storage under industrial conditions. In the case of these specific MOFs, the M_2(*m*-dobdc) MOF series with open metal sites, there is a need to develop more accurate polarized force fields for H_2

and CO_2 to metal interactions. We believe that future efforts should involve quantum mechanical calculations to parameterize these interactions. This is a direction we intend to explore in our future studies.

5.5. References

[1] D.E. Jaramillo, H.Z.H. Jiang, H.A. Evans, R. Chakraborty, H. Furukawa, C.M. Brown, M. Head-Gordon, J.R. Long, Journal of the American Chemical Society 143 (2021) 6248–6256.

[2] H. Joshi, S. Pakhira, International Journal of Hydrogen Energy 79 (2024) 1139–1154.

[3] H. Joshi, N. Sinha, K. Parveen, S. Pakhira, Energy and Fuels 37 (2023) 19771–19784.

[4] M.T. Kapelewski, T. Runčevski, J.D. Tarver, H.Z.H. Jiang, K.E. Hurst, P.A. Parilla, A. Ayala, T. Gennett, S.A. Fitzgerald, C.M. Brown, J.R. Long, Chemistry of Materials 30 (2018) 8179–8189.

[5] H.R. Abid, A. Hanif, A. Keshavarz, J. Shang, S. Iglauer, Energy and Fuels 37 (2023) 7260–7267.

[6] R. Chakraborty, K.M. Carsch, D.E. Jaramillo, Y. Yabuuchi, H. Furukawa, J.R. Long, M. Head-Gordon, Journal of Physical Chemistry Letters 13 (2022) 10471–10478.

[7] S. Pakhira, J.L. Mendoza-Cortes, Journal of Physical Chemistry C 124 (2020) 6454–6460.

[8] X. Zhang, R.B. Lin, J. Wang, B. Wang, B. Liang, T. Yildirim, J. Zhang, W. Zhou, B. Chen, Advanced Materials 32 (2020) 1907995.

[9] L.J. Murray, M. Dinc, J.R. Long, Chemical Society Reviews 38 (2009) 1294–1314.

[10] J.R. Li, J. Sculley, H.C. Zhou, Chemical Reviews 112 (2012) 869–932.

[11] Y. Chen, W. Lu, M. Schröder, S. Yang, Accounts of Chemical Research 56 (2023)

2569–2581.

[12] N.L. Rosi, J. Eckert, M. Eddaoudi, D.T. Vodak, J. Kim, M. O'Keeffe, O.M. Yaghi, Science 300 (2003) 1127–1129.

[13] M.T. Kapelewski, S.J. Geier, M.R. Hudson, D. Stück, J.A. Mason, J.N. Nelson, D.J. Xiao, Z. Hulvey, E. Gilmour, S.A. Fitzgerald, M. Head-Gordon, C.M. Brown, J.R. Long, Journal of the American Chemical Society 136 (2014) 12119–12129.

[14] H. Wu, W. Zhou, T. Yildirim, Journal of the American Chemical Society 131 (2009) 4995–5000.

[15] A.M.P. Peedikakkal, I.H. Aljundi, ACS Omega 5 (2020) 28493–28499.

[16] M. Witman, S. Ling, A. Gladysiak, K.C. Stylianou, B. Smit, B. Slater, M. Haranczyk, Journal of Physical Chemistry C 121 (2017) 1171–1181.

[17] A. Ahmed, S. Seth, J. Purewal, A.G. Wong-Foy, M. Veenstra, A.J. Matzger, D.J. Siegel, Nature Communications 10 (2019) 1568.

[18] US Department of Energy, U.S Drive (2017) 1–29.

[19] A. Ahmed, Y. Liu, J. Purewal, L.D. Tran, A.G. Wong-Foy, M. Veenstra, A.J. Matzger, D.J. Siegel, Energy and Environmental Science 10 (2017) 2459–2471.

[20] X. Zhang, R.B. Lin, Z.A. Alothman, O. Alduhaish, T. Yildirim, W. Zhou, J.R. Li, B. Chen, Inorganic Chemistry Frontiers 10 (2022) 454–459.

[21] S.K. Verma, M.A. Shaz, T.P. Yadav, Energy Storage 4 (2022) 1–13.

[22] D. Dubbeldam, S. Calero, D.E. Ellis, R.Q. Snurr, Molecular Simulation 42 (2016) 81–101.

[23] A.K. Rappé, W.A. Goddard, Journal of Physical Chemistry 95 (1991) 3358–3363.

[24] C. Altintas, S. Keskin, Molecular Systems Design and Engineering 5 (2020) 532–543.

[25] M. Sedighi, M.R. Talaie, H. Sabzyan, S. Aghamiri, P. Chen, Fuel 308 (2022) 121965.

[26] X. Wang, S. Ramírez-Hinestrosa, J. Dobnikar, D. Frenkel, Physical Chemistry Chemical Physics 22 (2020) 10624–10633.

[27] A. K. Rappi, C. J. Casewit, K. S. Colwell, W. A. Goddard III, W. M. Skiff, Journal of the American Chemical Society 114(1992) 10024–10035.

[28] S.L. Mayo, B.D. Olafson, W.A. Goddard, Journal of Physical Chemistry 94 (1990) 8897–8909.

[29] G. Garberoglio, Langmuir 23 (2007) 12154–12158.

[30] D. Sengupta, P. Melix, S. Bose, J. Duncan, X. Wang, M.R. Mian, K.O. Kirlikovali, F. Joodaki, T. Islamoglu, T. Yildirim, R.Q. Snurr, O.K. Farha, Journal of the American Chemical Society 145 (2023) 20492–20502.

[31] N.T. Xuan Huynh, O.M. Na, V. Chihaia, D.N. Son, RSC Advances 7 (2017) 39583–39593.

[32] B.J. Bucior, N.S. Bobbitt, T. Islamoglu, S. Goswami, A. Gopalan, T. Yildirim, O.K. Farha, N. Bagheri, R.Q. Snurr, Molecular Systems Design and Engineering 4 (2019) 162–174.

[33] S. Bureekaew, S. Amirjalayer, M. Tafipolsky, C. Spickermann, T.K. Roy, R. Schmid, Physica Status Solidi (B) Basic Research 250 (2013) 1128–1141.

[34] M.A. Addicoat, N. Vankova, I.F. Akter, T. Heine, Journal of Chemical Theory and Computation 10 (2014) 880–891.

[35] J. Liu, J. T. Culp, S. Natesakhawat, B. C. Bockrath, B. Zande, S. G. Sankar, G. Garberoglio, J. K. Johnson, Journal of Physical Chemistry C 111(2007) 9305-9313.

[36] V. Buch, Journal of Chemical Physics 100 (1994) 7610–7629.

[37] F.D.D. Levesque, Journal of Chemical Physics 109 (1998) 4981–4984.

[38] T. Pham, K.A. Forrest, R. Banerjee, G. Orcajo, J. Eckert, B. Space, Journal of Physical Chemistry C 119 (2015) 1078–1090.

[39] K. Momma, F. Izumi, Journal of Applied Crystallography 44 (2011) 1272–1276.

[40] D. Dubbeldam, S. Calero, T.J.H. Vlugt, Molecular Simulation 44 (2018) 653–676.

[41] L. Wang, Y. Sun, H. Sun, Faraday Discussions 151 (2011) 143–156.

[42] A.D. Becke, Journal of Chemical Physics 98 (1993) 5648–5652.

[43] S. Grimme, J. Antony, S. Ehrlich, H. Krieg, Journal of Chemical Physics 132 (2010) 154104.

[44] H. Joshi, S. Pakhira, ChemPhysChem 16 (2024) e202400237.

[45] D. Vilela Oliveira, J. Laun, M.F. Peintinger, T. Bredow, Journal of Computational Chemistry 40 (2019) 2364–2376.

[46] D.J. Frisch, M. J.; Trucks, G. W.; Schlegel, H. B.; Scuseria, G. E.; Robb, M. A.; Cheeseman, J. R.; Scalmani, G.; Barone, V.; Petersson, G. A.; Nakatsuji, H.; Li, X.; Caricato, M.; Marenich, A. V.; Bloino, J.; Janesko, B. G.; Gomperts, R.; Mennucci, B.; Hratch, Gaussian, Inc., Wallingford CT, 2019.

[47] Chemcraft, Graphical Software for Visualization of Quantum Chemistry Computations. https://doi.org/https://www.chemcraftprog.com.

[48] R. Dovesi, A. Erba, R. Orlando, C.M. Zicovich-Wilson, B. Civalleri, L. Maschio, M. Rérat, S. Casassa, J. Baima, S. Salustro, B. Kirtman, Wiley Interdisciplinary Reviews: Computational Molecular Science 8 (2018) e1360.

[49] J. Laun, D. Vilela Oliveira, T. Bredow, Journal of Computational Chemistry 39 (2018) 1285–1290.

[50] L.D. Gelb, K.E. Gubbins, Langmuir 15 (1999) 305–308.

[51] A.H. Farmahini, K. Limbada, L. Sarkisov, Adsorption 28 (2022) 219–230.

[52] R. Gadiou, S.E. Saadallah, T. Piquero, P. David, J. Parmentier, C. Vix-Guterl, Microporous and Mesoporous Materials 79 (2005) 121–128.

[53] M. Dinča, A. Dailly, Y. Liu, C.M. Brown, D.A. Neumann, J.R. Long, Journal of the American Chemical Society 128 (2006) 16876–16883.

[54] M. Dincă, J.R. Long, Angewandte Chemie - International Edition 47 (2008) 6766–6779.

[55] J.A. Mason, M. Veenstra, J.R. Long, Chemical Science 5 (2014) 32–51.

[56] S.S. Han, W.Q. Deng, W.A. Goddard, Angewandte Chemie - International Edition 46 (2007) 6289–6292.

[57] Q. Yang, C. Zhong, Journal of Physical Chemistry B 110 (2006) 17776–17783.

[58] G. Garberoglio, A.I. Skoulidas, J.K. Johnson, Journal of Physical Chemistry B 109 (2005) 13094–13103.

[59] M. Gallo, D. Glossman-Mitnik, Journal of Physical Chemistry C 113 (2009) 6634–6642.

[60] S. Keskin, J. Liu, R.B. Rankin, J.K. Johnson, D.S. Sholl, Industrial and Engineering Chemistry Research 48 (2009) 2355–2371.

[61] P. García-Holley, B. Schweitzer, T. Islamoglu, Y. Liu, L. Lin, S. Rodriguez, M.H. Weston, J.T. Hupp, D.A. Gómez-Gualdrón, T. Yildirim, O.K. Farha, ACS Energy Letters 3 (2018) 748–754.

[62] R. Chakraborty, J.J. Talbot, H. Shen, Y. Yabuuchi, K.M. Carsch, H.Z.H. Jiang, H. Furukawa, J.R. Long, M. Head-Gordon, Physical Chemistry Chemical Physics 26 (2024) 6490–6511.

[63] P. Ramirez-Vidal, R.L.S. Canevesi, A. Celzard, V. Fierro, ACS Applied Nano Materials

5 (2022) 759–773.

[64] H. Frost, T. Düren, R.Q. Snurr, Journal of Physical Chemistry B 110 (2006) 9565–9570.

[65] H. Frost, R.Q. Snurr, Journal of Physical Chemistry C 111 (2007) 18794–18803.

[66] I. Cabria, International Journal of Hydrogen Energy 50 (2024) 160–177.

[67] J. Fu, H. Sun, Journal of Physical Chemistry C 113 (2009) 21815–21824.

[68] S.S. Kaye, A. Dailly, O.M. Yaghi, J.R. Long, Journal of the American Chemical Society 129 (2007) 14176–14177.

[69] K.M. Thomas, Catalysis Today 120 (2007) 389–398.

[70] J.A. Villajos, C-Journal of Carbon Research 8 (2022) 5.

CHAPTER 6

Future Research Scope

Both the MOFs and COFs have emerged as highly promising materials in recent years, demonstrating significant potential for novel applications such as gas separation and storage, drug delivery, CO_2 capture, photocatalysis, and electrocatalysis. Computational materials science, physics and materials chemistry play an important role in providing molecular-level insights into their performance and highlighting the structural features and mechanisms for various applications. The impact of pore sizes, topology, functional groups, and configurational modifications of MOFs and COFs on gas storage, adsorption and separation processes, CO_2 capture, H_2O harvesting and catalytic activities can be explored using computational simulations.

6.1. Linker functionalization and node modification

We propose that future studies focus on linkage engineering to enhance the structural stability and functional performance of these porous materials, which makes them more effective in real-world applications.[1] Incorporating halogen, -OH, and -NH_2 groups into the organic ligands of MOFs has been shown to enhance gas adsorption and separation performance.[2] Similarly, mixed-metal nodes in MOFs have received significant attention for enhancing host-guest interactions and thereby increasing binding strength.[3,4] Our focus will be to apply the same strategies in novel MOF materials from the computational database and to predict their gas adsorption behavior and various temperature-pressure conditions.

6.2. Designing of hybrid materials and MOF-COF composites

The design of hybrid materials would be an effective approach to improve catalytic efficiency. Integrating COFs with other materials, such as graphene, carbon nanotubes, and MOFs, results in advanced composites with extraordinary performance.[5–7] Our future studies should aim to develop high-throughput computational screening approaches to identify the most suitable MOFs and COFs for specific applications. Some previous studies reported that MOF–COF composites show remarkable catalytic activity in various chemical reactions due to the

synergistic interplay between their constituent structures.[6,7] This synergy arises from the complementary functionalities of MOFs and COFs, enabling unique reaction pathways and enhanced performance compared to their individual components.

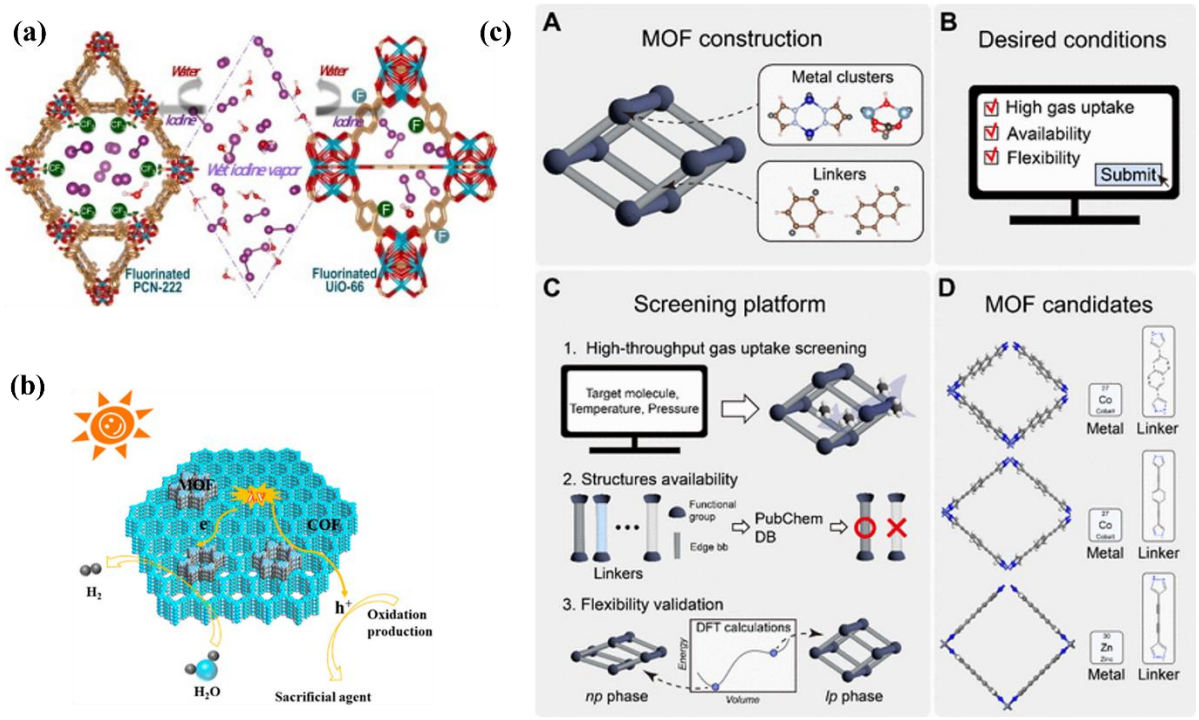

Figure 6.1. *Fluorinated metal–organic frameworks PCN-222 and UiO-66,[8] (b) MOF/COF hybrid photocatalysts,[9] (c) data-driven design of flexible metal−organic frameworks for gas storage.[10]*

One key advantage of MOF–COF composites is their ability to facilitate multistep catalytic processes within a single framework. For instance, Zhao *et al*. developed a layered catalytic system in which palladium nanoparticles (Pd NPs) were embedded within a UiO-66-NH_2 MOF core and encapsulated by a COF outer shell, forming the Pd/UiO-66-NH_2@COF composite.[11] This structure displayed exceptional catalytic efficiency for olefin hydrogenation, with the COF shell acting as a size-selective barrier, ensuring selective substrate access and improved reaction control. By tuning the pore size, electronic properties, and functionalities of MOFs and COFs, a highly efficient, multifunctional catalytic system can be rationally designed for environmental and industrial applications. Computational simulations could also play a crucial role in understanding reaction mechanisms and guiding the rational design of next-generation MOF–COF composites.

6.3. High-throughput computational screening and development of force fields for flexible frameworks

A major challenge that persists is the long-term stability of MOFs under demanding operational environments. Overcoming these limitations requires interdisciplinary collaboration that integrates characterization, synthesis, theory and computation. The integration of machine learning (ML) algorithms with artificial intelligence (AI) models has already transformed the screening and discovery process of MOFs and COFs.[12–14] By integrating ML algorithms with a large computational database, researchers can effectively identify potential candidates for diverse energy-related applications. Molecular simulations coupled with data-driven methods are a powerful tool for accelerating the design and discovery of MOFs for a wide range of applications, particularly gas adsorption. However, several approximations are typically made to reduce computational cost.

Recently Song *et al.* reported a machine learning-guided framework for identifying and optimizing MOFs for volumetric methane storage. An Extra Trees Regressor trained on grand canonical Monte Carlo simulation data from the CoRE MOF 2024 database achieved an R^2 of 0.96, enabling high-throughput computational screening. UMCM-4, MUF-8, and MOF-5 emerged as top candidates, with experimentally measured working capacities of 225, 225, and 231 $cm^3(stp)\ cm^{-3}$, respectively, that align closely with model predictions.[15] Another study integrates GCMC simulations with machine learning to predict hydrogen storage performance across a dataset of 98,695 MOFs under temperature–pressure swing conditions. Feed-Forward and Pattern Recognition neural networks, optimized using the Equilibrium Optimizer and Genetic Algorithm, were employed to model both gravimetric and volumetric storage capacities with high fidelity. Structural analysis identified pore volume and void fraction as the most influential descriptors governing hydrogen uptake. Large-scale screening through this integrated framework identified 12 MOFs that surpass the benchmark MOF-5, achieving gravimetric and volumetric capacities exceeding 8.27 wt.% and 51.94 g-H_2/L, respectively. The work shows that coupling physics-based simulation with ML-driven optimization offers a computationally efficient and reliable route for accelerating the discovery of next-generation hydrogen storage materials.[16]

High-throughput computational screening (HTCS) studies often treat MOFs as rigid, defect-free crystals, whereas real MOFs are flexible and often contain structural defects. Considering such flexibility in MOFs significantly increases computational time and cost. Most HTCS studies rely on generic force fields, such as the universal force field (UFF), to describe interactions between gas molecules and framework atoms in MOFs. These models may fail to capture specific interactions in MOFs with open metal sites and unique functional groups with the polarized gas molecules (e.g. CO_2), indicating the urgent need for specialized force fields to achieve more accurate framework-guest interaction descriptions. To overcome the limitations of generic force fields, researchers are increasingly integrating density functional theory (DFT) to fit the interaction potentials and provide accurate energy predictions in flexible MOFs.[17] Incorporating DFT-derived potential energy surfaces into Grand Canonical Monte Carlo (GCMC) simulation significantly enhances the reliability of adsorption predictions by improving the parametrization of force fields. Recently, Yang *et al.* addressed a fundamental limitation in existing CO_2 adsorption databases by replacing conventional Lennard-Jones force fields with a physically rigorous van der Waals force field based on the Exp-PE potential, which more accurately captures CO_2-CO_2 and CO_2-framework interactions, particularly at high pressure. A high-fidelity adsorption database was constructed on this basis, and quadrupole-responsive descriptors were introduced to explicitly account for anisotropic electrostatic character of CO_2, yielding measurable improvements in machine learning predictive accuracy. Large-scale screening of COF and MOF structures using this framework identified COF-50 and COF-364 as exceptional candidates, with CO_2 working capacities of 13.58 and 12.43 mol/kg, respectively, surpassing those of all currently reported porous materials. [18]

6.4. Combination of computational insights and theoretical predictions with real-world MOF synthesis

Despite significant computational progress, only a limited fraction of computationally predicted MOFs from various databases have been experimentally synthesized. Challenges such as chemical and thermal stability, as well as stability in humid conditions, hinder the translation of computational discoveries into experimental realization. Overall, the future of MOF and COF research demands close collaboration among computational scientists,

experimentalists, and data scientists. By combining advanced simulations, robust machine learning frameworks, and an open-access database, researchers can enhance reproducibility, accelerate discoveries, and bridge the gap between theoretical predictions and real-world performance in adsorption and catalysis applications in the near future.

6.5. References

[1] Y. Cai, A.R. Kulkarni, Y. Huang, D.S. Sholl, K.S. Walton, Crystal Growth & Design 14(2014) 6122-6128.

[2] M. Batista, A. Karmakar, A.A.C.D. Santos, N. Pagliaricci, E.C.B.A. Alegria, A. Martin-calvo, J. Jos, S. Calero, M. F, C. Guedes, R. Pettinari, A.J.L. Pombeiro, ACS Applied Materials & Interfaces 16(2024) 20626-20641.

[3] X. Li, G. Xiong, M. Shi, Y. Wang, L. Wang, Z. Gu, W. Zhu, Y. Zhang, Inorganic Chemistry 64(2025) 11155-11164.

[4] M. Burud, S.A. Patil, V. Jadhav, P. Chougale, S. Mane-gavade, R. Ustad, J. Shen, A. Supale, S. Sabale, D. Kim, Energy and Fuels 39(2025) 13648-13657.

[5] J. Xu, W. Tang, C. Yang, I. Manke, N. Chen, F. Lai, T. Xu, S. An, H. Liu, Z. Zhang, Y. Cao, N. Wang, S. Zhao, D. Niu, R. Chen, ACS Energy Letters 6(2021) 3053-3062.

[6] J. Fu, S. Das, G. Xing, T. Ben, V. Valtchev, S. Qiu, Journal of the American Chemical Society 138(2016) 7673-7680.

[7] Q. Xin, Y. Wang, X. Zhang, D. Wu, M. Wang, W. Huang, K. Wan, J. Wu, X. Wang, N. Gao, Y. Zhang, ACS Applied Materials & Interfaces 17(2025) 64898-64909.

[8] W. Zhang, J. Zhang, X. Dong, M. Li, Q. He, S. Zhao, Chemical Engineering Journal 461 (2023) 142058.

[9] P. Xue, X. Pan, J. Huang, Y. Gao, W. Guo, J. Li, M. Tang, Z. Wang, ACS Applied Materials & Interfaces 13(2021) 59915-59924.

[10] Y. Lim, B. Kim, J. Kim, Chemistry of Materials 36(2024) 5465-5473.

[11] J. Yuan, L. Zhang, X. Zhang, ACS Applied Energy Materials 8(2025) 10311-10320.

[12] F. Fajardo-rojas, R. Anderson, M. Li, R. Chang, A.G. Diego, Chemistry of Materials 37(2025) 5502-5514.

[13] Z. Xuan, Industrial & Engineering Chemistry Research 64(2025) 2926-2936.

[14] S. Ge, Z. Wang, J. Pei, Journal of Chemical Information and Modelling 65(2025) 11778-11795.

[15] M. Song, R. Gao, J. Huang, Y. Li, K. Wang, C. Hou, H. Wang, H. Lei, Z. Luo, C. Shu, Y. Guo, Q. Pang, B. Tu, Journal of the American Chemical Society (2026).

[16] S. Khairandesh, M. Lotfi, A. Larimi, et al. Scientific Reports 16 (2026), 14114.

[17] R. Zheng, X. Wu, S.A. Mohamed, J. Jiang, Chemistry of Materials 37(2025) 4807-4817.

[18] Y. Lang, Y. Pan, M. Xu, X. Wei, R. Duan, S. Li, D. Zhai, L. Sun, W. Deng, Li. Yang, Journal of Chemical Theory and Computation 22 (2026) 3023–3031.

Appendix-A

Crystallographic Information Files (.cif) of MOFs

(a) Mn_2(*m*-dobdc)

data_Mn_2(*m*dobdc)
_audit_creation_date 2024-11-11
_audit_creation_method 'VESTA'
_symmetry_space_group_name_H-M 'R3M'
_symmetry_Int_Tables_number 160
_symmetry_cell_setting trigonal
_cell_length_a 25.6825
_cell_length_b 25.6825
_cell_length_c 6.6889
_cell_angle_alpha 90.0000
_cell_angle_beta 90.0000
_cell_angle_gamma 120.0000
loop_
_atom_site_label
_atom_site_type_symbol
_atom_site_fract_x
_atom_site_fract_y
_atom_site_fract_z
_atom_site_charge

C001	C	0.20828	0.32204	-0.17020	0.396
C007	C	-0.13425	-0.36282	-0.04057	-0.386
C013	C	-0.09097	-0.36844	-0.16604	0.523
MN019	Mn	-0.29615	-0.00713	0.11496	1.062
O025	O	0.26022	0.33679	-0.07574	-0.530
O031	O	-0.03772	-0.34977	-0.09733	-0.584
O037	O	-0.43863	-0.05607	-0.00827	-0.474
C043	C	0.16406	0.32812	-0.07050	-0.366
H046	H	0.17172	0.34345	0.08278	0.133
C049	C	-0.18607	-0.37214	-0.13428	0.245
H052	H	-0.19290	-0.38579	-0.28902	-0.014

(b) Fe_2(*m*-dobdc)

data_Fe_2(*m*dobdc)
_audit_creation_date 2025-04-17

```
_audit_creation_method                   'VESTA'
_symmetry_space_group_name_H-M    'R3M'
_symmetry_Int_Tables_number      160
_symmetry_cell_setting           trigonal
_cell_length_a                   25.6484
_cell_length_b                   25.6484
_cell_length_c                   6.7678
_cell_angle_alpha                90.0000
_cell_angle_beta                 90.0000
_cell_angle_gamma                120.0000
loop_
_atom_site_label
_atom_site_type_symbol
_atom_site_fract_x
_atom_site_fract_y
_atom_site_fract_z
_atom_site_charge

C001   C    0.33473   0.21531  -0.08647    0.352
C007   C    0.01922  -0.44281   0.04376   -0.336
C013   C   -0.30701  -0.06046   0.24921    0.493
FE019  Fe   0.00879  -0.28857  -0.13283    0.922
O025   O    0.32043   0.25208   0.01155   -0.462
O031   O    0.00919  -0.35740  -0.01707   -0.544
O037   O   -0.28639  -0.05519   0.07616   -0.437
C043   C    0.32857   0.16429   0.01009   -0.317
H046   H    0.31387   0.15694   0.16237    0.128
C049   C   -0.30519  -0.15260   0.28546    0.212
H052   H   -0.29176  -0.14588   0.13224   -0.001
```

(c) Co_2(*m*-dobdc)

```
data_Co2(mdobdc)
_audit_creation_date                    2024-11-11
_audit_creation_method                  'VESTA'
_symmetry_space_group_name_H-M    'R3M'
_symmetry_Int_Tables_number       160
_symmetry_cell_setting            trigonal
_cell_length_a                    25.8734
_cell_length_b                    25.8734
_cell_length_c                    6.7677
_cell_angle_alpha                 90.0000
_cell_angle_beta                  90.0000
```

```
_cell_angle_gamma          120.0000
loop_
_atom_site_label
_atom_site_type_symbol
_atom_site_fract_x
_atom_site_fract_y
_atom_site_fract_z
_atom_site_charge
C001    C     0.21163    0.32437   -0.17033    0.901
C007    C    -0.13390   -0.36090   -0.04000    0.383
C013    C    -0.09120   -0.36780   -0.16320   -0.359
CO019   Co   -0.29107   -0.00513    0.11067    0.475
O025    O     0.25963    0.33657   -0.08133   -0.496
O031    O    -0.03840   -0.34850   -0.09610   -0.502
O037    O    -0.44213   -0.05687   -0.00067   -0.416
C043    C     0.16598    0.33197   -0.07733   -0.321
H046    H     0.17313    0.34627    0.07867    0.117
C049    C    -0.18595   -0.37190   -0.12500    0.239
H052    H    -0.19135   -0.38270   -0.28200   -0.007
```

(d) Ni_2(*m*-dobdc)

```
data_Ni2(mdobdc)
_audit_creation_date                    2024-11-11
_audit_creation_method                  'VESTA'
_symmetry_space_group_name_H-M          'R3M'
_symmetry_Int_Tables_number             160
_symmetry_cell_setting                  trigonal
_cell_length_a                25.9066
_cell_length_b                25.9066
_cell_length_c                6.1485
_cell_angle_alpha             90.0000
_cell_angle_beta              90.0000
_cell_angle_gamma             120.0000
loop_
_atom_site_label
_atom_site_type_symbol
_atom_site_fract_x
_atom_site_fract_y
_atom_site_fract_z
_atom_site_charge
C001   C     0.11767   -0.21122   -0.15061    1.235
```

C007	C	-0.22732	0.13460	-0.02849	0.393
C013	C	-0.26900	0.08905	-0.17755	-0.409
NI019	Ni	0.28073	0.28514	0.09991	0.558
O025	O	0.08019	-0.26458	-0.05579	-0.590
O031	O	-0.28187	0.03501	-0.15622	-0.632
O037	O	0.38025	0.43876	-0.00974	-0.551
C043	C	0.16903	-0.16903	-0.04302	-0.35
H046	H	0.17845	-0.17845	0.11867	0.126
C049	C	-0.18805	0.18805	-0.12558	0.263
H052	H	-0.19622	0.19622	-0.29048	-0.016